WASM: Minerals, Energy and Chemical Engineering

Electrokinetic Measurements in Intact Core Samples at Reservoir Conditions with the Application to CO2 Geological Storage

Miftah Hidayat

This thesis is presented for the collaborative Degree of
Doctor of Philosophy
of

University of Aberdeen
and

Curtin University

February 2023

Declaration

I declare that this thesis is my own work and composed by me under the supervision of Dr Jan Vinogradov, Dr Mohammad Sarmadivaleh, Dr David Vega-Maza, Professor Jos Derksen and Professor Stefan Iglauer. The work was performed at the University of Aberdeen and Curtin University, as part of collaborative joint PhD program. This thesis has not been accepted in any previous application for a degree and all sources of information are fully acknowledge

Signature:

Name and date: Miftah Hidayat, February 2023

Abstract

Carbon geological storage (CGS) defined as a practice of injecting CO_2 into subsurface formations to reduce anthropogenic CO_2 emissions in the atmosphere. This option has become popular in recent years as the technology has been successfully implemented in the several subsurface formations (e.g., Sleipner gas field in Norway). However, some scientific aspects still need improvements in order to minimise the risks associated with the implementation of CGS projects. One of the main issues in deploying CGS projects is to ensure the security of storage and to maximise the efficiency of CGS. To maximise the capacity and minimise the risk of CO_2 leakage, an essential property called the wettability of geological target formations must be accurately evaluated. In subsurface settings containing CO_2, the wettability is controlled by the interactions of rock surface-CO_2-water interfaces. These interactions can be characterised by an electrical property termed the zeta potential.

This dissertation reports a fundamental study of the zeta potential under typical CGS conditions, characterised by high pressure and elevated temperature conditions. Novel measurements of zeta potential using the streaming potential method in intact rock samples under supercritical CO_2 conditions are presented. To cover a broad range of potential CGS sites, the measurements were conducted at various experimental conditions covering single- and multi-phase flows, broad ranges of pressure, temperature, amount of dissolved CO_2, compositional variety of aqueous solutions and rock mineralogy. Additionally, a new surface complexation model that provides important insights into complex interactions between different fluids and minerals**,** thus explaining the underlying physics of the zeta potential**,** was developed and validated.

The first part of this dissertation reports the single-phase zeta potential measurements, where the investigations were conducted in an intact 'clean' (99 wt.% quartz) and 'clayey' (1 wt.% - 4 wt.% clay content and 2 wt.% - 6 wt.% feldspars content) sandstone using two pore water conditions, namely the 'dead water' defined as an aqueous solution equilibrated with atmospheric CO_2, and the 'live water' defined as an aqueous solution equilibrated with pure CO_2 at elevated temperature and high pressure consistent with CGS conditions. In addition, to investigate the effect of fractures combined with the impact of feldspars and micas in rocks, single-phase dead water zeta potentials were measured on a fractured gneiss sample under varying confining pressures. The results show that the zeta potential of dead and live water in clean sandstone is controlled by water pH. The temperature, salts type, and dissolved CO_2 affected the water pH thus indirectly affecting the zeta potential. At the same time, the zeta potential of dead and live solutions in the clayey sandstone was less negative compared to that measured in the clean sandstone under identical conditions, which was attributed to the

presence of clays and feldspars. Furthermore, the dead water zeta potential in the fractured gneiss sample was found to be unique and dissimilar to the data obtained for clean and clayey sandstones or carbonates. This result is explained by the presence of micas and feldspars in gneiss sample, both of which were reactive with multi-valent ions in the solution.

In the second part of the dissertation the multi-phase zeta potential in intact clean sandstone under supercritical CO_2 conditions investigated. A novel experimental methodology was developed to accommodate the injection of supercritical CO_2 into a rock sample fully saturated with live water. At residual CO_2 saturation, the results demonstrate that the zeta potential of CO_2-water interfaces had a significant contribution to the overall multi-phase zeta potential when the wetting state shifted from water-wet to more CO_2-wet. In contrast, the contribution of the zeta potential of CO_2-water interface became less significant when the wettability of the system shifted toward more water-wet.

Lastly, the dissertation concludes with a new surface complexation model developed in order to understand the behavior of the calcite-water zeta potential over a wide range of ionic strength and chemical composition. A novel approach of decreasing capacitance with increasing ionic strength was implemented to simulate the zeta potential. Moreover, the new model was tested for accurately predicting calcite-water zeta potentials at equilibrium and non-equilibrium conditions, given the concentration of all ionic species were provided. The predictions were successfully validated against published experimental data.

The results produced from this research are essential for improved understanding of zeta potential, particularly in characterising wettability of the subsurface geological settings for CGS applications. The obtained measurements of the zeta potential combined with the improved understanding of the complex electrochemical interactions from modelling, provide important insights in how some conditions including water composition and salinity, pressure, temperature and the amount of dissolved CO_2 affect the zeta potential. Moreover, the effect of specific ions presents in the water and having an impact on the zeta potential and therefore, the wetting state of CO_2-water-rock systems is also investigated. The reported results improve our understanding of the relationship between the zeta potential and wettability, hence providing a means for assessing the suitability of the potential storage formations and evaluating the efficiency and the security of CGS projects.

Acknowledgements

I would like to express my sincere gratitude to my supervisor, Dr Jan Vinogradov, for his never-ending support, encouragement, and guidance throughout my PhD studies. My special thanks are also extended to my supervisor at Curtin University, Dr Mohammad Sarmadivaleh, for his help and assistance during my stay in Perth, Australia. I would also like to thank my co-supervisors, Dr David Vega-Maza, Professor Jos Derksen and Professor Stefan Iglauer, for their time and valuable discussion throughout my research project. Special thanks go to Dr Philippe Leroy, Dr Damien Jougnot and Dr Mohamed Azaroual for their time and valuable insight regarding the surface complexation model. Also, Dr Jean-Christophe Comte, Dr David Healy and Yogendra Kumar for their fruitful discussion and collaboration on fractured rocks. I thank Professor Abbie McLaughlin for her help in XRD measurement and Mr John Still for helping in SEM analysis.

I would like to acknowledge my sponsor, Aberdeen-Curtin Alliance, for the financial support during my PhD studies. Big thanks to Dr Stephen Hill and Mr Vimal Subramanian for their help in the Alliance. In addition, I would also like to thank the Edith Cowan University for funding the design, manufacturing and testing of the experimental setup through RG14747 research grant awarded to the University of Aberdeen. Furthermore, I would like to express my gratitude to Dr Yukie Tanino from University of Aberdeen as my internal examiners for taking her time to review this thesis. My gratitude is also extended to Professor Matthew Jackson from Imperial College London, Professor Christoph Arns from UNSW Sydney and Dr Stephanie Vialle from Curtin University for their valuable input and feedback to improve this thesis.

Lastly, I would like to say a huge thanks and my sincere appreciation to everyone for helping me in anyways during this journey so that I could finish this thesis.

Publications

Journal Articles

- *Hidayat, M., Sarmadivaleh, M., Derksen, J., Vega-Maza, D., Iglauer, S. and Vinogradov, J., 2022. Zeta potential of CO_2-rich aqueous solutions in contact with intact sandstone sample at temperatures of 23 C and 40 C and pressures up to 10.0 MPa. Journal of Colloid and Interface Science, 607, pp.1226-1238. Candidate contribution: Design of experiments, Investigation, Formal analysis, Validation, Visualization, Writing – original draft, Writing – review & editing.*

- *Hidayat, M., Sarmadivaleh, M., Derksen, J., Vega-Maza, D., Iglauer, S. and Vinogradov, J., 2022. Zeta potential of a natural clayey sandstone saturated with carbonated NaCl solutions at supercritical CO_2 conditions. Geophysical Research Letters, 49(15), pp.e2022GL099277. Candidate contribution: Design of experiments, Investigation, Formal analysis, Validation, Visualization, Data curation, Writing – original draft, Writing – review & editing.*

- *Vinogradov, J., Hidayat (corresponding author), M., Sarmadivaleh, M., Derksen, J., Vega-Maza, D., Iglauer, S., Jougnot, D., Azaroual, M. and Leroy, P., 2022. Predictive surface complexation model of the calcite-aqueous solution interface: The impact of high concentration and complex composition of brines. Journal of Colloid and Interface Science, 609, pp.852-867. Candidate contribution: Software, Investigation, Validation, Formal analysis, Data curation, Visualization Writing – original draft, Writing – review & editing.*

- *Vinogradov, J., Hidayat, M., Kumar, Y., Healy, D. and Comte, J.C., 2022. Laboratory measurements of zeta potential in fractured Lewisian gneiss: implications for the characterization of flow in fractured crystalline bedrock. Applied Sciences, 12(1), p.180. Candidate contribution: Design of experiments, Investigation, Formal analysis, Validation, Visualization, Writing – original draft, Writing – review & editing.*

Conference Presentations

- *Hidayat, M., Vinogradov, J., Sarmadivaleh, M., Iglauer, S., Vega-Maza, D. and Derksen, J., 2023. New Insights into Underlying Mechanisms of CO_2 Wettability and Residual Saturation from Laboratory Measurements of Multi-Phase Zeta Potential in Supercritical CO_2-Rock-Brine Systems. EGU General Assembly 2023, Vienna, 23 – 28 April 2023 (abstract accepted).*

- *Hidayat, M., Vinogradov, J., Leroy, P., Jougnot, D., Derksen, J., Iglauer, S., Vega Maza, D. and Sarmadivaleh, M., 2021. Zeta potential of calcite-water interface: an improved model for high ionic strength conditions. Goldschmidt2021, Lyon (Virtual), 4-9 July 2021.*

- *Hidayat, M., Vinogradov, J., Iglauer, S., Vega-Maza, D., Derksen, J., and Sarmadivaleh, M., 2021. Streaming Potential Measurement at Supercritical CO_2 Condition. Twenty-First Symposium on Thermophysical Properties, Colorado (Virtual), 20-25 June 2021.*

- *Hidayat, M., Vinogradov, J., Iglauer, S., and Sarmadivaleh, M. Evolution of Modelling Zeta Potential: Impact of Brine Compositions and Concentration, EGU General Assembly 2020, Vienna, 4 – 8 May 2020.*

- *Vinogradov, J., Hidayat, M., Iglauer, S., Sarmadivaleh, M., and Vega-Maza, D. Zeta potential of calcite-brine interface - new insights into the effect of brine composition and concentration. AGU Fall Meeting, 9 – 13 December 2019, San Francisco, California, USA.*

- *Hidayat, M., Vinogradov, J., Vega-Maza, D., Iglauer, S., and Sarmadivaleh, M., 2018. Electrokinetic measurements in intact core samples at reservoir conditions with the application to CO_2 injection for enhanced oil recovery and geological storage. ETP Annual Conference, 29th October 2018, Glasgow, Scotland, United Kingdom.*

Table of Contents

List of Tables

List of Figures

Chapter 1 General Introduction

1.1. Background

A recent global meeting of the COP (Conference of the Parties) 26 brought numerous countries together to get them to commit to tackling climate change by reducing greenhouse gas (CO_2) emissions in the atmosphere. The US National Oceanic and Atmospheric Administration (NOAA) has reported that the carbon dioxide (CO_2) concentration in the atmosphere reached 417 ppm (parts per million) in March 2022 (*NOAA,* 2022), indicating an increase of nearly 30% over the last half century. This constant increase in CO_2 content has become a significant contributor to increases in the earth's temperature (*Davis et al.,* 2010; *Leduc et al.,* 2016). Therefore, to prevent further catastrophic impacts on our planet, this research will focus on improving our understanding of the application of CO_2 injections for carbon geological storage application.

Carbon geological storage (CGS) has been identified as one of the key solutions for reducing anthropogenic greenhouse gas (CO_2) emission in the atmosphere (*IPCC,* 2005). CGS is part of the complex process known as carbon capture and storage. Generally, the overall carbon capture and storage process is divided into three main stages, including (e.g., *Pires et al.,* 2011; *Raza et al.,* 2019; *Ali et al.,* 2020):

i. 'Capturing' CO_2. At this stage, CO_2 is captured directly from the atmosphere and/or significant sources of CO_2, such as fossil fuel/coal power plants and the cement industry. Then, the captured CO_2 is processed and compressed before transporting it safely to storage sites.

ii. 'Transporting' CO_2 via a network of pipelines and/or cargo ships to the storage sites.

iii. 'Storing' CO_2 by injecting it into suitable geological subsurface formations so that CO_2 remains underground permanently.

According to the recent report published by the International Energy Agency (IEA), the total global CO_2 emission in 2021 was 36.3 giga tonnes (Gt), which increased by 2.1 Gt from 2020 levels (*IEA*, 2022). Further, a report from Global Carbon Capture and Storage Institute showed an increasing trend of the development of commercial carbon capture and storage facilities worldwide from 60 million tonnes a year (Mtpa) of capture capacity in 2017 to 149 Mtpa in September 2021 (*Global CCS Institute,* 2021). Moreover, the potential storage capacity in sedimentary formations is in the range of 5,000 – 25,000 Gt of CO_2 worldwide (*de Connick and Benson,* 2015). Considering the enormous potential in subsurface storage formations combined with a growing number of carbon capture and storage facilities, tackling climate change becomes viable.

Despite the rapid development of CGS projects, two challenges have been identified that are hampering the progress. Firstly, the biggest question remains as to whether CGS is safe to implement. The fear of CO_2 leakage from storage sites and concerns as to whether the CGS project might fail to reduce atmospheric CO_2 are major obstacles (*IPCC*, 2018).

Secondly, there are concerns as to whether the project of carbon capture and storage can be made commercially viable, as stated in the report by *Butler* (2020). Therefore, some help from the government in the development stages, such as incentives, becomes an essential pre-condition for project feasibility.

As a researcher working on the engineering side, this dissertation will address the first challenge of how to safely store CO_2 in subsurface formations without fearing any leakage. Numerous studies have been carried out in the past to understand the parameters affecting CO_2 behaviour in the subsurface. Many of them reported the wettability of the subsurface system as one of the important factors that dictate CO_2 flow behaviour in the subsurface formations (*Al-Khdheeawi et al.,* 2017; *Al-Khdheeawi et al.,* 2018; *Valle et al.,* 2018), hence defining the efficiency of CO_2 trapping mechanisms. Research related to the impact of wettability on CGS is still on-going thus indicating that the phenomenon is still not fully understood. Therefore, investigating the wettability of the subsurface system when CO_2 interacts with subsurface rocks and formation water from more fundamental perspectives can potentially lead to an improved understanding of this complex process and a more successful CGS project.

Wettability controls the behaviour of CO_2 in underground storage formations. After CO_2 is injected, it will interact with formation water and rock minerals and disturb the equilibrium condition in the subsurface system. As CO_2 is less dense than formation water, CO_2 will move upward, and therefore excellent impenetrable sealing rocks are required to hold CO_2 stay in place. In order to prevent CO_2 from penetrating the sealing rocks, which will lead to leakage, the wetting state of the sealing rocks has to be wetted completely by water, so that CO_2 as a non-wetting phase is had to have a high capillary entry pressure to be able to displace it.

Furthermore, the wettability of the subsurface system is not fixed. Several parameters, including pressure, temperature, formation water compositions, rock mineralogy and dissolved CO_2 in the formation water, are reported to affect the wettability. Therefore, to improve the understanding of wettability and its impact on CGS application, this dissertation comprises a description of the fundamental principles characterising the wettability in potential rock formations as a function of various parameters mentioned above. The results obtained from this study provide meaningful insights into underlying physico-chemical mechanisms

responsible for CO_2-water-rock wettability and therefore, are helpful in designing future CGS projects in a safer and more efficient way.

1.2. Aim and objectives

In order to safely store CO_2 in subsurface geological formations, the wettability of the potential rock samples must be characterised accurately. The wettability is affected by the interaction between formation water and CO_2/mineral of rock surface at the interfaces. These interactions (i.e., electrostatic interaction) play a key role in thermodynamics of wettability (*Jackson et al.,* 2016a; *Hirasaki,* 1999) and it can be characterised using an electrical property known as the zeta potential.

The aim of this research is to improve the understanding of the zeta potential at reservoirs conditions consistent with CGS applications. This dissertation consists of two primary investigations using experimental and numerical approaches with four main novelties, namely the use of live water (CO_2-rich water) for single-phase experiments, combining immiscible supercritical CO_2 with live water in multi-phase experiments, using dead water for single-phase experiments in a fractured rock system and developing a reliable surface complexation model for carbonates. The development of a surface complexation model in carbonates was based on the adsorption reactions between calcite surface sites and ions in the aqueous solution.

To fulfil the research aim, the objectives of the experimental investigation are as follows:

- To acquire new data on live water-quartz zeta potentials. It is widely known that quartz is the main mineral in sandstones, which is one of the potential sedimentary rocks to store CO_2. To date, there have been no experimental measurements of the zeta potential in a live water-quartz system. Therefore, the experiment is started by using an intact clean (pure quartz) sandstone sample saturated with CO_2-rich water. Note that clean sandstone is also stable under low pH conditions, pH range of 1.0 – 4.0 (*Crundwell,* 2017), which is good as a starting point of the investigation as there have been no published studies before.

- To acquire new data on live water-clayey sandstone zeta potentials. A significant amount of other minerals such as clays and feldspars in sandstone have been shown to significantly impact the measured zeta potential (e.g., *Li et al.,* 2018; *Alarouj et al.,* 2021). However, there are no available data on the zeta potential under the conditions typical for CO_2 sequestration applications. Therefore, the changes in the zeta potential of clayey sandstone samples saturated with CO_2-rich water will be investigated.

- To acquire new data on the zeta potential of an intact clean sandstone sample when both live water and supercritical CO_2 are present in the pore space. The investigation

focuses only on live water-quartz system, in this experiment, supercritical CO_2 is injected into the rock sample as a separate phase. The experiment aims to elucidate the zeta potential of a live water-rock-CO_2 system and its relationship to wettability.

- To acquire new data on the zeta potential of an intact fractured gneiss sample with unique mineralogy. Fractured rock is mostly found in subsurface settings. Having a fracture in rocks leads to a potential leakage in the CGS project and affects the flow pathways. Hence, this experimental investigation aims to understand the effect of the fracture aperture on the zeta potential. Moreover, the uniqueness of gneiss mineralogy also provides new insights into how different minerals affect the zeta potential of gneiss compared to other rock samples. Therefore, the gneiss sample in this study, although not a typical rock of formations relevant to CGS, served as a test-rock for investigating the effect of multiple minerals and fracture, both of which are abundant in the subsurface formations.

Furthermore, the objective of the numerical investigation is as follows:

- To investigate the physical mechanisms behind the behaviour of the zeta potential in a wide range of ionic strength and complex brine compositions using the surface complexation model. Although the modelling approach was developed for carbonates (carbonates are also recognized as potential sedimentary target formations for the CGS projects), the proposed and validated physical mechanism of decreasing capacitance with the ionic strength of the solution can be implemented for all other rocks.

1.3. Thesis outline

Chapter 2 is a literature review. It discusses CO_2 injection into subsurface settings and explains CO_2 trapping mechanisms. This chapter also addresses the link between wettability and two primary trapping mechanisms, which yield to storage capacities and containment security. Furthermore, the theory of wettability, the electrical double layer, the zeta potential, and experimental evidence of the relationship between the zeta potential and wettability are presented. In addition, the main differences between the two main methods used to measure zeta the potential, namely the electrophoretic mobility method and the streaming potential method, are presented.

Chapter 3 reports novel data on the zeta potential of CO_2-rich aqueous solutions on natural clean sandstone at temperatures of 23°C and 40°C and pressures up to 10.0 MPa. The chapter describes the development of a new experimental methodology to measure the zeta potential in an intact sandstone sample using the streaming potential method under high

pressure and elevated temperature conditions. The chapter also addresses the difference between ‘dead’ and ‘live’ water experiments and the impact of different pressures, temperatures, water compositions and dissolved CO_2 on the zeta potential.

Chapter 4 presents novel data on the zeta potential of a CO_2-rich NaCl solution on natural clayey sandstone at supercritical CO_2 conditions. The chapter aims to understand the impact of a different mineralogy on the zeta potential using a simple NaCl solution saturated with CO_2 at the high pressure and elevated temperature typical for CO_2 geological sequestration.

Chapter 5 features novel multi-phase experimental zeta potential data from an intact clean sandstone sample at supercritical CO_2 conditions. An experimental protocol featuring multi-phase experiments is developed to accommodate the injection of supercritical CO_2 as the immiscible phase. The chapter also examines the relationship between the zeta potential of rock-water and CO_2-water interfaces under fully saturated live water and residual conditions. The zeta potentials of these two interfaces are then interpreted and normalised to find their links to wettability and CO_2 recovery.

Chapter 6 reports the first time measurement of zeta potential on an intact fractured gneiss sample. This chapter addresses the effect of different confining pressures, and water compositions along with the uniqueness of gneiss mineralogy on the measured zeta potential. Despite the fact that the zeta potential data on fractured gneiss rocks is rare and not as mature as sedimentary rocks, this chapter sheds light on the zeta potential of a fractured system, which is useful for the characterisation of other fractured rocks (e.g., carbonates) and provides new information from the mineralogy perspective.

In chapter 7, the result of numerical investigation via surface complexation model to predict zeta potential at calcite-water interfaces is presented. The chapter presents the detailed development of the surface complexation model for simulating the zeta potential under a wide range of ionic strengths and complex water conditions. The simulated zeta potentials match up well with multiple experimental zeta potentials under equilibrium and non-equilibrium conditions. Moreover, we propose a new physical explanation of the effects of high salinity on the zeta potential.

Lastly, in Chapter 8, the results from Chapter 3 – Chapter 7 are summarized. Also, the key conclusions regarding the zeta potential and wettability on CGS applications are presented here. This chapter ends with recommendations and suggestions for future wor

Chapter 2 Literature review

2.1. Carbon geological storage (CGS)

The practice of injecting CO_2 into subsurface geological formations has been investigated and implemented for decades. For example, one of the first CO_2 injection projects happened in 1972 at the Kelly-Snider oil field in Texas (*Nabi et al.,* 2019). The main objective of CO_2 injection initially was to improve oil recovery in depleted hydrocarbon reservoirs, also known as CO_2 enhanced oil recovery (EOR) method. The main advantage of using CO_2 as the injected gas is that CO_2 has low minimum miscibility pressure (MMP; is the minimum pressure of the injected gas that becomes miscible with oil at the reservoir temperature) compared to other gases (*Gozalpour et al.,* 2005). Furthermore, increasing global temperature due to increasing anthropogenic CO_2 emissions has become a major problem in recent years. Therefore, the objective of CO_2 injection was extended from only improving oil recovery through CO_2 injection to storing CO_2 in subsurface geological formations.

Carbon geological storage (CGS) is recognised as one of the promising methods to dispose of CO_2 by injecting it into subsurface geological formations for permanent storage. Several researchers have identified the subsurface sedimentary fresh and/or saline aquifers, including sandstone (*Baklid et al.,* 1996; *Leetaru et al.,* 2009; *Koukouzas et al.,* 2018) and/or carbonate formations (*Whittaker et al.,* 2003; *André et al.,* 2007; *Arif et al.,* 2017), depleted hydrocarbon reservoirs (e.g., *Benson and Cole,* 2008; *Kelemen et al.,* 2019), and coal layers (e.g., *Li et al.,* 2014; *Kou et al.,* 2021) as potential target formations (**Figure 2.1**). Recent evidence from CO_2 sequestration project in Iceland indicates that basalt rocks can also be efficient and safe hosts (*Gislason et al.,* 2010; *Snæbjörnsdóttir et al.,* 2018; *von Strandmann et al.,* 2019). Further, it is possible that other geological formations, such as granite, will be considered suitable candidates in the near future (*Liu et al.,* 2003; *Fujii et al.,* 2009; *Ré et al.,* 2014).

Focusing on deep sedimentary subsurface formations (i.e., depleted oil reservoirs and fresh/saline aquifers), CO_2 is stored in its supercritical state (critical pressure and temperature of CO_2 is 7.38 MPa and 31.1°C), as typical depths of these formations exceed 800 m (*Bruant et al.,* 2002; *IPCC*, 2005; *Iglauer*, 2018). In such conditions, CO_2 tends to move upward due to its buoyancy and therefore, carbon dioxide trapping mechanisms are required to hold CO_2 safely in place. Furthermore, there are various numbers of successful large-scale CO_2 storage projects in sedimentary formation worldwide (e.g., Sleipner; *Baklid et al.,* 1996 and Snøhvit; *Shi et al.,* 2013) and thus, proving that CGS is possible and safe.

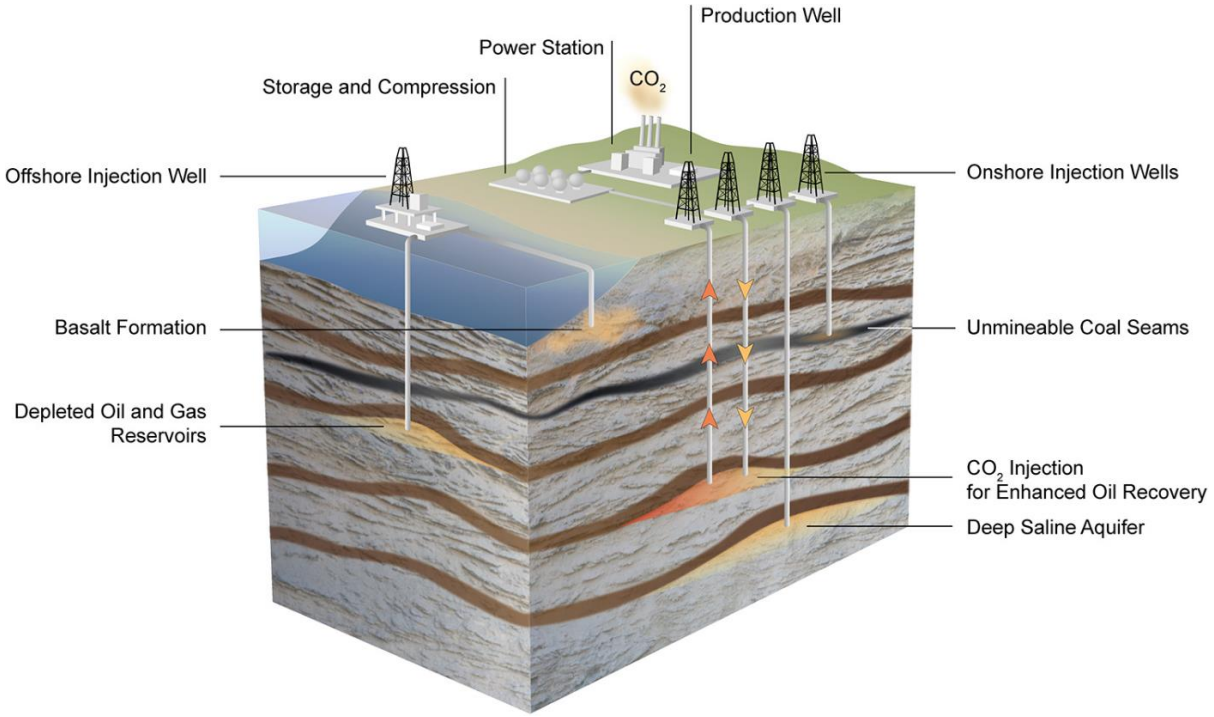

Figure 2.1. Schematic of the overall of CSS project (*Ali et al.,* 2022)

2.2. Carbon dioxide (CO_2) trapping mechanism

The efficiency of the CGS project on the potential subsurface formations depends on various trapping mechanisms. These trapping mechanisms include structural and stratigraphic trapping (e.g., *Iglauer*, 2017; *Iglauer*, 2018), residual trapping (e.g., *Juanes et al.,* 2006; *Hesse et al.,* 2008; *Qi et al.,* 2009), dissolution trapping (e.g., *El-Maghraby et al.,* 2012; *Agartan et al.,* 2015; *Soltanian et al.,* 2017; *Chen et al.,* 2018) and mineral trapping (e.g., *Matter et al.,* 2016; *Pogge von Strandmann et al.,* 2019; *Clark et al.,* 2020; *Snæbjörnsdóttir et al.,* 2020), as illustrated in **Figure 2.2**. After CO_2 is injected into the target geological formation, the trapping mechanisms operate on different time scales as CO_2 interacts with rocks and formation water over time. As a result, different trapping mechanisms provide different contribution in terms of containment security, as shown theoretically in **Figure 2.4**. Structural and residual trapping are considered the primary trapping mechanisms for the first few centuries. Therefore, understanding the parameters controlling these trapping mechanisms is crucial to assess the total storage capacity and assure its security.

2.2.1. Structural trapping

Structural trapping relies on the caprock (sealing rock), which acts as a seal/barrier and is located around the porous reservoir rock to prevent outward migration of CO_2. After CO_2 is injected into a target reservoir, due to the density difference between CO_2 and formation water, CO_2 tends to move upward and must be stopped by the caprock to inhibit leakage. Thus, the

caprock has to have a high capillary entry pressure (i.e., completely water-wet condition) to prevent the invasion of CO_2 (*Iglauer et al.,* 2015a). Therefore, understanding the wetting state of caprocks is crucial for successful deployment of CGS project.

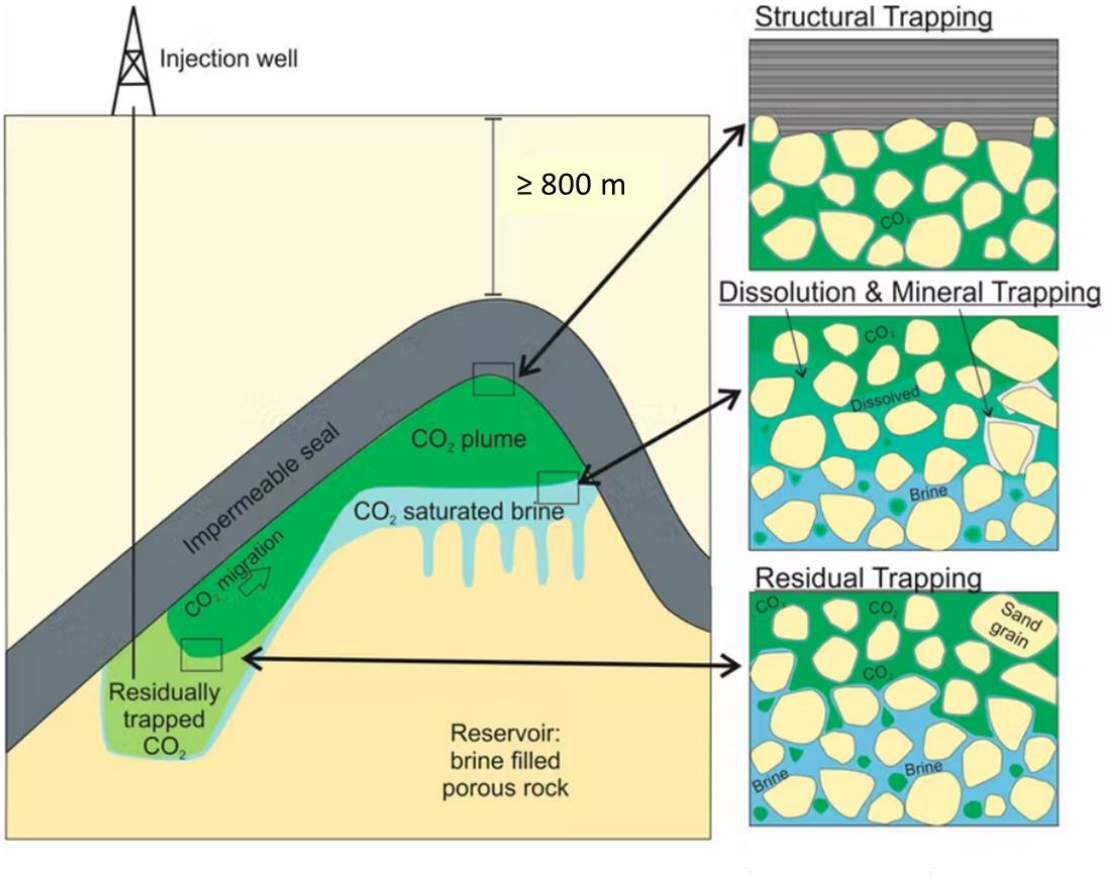

Figure 2.2. An illustration of CO_2 trapping mechanisms in the subsurface formation; the image was adapted from *Flude and Alcade* (2020)

A published study by *Iglauer et al.* (2015b) reported that the wetting state of CO_2-brine/water-rock mineral system can be classified based on contact angle measurement (see **Figure 2.3**). The detailed classification of the wetting state according to *Iglauer et al.* (2015b) are: i) complete wetting of water (water contact angle, $\theta = 0°$), ii) strongly water-wet ($\theta = 0° - 50°$), iii) weakly water-wet ($\theta = 50° - 70°$), iv) intermediate wet ($\theta = 70° - 110°$), v) weakly CO_2-wet ($\theta = 110° - 130°$), vi) strongly CO_2-wet ($\theta = 130° - 180°$) and vii) complete nonwetting of water ($\theta = 180°$).

Under ideal conditions, the caprock should remain wetted by water (completely water-wet condition) so that CO_2 stays in the reservoir rock. This assumption has been used for decades to estimate storage capacities. An experimental investigation by *Iglauer et al.* (2015a) showed that the contact angles of eight caprock samples reached up to 70° under typical subsurface

conditions (high pressure and temperature condition). These results imply that the wetting state under such conditions was likely to be either weakly water-wet or intermediate-wet, contradicting with the above assumption and thus, reducing the storage security and capacities of the geological formations. Hence, Iglauer and co-workers concluded that the wettability of cap rock-water-CO_2 system is an essential parameter for the structural trapping mechanism (*Iglauer et al.,* 2015a; 2015b, *Al-Yaseri et al.,* 2016).

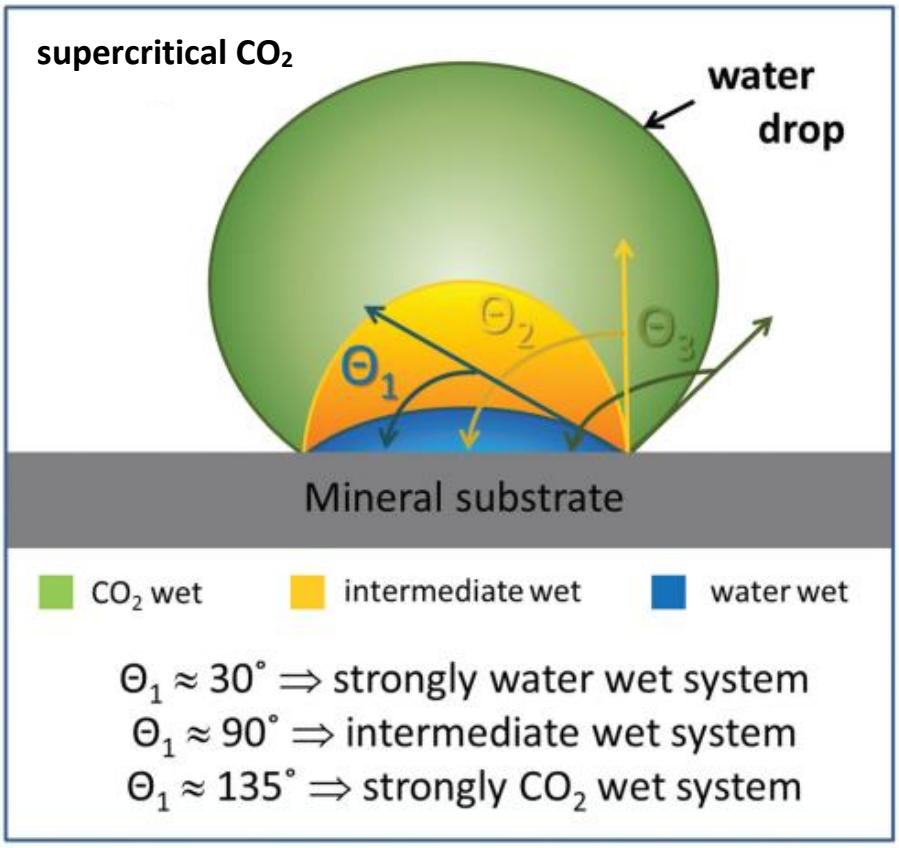

Figure 2.3. Illustration of different contact angles measurement: strongly water-wet (blue), intermediate-wet (yellow), and CO_2-wet (green); this image was adapted from *Iglauer et al. (*2015b*).*

In addition, despite the importance of the wetting state in the geological formations, rock integrity also depends on CO_2 injection pressure. A high rate of CO_2 injection can lead to overpressure condition resulting a fracture and/or fault activation in the caprock itself and provide a channel for CO_2 to escape (*Chiaramonte et al.,* 2008). Hence, the optimum CO_2 injection rate must be designed carefully by considering geomechanical rock properties of the storage formations to avoid a fracture and/or fault activation during the injection process.

2.2.2. Residual trapping

Residual trapping, also known as capillary trapping, traps CO_2 (or any other non-wetting fluid) in small clusters in the pore space. After CO_2 is injected into the target formation, it displaces the formation water in the pore space. As CO_2 behaves as a non-wetting phase, the wetting

phase (formation water) is imbibed back into the pore space filled with CO_2 (*Juanes et al.,* 2006; *Hesse et al.,* 2008). Consequently, as a result of the process known as snap-off CO_2 is separated into small clusters and gets trapped by the formation water due to capillarity, thus becoming permanently immovable.

Several studies investigated the impact of the relative permeability hysteresis on the residual (capillary) trapping mechanism (e.g., *Juanes et al.,* 2006; *Krevor et al.,* 2012). Relative permeability is a parameter used to describe multiphase flow behaviour and the wetting state in porous media. *Juanes et al.* (2006) reported that the relative permeability hysteresis must be considered in order to correctly determine the distribution of the injected CO_2 on the residual trapping. In the case of no hysteresis, the injected CO_2 migrates upward and forms a mobile gas cap at the top of the subsurface formation, while the result from the hysteresis case shows that the injected CO_2 spreads out and traps as a residual phase (*Juanes et al.,* 2006).

Furthermore, residual trapping also depends on the wetting state of the reservoir (e.g., *Soroush et al.,* 2003; *Rahman et al.,* 2016; *Al-Khdheeawi et al.,* 2017; *Al-Khdheeawi et al.,* 2018; *Valle et al.,* 2018). For example, a simulation study by *Al-Khdheeawi et al.* (2017) analysed the effects of five different wettability systems (strongly water-wet, weakly water-wet, intermediate-wet, weakly CO_2-wet and strongly CO_2-wet) on the reservoir and its impact on CO_2 storage capacity and migration in deep saline aquifers. The authors found that the contribution of residual trapping mechanism increased when the wetting state shifted from the strongly CO_2-wet condition to the strongly water-wet condition. Further, in CO_2-wet condition, CO_2 migrated upwards and created a 'candle-like shape', while the water-wet condition caused CO_2 to sink and create a 'rain-drop-shaped' plume (*Al-Khdheeawi et al.,* 2017). In addition, *Valle et al.* (2018) investigated the impact of supercritical CO_2 injections on three different sandstone samples saturated with brine. They found that more water-wet conditions are preferable for CO_2 storage (see the details of the experimental procedures and results in *Valle et al.,* 2018). Hence, based on the presented evidence, the understanding of the residual trapping mechanism is essential in order to maximise the amount of CO_2 trapped in the subsurface formations.

2.2.3. Dissolution trapping

Dissolution trapping, also known as solubility trapping, occurs when the injected CO_2 dissolves in the formation water and forms carbonic acid, which then dissociates into hydrogen and bicarbonate ions, then carbonate ions. The distribution of these species in the solution is controlled by the pH, where H_2CO_3 is dominant at pH ≤ 4, HCO_3^- is dominant for a pH within the range 6 – 9 and CO_3^{2-} become the main species at pH ≥ 10 (see Figure 6 in *Al Mahrouqi*

et al., 2017). The chemical reactions for these species are (*Zeebe and Wolf-Gladrow,* 2001; *Millero,* 2007; *Adamczyk et al.,* 2009):

$$CO_2 + H_2O \Leftrightarrow H_2CO_3 \quad 2.1$$

$$H_2CO_3 \Leftrightarrow H^+ + HCO_3^- \quad 2.2$$

$$HCO_3^- \Leftrightarrow H^+ + CO_3^{2-}. \quad 2.3$$

The amount of CO_2 that can be dissolved in formation water depends on several parameters, such as pressure, temperature, brine composition and ionic strength. Numerous experimental and numerical investigations related to the solubility of CO_2 under different conditions have been conducted to improve the understanding of this trapping mechanism (*Tong et al.,* 2013; *Zhao et al.,* 2015a, 2015b, 2015c). Also, formation water that is saturated with CO_2 becomes denser than pure water (*Garcia,* 2001; *McBride-Wright et al.,* 2015; *Calabrese et al.,* 2019). As a result, it will sink rather than move upward, reducing the risk of CO_2 leakage and increasing long-term storage security. The only drawback of this mechanism is the low dissolution rate of CO_2 in formation water. It takes around 100 years after the injection process for this trapping mechanism to have a significant impact in terms of storage security (see **Figure 2.4**). This problem can be tackled by enhancing CO_2 dissolution rate by injecting CO_2 into interbedded high- and low-permeability reservoir rocks, as reported by *Gilmore et al.* (2020). The authors argued that at early times after the injection, CO_2 will tend to travel in the high permeability rocks, which triggers the advective flux and hence, increases the surface area between CO_2 and surrounding water, thus increasing CO_2 dissolution rates. At the transition between the early time and the intermediate, as the CO_2 accumulates in the high permeability rocks, the diffusion dominated regime occurs, enhancing CO_2 dissolution rates. At the late times, when the CO_2 saturation reaches the water in the low permeability rocks dampening diffusion, therefore causing a return of advective dominated regime.

2.2.4. Mineral trapping

Mineral trapping occurs when the dissolved CO_2 reacts with rock minerals via geochemical reactions. The injected CO_2 interacts with the formation water and forms carbonic acid (which dissociates into H^+, HCO_3^- and CO_3^{2-} - see **Equations 2.1 – 2.3**), yielding a lower equilibrium pH of the formation water saturated with CO_2 (*Zeebe and Wolf-Gladrow,* 2001; *Millero,* 2007; *Adamczyk et al.,* 2009). Moreover, the amount of carbonic acid also depends on the concentration of the dissolved CO_2, which is subject to the pressure, temperature, composition, and salinity of the formation water in the reservoir (*Zhao et al.,* 2015a, 2015b, 2015c). Furthermore, as the water becomes more acidic (i.e., has a significant amount of carbonic acid), reactions are triggered between the carbonic acid and rock minerals containing

divalent ions of Ca^{2+}, Mg^{2+} and Fe^{2+}, resulting in the formation of carbonaceous minerals (*Ding et al.,* 2018). The chemical reactions for this process are (*Ding et al.,* 2018):

$$Ca^{2+} + HCO_3^- \Leftrightarrow CaCO_3(s) + H^+ \quad 2.4$$

$$Mg^{2+} + HCO_3^- \Leftrightarrow MgCO_3(s) + H^+ \quad 2.5$$

$$Fe^{2+} + HCO_3^- \Leftrightarrow FeCO_3(s) + H^+. \quad 2.6$$

Based on the above reactions, this trapping mechanism relies on the geochemical process and is mainly relevant for basaltic rocks, which contain minerals that can release Ca^{2+}, Mg^{2+} and Fe^{2+}. In addition, some of reservoir rocks containing minerals that can release Ca^{2+}, Mg^{2+} and Fe^{2+} (e.g., carbonates) also become a potential subsurface storage formation. This trapping mechanism can be enhanced by dissolving CO_2 into injected water at the surface and therefore, making the injected water acidic prior to injection. This strategy has been proved to trap CO_2 by mineralisation in basaltic rocks, implemented by Carbfix in the Iceland (e.g., *Matter et al.,* 2016).

2.3. Wettability

Wettability can be described as a tendency of one fluid to spread over a solid surface in the presence of another immiscible fluid (*Anderson,* 1986a; *Ahmed,* 2010). This property has attracted numerous scientific investigations due to its wide range of applications, including underground gas storage (e.g., *Tokunaga,* 2012; *Iglauer et al.,* 2015a; *Higgs et al.,* 2022), hydrocarbon recovery (e.g., *Jackson et al.,* 2016a; *Collini et al.,* 2020), lithium batteries (e.g., *Xie et al.,* 2017), cement products (e.g., *Ruan et al.,* 2021), renewable energy (e.g., *Zanganeh et al.,* 2020) and dentistry (e.g., *Morra et al.,* 2018; *Rupp et al.,* 2018).

As mentioned in previous sections, wettability is one of the essential factors controlling the structural and residual trapping mechanisms. To emphasise the importance of wettability in the CGS project, these two primary trapping mechanisms (structural and residual) have the most significant contributions to holding injected CO_2 in place safely at early stages (see **Figure 2.4**). Failure to accurately characterise this parameter could lead to CO_2 leakage (*Al-Yaseri et al.,* 2021), leading to potentially catastrophic impacts on the environment (e.g., *Patil et al.,* 2010; *Molari et al.,* 2018). Hence, a solid understanding of the wettability of geological subsurface formations is necessary to minimize the risk of CO_2 leakage and to increase the storage capacity.

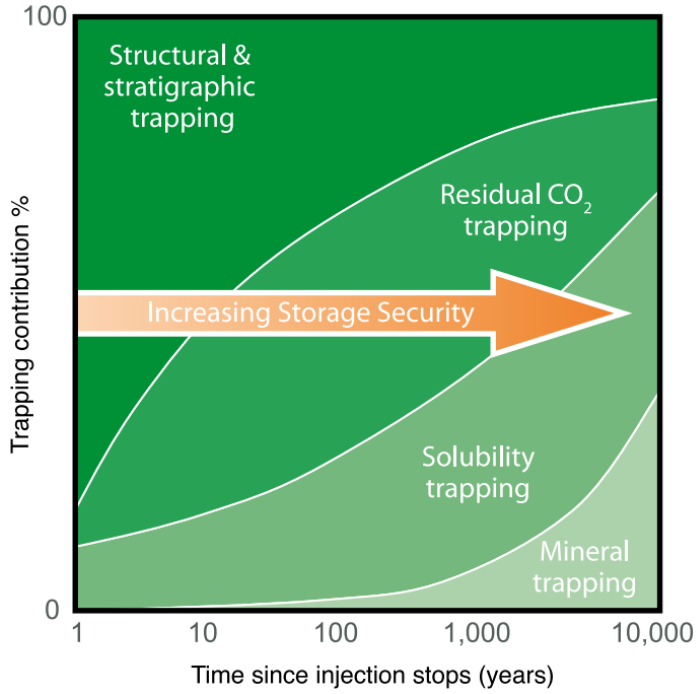

Figure 2.4. The contribution of each trapping mechanism over time to hold the injected CO_2 safely in place. The image was taken from *IPCC* (2005)

There have been several methods to experimentally characterise the wettability reported in the literature. Each of these methods has advantages and disadvantages of their respective measurement protocols that replicate different conditions of interest. Summary of commonly used methods to measure wettability are discussed below.

2.3.1. Contact angle test

The most common direct quantitative approach for measuring wettability is the contact angle. Among the available methods, the sessile drop method is commonly used owing to its simplicity and rapid measurement (*Kwok and Neumann,*1999; *Guancheng,* 2018; *Kung et al.,* 2019). It relies on the interaction between a drop of a fluid phase (e.g., water) and a stationary solid surface (e.g., rock). The measurement obtained from this method is called the static contact angle. The angle is measured at the point of contact (three-phase contact line) between the fluid phase and the rock surface using direct optical imaging (see **Figure 2.5**). Although it is a simple method, it has several disadvantages including the hysteresis effect (*Anderson,* 1986b; *Guancheng,* 2018), heterogeneity of the rock sample (*Morrow,* 1975; *Guancheng,* 2018) and surface contamination (*Anderson,* 1986b; *Iglauer et al.,* 2014), that influence the result of the contact angle measurement. The hysteresis effect is primarily caused by the surface roughness and heterogeneity (*Hubbe,* 2001; *Chau et al.,* 2009; *Rudawska,* 2019). Under ideal conditions, when the solid surface is smooth and homogeneous, the hysteresis effect should not exist, and the droplet should begin to move as soon as the solid surface is tilted. However, in reality, the droplet remains in place even when

rock surface is tilted owing to surface irregularities. Realistically, a smooth and homogeneous surface is impossible to obtain considering the surfaces of porous media. The temporal changes in the droplet owing to the time-dependant of chemical interactions (*Hubbe,* 2001; *Rudawska,* 2019), liquid-solid surface interactions (*Rudawska,* 2019), the penetration of the droplet into the surface and the reorganisation of particles on the surface (*Rudawska,* 2019) also cause hysteresis.

The hysteresis effect can also be observed while measuring the dynamic contact angle using the tilting plate method. In this method, a drop of the fluid phase is placed on a tilted solid surface, which is aligned at a specific tilting angle. The advancing and receding contact angles can be measured simultaneously, and the difference between the two measurements is called the contact angle hysteresis (e.g., *Chau et al.,* 2009; *Butt et al.,* 2022). The advancing contact angle is measured at the leading edge of the droplet, whereas the receding contact angle is measured at the trailing edge of the droplet before the droplet moves along the tilted rock surface. Although the hysteresis effect can be analysed using this method, the presence of surface contaminants influences the accuracy of the contact angle measurement by increasing the value of the measured angle (e.g., *Iglauer et al.,* 2014), leading to a biased analysis.

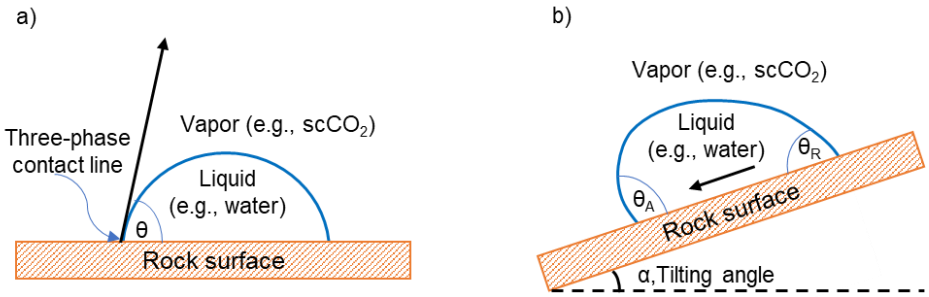

Figure 2.5. A schematic of (a) static contact angle and (b) dynamic contact angle using tilting plate method. θ is contact angle at static condition, θ_A is advancing contact angle and θ_B receding contact angle.

Owing to recent advances of X-ray micro-computed tomography (micro-CT), micro-CT imaging is recently gain a popularity to use in experimental pore scale displacement to examine multiphase flow in porous media. Using this technology, the in-situ contact angle can be measured at the pore scale between the fluid–fluid and fluid–rock surfaces, under typical natural subsurface conditions (e.g., *Andrew et al.,* 2014). This in-situ measurement provides more representative conditions, including under high pressure and temperature conditions, considering pore texture, surface roughness and the effect of displacement in porous media.

The initial approach for measuring the in-situ contact angle is to manually analyse the raw 2D images obtained through micro-CT imaging by positioning the image perpendicular to the three-phase contact line. This approach was successfully applied to measure the contact angle of a CO_2–brine–carbonate system after imbibition at a pressure of 10 MPa and temperature of 50 °C (*Andrew et al.*, (2014). *Lv et al.* (2017) also adopted this approach to estimate the in-situ contact angle at drainage and imbibition of CO_2 in a glass-bead pack and quartz-sand pack with $scCO_2$ (pressure of 8.0 MPa and temperature of 40 °C) and gaseous CO_2 (ambient condition). The same approach was implemented by *Tudek et al.* (2017) for a liquid CO_2–brine–sandstone system, thereby demonstrating that the manual approach can be employed for various systems. However, a significant drawback of this approach is that it is extremely time-consuming, and it can also result in measurement errors due to human bias (*Ibekwe et al.,* 2020; *Yang and Zhou,* 2020). To simplify the manual process and minimise the error, several researchers have developed automatic approaches to determine the in-situ contact angle (e.g., *AlRatrout,* 2017; *Ibekwe et al.,* 2020; *Yang and Zhou,* 2020), which is useful in obtaining an accurate characterisation of wettability at the pore scale.

Based on the measured angle and the method used to measure it – static/dynamic/in-situ measurement – the wetting state can be classified into non-wetting (i.e., water contact angle ≥ 90°) and wetting (i.e., water contact angle < 90°) conditions (e.g., *Kulkarni and Shaw,* 2015). Other classifications of the wetting state also exist from other literatures. *Triber and Owen* (1972) divided the wetting state into three categories, including water-wet (water contact angle = 0° - 75°), intermediate-wet (water contact angle = 75° - 105°) and oil-wet (water contact angle = 105° - 180°) conditions. Further, *Dake* (1978) is also classified the wettability into three categories, including water-wet (0° < water contact angle < 90°), intermediate-wet (water contact angle ≈ 90°) and oil-wet (90° < water contact angle < 180°) conditions. Meanwhile, based on the water contact angle with the rock surface in the presence of $scCO_2$, *Iglauer et al.* (2015b) reported that the wetting state can be classified into five categories, ranging from complete wetting (water contact angle = 0°) to complete non-wetting (water contact angle = 180°) conditions. Further details regarding this classification system are provided in Chapter 2.2.1.

2.3.2. Amott (Amott-Harvey) test

The Amott test was introduced by Earl Amott in 1959 (*Amott,* 1959) to characterise the average wettability of a core containing water and oil in the pore space. The main principle of this test is that the wetting phase will displace the non-wetting phase in the tested core. The Amott method relies on the volume of water and oil produced by spontaneous imbibition and force displacement. The Amott displacement of water-ratio (I_w) and oil-ratio (I_o) can be expressed as follows: (*Amott,* 1959):

$$I_w = \frac{V_{wsi}}{V_{wsi} + V_{wfd}} \quad 2.7$$

$$I_o = \frac{V_{osi}}{V_{osi} + V_{ofd}}\,, \quad 2.8$$

where V_{wsi} and V_{osi} are the volumes of water and oil, respectively, that are spontaneously imbibed, and V_{wfd} and V_{ofd} are the additional volumes of water and oil, respectively, that can be forced into the sample through force displacement. The wettability of the core can be considered water-wet when I_w is positive and I_o is zero, whereas it can be considered oil-wet when I_w is zero and I_o is positive (*Anderson,* 1986b).

A modified Amott test, which is known as the Amott–Harvey test is also widely used to evaluate wettability. The Amott–Harvey test primarily differs from the original Amott test in its initial preparation stage. In the original Amott test, the preparation stage only consists of displacing the volume of oil in the core until the residual oil saturation stage. In the Amott–Harvey test, after reaching the residual oil saturation stage, an additional step is performed, wherein the water is displaced until the irreducible water saturation stage. Subsequently, the test begins and follows the same procedure as the original Amott test (see *Amott,* 1959 for details). The Amott–Harvey wetting index (I_{AH}) is:

$$I_{AH} = I_w - I_o, \quad 2.9$$

where $0.3 \leq I_{AH} \leq 1.0$ indicates a water-wet state, $-0.3 \leq I_{AH} \leq 0.3$ indicates a neutral-wet state and $-0.3 \leq I_{AH} \leq -1.0$ indicates an oil-wet state (*Anderson,* 1986b). Although the effects of heterogeneity and the natural surface roughness of the core are implicitly involved in the measurement, the results of the Amott and Amott–Harvey wettability tests are insensitive to the near neutral wetting state (*Anderson,* 1986b).

2.3.3. US Bureau of Mines (USBM) test

Like the Amott test, USBM test (*Donaldson et al.,* 1969) is used to determine the average wettability of a core. The USBM test uses capillary pressure curves to quantify the wetting state of a system. **Figure 2.6** shows the typical result of the capillary pressure curves obtained from full displacement cycles. The USBM index (I_{USBM}) can be expressed as follows (Donaldson et al., 1969):

$$I_{USBM} = \log\left(\frac{\mathrm{A}_1}{\mathrm{A}_2}\right), \quad 2.10$$

where A_1 and A_2 are the areas under the capillary pressure curves of the oil and water drive processes, respectively (see **Figure 2.6**). The core is characterised as water-wet when I_{USBM} is ≈ +1, oil-wet when I_{USBM} is ≈ −1 and neutral-wet when I_{USBM} is ≈ 0 (*Anderson,* 1986b).

Unlike the Amott test, the USBM test is sensitive to the near neutral wetting condition. However, it cannot differentiate fractional (mixed) wettability in a system.

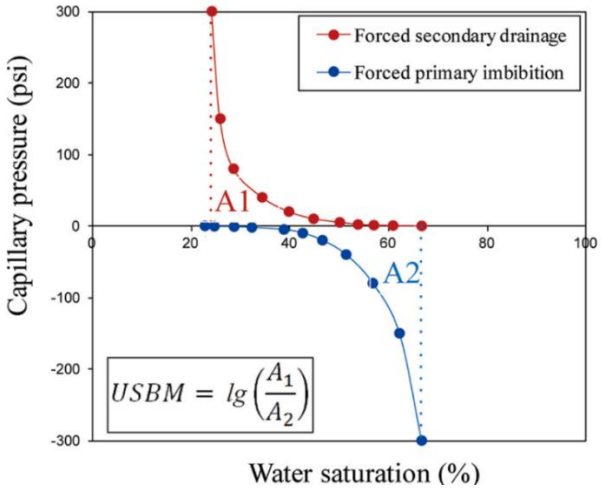

Figure 2.6. Typical result of standard USBM test (*Mirzaei-Paiaman,* 2022)

2.3.4. Zeta potential test

Another parameter used to characterise the wettability is the zeta potential, which can be obtained using the streaming potential method (e.g., *Jackson et al.,* 2016a) and electrophoretic mobility method (e.g., *Kosmulski et al.,* 2002, *Kosmulski and Dahlsten,* 2006). These methods have become increasingly popular in recent years because the zeta potential represents the electrostatic forces between the water-rock and water-non-aqueous phase fluid (NAPF; e.g., CO_2, oil) interfaces. The electrostatic force is an essential component of the total disjoining pressure and consequently, it contributes to wettability (*Hirasaki,* 1991; *Busireddy and Rao,* 2004; *Jackson et al.,* 2016a). The main benefit of using the streaming potential method instead of the electrophoretic mobility method to measure the zeta potential is the use of a real rock sample (e.g., *Walker and Glover,* 2018) or sandpack (e.g., *Vinogradov et al.,* 2018) to represent porous media during the measurement. Moreover, the streaming potential method can be extended to elevated temperature, pressure and ionic strength conditions that limit electrophoretic mobility. The streaming potential measurement can also be used in the field or downhole by recording the voltage in response to fluid flows. Therefore, the streaming potential method has wide applicability, from laboratory to field applications. The measurement of the zeta potential through the electrophoretic mobility and streaming potential methods is discussed in detail in Section 2.5.

Based on the fundamental thermodynamics of wettability, there are three principal forces that act between the rock-water and water-NAPF (e.g., CO_2) interfaces that are related to the total disjoining pressure. These forces are: 1) structural, $\Pi_{\text{structural}}$, 2) van der Waals, $\Pi_{\text{van der Waals}}$, and 3) electrostatic forces, $\Pi_{\text{electrostatic}}$ (*Hirasaki,* 1991; *Busireddy and Rao,* 2004; *Jackson et*

al., 2016a). The contributions of these three forces to the disjoining pressure and wetting film stability are illustrated in **Figure 2.7**. The total disjoining pressure (Π_{total}) is the sum of structural, van der Waals and electrostatic components and can be expressed using **Equation 2.11** (*Busireddy and Rao,* 2004).

$$\Pi_{\text{total}} = \Pi_{\text{structural}} + \Pi_{\text{van der Waals}} + \Pi_{\text{electrostatic}} \qquad 2.11$$

The structural forces, also known as the hydration forces, are short-range repulsive forces, which implies that they make a positive contribution to the disjoining pressure (*Jackson et al.,* 2016a; *Xie et al.,* 2016). The van der Waals forces can be either attractive or repulsive, depending on the polarity of the Hamaker constant (i.e., a coefficient related to the interactive van der Waals energy to the distance between separation of two molecules; *Hirasaki,* 1991; *Donaldson and Alam,* 2008). When the Hamaker constant is positive, the van der Waals forces are attractive and make a negative contribution to the disjoining pressure (*Hirasaki,* 1991). Conversely, a negative Hamaker constant means that the van der Waals forces are repulsive and provide a positive contribution to the disjoining pressure (*Hirasaki,* 1991).

Lastly, the electrostatic forces occur when two interfaces interact while having a non-zero electric interfacial potential, which results from the so-called Electrical Double Layer (EDL) arrangement. This force can be positive (repulsive) or negative (attractive) depending on the ionic strength, brine composition and pH (e.g., *Vinogradov et al.,* 2018). Moreover, the electrostatic forces can vary with temperature (*Vinogradov and Jackson,* 2015), rock mineralogy (*Li et al.,* 2018; *Alarouj et al.,* 2021) and partial CO_2 pressure (*Heberling et al.,* 2011). **Figure 2.7** illustrates how the magnitude and polarity of the electrostatic forces affect the total disjoining pressure. Hence, knowledge of these forces is essential, as they can control the stability of the wetting film.

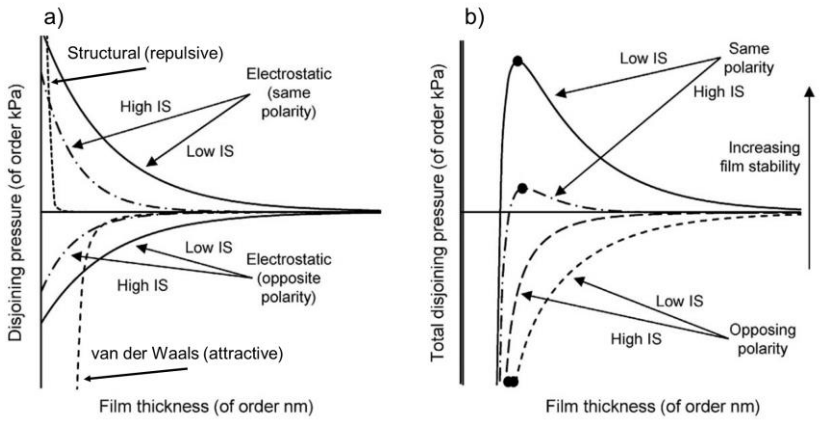

Figure 2.7. The (a) contributions of the forces, including the structural forces (dotted line), van der Waals forces (dashed line) and electrostatic forces (solid and dot-dashed lines), on disjoining pressure, and (b) the disjoining pressure based on (a), where IS is the acronym for ionic strength; the image is modified from *Jackson et al.* (2016a).

2.4. Electrical Double Layer (EDL) theory

The electrical double layer (EDL) at rock-water interface is established when the minerals at the rock surface interact with an aqueous solution. This interaction causes the rock surface to become electrically charged with what is known as the surface charge. The charge at the rock surface is then balanced by the opposite charge from ionic species of the aqueous solution to maintain electrical neutrality, thus resulting in separation of the electrical charge termed the electrical double layer (EDL; **Figure 2.8**; *Hunter,* 1981). For example, when the rock surface is negatively charged, it will attract the opposite charges (i.e., positive counter-ions) from the solution close to the rock surface and 'push away' (exclude) ions of the same polarity (i.e., negative co-ions) from the rock surface. The detailed development of surface charges for both silica and calcite, which represent two major sedimentary formations (sandstone and carbonate, respectively) will be discussed in the following subsection (see subsection 2.4.1).

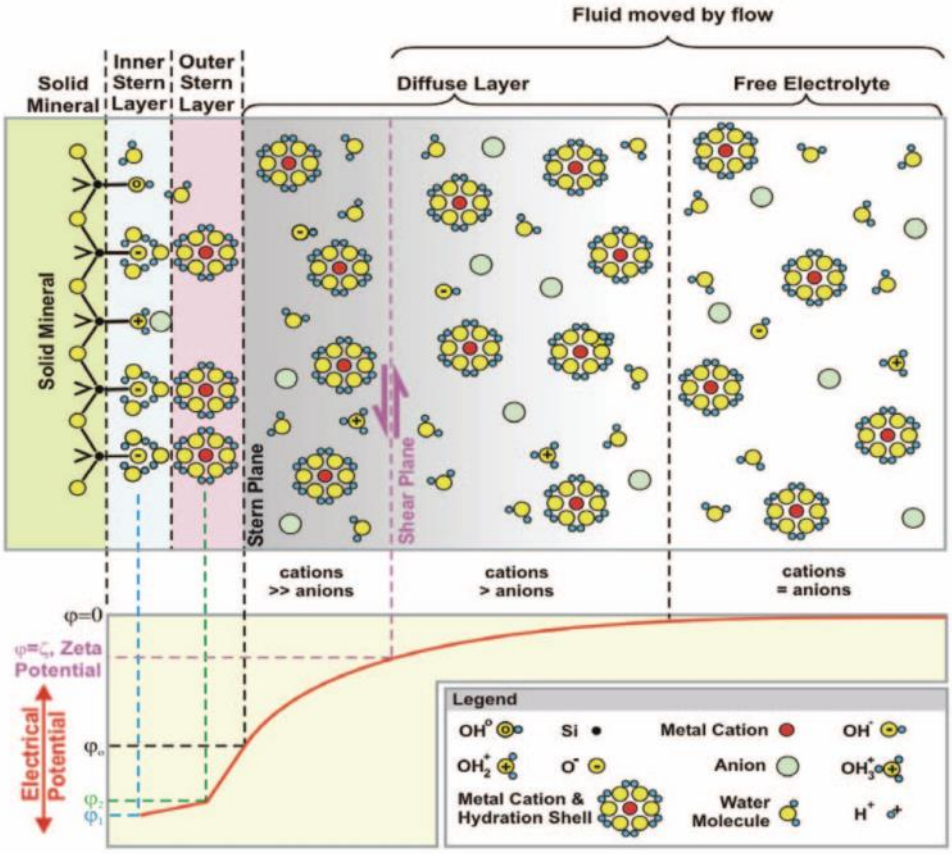

Figure 2.8. Illustration of the electrical double layer of rock surface with the solution at the interface, adapted from *Glover and Jackson* (2010). Here, the authors consider the rock surface is silica (silica is the main mineral of quartz) and the overall surface charge is negative (see detail in *Glover and Jackson,* 2010).

The region of ions located next to the rock surface is called the Stern layer and it is considered to be the first layer of EDL (see **Figure 2.8**). The Stern layer consists of two planes, namely the Inner and Outer Helmholtz Plane (IHP and OHP, respectively). The IHP generally

describes the location of un-hydrated salt ions directly attached to the rock surface, while the OHP is defined as the location of the hydrated ions from the solution that are firmly attached to the rock surface (e.g., *Al Mahrouqi et al.,* 2017). The electric potential within the Stern layer is similar to the variation of the potential between two parallel plates of a capacitor (e.g., *Heberling et al.,* 2014), which changes linearly between the plates.

In general, counter-ions in the Stern layer cannot completely balance the charge on the rock surface; therefore, counter-ions from the solution will be attracted to the interface to balance this excess charge, and these counter-ions will reside in the so-called diffuse layer. In the diffuse layer, the ions are also attracted to the rock surface. The charge density of counter-ions in the diffuse layer exponentially decreases with an increasing distance from the OHP and throughout the diffuse layer, following the Boltzmann distribution law as suggested by the Gouy-Chapman theory (*Hunter,* 1981). Within the diffuse layer, there exists a plane called the shear/slip plane, which separates hydraulically immobile and mobile ions (see **Figure 2.8**). Consequently, the ions in the mobile part can be moved by different thermodynamic potential gradients (concentration, temperature and pressure). The electric potential at the shear plane is defined as the zeta potential (*Hunter,* 1981). Some of surface complexation models that describe the EDL consider the location of shear plane to coincide with OHP and thus, the zeta potential represents the electric potential at the OHP (e.g., *Heberling et al.,* 2014; *Li et al.,* 2016).

Considering the behaviour of ions in the EDL, the movement of ions in the EDL under the influence of pressure is called the electrokinetic phenomena (*Cerepi et al.,* 2006). Several types of EK phenomena have been identified, including electrophoresis, streaming potential, electro-osmosis and sedimentation potential (see details in *Delgado et al.,* 2007). However, only the streaming potential and electrophoresis will be discussed in this study, as these phenomena are commonly utilised to measure the zeta potential.

3.4.1. Rock surface charge development in aqueous solution

For quartz (silica) surfaces, two main groups are considered to form the surface sites, namely the single-Si-coordinated ($>\mathrm{SiOH}$ - silanol) and double-Si-coordinated ($>\mathrm{Si_2O}$ - siloxane) groups (*Leroy et al.,* 2013; *Hiemstra et al.,* 1989). The estimated equilibrium constant of protonation of the surface siloxane group is very low, and thus, it can be considered completely inert (*Leroy et al.,* 2013; *Hiemstra et al.,* 1989; *Revil et al.,* 1999). Therefore, only $>\mathrm{SiOH}$ groups are considered to represent the silica surface, with two protonation/deprotonation reactions **(***Leroy et al.,* 2013; *Hiemstra et al.,* 1989):

$$> \mathrm{SiOH}^0 \Leftrightarrow > \mathrm{SiO}^- + \mathrm{H}^+ \quad 2.12$$

$$> \mathrm{SiOH}^0 + \mathrm{H}^+ \Leftrightarrow > \mathrm{SiOH}_2^+ \quad 2.13$$

Hiemstra et al. (1989) argued that the protonation of the neutral silanol group ($> \mathrm{SiOH}^0$) was unlikely to happen in the pH range of 2 – 12 due to very low surface equilibrium constant. Hence, the charge of the silica surface is dominated by the first reaction (**Equation 2.12**).

Considering only **Equation 2.12**, the relative concentration of silica surface sites is dictated by the solution pH (pH indicates the concentration of H^+ relative to OH^-) thus making pH the main control of the surface charge and zeta potential. Consequently, when the solution becomes more acidic, the protonation silanol increases, resulting in the less negative surface charge and the zeta potential, as confirmed previous experimental studies on the zeta potential at silica-water interfaces (e.g., *Kosmulski et al.,* 2002).

On the other hand, formation of the surface charge of calcite in an aqueous solution is more complex than that of silica. It is well known that calcite is soluble and can dissolve when in contact with an aqueous solution, which can be expressed as follows:

$$\mathrm{CaCO_3(s)} \Leftrightarrow \mathrm{Ca^{2+}(aq)} + \mathrm{CO_3^{2-}} \quad 2.14$$

In an open system where water is exposed to surrounding atmosphere, some of CO_2 from air will dissolve into the solution thus affecting the equilibrium solution pH (see **Equations 2.1-2.3**). The pH is related to the dissolved carbon speciation into carbonic acid, bicarbonate and carbonate ions along with calcium ions in the solution (e.g., *Anabaraonye et al.,* 2019; *Eriksson et al.,* 2007). Considering all these ions in the solution, the development of calcite surface charge is not necessarily dependent on just the solution pH, as in the case of the silica surface.

At first, the calcite lattice ions in contact with aqueous solutions get hydrated to form $> \mathrm{CaOH}_2^{+0.5}$, while $> \mathrm{CO}_3^{-0.5}$ remains unhydrated (*Heberling et al.,* 2011). Then, these two surface groups undergo deprotonation and protonation reactions in the hydrolysis layer (*Heberling et al.,* 2011), which can be expressed as:

$$> \mathrm{CaOH}_2^{+0.5} \Leftrightarrow > \mathrm{CaOH}^{-0.5} + \mathrm{H}^+ \quad 2.15$$

$$> \mathrm{CO}_3^{-0.5} + \mathrm{H}^+ \Leftrightarrow > \mathrm{CO_3H}^{+0.5} \quad 2.16$$

However, in a later study *Heberling et al. (2014)* updated their calcite surface reactions and suggested that direct protonation of $> \mathrm{CO}_3^{-0.5}$ does not take place and could be disregarded (**Equation 2.16**). *Heberling et al.* (2014) also argued that based on the theoretical study by *Villegas-Jimenez* (2009), water molecules did not adsorb onto $> \mathrm{CO}_3^{-0.5}$ surface groups with subsequent dissociation of OH^- to form $> \mathrm{CO_3H}^{+0.5}$. Based on both arguments, only

deprotonation of $> \mathrm{CaOH_2^{+0.5}}$ is considered (**Equation 2.15**), and three calcite surface sites are formed: $> \mathrm{CaOH^{-0.5}}$, $> \mathrm{CaOH_2^{+0.5}}$ and $> \mathrm{CO_3^{-0.5}}$ (see the detailed explanation in Chapter 7).

Considering only **Equation 2.15,** the solution pH is expected to dictate the surface charge of the calcite. However, this expectation fails to consider the adsorption of calcite lattice ions (Ca^{2+} and CO_3^{2-}) from the adjacent solution. A recent study by *Al Mahrouqi et al.* (2017) found that when the solution pH was kept constant, the zeta potential became increasingly positive with increasing amounts of Ca^{2+} in the solution. Hence, the surface charge of the calcite is controlled by the concentration of Ca^{2+}. This condition also implies that calcite's surface charge is sensitive to the concentration of specific ions (e.g., Ca^{2+}), which are known as the potential determining ions (PDIs). Variations in concentration of other divalent ions, such as Mg^{2+} and SO_4^{2-}, was shown to also affect the zeta potential of the calcite-water interface (*Alroudhan,* 2016; *Al Mahrouqi et al.,* 2017). Therefore, these ions are also considered to be PDIs.

All in all, the surface charge and the zeta potential of calcite in aqueous solution are controlled by the complex chemical adsorption of PDIs on the calcite surface. The example of reactions of Ca^{2+} and CO_3^{2-} with calcite surface sites are:

$$> \mathrm{CaOH^{-0.5}} + \mathrm{Ca^{2+}} \Leftrightarrow > \mathrm{CaOH^{-0.5}} - \mathrm{Ca^{2+}} \qquad 2.17$$

$$> \mathrm{CO_3^{-0.5}} + \mathrm{Ca^{2+}} \Leftrightarrow > \mathrm{CO_3^{-0.5}} - \mathrm{Ca^{2+}} \qquad 2.18$$

$$> \mathrm{CaOH_2^{+0.5}} + \mathrm{CO_3^{2-}} \Leftrightarrow > \mathrm{CaOH_2^{+0.5}} - \mathrm{CO_3^{2-}} \qquad 2.19$$

These complex reactions are located within the Stern layer. Further, previous studies by *Li et al.* (2016) and *Heberling et al*. (2014) assumed that the location of these reactions was at the end of the Stern layer (OHP), and the same assumption has been implemented in our model. The detailed development of the calcite surface complexation model and the complex reactions of the calcite surface sites are provided in Chapter 7.

2.5. Zeta potential measurements

The zeta potential is a representation of the electrochemical interactions at the interface between an aqueous solution (hereafter referred to as brine, electrolyte or water for simplicity) and the rock mineral/NAPF. In order to measure the zeta potential in such a system, there are two common available methods: 1) the electrophoretic mobility method (EPM) and 2) the streaming potential method (SPM), which will be discussed in the following subsections.

2.5.1. Electrophoretic mobility method (EPM)

The EMP is the most common method used to measure the zeta potential. To measure the zeta potential using the EPM, a sample must be of very small size and dispersed as a powder (solid) or emulsion (fluid) in the aqueous solution. The EPM relies on the relative motion

between the dispersed sample and the aqueous solution due to the application of an external electric field (*E*). As a result, the electrophoretic velocity (v_e) from the movement of the charged particles relative to the stationary solution is obtained, and the electrophoretic mobility (u_e) can be determined as the ratio between the velocity and the electric field (*Delgado et al.,* 2007). Further, to quantify the zeta potential (ζ) using the EPM, the Helmholtz–Smoluchowski (HS) equation for electrophoresis is used as follows (*Delgado et al.,* 2007):

$$u_e = \frac{\varepsilon \zeta}{\mu}, \qquad 2.20$$

where ε is the solution permittivity in [F·m^{-1}] and μ is the solution viscosity in [Pa·s].

There are several benefits to use the EPM for measuring the zeta potential, including relatively quick measurements and commercially available apparatus (zeta meter). On the other hand, there are four reasons why the EPM should not be used to measure the zeta potential with the application to real rocks, particularly in porous media, which are as follows (*Al Raoudhan et al.,* 2016; *Jackson et al.,* 2016a; *Al Mahrouqi et al.,* 2017):

i. The EPM requires very fine samples immersed in solution, so it does not consider the pore space complex topology (e.g., tortuosity, pore throats) in porous rock.
ii. Crushing a rock sample into fine particles to make it suitable for the EPM creates 'fresh' rock (mineral) surface sites. This increases the amount of active surface sites exposed to the solution that might affect the results.
iii. The volumetric ratios between the solution and the sample are not comparable when the solution is in contact with the rock surface in porous media. Moreover, the EPM cannot accommodate solutions with high ionic strength in its measurements.
iv. The EPM is limited to a maximum of two phases (i.e., rock powder-solution or oil/gas-solution) during the measurement and cannot accommodate the presence of a third phase (e.g., oil/gas), as commonly found in subsurface geological formations.

2.5.2. Streaming potential method (SPM)

The streaming potential method (SPM) relies on the difference of pressure (pressure gradient) to induce the flow of aqueous solution across the stationary saturated porous rock (**Figure 2.7**; e.g., *Delgado et al.,* 2007; *Jackson et al.,* 2012a).

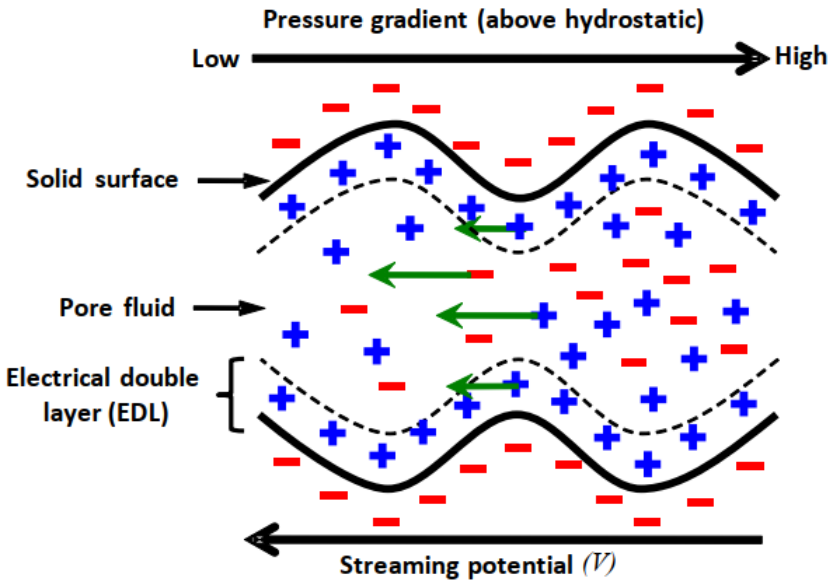

Figure 2.9. Schematic of the streaming potential in porous saturated rock. An EDL is formed between rock surface and fluid(water) at the interface. Some of excess charge in EDL is dragged along with fluid direction due to pressure gradient and giving rise to the streaming potential in the opposite direction. This image was adapted from *Jackson et al.* (2012a).

Assuming we have a negative surface charge of the rock surface, the ions of the opposite polarity (positive ions) from the aqueous solution try to balance the surface charge to maintain the electrical neutrality by forming the EDL. Along with the same flow direction, some of the excess counter-ions within the EDL are moved and create the streaming current (J_S). To balance this streaming current, a conduction current (J_C) is generated in the opposite direction, giving rise to a streaming potential. Hence, the total current density (J_T) can be expressed as follows (*Sill,* 1983; *Li et al.,* 2016):

$$J_T = J_S + J_C = -\sigma \nabla V + L \nabla P, \qquad 2.21$$

where σ is the electrical conductivity of saturated porous rock, ∇V is the electric potential gradient across the rock sample, L is the electrokinetic cross coupling term and ∇P is the pressure gradient across the rock sample. Under steady state conditions, with an isolated system and one-dimensional flow, the total current density is equal to zero ($j = 0$) and the streaming potential coupling coefficient (C_{SP}) can be determined as follows (*Sill,* 1983):

$$C_{SP} = \left.\frac{\Delta V}{\Delta P}\right|_{j=0}, \qquad 2.22$$

where ΔV is the stabilised voltage [V] and ΔP is stabilised pressure difference [Pa] across the rock sample. In order to interpret zeta potential from SPM, a modified HS equation accounting for the surface electrical conductivity is used and can be expressed as follows (*Jouniaux and Pozzi,* 1995; *Glover,* 2015):

$$C_{SP} = \frac{\varepsilon\zeta}{\mu\sigma_{rw}F}, \qquad 2.23$$

where ε is the water permittivity in [F·m^{-1}], μ is the dynamic water viscosity in [Pa·s], σ_{rw} is the electrical conductivity of the saturated rock sample in [S·m^{-1}] and F is the intrinsic formation factor and it can be determined by the ratio between the fluid conductivity (σ_w) and the saturated rock conductivity σ_{rw} at high ionic strength conditions. When the porous rock is saturated with high ionic strength solution, the surface conductivity becomes negligible, and the classical HS equation can be used to evaluate the zeta potential (*Jouniaux and Pozzi,* 1995):

$$C_{SP} = \frac{\varepsilon\zeta}{\mu\sigma_w}. \qquad 2.24$$

There is one disadvantage of using SPM to measure the zeta potential, which relates to the fact that the measurement represents the zeta potential averaged over many interfaces with only portion of them having identical properties (e.g., *Collini and Jackson,* 2022; *Alarouj et al.,* 2021). For example, if the rock sample is pure quartz, the averaged macro-scale zeta potential obtained from SPM should in theory be equal to the micro-scale zeta potentials of individual quartz-water interface; this has later been confirmed experimentally. However, if there are other than quartz minerals present in the rock sample (e.g., clays), the macro-scale zeta potential is an average of the micro-scale zeta potentials of quartz-water and clay-water interfaces. In terms of practicality, a SPM experiment consist of a very complex experimental protocol and time-consuming measurement (see the detailed experimental protocol in *Vinogradov et al.,* 2010). In contrast, there are three main advantages of using the SPM approach to measure zeta potential, particularly in porous media, which are:

i. The SPM can use an intact rock/sandpack to accurately represent the porous medium (e.g., *Walker et al.,* 2014; *Vinogradov et al.,* 2018). This condition can be achieved by placing the sample in a special core holder (see **Figure 3.1** in Chapter 3) and allowing only one-dimensional flow through the system. This core holder is equipped with pressure transducers and electrodes at each end to measure pressure difference and voltage across the sample simultaneously. Hence, when the steady state condition is reached, the measured stabilised voltage and pressure difference can be used to determine C_{SP} (**Equation 2.22**) and thus the zeta potential (**Equation 2.23** and/or **2.24**).
ii. The SPM can measure the zeta potential at elevated temperatures (e.g., *Vinogradov and Jackson,* 2015) and high ionic strength conditions (e.g., *Vinogradov et al.,* 2010; *Walker and Glover,* 2018), which EPM cannot do. These two conditions are essential to be implemented during the measurements, as they are typical of subsurface

geological formations relevant for CGS projects. For example, *Vinogradov and Jackson* (2015) reported that the zeta potential at low ionic strength condition (0.01M; M= mol·L^{-1}) in sandstone was negative and became less negative with increasing temperature (up to 150°C). Meanwhile, at high ionic strength condition (0.5M), the zeta potential was independent of temperature. Therefore, using the SPM in conditions close to those of the subsurface system is crucial for accurately interpreting the zeta potential.

iii. The SPM can measure two-phase flows (water and NAPF) inside the porous rock at the same time (e.g., *Jackson and Vinogradov,* 2012; *Jackson et al.,* 2016a; *Collini et al.,* 2020). Measuring the zeta potential under this condition provides the electrostatic interactions at two interfaces, namely the rock-water and NAPF-water interfacial zeta potentials, which can be used later for wettability characterisation. The details regarding the zeta potential measurements under multi-phase conditions will be discussed in subsequent sections.

2.6. Zeta potential and its link to the wettability

One of the most important applications of the zeta potential in porous saturated rock is the characterisation of wettability in subsurface geological formations. At the molecular level, the wettability is controlled by the electrostatic interactions between rock-water and NAPF-water interfaces (*Hirasaki,* 1991; *Jackson et al.,* 2016a). Due to the nature of subsurface formations, which have two fluid phases (water and NAPF) in the pore space simultaneously, only SPM that accurately represents real rock in target formations is suitable for the C_{SP} and zeta potential measurements and these will be discussed in this section.

Several experimental multi-phase streaming potential measurements have been done to understand the behaviour of C_{SP} as a function of fluid saturation (e.g., *Moore et al.,* 2004; *Revil and Cerepi,* 2004; *Vinogradov and Jackson,* 2011). In particular, two studies (*Revil and Cerepi,* 2004; *Vinogradov and Jackson,* 2011) reported that the C_{SP} fell to zero at residual water saturation after gas/water displacement at the end of drainage processes. Moreover, this finding is consistent with the theoretical study by *Vinogradov et al.* (2021) regarding the observation of zero C_{SP} at the residual water condition, which implies that non-wetting phase fluid (gas) in the pore space is non-conductive and prevents the rise of streaming current. In contrast, non-zero C_{SP} readings were observed at residual water saturation after oil(undecane)/water displacement (*Vinogradov and Jackson,* 2011) and liquid CO_2/water displacement (*Moore et al.,* 2004). This situation was likely caused by the flow of unmeasurable amount water in the pore space that yielded the non-zero streaming current. However, these studies did not obtain or explain the relationship between the measured properties and wettability.

A later experimental study by *Jackson and Vinogradov* (2012) found a link between measured zeta potential and wettability using SPM. The experiments were conducted using two carbonate core samples with similar properties, both fully saturated with the same brine at the temperature of 23°C. Prior to pumping each core sample with crude oil (drainage process), the zeta potential of each core sample was measured when only brine saturated the pore space (single-phase zeta potential; S_w = 1). At the end of the drainage process (when irreducible water saturation was achieved, $S_w = S_{wirr}$), the first sample was aged for 8 weeks at the temperature of 93°C, while the second sample was not. The next step was to pump the same brine into the oil saturated core samples (imbibition) until the residual oil saturation (S_{or}) was reached, after which the multi-phase zeta potential was measured at $S_w = 1 - S_{or}$.

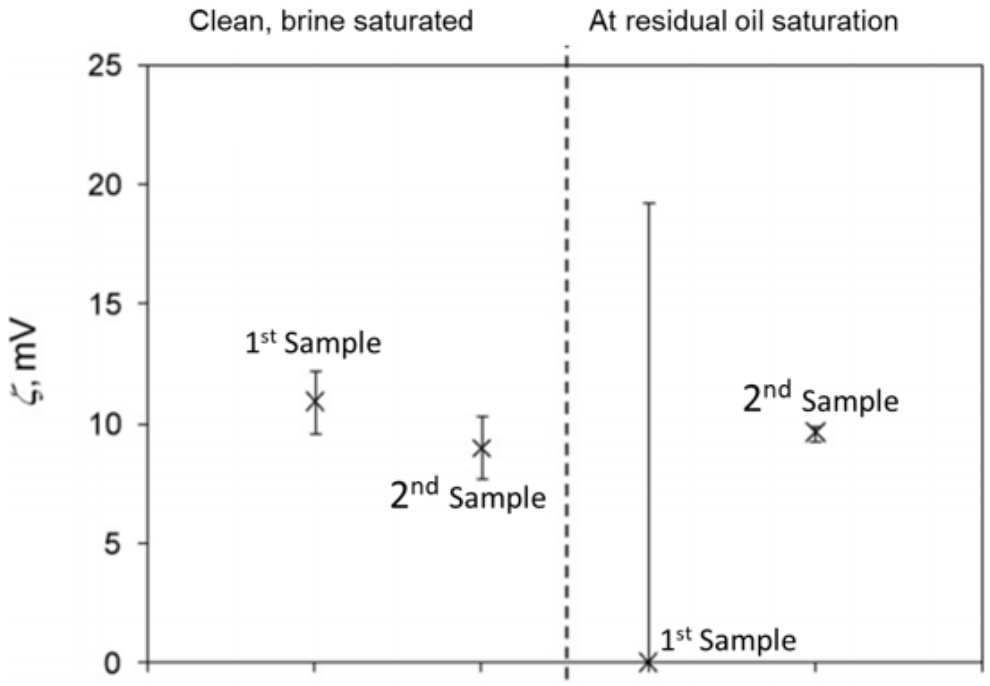

Figure 2.10. Zeta potential obtained from two different core samples, fully saturated with brine (left) and saturated with brine at residual oil (right), adopted from *Jackson and Vinogradov* (2012). The 1st sample was aged while the 2nd sample was non-aged.

The measured zeta potential at the residual oil saturation for the aged sample was substantially different compared to the single-phase zeta potential (see **Figure 2.10**). In contrast, the multi-phase zeta potential of the second non-aged sample was similar (within experimental uncertainty) to its initial condition (see **Figure 2.10**). The authors (*Jackson and Vinogradov,* 2012) suggested that after aging, the wetting state in the first sample was altered and thus some of the pore walls became oil-wet, while the rest remained water-wet (see Figure 8 in *Jackson and Vinogradov,* 2012 for the illustration of wettability alteration in the first sample). In water-wet conditions, the water is adjacent to the rock surface and forms the EDL at rock-water interface throughout the pore space. Thus, when the water flows in the pore

space, the excess charge is transported along the continuous rock-water interface, giving rise to the streaming current. On the other hand, in oil-wet conditions, some oil wets the rock surface and when it comes into contact with brine, the EDL of oil-water interface is formed. As a result, the EDL of the rock-water interface becomes discontinued, and when the water flows in the pore space, the streaming current becomes an average of individual contributions of the rock-water and oil-water interfaces.

Furthermore, *Jackson et al.* (2016a) conducted another study to understand the correlation between zeta potential and wettability using four different crude oils (oil samples A, B, C and D) and three brine compositions (namely FMB, SW and 20dSW) in a carbonate rock sample (Estaillades limestone). In this study, the authors also measured the Amott wettability index of water (I_w) to gain a better understanding of the wetting state of the tested core samples. The zeta potential was measured during the coreflooding experiment at room temperature (c. 23°C) when the sample was fully saturated with brine (single-phase zeta potential; $S_w = 1$) and at the residual oil saturation (multi-phase zeta potential; $S_w = 1 - S_{or}$). Before measuring the zeta potential at residual oil, the sample was aged for at least 4 weeks with crude oil and brine at the temperature of 80°C. A more detailed explanation regarding the experimental procedure can be found in *Jackson et al.* (2016a).

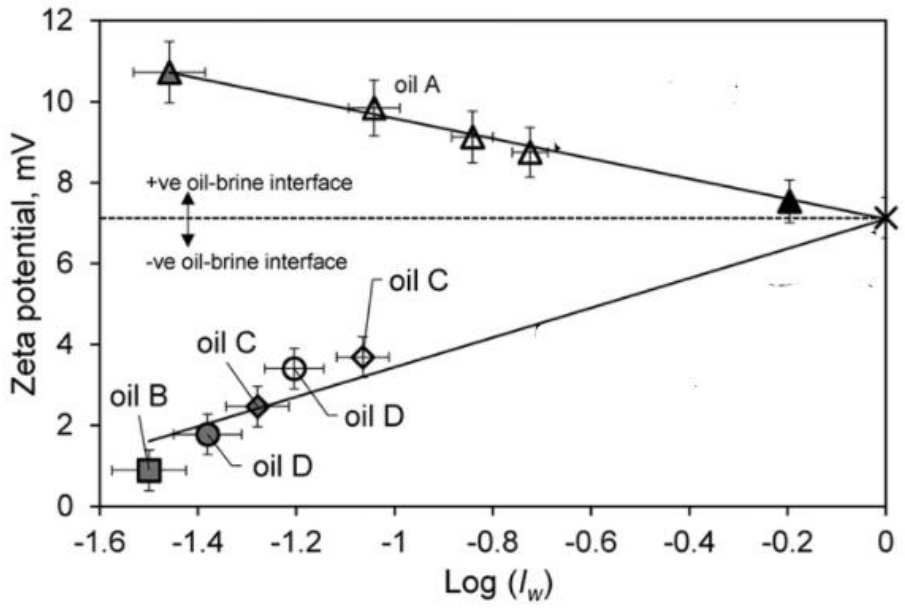

Figure 2.11. Zeta potential as a function of water wetting index for each of the four crude oils tested (A-D) aged with FMB. The image was adapted from *Jackson et al.* (2016a). Filled grey symbols represent aging in the absence of water, open symbols represent aging with water and the filled black triangle represents the non-aged sample. Log (I_w) = 0 represent fully saturated brine (water-wet) condition in the tested core sample.

Two distinct trendlines were observed from the results of *Jackson et al.* (2016a). The authors argued that the difference between the two trendlines was caused by the difference in polarity of oil sample(A)-water interface (positive), and of oil samples(B-D)-water interfaces (negative).

In oil samples B-D, the multi-phase zeta potential decreases linearly when the water wetting index decreases (**Figure 2.11**). This behaviour implies that the multi-phase zeta potential becomes smaller in magnitude when the wetting state shifts from water-wet to oil-wet. As the oils(B-D)-water interface polarity is negative, the initially positive rock-water zeta potential at water-wet condition decreases due to increasing contribution of negative oils(B-D)-water interface at oil-wet condition and yields to the smaller multi-phase zeta potential. On the other hand, in oil sample A, the multi-phase zeta potential increases when the water wetting index decreases (**Figure 2.11**), which implies that the zeta potential becomes more positive when the wetting state changes from water-wet toward oil-wet condition. This happens because the positive oil(A)-water interface significantly contributes at oil-wet conditions, giving a more positive multi-phase zeta potential.

Despite the different polarities of oil-water interface, one of the notable conclusions of this study was that the multi-phase zeta potential is controlled by the effective zeta potential of oil-water and rock-water interface. In more oil-wet condition, oil-water zeta potential significantly contributes to overall multi-phase zeta potential while in more water-wet conditions, rock-water zeta potential becomes dominant. In this study, *Jackson et al.* (2016a) also found that additional oil recovery was observed during controlled salinity waterflooding (CSW) when oil-water and rock-water interface had the same polarity and thus, created repulsive forces between the interfaces and stabilise the wetting film.

Lastly, a recent study by *Collini et al.* (2020) extended the experimental investigation of zeta potential and its link to the wetting state of carbonate samples and subsequently to improve oil recovery. The experiments were conducted at various conditions using seven oil samples, nine intact carbonate core samples, and three main types of brine compositions, namely formation brine, seawater and low salinity brine (see details in Table 1 of *Collini et al.,* 2020). Similar to *Jackson et al.* (2016a), the core samples were left to age with crude oil and brine for at least 4 weeks to allow the wettability alteration to occur at the temperature of 80°C. Further, the measurement of zeta potential was conducted at two different conditions, single-phase zeta potential (S_w = 1) and multi-phase zeta potential (after aging, $S_w = 1 - S_{or}$) with different experimental temperatures (23°C, 70°C, 80°C and 100°C).

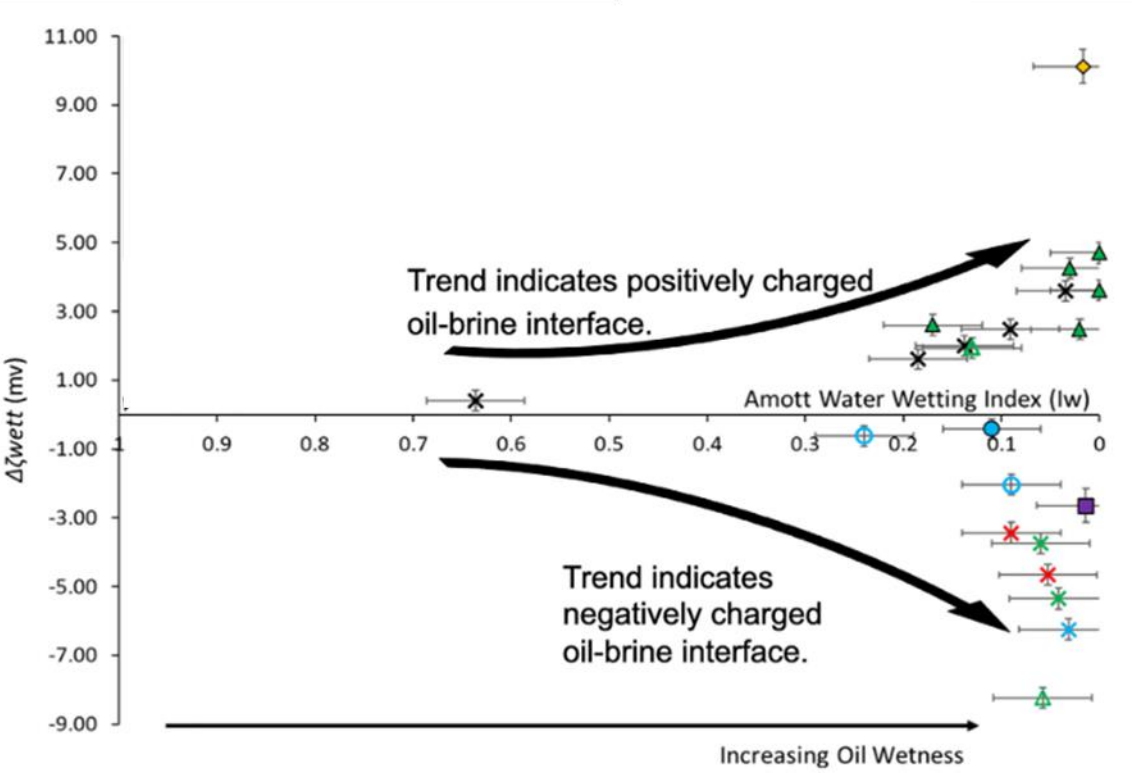

Figure 2.12. Changes in zeta potential measured in formation brine after aging for various experimental conditions (a range of crude oils, formation brine compositions carbonate core samples and temperatures, see detail of the experimental results in *Collini et al.* 2020). The water wetting index (I_w) equals 1 represents water-wet condition. The image was adapted from *Collini and Jackson* (2020).

Collini et al. (2020) expressed the difference between the measured single- and multi-phase zeta potential as $\Delta\zeta_{wett}$, which implied that the change in zeta potential was due to wettability alteration. $\Delta\zeta_{wett}$ is plotted against the wetting index (I_w), as shown in **Figure 2.12**, where small number of I_w means oil-wet condition. Moreover, **Figure 2.12** also indicates that with the increasing value of $|\Delta\zeta_{wett}|$, the wetting state changes toward oil-wet condition. This study found that no oil recovery was observed at the end of coreflooding experiments when the interpreted oil-water zeta potential had the opposite polarity with rock-water zeta potential. Hence, the authors suggested that the polarity of rock-water and oil-water interfaces should be the same to increase the electrostatic repulsive force between these two interfaces and subsequently gain more oil recovery. As a result, the polarity of the interpreted rock-water and the oil-water zeta potential (after aging) must be known in order to design the injected brine in such a manner as to achieve the same polarity for the two interfaces and yield to the improvement oil recovery.

2.7. Previous measurement of the zeta potential of CO_2 containing system

Numerous experimental measurements of the zeta potential have been conducted for a wide range of subsurface applications, including hydrocarbon recovery (e.g., *Jackson et al.,* 2016a, 2016b), geothermal resources (*Revil and Pezard*, 1998; *Vogt et al*., 2014), underground gas storage (*Moore et al.,* 2004), characterising a fractured subsurface system (*Jougnot et al.,* 2020), monitoring groundwater aquifers (*Graham et al.,* 2018; *MacAllister et al.,* 2018) and contaminant transport of nanoplastics in porous media (*Lu et al.,* 2021). However, the measurement of the zeta potential in the presence of CO_2 in rock and/or water systems is rare, particularly under conditions suitable for CO_2 underground storage.

A study by *Moore et al.* (2004) reported the measurement of the streaming potential in Berea sandstone samples saturated with tap water and liquid CO_2. The experiments were conducted at the maximum pressure of 6.5 MPa and temperature of 20°C. The authors reported that the streaming potential coupling coefficient before liquid CO_2 flooding was negative and decreased ten-fold from the initial value after the liquid CO_2 flooding (*Moore et al.,* 2004). Despite the fact that the authors did not report the value of the zeta potential explicitly, the polarity of zeta potential can be interpreted quantitively as the same as the reported streaming potential coupling coefficient, as both parameters are directly proportional. In addition, as the experiments were conducted in sandstone samples, which are widely known for the high pH dependency at the quartz-water interfaces (e.g., *Vinogradov and Jackson,* 2015; *Vinogradov et al.,* 2018), the equilibrium pH between the aqueous solution with rock sample becomes a crucial parameter. However, the authors did not report any pH measurements.

Furthermore, a study by *Ushikubo et al.* (2010) examined the zeta potential of CO_2-water interface by generating CO_2 gas bubbles in ultrapure water. The experiments were conducted at the temperature of 20°C and pressure of 0.1 MPa using the electrophoretic mobility method (EPM). The zeta potential of CO_2 gas in ultrapure water was negative and became more negative with increasing water pH. Similar findings were also reported by an experimental study of *Kim and Kwak* (2017), in which the authors reported the measurements of zeta potential of CO_2-water interface at the maximum pressure of 0.2 MPa in 0.01M (M = mol·L^{-1}) NaCl solution with unreported temperature of experiments. The zeta potentials for the pH range of 3 – 11 were negative and decreased with increasing solution pH. Lastly, the most recent study by *Phan et al.* (2020) generated CO_2 bubbles in the deionized pure water at three different pressures of CO_2 (0.30, 0.35 and 0.40 MPa) at the temperature of 25°C. The results of their experiments were consistent with the previous studies (*Ushikubo et al.* 2010; *Kim and Kwak,* 2017). Therefore, we can conclude that the findings of CO_2-water zeta potentials for all

these three studies (i.e., *Ushikubo et al.* 2010; *Kim and Kwak,* 2017; *Phan et al.* 2020) are negative and controlled by solution pH, however none of the studies investigated CO_2 in its supercritical state.

Chapter 3 Zeta potential of CO_2-rich aqueous solutions in contact with intact sandstone sample at temperatures of 23°C and 40°C and pressures up to 10.0 MPa*

) The text for this chapter was prepared for publication and it was accepted during the registration period of my study in Journal of Colloid and Interface Science. The final version of the published paper can be seen at https://doi.org/10.1016/j.jcis.2021.09.076

3.1. Introduction

Quartz is a common mineral comprising 12% of the Earth's crust (*Ronov and Yaroshevsky*, 1969). Quartz is also the constituent mineral of sandstone formations, and it can be found in many subsurface settings including aquifers (e.g., *Edmunds et al.,* 1982; *Edmunds and Smedley*, 2000), hydrocarbon reservoirs (e.g., *Coop and Willson,* 2003; *Gulamali et al.,* 2011) and geothermal sources (e.g., *Aquilina et al.,* 1997; *Schmidt et al.,* 2017). To characterise the subsurface flows in such settings, a variety of electrical geophysical methods are available including electrical resistivity tomography (e.g., *Daily et al.,* 1992; *Ogilvy et al.,* 2009), electro-seismic (injecting electric current and measuring the resulting seismic energy; e.g., *Haartsen and Pride,* 1997; *Jouniaux and Zyserman,* 2016), seismo-electric (generating a seismic wave and measuring the resulting electric field; e.g., *Jouniaux and Zyserman,* 2016; *Peng et al.,* 2020) and self-potential (SP) (voltage that arises in response to existing gradients in pressure, concentration or temperature; e.g., *Jouniaux et al.,* 2009; *Revil and Jardani,* 2013) measurement. The SP has been shown to be an efficient method to characterise single- and multi-phase flows in the subsurface, especially in sandstone reservoirs (e.g., *Jackson et al.,* 2012a; *Vinogradov and Jackson.,* 2015). Moreover, the SP method can characterise permeability heterogeneities (e.g., fractures, faults, and variable permeability zones; *Vogt et al.,* 2014; *Jougnot et al.,* 2020).

The SP method relies on electrochemical processes that arise in response to the establishment of an electrical double layer (EDL) at the rock-water interface; this can be characterised by the zeta potential (e.g., *Hunter,* 1981; *Revil et al.,* 1999). The zeta potential also plays an important role in determining the wettability (e.g., *Collini et al.,* 2020); while the wetting state controls the pore occupancy of aqueous solutions (hereafter referred to as water for simplicity) and non-aqueous phase fluids (NAPF) in multi-phase systems, and thus strongly influences fluid saturations and flow patterns, e.g. in CO_2 geological storage (CGS) (*Pentland.,* et al 2011), hydrocarbon recovery (*Green and Willhite,* 1998), or H_2 geo-storage (*Iglauer et al.,* 2021).

There are three principal forces (namely van der Waals, structural and electrostatic forces (*Hirasaki,* 1991) that act between rock-water and NAPF-water interfaces; these forces determine the disjoining pressure, which in turn controls the wetting state. Structural forces

are always repulsive, thus implying a positive (repulsive) contribution to the disjoining pressure (*Hirasaki,* 1991; *Jackson et al.,* 2016a), while van der Waals forces depend on properties of all constituent phases (refractive index, dielectric constant and absorption frequency), and these forces can be characterised by the Hamaker theory, resulting in either positive or negative (*Israelachvili,* 1974; *Hirasaki,* 1991; *Adair et al.,* 2001) to the disjoining pressure. Electrostatic forces can also be positive or negative (*Hirasaki,* 1991; *Misra et al.,* 2019) depending on rock mineralogy, water pH, ionic strength and chemical composition. The magnitude and polarity of the electrostatic forces depend on the interfacial zeta potentials, which can vary substantially (*Jackson et al.,* 2016a), therefore these forces play a key role in controlling the wettability.

In order to accurately characterise the wettability, the measured experimental data of zeta potential of rock-water and NAPF-water interfaces is essential. There are two common methods available for measuring zeta potential; namely the electrophoretic mobility and streaming potential. The electrophoretic mobility method (EPM) relies on the motion of the dispersed phase (either rock or NAPF) relative to the continuous stationary water phase under the influence of an applied electric field (*Delgado et al.,* 2007). In contrast, the streaming potential method (SPM) is based on the flow of water through a stationary porous medium, which may also contain NAPF, under the influence of a pressure gradient (*Revil et al.,* 1999; *Delgado et al.,* 2007). The benefits of using EPM include a relative ease of use commercially available instruments. However, the measurement conditions are far from representative of deep subsurface settings for several reasons. Firstly, EPM cannot currently be used under high pressure and elevated temperature conditions, or with high ionic strength electrolytes (>1.0 M), the conditions that are typical for deep rock formations (*Jackson et al.,* 2016a). Secondly, EPM requires either a powdered mineral sample or emulsified NAPF dispersed in water and therefore, it cannot capture the true complex pore space topology (*Jackson et al.,* 2016a). Finally, EPM cannot take into account a third phase, which is needed for multi-phase flow (e.g., water and gas) (*Alroudhan et al.,* 2016). In contrast, SPM can be used on intact sandstone samples (e.g., *Walker et al,* 2014; *Walker and Glover,* 2018), at elevated temperature (e.g., *Vinogradov and Jackson,* 2015), using low-to-high salinity electrolytes of simple and complex composition (e.g., *Vinogradov et al.,* 2010) and also on multi-phase systems containing water, NAPF and minerals at the same time (e.g., *Vinogradov and Jackson,* 2011; *Collini and Jackson,* 2021). However, conducting SPM experiments is challenging and time consuming, especially under the typical deep subsurface settings (high pore pressure and elevated temperature). Acquisition of the high pore pressure and elevated temperature data is particularly important as gas (CO_2) under these conditions (e.g., CO_2 injected into subsurface formations for long-term sequestration) dissolves in water to a higher

degree and alters the ionic composition, reduces pH, so that the resulting aqueous solution becomes the so-called carbonated water (C_water). Such changes in water chemistry will have an impact on the C_water-rock and C_water-NAPF zeta potentials and will ultimately affect the wettability and dynamics of flow of each fluid. Note that the term C_water used in this study corresponds to any aqueous solution with non-zero concentration of dissolved CO_2.

Several attempts have been made to measure the zeta potential in CO_2 containing systems. A recent study published by *Kim and Kwak* (2017) reported the zeta potential of CO_2-water interfaces using EPM. The experiments were conducted by bubbling CO_2 gas through 0.01M NaCl solution. The zeta potential was reported to be negative, but the experiments were conducted at atmospheric pressure and unreported temperature. Another study by *Moore et al.* (2004) reported measurements of the zeta potential using SPM in Berea sandstone samples saturated with tap water and liquid CO_2. The experiments were conducted at a maximum pressure of 6.5 MPa and temperature of 20°C, so that the latter value is not consistent with the expected temperature of 38ºC normally found at the depth that corresponds to 6.5 MPa (*Liebscher et al.,* 2013). The single-phase zeta potential was measured in a rock sample fully saturated with water, which was not carbonated prior to the experiments, i.e., the amount of dissolved CO_2 corresponded to the atmospheric level. The experiment was repeated with water and immiscible liquid CO_2 and the effective (i.e., multi-phase) zeta potential was found to be negative and approximately ten-fold smaller in magnitude compared with the single-phase zeta potential. However, *Moore et al.* (2004) did not report single-phase zeta potential measurements conducted with C_water under the same experimental conditions, hence the contribution of the zeta potential at the interface between water and immiscible liquid CO_2 could not be quantified. Moreover, *Moore et al.* (2004) did not report the equilibrium pH of water during the experiments, to indicate whether chemical equilibrium between the mineral, water and liquid CO_2 was established. Since pH is known to have a strong effect on the silica-water zeta potential (*Vinogradov and Jackson,* 2015; *Vinogradov et al.,* 2018), uncertainty exists in relation to *Moore et al.* (2004)'s reported multi-phase zeta potential results. Furthermore, to the best of our knowledge, no experimental zeta potential data for C_water-rock or C_water-immiscible CO_2 interfaces under high pressure and elevated temperature conditions has been reported (which are typical for deep subsurface formations). Note that in CGS, CO_2 is stored below a depth of 800 m, so that the CO_2 exists in a dense supercritical phase (*IPCC,* 2005; *Iglauer,* 2018), pressure ≥ 7.38 MPa and temperature ≥ 31.1°C.

In the absence of such measured zeta potential data, several models have been proposed with which the wettability of sandstones can be predicted. For instance, *Tokunaga* (2012) and *Kim et al.* (2012) reported an analytical model of water film stability based on DLVO (Derjaguin,

Landau, Verwey, Overbeek) theory; the model was used to simulate CO_2 geological storage (CGS) conditions in sandstone reservoirs. The model required knowledge of the electrostatic interactions between silica-water and CO_2-water interfaces, to calculate the corresponding contribution to the disjoining pressure, and the model was implemented using compression approximation (*Gregory,* 1975). *Tokunaga* (2012) and *Kim et al.* (2012) assumed that the zeta potential of the silica-water interface was -25 mV for 0.01 M ionic strength solution, and -5 mV for 2 M ionic strength. Both *Tokunaga* (2012) and *Kim et al.* (2012) assumed a zero zeta potential at the CO_2-water interface. However, neither of the assumed values was validated due to a lack of experimental data under true CGS conditions. Moreover, when the CO_2 dissolves in water at high pressure, and the pH of C_water becomes substantially lower (*Adamczyk et al.,* 2009; *Peng et al,* 2013), the zeta potential of C_water-silica interfaces should become vanishingly small (*Kosmulski et al.,* 2002). This, however, is inconsistent with the assumed values by *Tokunaga* (2012) and *Kim et al.* (2012), thus their wettability estimates are also doubtful.

Therefore, the main aim of this study is to develop an experimental methodology and for the first time measure the streaming potentials in intact sandstone samples under high pressure and elevated temperature, using C_water, to improve our understanding of the electrochemical processes that take place at silica-water interfaces. The outcomes of this study will, among other applications, better inform CGS, hydrocarbon recovery and geothermal projects. This work also provides fundamental petrophysical data essential for a broad range of Earth sciences.

3.2. Materials and methods

3.2.1. Materials

A cylindrical Fontainebleau sandstone sample was used in this study. Petrophysical properties of the sample listed in **Table 3.1** suggest partial cementation, in line with the values of porosity and formation factor (*Walker and Glover,* 2018), which was important for repeated saturation. Prior to conducting the streaming potential measurements, the sample was thoroughly cleaned following the procedure reported by *Alroudhan et al.* (2016).

We used synthetic single-salt solutions made with reagent-grade NaCl, $CaCl_2.2H_2O$, $MgCl_2.6H_2O$, and Na_2SO_4 (Sigma Aldrich, Australia) dissolved in deionized (DI) water. The DI water (electrical resistivity 15 MΩ·cm -18 MΩ·cm) was supplied by a filtering system from Ibis Technology (Ascot, Australia). The ionic strength of all four solutions was kept constant at 0.05 M during preparation under laboratory (ambient) pressure and 23^{o}C temperature. Although the 0.05 M ionic strength is lower than that of a typical deep aquifer or hydrocarbon reservoir identified for implementation of CGS, the concentration was selected as an initial point in this

proof-of-concept study, and further work probing higher concentration is planned. All laboratory experiments were conducted using two types of aqueous solutions: 'dead' and 'live' water. The dead water was a synthetic aqueous solution fully equilibrated with atmospheric CO_2 (which corresponds to partial CO_2 pressure of $10^{-3.44}$ atm and to a dissolved CO_2 concentration of 1.487×10^{-5} M; *Li et al.,* 2016). The CO_2 content of the dead water remained unchanged throughout the experiment. On the other hand, to prepare the live water we used a salt solution prepared under ambient pressure and temperature, which subsequently was brought in contact with pure CO_2 (supplied by Coregas, Australia, with the mole fraction ≥ 0.99) in a mixing reactor (*El-Maghraby et al.,* 2012). The system was pressured and heated to target experimental pressure and temperature. Allowing CO_2 and water to mix for a long period of time in the reactor (no less than 3 hours); while measuring the volume of the CO_2 cap until it stabilised under constant pressure, the thermodynamic equilibrium between water and CO_2 was established. The target pressure and temperature that corresponded to the live water equilibrium was maintained throughout each experiment.

Prior to carrying out the streaming potential measurements with dead water, the saturated rock sample was placed in a core holder, and the entire system was sealed from atmosphere. The detailed experimental protocol of the streaming potential measurement using both dead and live water is provided in subsequent sections.

Table 3.1. Petrophysical properties of the Fontainebleau sandstone sample used in this study. Mineralogy of the sample was taken from (*Vinogradov et al.,* 2010; *Al Saadi et al.,* 2017; *Cherubini et al.,* 2019). Sample porosity was measured by gas (N_2) expansion using AP-608 Automated Permeameter and Porosimeter (Coretest System Inc, USA). The formation factor was obtained with five dead NaCl solutions with ionic strength between 0.05 M and 1 M. The liquid permeability was calculated using Darcy's Law from the slope of linear regression of the flow rate against the pressure difference during the streaming potential measurements using at least four different flow rates with confirmed the quality of regression (R^2) is high ($R^2 \geq 0.98$).

Sample	Fontainebleau sandstone
Mineralogy	>99 wt.% quartz
Porosity	9.0 ± 1.0%
Liquid Permeability	70 ± 5 mD ($6.91 \times 10^{-14} \pm 4.93 \times 10^{-15}$ m^2)
Dimensions	Length = 0.0783 m, Diameter = 0.0382 m
Formation Factor, *F*	58 ± 2

3.2.2. Measurements of pH and water and saturated rock electrical conductivity

The dead water experiments were conducted at pore pressures up to 10 MPa and temperatures up to 40°C. Since the concentration of dissolved CO_2 remained constant at atmospheric level during the dead water experiments (in the closed system), effluent water samples were regularly collected and pH values and electrical conductivities were measured outside the system using a FiveGo pH meter (Mettler Toledo, accuracy of 0.01 pH units) and a Jenway 4520 conductivity meter (Cole-Palmer, 0.5% accuracy), respectively.

The live water experiments were carried out over the same pressure ranges (up to 10 MPa backpressure) and temperatures of 40°C. Live water pH values were measured using an in-line high-pressure pH meter (model number of pH-G-10"-T375-NPT250A-C276, Corr Instruments, LLC, accuracy of 0.01 pH units). Both pH meters, as well as the conductivity meter were regularly calibrated using standard solutions and manufacturer's recommended procedure.

The chemical equilibrium between the rock sample and all aqueous solutions was assured using pH and water electrical conductivity measurements on a regular basis as detailed by *Vinogradov and Jackson* (2015). The solution was pumped from the injection pump to the receiving pump through the rock sample and then back again repeatedly. The equilibrium condition was obtained when the measured pH and water conductivities from both pumps was constant and equal within 2% tolerance. Therefore, the measured pH values and water conductivities reported here represent the equilibrium values (for a given solution, pressure and temperature). Dead and live water properties are provided in **Table 3.2**.

The saturated rock conductivity (σ_{rw}) was measured in-situ using a pair of internal electrodes and following the procedure of *Vinogradov et al.,* (2010). The internal electrodes were connected to a BK Precision 891 LCR Meter, and AC was induced sweeping over the frequency range of 20 Hz to 300 KHz (1KHz = 1000 Hz). The measurement was conducted inside the oven to keep the constant temperature condition while the coreflooding cell was kept pressurised. The reactance (*X*) was then calculated from the measured total impedance (*Z*) and the resistance (*R*) over the frequency range by,

$$X = \sqrt{Z^2 - R^2}. \qquad 3.1$$

The value of the R_x at the minimum *X* was used to calculate the σ_{rw} using equation below,

$$\sigma_{rw} = \frac{L}{R_x \pi r^2}, \qquad 3.2$$

where *L* is length of the core sample and *r* is the radius of the core sample. The intrinsic formation factor (*F*) was obtained prior to carrying out the streaming potential measurements

using NaCl solutions between 0.05M and 1M, and following the protocol of *Vinogradov et al.* (2010).

Table 3.2. Dead and live water properties for all tested experimental conditions, where P is the pore pressure, T is the experimental temperature, σ_w is the elctrical conductivity of tested solution. pH values reported for all dead water experiments correspond to partial CO_2 pressure of $10^{-3.44}$ atm. The ionic strength of all solution was kept constant at 0.05 M. The reported uncertainties in the table are based on both the instrument accruracy and measurement repeatability. The total uncertainty in σ_w was ± 0.01 $S \cdot m^{-1}$ in all experiments.

Solution	P, MPa	T, ºC	Solution type	pH value	σ_w, $S \cdot m^{-1}$
NaCl	0.2	23	Dead water	7.10 ± 0.10	0.55
	4.5	23	Dead water	7.00 ± 0.10	0.55
	7.5	23	Dead water	7.10 ± 0.10	0.56
	10.0	23	Dead water	7.20 ± 0.10	0.55
	0.2	40	Dead water	6.30 ± 0.20	0.61
	4.5	40	Dead water	6.30 ± 0.20	0.60
	7.5	40	Dead water	6.20 ± 0.20	0.61
	10	40	Dead water	6.20 ± 0.20	0.60
	4.5	40	Live water	3.80 ± 0.10	0.65
	7.5	40	Live water	3.50 ± 0.10	0.64
	10.0	40	Live water	3.33 ± 0.05	0.55
$CaCl_2$	0.2	23	Dead water	6.20 ± 0.10	0.34
	7.5	23	Dead water	6.20 ± 0.10	0.34
	0.2	40	Dead water	5.60 ± 0.20	0.46
	7.5	40	Dead water	5.50 ± 0.20	0.46
	7.5	40	Live water	3.17 ± 0.05	0.54
$MgCl_2$	0.2	23	Dead water	6.90 ± 0.10	0.37
	7.5	23	Dead water	6.80 ± 0.10	0.37
	0.2	40	Dead water	6.05 ± 0.20	0.51

	7.5	40	Dead water	6.10 ± 0.20	0.51
	7.5	40	Live water	3.40 ± 0.05	0.50
Na_2SO_4	0.2	23	Dead water	7.80 ± 0.10	0.36
	7.5	23	Dead water	7.70 ± 0.10	0.36
	0.2	40	Dead water	6.70 ± 0.20	0.48
	7.5	40	Dead water	6.70 ± 0.20	0.48
	7.5	40	Live water	3.60 ± 0.10	0.59

3.2.3. Experimental setup

The streaming potential measurements were conducted in a high pressure-high temperature (HPHT) coreflooding apparatus (schematically shown in **Figure 3.1**). The coreflooding apparatus was placed inside an oven with controlled temperature (accuracy of ± 1°C). For the dead water experiments, the branch of the experimental apparatus comprising units #10 - #12 (**Figure 3.1**), used for preparing live water, was disconnected from the rest of the setup.

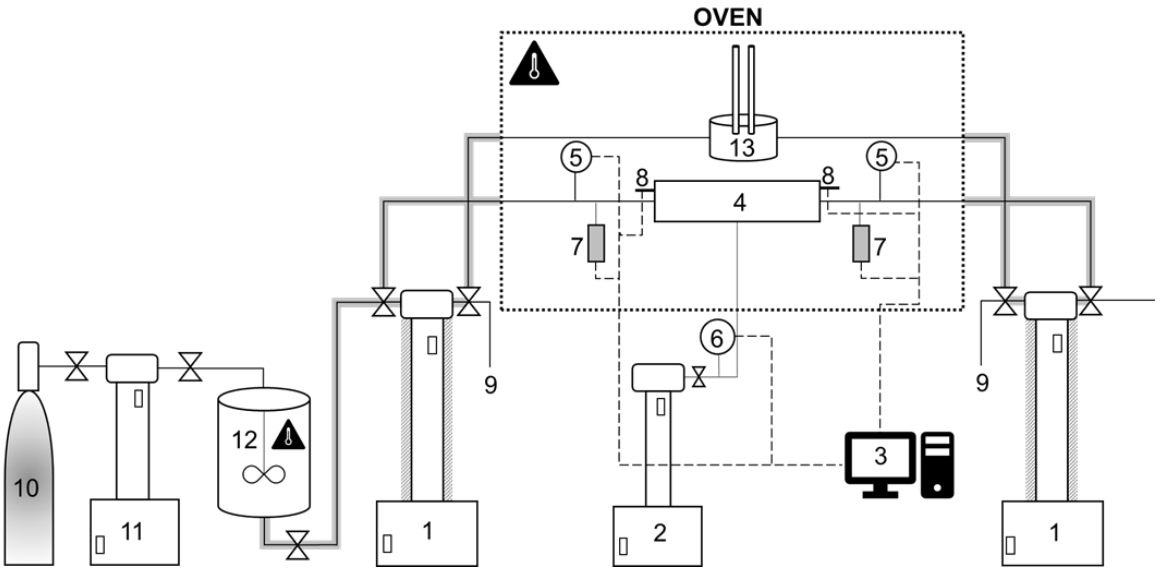

Figure 3.1. The experimental apparatus used in streaming potential measurements. The solid grey lines represent flowlines and the dashed grey lines represent electrical connections. (#1) heated 500D Hastelloy ISCO pumps to the left and to the right of the core holder; (#2) 500D is a stainless steel ISCO pump used to induce the confining pressure around the rock sample; (#3) data acquisition system; (#4) is the HPHT coreflooding cell (core holder); (#5) two high precision pressure transducers; (#6) high precision pressure transducer used to monitor the confining pressure; (#7) external electrodes to the left and to the right of the core holder; (#8) internal electrodes to the left and to the right of the core holder; (#9) are sampling tubes to the left and to the right of the core holder; (#10) CO_2 cylinder; (#11) 260D Stainless steel ISCO pump used for pumping CO_2 into the mixing reactor; (#12) heated Parr mixing reactor; (#13) high pressure in-line pH meter.

The pressure difference across the core sample was measured continuously with a high precision Keller-Druck pressure transducer (series 33X, 0.1% accuracy). Furthermore, the voltage across the sample was recorded with a NI 9207 voltmeter with high internal impedance (>1 GΩ) and 0.52% accuracy. Two high precision syringe pumps (#1 in **Figure 3.1**; 500D Hastelloy ISCO) were used as injector and receiver to induce water flow in either direction through the sample. The pump used as injector was set to deliver water at a constant flow rate while the receiving pump on the opposite side was set at a constant receiving pressure (i.e., maintaining a constant back pressure during the experiment). During all coreflooding experiments, the difference between the confining pressure and the pore pressure was kept constant at approximately 3 MPa. The maximum difference between the injection and the outlet pressure that corresponds to the highest tested flow rate was 0.14 MPa. Constant target temperature was maintained during the experiments by heating cylinders of both pumps with an embedded water jacket and insulating all flowlines outside the oven to prevent heat losses. Upon completion of each streaming potential experiment, the saturated rock conductivity was measured using the internal electrodes (#8) connected to a BK Precision 891 LCR meter (0.05% accuracy), by sweeping the applied alternate voltage frequency between 20 Hz and 300 KHz.

3.2.4. Streaming potential measurements in rock samples saturated with dead water

The streaming potential method was used to obtain the zeta potential of the rock-water interface. The method relies on the assumption that at steady state, the streaming current is balanced by the conduction current during one-directional flow of water through the porous medium, consistent with our core flooding experiments where stable pressure and voltage were established across the rock sample. To achieve such conditions, the paired-stabilized (PS) method described in *Vinogradov and Jackson* (2011) was implemented to measure the streaming potential coupling coefficient (C_{SP}). Employing the PS method also allowed us to eliminate any asymmetry in the electrode potential as detailed in (*Vinogradov et al.,* 2010). C_{SP} was interpreted from the slope of linear regression of stabilised (normalised) voltage (see Equation 7a in *Vinogradov et al.,* 2010) as a function of stabilised pressure difference (normalised ∆P; see Equation 7b in *Vinogradov et al.,* 2010). The zeta potential (ζ) was then calculated via the modified Helmholtz-Smoluchowski equation (which accounts for the surface electrical conductivity *Jouniaux and Pozzi,* 1995; *Revil et al., 1999; Glover,* 2015):

$$C_{SP} = \frac{\Delta V}{\Delta P} = \frac{\varepsilon \zeta}{\mu \sigma_{rw} F} \qquad 3.3$$

where ΔV is the stabilised voltage in [V], ΔP is stabilised pressure [Pa], ε is the water permittivity in [F·m^{-1}], μ is the water dynamic viscosity in [Pa·s], σ_{rw} is the electrical conductivity of the saturated rock sample in [S·m^{-1}] and F is the intrinsic formation factor, which was found

to be constant for all tested solutions implying negligibly small surface conductivity even at the lowest tested ionic strengths (refer to **Appendix A**). Note that since the intrinsic formation factor was constant for all tested solutions (F = 58; refer to **Appendix A**), **Equation 3.1** reduces to the classical Helmholtz-Smoluchowski equation and water conductivity can also be used to compute the zeta potential. We calculated ε and μ to account for the temperature and ionic strength using the approach provided in *Saunders et al.* (2012). The details regarding the calculation can be referred to Appendix A in *Saunders et al.* (2012).

3.2.5. Streaming potential measurements in rock samples saturated with live water

The live water experiments required several modifications to the apparatus and the experimental protocol due to the corrosive nature of the live water. The new procedure in detailed below.

During the rock sample preparation step, an additional layer of thin polytetrafluoroethylene (PTFE) tape was wrapped around the rock sample, and a PTFE heat shrinkable sleeve was placed around the PTFE taped sample. The entire assembly was then placed inside a Viton sleeve, which was thus isolated from the corrosive pore fluid. The sample inside the Viton sleeve was mounted into the core holder (#4) and pressurized with dead water as a confining fluid (note that Viton is not compatible with acids).

For preparing live water, 500 mL dead water was placed in the mixing reactor (#12), and the reactor was closed with a small air cap left above of the dead water. The reactor was heated overnight by circulating hot water in its water jacket to the target 40°C at atmospheric pressure so that the experimental temperature was established.

Fluid equilibration started with the delivery of CO_2 at 4 MPa from the CO_2 cylinder (#10) to the pre-emptied high precision syringe pump (#11). Subsequently, the CO_2 in the pump was pressurized to the target pore pressure (4.5 MPa, 7.5 MPa or 10 MPa), and pumped through flowlines into the mixing reactor using constant pressure delivery mode. The volume of the CO_2 remaining in the pump (#11) was constantly monitored every 15 minutes, and the pressure in the reactor (#12) was equilibrated with that of the pump (#11) using the constant pressure delivery mode, and the gas entrainment stirrer inside the reactor was activated to rigorously mix the liquid phase (water) and the CO_2 cap at the top (thus accelerating the equilibration; *El-Maghraby et al.,* 2012). Equilibrium between the water and CO_2 phases was assumed to have been established when the volume of CO_2 inside the pump ceased to decrease and remained constant for at least 3 hours thus indicating that no additional CO_2 dissolved in water. At this stage, we assumed the water was fully saturated with CO_2 and it was transferred from the reactor to the injection pump (#1, to the left of the core holder in **Figure 3.1**) for the experiments.

Due to technical limitations of the injection pump (#1), all of the live water in the reactor (#12) was transferred to the pump (#1 to left of the core holder in **Figure 3.1**) containing approximately 5 mL of dead water. Moreover, the setup's dead volumes (valves, tubing), the pore space of the rock sample, and the receiving pump (#1 to the right of the core holder in **Figure 3.1**) also contained pressured (to the same pressure as that in the injection pump) dead water. In total, 400 mL of fully CO_2 saturated live water was mixed with approximately 30 mL of dead water remaining in the system, thus disturbing the chemical and thermodynamic equilibrium. Therefore, slightly undersaturated solution was induced from left to right and back again. The procedure that usually lasted for at least 2 days was repeated several times while regularly measuring the pH, rock permeability, electrical conductivity of the sample and C_{SP}, until all properties stabilised at constant values (within 2% tolerance). The confirmed stability of electrical conductivity of the saturated rock sample and its permeability throughout the equilibration period also indicated there was no measurable dissolution or precipitation of minerals.

The streaming potential measurements then commenced and were completed using at least 4 different flow rates following the recommended PS procedure (*Vinogradov and Jackson,* 2011). To measure the voltage across the rock sample in live water experiments only the internal electrodes (#8) were used (details on design and materials used for the internal electrodes are provided in *Vinogradov et al.,* 2010) due to their higher stability relative to that of the external electrodes. Note that *Vinogradov et al.* (2010) reported that the external electrodes were more stable compared to the internal electrodes, which contrasts our experimental observation. We hypothesize, that under supercritical CO_2 conditions of our experiments, the ceramic disks located inside the external electrode casings became chemically unstable, resulting in less stable voltage.

The zeta potential was interpreted from the measured C_{SP} using **Equation 3.1**, for which the updated values of σ_{rw}, ε and μ of live water were required (F remained constant in all reported single-phase experiments).

The live water saturated rock conductivity (σ_{rw}) was measured in each experiment. Live water electrical conductivity (σ_w) was calculated by multiplying the intrinsic formation factor (assumed to be constant and equal to that measured with the corresponding dead water) by the live water saturated rock conductivity and all values are reported in **Table 3.2**. The live water ionic strength (salinity) was determined using σ_w (refer to section 2.6 in *Vinogradov et al.,* 2010), and the salinity was then used to adjust the permittivity of live water (ε) using the approach described in *Saunders et al.* (2012).

The viscosity of the live water (μ_{lw}) at given pressure and temperature was then calculated via the approach proposed by *Islam and Carlson* (2012):

$$\mu_{lw} = \mu_s \times (1 + 4.65 x_{\mathrm{CO}_2}^{1.0134}) \qquad 3.4$$

where μ_s in [Pa·s] is the viscosity of dead water as a function of pressure and temperature, and $x\mathrm{CO}_2$ is the mass fraction of dissolved CO_2 at experimental conditions. Due to the lack of published measurements of μ_s for all tested salt types and temperatures of our dead solutions, we adopted the approach of *Saunders et al.,* (2012) to infer the dead water viscosity from the measured electrical conductivity. The calculated values of μ_s for our dead solutions were compared against available published data (for the same salts at concentrations and temperatures consistent with our experimental conditions), and the discrepancy was found to be less than 2% thus confirming the appropriateness of the approach.

The mass fraction of dissolved CO_2 ($x\mathrm{CO}_2$) was evaluated using the model of *Zhao et al.* (2015b, 2015c) and validated for 0.05M NaCl live water against the experimental values reported by *Islam and Carlson* (2012) for 40ºC and 7.5 MPa, and was found to be identical within 1% discrepancy.

The exponent in **Equation 3.2** was assumed to be constant for all types of live water investigated here, since it only defines how the solubility of CO_2 depends on the salt type, and the solubility was reported to be nearly identical for all tested salts at ionic strength of 0.05M (e.g., *Liu et al.,* 2011).

3.3. Result and discussion

3.3.1. Streaming potential coupling coefficient measurements

Typical results of PS experiments for select experimental conditions are shown in **Figure 3.2**. The noise level of the stabilised voltage measured for live water (**Figure 3.2c**) was considerably higher than for dead water (**Figure 3.2a**). Moreover, the static voltage (i.e., the voltage that corresponds to no-flow conditions and zero pressure difference across the sample) measured for live water did not always return to the exact initial value (as prior to the core flooding experiment), thus contributing to additional error in the streaming potential coupling coefficient and the corresponding zeta potential.

Experimental repeatability at a given flow rate with live water was also poorer when compared with dead water (compare the scatter for a given pressure difference in **Figures 3.2b** and **3.2d**). The values of all measured streaming potential coupling coefficients inclusive of all experimental uncertainties (obtained from the variation in the slope of the linear regression within the error bars that account for the noise level and repeatability, as shown in **Figures 3.2b** and **3.2d**) are summarized in **Table 3.3**.

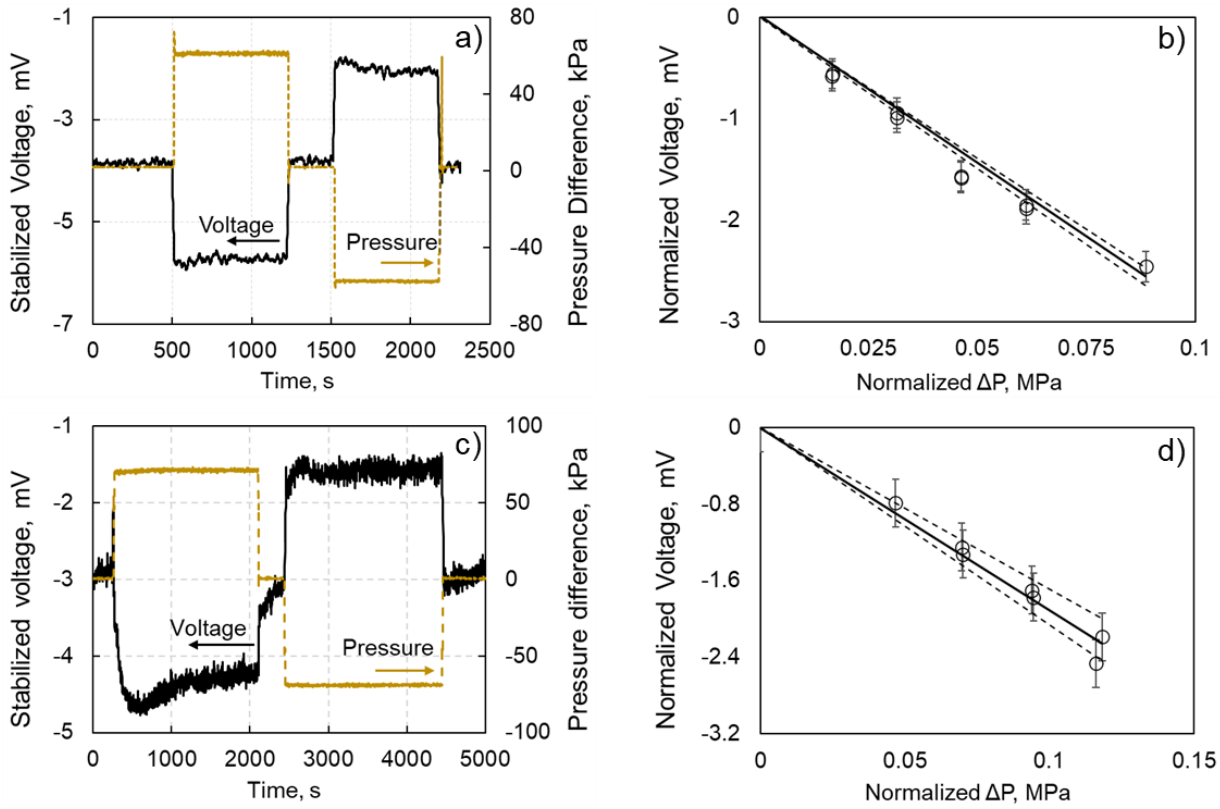

Figure 3.2. Typical results of paired stabilised (PS) experiments (a, c) and the streaming potential coupling coefficient represented by the linear slope of the stabilised voltage, ΔV, plotted against the stabilised pressure difference, ΔP (b, d). (a) dead NaCl solution pumped at a constant rate of 4 ml/min, temperature of 23°C and pore pressure of 7.5 MPa); (b) C_{SP} interpreted from the data of (a); (c) typical data of PS experiment carried out with live NaCl solution at constant rate of 6 ml/min, temperature of 40°C, pressure of 7.5 MPa; d) C_{SP} interpreted from the data of (c). Dashed lines represent possible variation of C_{SP} within the total experimental uncertainty denoted by the error bars. Error bars in (b,d) represent the noise level of voltage during the measurement.

3.3.2. Dead water zeta potential

Zeta potentials for dead water remained negative for all tested conditions. Moreover, for any given temperature and salt type, the zeta potential was independent of the pore pressure (**Figure 3.3a**). Dead water equilibrium pH values were also independent of pore pressure for any given salt type (**Figure 3.3b**), which implied that the amount of dissolved CO_2 remained constant during the experiments. However, pH decreased with increasing temperature, consistent with previously reported studies (*Millero et al.,* 2009; *Vinogradov and Jackson,* 2015; *AlMahrouqi et al.,* 2016; *Vinogradov et al.,* 2018).

The largest in magnitude zeta potential was obtained with Na_2SO_4, and it became progressively smaller in magnitude when using NaCl, $MgCl_2$ and $CaCl_2$, ($|\zeta_{Na_2SO_4}| > |\zeta_{NaCl}| > |\zeta_{MgCl_2}| > |\zeta_{CaCl_2}|$). A difference of less than 1 mV between the zeta potentials of $MgCl_2$ and $CaCl_2$ was observed for both salts at both temperatures of 23°C and 40°C. Although this

difference was small, it was comparable to the difference of 2mV reported by *Vinogradov et al.,* (2018) for the same salt types. The measured pH of solutions in contact with the sample became smaller with the transition from Na_2SO_4 to NaCl, followed by $MgCl_2$ and $CaCl_2$ ($\mathrm{pH}_{\mathrm{Na_2SO_4}} > \mathrm{pH}_{\mathrm{NaCl}} > \mathrm{pH}_{\mathrm{MgCl_2}} > \mathrm{pH}_{\mathrm{CaCl_2}}$), qualitatively consistent with previously published studies (*Datta et al.,* 2009; *Vinogradov et al.,* 2018)

Table 3.3. Streaming potential coupling coefficient (C_{SP}) measured for all tested experimental conditions. The ionic strength of all solution was kept constant at 0.05 M. The reported uncertainties in the table are based on both noise level and repeatability, both of which results in linear regressions slope variation as shown in **Figure 3.2b** and **Figure 3.2d**.

Water	Pressure, MPa	Temperature, ºC	Condition	C_{SP}, mV/MPa
NaCl	0.2	23	Dead water	-29.9 ± 0.07
	4.5	23	Dead water	-29.9 ± 0.07
	7.5	23	Dead water	-29.9 ± 0.07
	10.0	23	Dead water	-30.7 ± 0.07
	0.2	40	Dead water	-28.8 ± 0.10
	4.5	40	Dead water	-28.3 ± 0.10
	7.5	40	Dead water	-28.5 ± 0.10
	10.0	40	Dead water	-28.3 ± 0.10
	4.5	40	Live water	$-23.6^{+\,1.20}_{-\,1.30}$
	7.5	40	Live water	$-19.0^{+\,2.00}_{-\,1.60}$
	10.0	40	Live water	$-18.1^{+\,1.80}_{-\,0.70}$
$CaCl_2$	0.2	23	Dead water	-26.5 ± 0.07
	7.5	23	Dead water	-26.9 ± 0.07
	0.2	40	Dead water	-25.3 ± 0.10
	7.5	40	Dead water	-25.4 ± 0.10
	7.5	40	Live water	$-17.6^{+\,0.90}_{-\,1.20}$
$MgCl_2$	0.2	23	Dead water	-28.0 ± 0.07
	7.5	23	Dead water	-28.4 ± 0.07

	0.2	40	Dead water	-27.4 ± 0.07
	7.5	40	Dead water	-27.3 ± 0.07
	7.5	40	Live water	$-17.8^{+1.40}_{-1.00}$
Na_2SO_4	0.2	23	Dead water	-56.4 ± 0.12
	7.5	23	Dead water	-55.6 ± 0.12
	0.2	40	Dead water	-44.8 ± 0.20
	7.5	40	Dead water	-43.1 ± 0.20
	7.5	40	Live water	$-24.1^{+1.20}_{-2.20}$

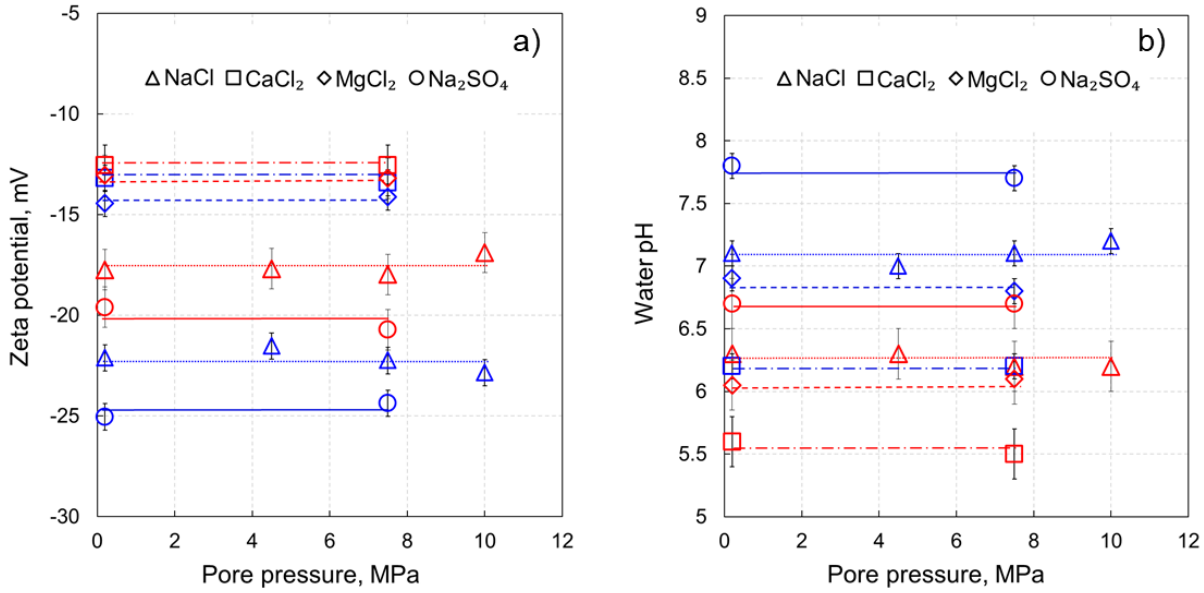

Figure 3.3. Zeta potential a) and pH values b) as a function of pore pressure for all dead water experiments. Blue symbols denote experiments conducted at 23°C; red symbols denote experiments conducted at 40°C. Error bars of zeta potential represent the experimental uncertainty obtained from the variation in the slope of the linear regression of C_{SP} while error bars of pH represent the variation of pH during the experiment.

To quantify the effect of salt type and temperature, zeta potential and water pH were plotted versus temperature (**Figure 3.4**). The zeta potential became more positive with increasing temperature, while water pH decreased with increasing temperature, consistent with previously published results (*Vinogradov and Jackson*, 2015; *Vinogradov et al.,* 2018). The highest rate of increase in the zeta potential with temperature was observed for NaCl (a change of +4.3 mV when transitioning from 23°C to 40°C). An increase in zeta potential (+4.3 mV) was also observed for Na_2SO_4 when temperature increased from 23°C to 40°C. In

contrast, zeta potential increased with increasing temperature by 1.0 mV for both, $CaCl_2$ and $MgCl_2$, when temperature increased from 23°C to 40°C. Therefore, a weaker temperature dependence of the zeta potential was observed for $CaCl_2$ and $MgCl_2$, again consistent with *Vinogradov et al.* (2018).

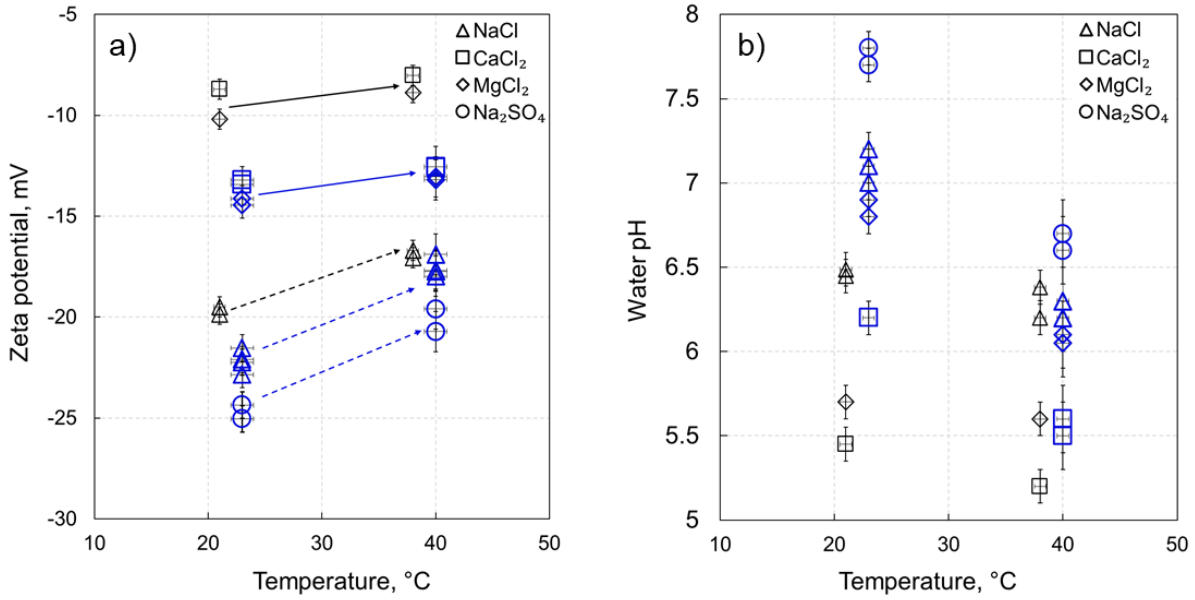

Figure 3.4. Zeta potential a) and pH values b) as a function of temperature for all tested dead water experiments. The data for NaCl, $CaCl_2$, $MgCl_2$ and Na_2SO_4 obtained in this work are shown in blue. Also shown for comparison are the data in black obtained with Fontainebleau sandpacks saturated with 0.015 M solution NaCl, $CaCl_2$ and $MgCl_2$ reported by *Vinogradov et al.* (2018). Error bars in (a) represent the experimental uncertainty obtained from the variation in the slope of the linear regression of C_{SP}. Error bars in (b) represent the variation of pH during the experiment.

However, the rate of pH change with temperature was higher when compared to *Vinogradov et al.* (2018). Moreover, the pH values measured in our experiments were generally larger than those in *Vinogradov et al.,* (2018) for the same salt type at any given temperature. The ionic strength used by *Vinogradov et al.* (2018) was 0.015 M, which is more than three-fold lower than that tested in this study, hence their zeta potentials at lower salinity were expected to be larger in magnitude compared to ours. Since the zeta potentials reported by *Vinogradov et al.* (2018) were smaller in magnitude compared with our results, we believe that their pH values were correct, although different from ours, and had stronger effect on the zeta potential than salinity.

Our results suggest that temperature and salt type affect the pH, which in turn affects the magnitude of the zeta potential of sandstones saturated with dead water (**Figure 3.5**). Based on the results for dead water we propose two distinct linear correlations:

$$\zeta_M[mV] = -4.86 \times pH + 12.57;\ R^2 = 0.976 \qquad 3.5$$

$$\zeta_D[mV] = -1.35 \times pH - 4.96;\ R^2 = 0.973, \qquad 3.6$$

where ζ_M and ζ_D denote the zeta potential for water containing monovalent (Na^+) or divalent (Ca^{2+} and/or Mg^{2+}) cations, respectively. Regardless of anion type (Cl^- or SO_4^{2-}) all experimental points for Na^+ containing solutions align on the same trendline, and so do the points for all $CaCl_2$ and $MgCl_2$ experiments regardless of the cation type (**Figure 3.5**).

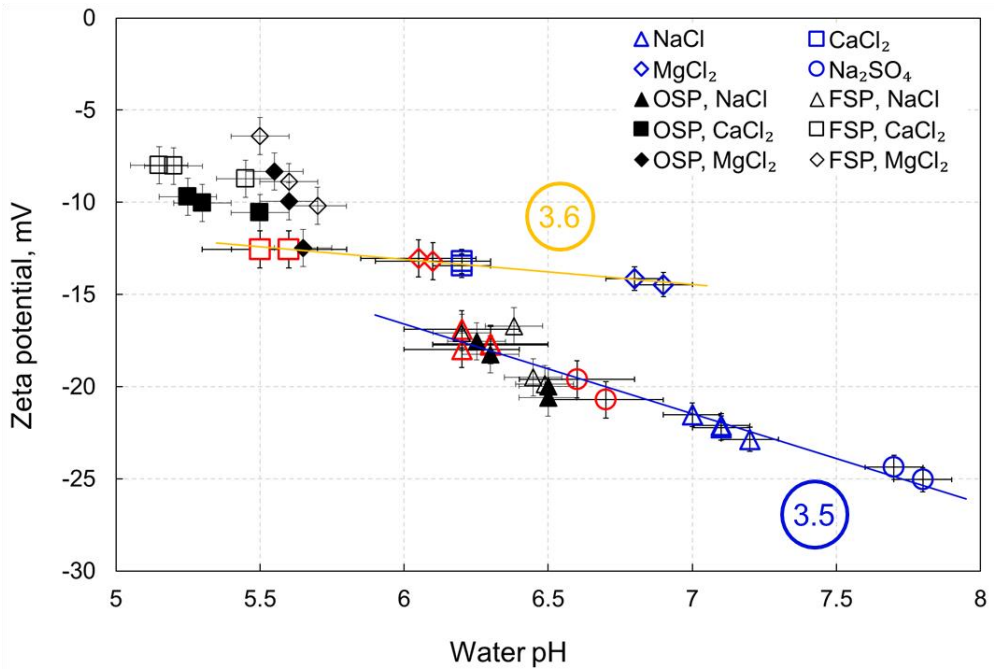

Figure 3.5. Zeta potential as a function of dead water pH for different salt types. Our data are shown in colored symbols; literature data are shown in black (*Vinogradov et al.,* 2018) and corresponds to Ottawa (OSP) and Fontainebleau (FSP) sandpacks (both >99 wt.% quartz content) saturated with 0.015 M dead water. Blue symbols correspond to 23°C, red symbols correspond to 40°C. The blue trendline indicates the linear relationship between the zeta potential of Na^+ containing salts (NaCl, Na_2SO_4) and pH (**Equation 3.5**). The yellow trendline indicates the linear correlation between zeta potential and pH of dead $CaCl_2$ and $MgCl_2$ solutions (**Equation 3.6**). Error bars of zeta potential represent the experimental uncertainty obtained from the variation in the slope of the linear regression of C_{SP} while error bars of pH represent the variation of water pH during the experiment.

The trend obtained for Na^+ solutions (**Equation 3.5**) is identical to that reported for zeta potentials of sandpacks (*Vinogradov et al.,* 2018). However, as seen in **Figure 3.5** the zeta potentials at 23°C measured in this work (blue triangles) were more negative compared with values of *Vinogradov et al.* (2018) and corresponded to higher pH values. The values that correspond to 40°C were consistent with those reported by *Vinogradov et al.* (2018) thus implying stronger temperature effect on both pH and zeta potentials.

In contrast, the trend for divalent cations (**Equation 3.6**) had a flatter slope, compared with that of **Equation 3.5**. Such flattening of the slope is consistent with the pH dependence of $CaCl_2$ solution relative to that of NaCl proposed by *Vinogradov et al.* (2018). Overall, however,

all our ζ_D were more negative than those reported by *Vinogradov et al.* (2018), except for the value at pH = 5.7.

The effect of temperature on pH of divalent solutions ($CaCl_2$, $MgCl_2$), denoted by the shift from blue to red symbols in **Figure 3.5**, was substantially more pronounced in this work compared to *Vinogradov et al.* (2018). Moreover, *Vinogradov et al.* (2018) also suggested that the response of ζ_D to varying pH of $CaCl_2$ solution was different to that of $MgCl_2$, and they attributed this difference to a higher activity of Mg^{2+} towards the mineral surface compared with Ca^{2+} at elevated temperature, i.e. fully hydrated Mg^{2+} at ambient temperature has larger diameter than Ca^{2+} making the latter to be closer to the mineral surface and thus more active (*Datta et al.,* 2009), but at higher temperatures it becomes smaller by losing hydration shells at a higher rate, approaches the mineral surface closer and becomes more active. We did not observe any difference in response of ζ_D to varying pH of either solution at elevated temperature, but we only investigated temperatures of 23°C and 40°C whilst the data presented by *Vinogradov et al.* (2018) included experiments conducted at 70°C and 120°C where the split in response of ζ_D to pH for $CaCl_2$ and $MgCl_2$ was observed. Using **Equations 3.5** and **3.6** allows to accurately predict the expected zeta potential as a function of pH for single salt electrolytes. However, additional work is required to investigate whether the proposed trends can be interpolated for mixtures of different salts.

To validate the proposed correlations between water pH and the zeta potential (**Equations 3.5 and 3.6**) we compared the values computed using these equations against previously published experimental data. *Walker and Glover* (2018) obtained over 100 zeta potential measurements on intact Fontainebleau sample (F3Q) at 23°C at reported pH of 6.48 and ambient pressure (i.e., atmospheric content of dissolved CO_2, hence dead water). From the entire NaCl salinity range tested by *Walker and Glover* (2018), the closest to the ionic strength tested in this study was 0.062 M, for which *Walker and Glover* (2018) reported the measured zeta potential of -18±1mV. Using **Equation 3.5** and pH of 6.48 (*Walker and Glover,* 2018) the calculated $\zeta_M = -18.92$ mV, which lies within the experimental uncertainty and consistent with the value of -18 mV predicted by the pH dependence of the zeta potential model (*Glover,* 2018).

Another study that reported measurements of the zeta potential in intact sandstone samples saturated with 0.01 M dead NaCl was published by *Vinogradov and Jackson* (2015). In that study the authors reported pH of 6.75±0.03 measured in experiments with St Bees1, St Bees 2, Doddington and Stainton samples at 22±1°C. For all four sandstone samples saturated with 0.01 M dead NaCl at ambient pressure the reported zeta potential was -22±0.4mV. Using our

regression for pH dependence of the zeta potential defined by **Equation 3.5**, the estimated value was found to be -20.24 mV thus validating our approach.

To confirm our proposed model for ζ_D obtained with dead solutions, we compared predictions on the zeta potential made using **Equation 3.6** against published experimental data (*Thanh and Sprik,* 2016) obtained with Berea sandstone saturated with 10^{-3} M $CaCl_2$ and $MgCl_2$ solutions at pH between 6.0 and 7.5. Our model yields ζ_D for both solutions between -13.06 mV and -15.09 mV (depending on the used pH value) compared with -9.3 mV and -6.6 mV reported by *Thanh and Sprik* (2016) for $MgCl_2$ and $CaCl_2$, respectively. The values obtained using **Equation 3.6** are more negative in comparison to those measured by by *Thanh and Sprik* (2016) and we attribute this difference to presence of clay minerals in the work of by *Thanh and Sprik* (2016), which are known to be more reactive towards divalent cations. On the other hand, the zeta potential reported in the same paper for 10^{-3} M NaCl and Na_2SO_4 at pH between 6.0 and 7.5 was also compared against our model (**Equation 3.5**). Our prediction for ζ_M was found to be in the range between -16.59 mV and -23.88 mV (corresponding to pH range), which is in a good agreement with the reported by by *Thanh and Sprik* (2016) values of -23.9 mV and 24.4 mV for NaCl and Na_2SO_4, respectively.

3.3.3. Live water zeta potential

Due to initial mixing of 400 mL of live water with 30 mL of dead water, the resulting pH of all re-equilibrated solutions in this study were approximately 0.8 pH units higher than those measured by *Li et al.* (2018) and *Peng et al.* (2013) for the same pressure.

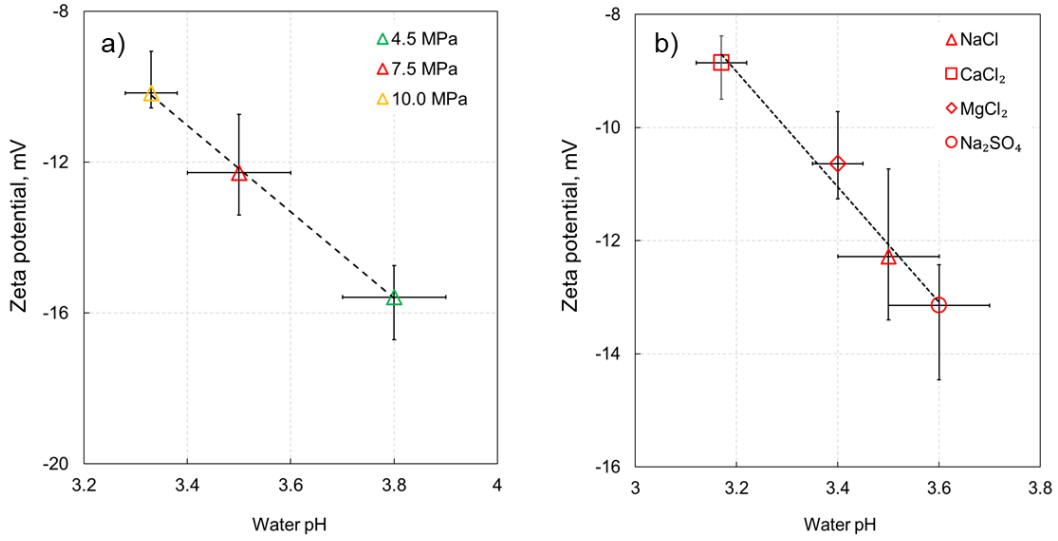

Figure 3.6. Zeta potential as a function of live water pH for a) NaCl solutions (with varying pore pressure and therefore different amount of dissolved CO_2) and b) all salt types at pore pressure of 7.5 MPa. All data were measured at 40°C. The linear regressions in both figures correspond to **Equation 3.7**. Error bars of zeta potential represent the experimental uncertainty obtained from the variation in the slope of the linear regression of C_{SP} while error bars of pH represent the variation of water pH during the experiment.

Increasing pore pressure resulted in increased CO_2 dissolution and formation of carbonic acid, and thus a decreasing water pH and consequently a more positive zeta potential (**Figure 3.6a**). All three zeta potentials measured with NaCl at 4.5 MPa, 7.5 MPa and 10 MPa linearly correlated with the corresponding water pH, with the slope of the linear regression (**Equation 3.7**), which was significantly different from that obtained with dead Na^+ containing solutions (**Equation 3.5**). Furthermore, all four salt types tested at 7.5 MPa lie on a linear trendline (**Figure 3.6b**), with the slope consistent with that of **Figure 3.6a**:

$$\zeta_L[mV] = -10.90 \times pH + 26.02;\ R^2 = 0.988 \qquad 3.7$$

A summary plot including both, dead and live water solutions, is presented in **Figure 3.7**, which suggests that either: a) **Equation 3.6** should be used for both dead and live $CaCl_2$/$MgCl_2$ solutions, while **Equation 3.5** should be used for dead NaCl/Na_2SO_4 and **Equation 3.7** should be used for live NaCl/Na_2SO_4 solutions; or alternatively b) **Equation 3.7** should be used for all types of live solutions (green regression in **Figure 3.7**) while **Equations 3.5** and **3.6** should be used for dead NaCl/Na_2SO_4 and $CaCl_2$/$MgCl_2$ solutions, respectively.

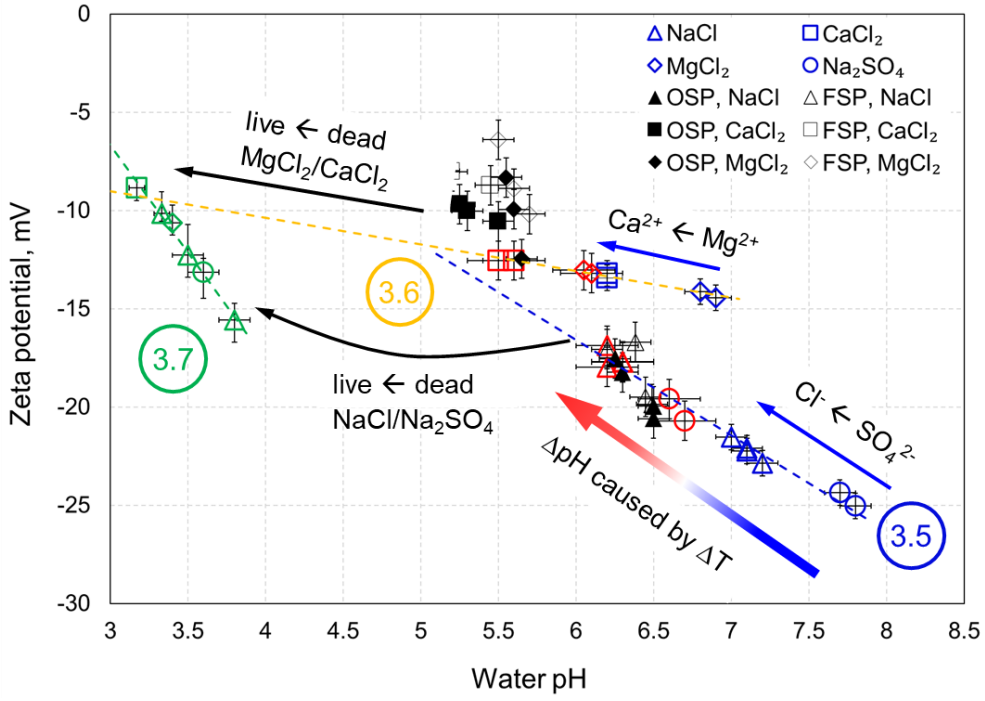

Figure 3.7. Zeta potentials measured versus pH of dead and live aqueous solutions. Our data across all pore pressures, temperatures and salt types are shown in color. Literature data for Ottawa and Fontainebleau sandpacks (OSP and FSP, respectively) saturated with 0.015 M dead water (*Vinogradov et al.,* 2010) are shown in black. The blue and red symbols correspond to 23°C and 40°C, respectively. The blue and yellow trendlines are the same as in **Figure 5** and correspond to **Equations 3.5** and **3.6**, respectively. The green trendline is identified for all dead water data and given by **Equation 3.7**. The arrows are added to explain the mechanisms of the zeta potential variation along and/or between the trendlines. Error bars of zeta potential represent the experimental uncertainty obtained from the variation in the slope of the linear regression of C_{SP} while error bars of pH represent the variation of water pH during the experiment.

All of the regressions proposed here for dead and live water solutions (**Equations 3.5-3.7**) appear to have a non-zero intercept with the horizontal axis, which is defined as the Isoelectric Point (IEP) that identifies the value of pH that results in a zero zeta potential. For the experiments with dead NaCl and Na_2SO_4 solutions, the IEP is calculated using **Equation 3.5** and equals 2.59, while the corresponding value for all live water solution calculated using **Equation 3.7** is 2.39. Both values are consistent with a published study that reported IEP for quartz and NaCl to be in the range between pH2.2 and pH2.5 (*Kosmulski et al.,* 2002). However, the IEP found for $CaCl_2$ and $MgCl_2$ (**Equation 3.6**) appears to be at pH of -3.67, which is inconsistent with all previously published results. Therefore, we hypothesize that the regression for pH dependence of the zeta potential with divalent cation salts is not linear throughout the entire range of pH and changes slope at pH around 3.3 where the regression defined by **Equation 3.6** intersects with the regression given by **Equation 3.7**. This hypothesis is consistent with our results for Na^+ containing solution that appear to switch from the pH dependence defined by **Equation 3.5** to that given by **Equation 3.7**. Moreover, a published experimental study (*Lorne et al.,* 1999) on crushed Fontainebleau samples saturated with NaCl of resistivity of 100 Ω·m (equivalent to ionic strength of 10^{-3} M) demonstrated that pH dependence of the zeta potential was non-uniform. The rate of increase of the measured by *Lorne et al.* (1999) zeta potential with decreasing pH was nearly linear but became significantly steeper below pH ≈ 3.5 and had IEP at pH = 2.5, so that both observations are consistent with our results.

To confirm the pH dependence of ζ_M, ζ_D and ζ_L across the entire pH range, additional experiments at pore pressures that correspond to pH between 4 and 6 for Na^+ containing solutions, and between pH = 3.5 and pH = 5.5 for $CaCl_2$ and $MgCl_2$ are required to cover the intermediate pH range. Moreover, additional experiments are also required for all types of solutions at pore pressures that correspond to pH < 3.2 (i.e., higher partial CO_2 pressure) to investigate the pH dependence of ζ_M and ζ_D under these live water conditions.

3.4. Implications for CO_2 geological storage

The empirical trends for the zeta potential as a function of water pH (**Equations 3.5-3.7**) proposed in this study bear a significant scientific and technological value as they can be used for predicting the expected zeta potential for shallow subsurface settings (low pressure and hence dead water-like behavior of the fluid), as well as for deep formations characterised by high content of dissolved CO_2 (live water-like behavior of the fluid). From the proposed correlations the streaming potential coupling coefficient can be interpreted using Helmholtz-Smoluchowski equation and used for monitoring and characterising subsurface flows of injected CO_2 or carbonated water during CGS (*Moore et al.,* 2004). Moreover, the correlations

are important when applied to monitoring movement of water in subsurface settings characterised by variable pH such as hydrocarbon reservoirs (e.g., *Jackson et al.,* 2012a), groundwater (*Graham et al.,* 2018; MacAllister et al., 2018) or geothermal (*Cabahug and Angcoy Jr,* 2013) systems. Our results demonstrate that temperature does not directly affect the zeta potential, instead it affects solubility of CO_2 and pH of aqueous solutions, which in turn impacts the zeta potential. In this sense, laboratory measurements of natural water pH or under varying temperature and CO_2 pressure can be acquired and zeta potential interpreted from the measured values using **Equations 3.5-3.7**.

Moreover, the proposed empirical correlations for the mineral-water zeta potential can be incorporated in the classical DLVO theory (e.g., *Tokunaga,* 2012) to yield system's wettability thus quantifying the potential of residual trapping of CO_2 during geological sequestration in sandstone formations. For instance, our results suggest that higher reservoir pressure that corresponds to enhanced CO_2 dissolution will results in lower pH and smaller in magnitude rock-water zeta potential thus implying a smaller electrostatic component of the disjoining pressure and hence, less water-wet conditions. In such case, pure sandstone reservoirs (>95 wt.% quartz) might be deemed inappropriate for CO_2 injection for geological storage and other formations containing more clays, which are known to make zeta potential larger in magnitude (compare the reported zeta potential measured on Buff Berea, Grey Berea and Parker sandstones saturated with 0.5% NaCl, $CaCl_2$ and $MgCl_2$ in *Shehata and Nasr-El-Din* (2015), to be considered. On the other hand, our results suggest that residual CO_2 trapping controlled by wettability can potentially be improved by making the rock more water-wet via injection of NaCl or Na_2SO_4 rich water of low salinity prior to injecting CO_2 for geological storage. Such procedure would lead to a larger in magnitude negative zeta potential at rock-water interface, so that the shift towards more water-wet conditions would occur assuming that the zeta potential at CO_2-water interface is also negative.

Furthermore, higher CO_2 pressure, and therefore, higher dissolved CO_2 concentration, causes the equilibrium pH to decrease thus also affecting the mineralization of carbonate and therefore, the CO_2 ultimate storage capacity (*Morse and Arvidson*, 2002; *Kaszuba et al.,* 2003; *Druckenmiller and Mercedes Maroto-Valer,* 2005).

Despite the fact that our results have been able thus far to accurately predict zeta potential under ambient and supercritical CO_2 conditions, additional experiments are required to quantify the pH dependence of the zeta potential for intermediate pH range of 4.0 - 5.5 for all types of salts. Additional work is also required to test the pH dependence of the zeta potential for pH < 3, for mixtures of salts to replicate complex natural aqueous solutions that saturate

geological porous media, as well as for higher ionic strength solutions typically found in deep sandstone formations such as deep saline aquifers or depleted hydrocarbon reservoirs.

3.5. Conclusions

We have developed the experimental methodology and for the first time successfully carried out the streaming potential measurements in intact sandstone sample saturated with CO_2-rich aqueous solutions of 0.05 M ionic strength under high pressure (up to 10 MPa) and elevated temperature (up to 40^{o}C) conditions. For the first time, all streaming potential measurements on silica in contact with aqueous solutions fully equilibrated with CO_2 (live water experiments) were obtained at equilibrium conditions of pressure and temperature that correspond to CO_2 at supercritical state. The zeta potential was carefully interpreted from the measurements and we found that:

1. The zeta potential for all tested solutions, pressure and temperature was negative, which implied that the electrical charge at rock-water interface was always negative and non-zero.

2. The zeta potential of all dead solutions was found to be independent of pore pressure but decreased with increasing temperature; this finding is consistent with previously published data obtained at ambient pressure (*Vinogradov et al.,* 2018).

3. The zeta potential of all dead solutions was found to be different for NaCl/Na_2SO_4 compared with that of $CaCl_2$/$MgCl_2$.; the finding for Na_2SO_4 is new but the observation for NaCl vs $CaCl_2$/$MgCl_2$ is consistent with the reported results (*Vinogradov et al.,* 2018).

4. The negative zeta potential of all live solutions decreased in magnitude with increasing pore pressure, reflecting the effect of enhanced CO_2 dissolution under high pressure, which caused pH to decrease; the effect of CO_2 dissolution on the zeta potential has been quantified for the first time in this study.

5. Our results indicate that pH of dead and live solutions is the only control of the zeta potential so that salt type, pore pressure and temperature indirectly affect it via having an impact on pH.

6. We proposed three linear empirical correlations with a high coefficient of determination ($R^2 > 0.97$) to predict the zeta potentials as a function of water pH. The correlations reflect a different response of the zeta potential to presence of mono- or divalent cations in dead solutions, and a distinctly different response to the live water conditions. The correlation for the live water is the first of a kind, thus providing a good

source for validating surface complexation models for silica in contact with carbonated aqueous solutions at supercritical CO_2 conditions.

7. The proposed correlations were validated against published experimental data and were confirmed to accurately predict the zeta potential of dead solutions. The iso-electric point predicated by our live water correlation was found to be similar to that published for dead water solutions (*Kosmulski et al.,* 2002).

8. Our novel results have significant implications for many subsurface settings where high concentration of dissolved CO_2 is expected. Potential applications include management of aquifers, geothermal sources and CGS. Moreover, an improved understanding of the zeta potential of silica-water systems under supercritical CO_2 conditions resulting from this study will inform future studies on thermodynamics of wettability (*Tokunaga,* 2012), colloid stability and use of nanoparticles (*Bueno et al.,* 2022).

Future experimental work will aim at acquiring zeta potential values at the condition of CO_2-rich aqueous solutions with pH between 4.0 and 5.5, CO_2 pressure higher than 10 MPa that corresponds to pH below 3, ionic strength higher than 0.1 M, and complex background solutions. Moreover, the planned experimental work will investigate impact of grain size, shape, packing and roughness on the zeta potential as well as alternative experimental methods (*Peng et al.,* 2019). These experiments will complement the data reported here and expand the range of tested conditions not covered in this work, thus further improving our understanding of the zeta potential at the silica-water interfaces under conditions relevant to CGS. The results will also be used to inform future surface complexation and molecular dynamics simulation studies aimed at describing silica-water-CO_2 systems under CSG conditions.

Chapter 4 Zeta potential of a natural clayey sandstone saturated with carbonated NaCl solutions at supercritical CO_2 conditions*

**) The text for this chapter was prepared for publication and it was accepted during the registration period of my study in Geophysical Research Letters. The final version of the published paper can be seen at https://doi.org/10.1029/2022GL099277*

4.1. Introduction

Zeta potential is a physicochemical property of interfaces between aqueous solutions (termed brines or electrolytes for simplicity) and minerals or other fluid phases. The mineral-brine zeta potential is interpreted from the measured streaming potential that arises due to pressure gradients in rocks saturated with electrolytes (*Hunter,* 1981; *Jackson et al.,* 2012a). Many experimental and modelling studies reported the importance of the zeta potential for a broad range of applications for silica-brine systems, due to abundance of such formations. These applications include CO_2 geo-sequestration (CGS, e.g., *Moore et al.,* 2004), hydrocarbon recovery (e.g., *Jackson et al.,* 2016b), geothermal resources (e.g., *Revil and Pezard,* 1998; *Jardani et al.,* 2008), characterisation of flow through fractured systems (e.g., *Jougnot et al.,* 2020; *Vinogradov et al.,* 2022a), and management of groundwater aquifers (e.g., *MacAllister et al.,* 2018).

The zeta potential of sandstone saturated with electrolytes at various conditions has been widely investigated experimentally covering high salinity (*Walker and Glover,* 2018), elevated temperature (*Vinogradov and Jackson 2015*), multi-phase flows (*Sprunt et al.,* 1994; *Revil and Cerepi,* 2004) and complex composition of brines (*Thanh and Sprik,* 2016). However, the only published data on zeta potentials of natural sandstones at relevant to CGS conditions (elevated temperature, high pore pressure, high CO_2 content) are limited to quartz dominated rock sample (*Hidayat et al.,* 2022, hereafter referred to as H22), where measurements carried out on a 'clean' Fontainebleau (>99 wt.% quartz) sample at pore pressures up to 10 MPa and temperatures up to 40^{o}C were reported. The authors found that the zeta potential remained negative, decreased in magnitude with increasing content of dissolved CO_2, which resulted in a lower equilibrium pH. Many natural sandstone reservoirs comprise a broad range of various minerals, including clays, micas, feldspars and carbonates. Therefore, the dependence of the zeta potential on mineralogy of sandstones under varying pore pressure, brine concentration and CO_2 content conditions, relevant to CGS remains largely unknown.

In the absence of experimental data of the zeta potential at such conditions, we report for the first time zeta potentials measured for a natural sandstone comprising quartz, feldspars, and clay minerals, in contact with CO_2-rich NaCl solutions. The experimental pore pressure and temperature conditions were varied between 0.2 MPa to 10 MPa and between 23°C and 40°C,

respectively. We demonstrate that the zeta potential response to varying pore pressure is unique and different from that of clean sandstone samples.

4.2. Materials and methods

A single cylindrical San Saba sandstone sample was used in this study. The petrophysical properties of the sample are provided in **Table 4.1**.

Table 4.1. Petrophysical and mineralogical properties of the San Saba sample used in this study. Mineralogy of the sample is provided as a range of the main constituents based on published studies of *Connoloy et al.* (2019) and *Al-Shajalee et al.* (2020) and independently confirmed using X-Ray Diffraction (XRD) and Scanning Electron Microscopy (SEM) carried out in this study.

Sample	San Saba
Mineralogy	87.7 wt.%– 95.2 wt.% quartz 2.3 wt.% – 6.2 wt.% microcline 1.9 wt.% – 4.0 wt.%albite 1.1 wt.% – 3.3 wt.% kaolinite 0.9 wt.% – 1.0 wt.% illite
Porosity	21.0 ± 1.0%
Liquid Permeability	35.0 ± 1.0 mD
Dimensions	Length = 7.61 cm Diameter = 3.82 cm
Formation Factor, *F*	159 ± 8

Prior to conducting the streaming potential measurements, the San Saba sample was cleaned following the procedure reported by *AlRoudhan et al.* (2016). The porosity of the sample was measured using the gas (N_2) expansion method in AP-608 Automated Permeameter and Porosimeter (Coretest System Inc, USA). The liquid permeability and the formation factor (using NaCl solutions of concentration ranging between 0.1 M and 1.0 M) were calculated following the procedure reported in *Vinogradov et al.* (2010).

The experiments were conducted using NaCl aqueous solutions of varying ionic strength and were divided into two main groups corresponding to the electrolyte conditions: dead and live electrolytes. The former relates to a synthetic aqueous solution fully equilibrated with atmospheric CO_2, whereas the latter salt solution prepared under ambient pressure and

temperature is brought into contact with pure CO_2 in a mixing reactor establishing thermodynamic equilibrium at different temperatures and pressures (for further details, refer to the definition of dead and live electrolytes in H22). Although the solution used in this investigation comprised only NaCl which was not quite representative of the composition of natural brines, the NaCl was selected as an initial point in the proof-of-concept experiment, and further work with complex brine compositions similar to natural brines is planned.

To prepare dead and live electrolytes, we followed the experimental protocol reported by H22 to make sure the dead and live electrolytes reached full chemical equilibrium with the rock sample before the experiment commenced. The pH and conductivity of the dead electrolytes were regularly measured using a FiveGo pH meter (Mettler Toledo, accuracy of 0.01 pH units) and a Jenway 4520 conductivity meter (Cole-Palmer, 0.5% accuracy), respectively. Furthermore, an in-line high pressure pH meter (model number of pH-G-10"-T375-NPT250A-C276, Corr Instruments, LLC, accuracy of 0.01 pH units) was used to measure pH of live electrolytes. The equilibrium pH and conductivity of all tested NaCl solutions are provided in **Table 4.2**.

Table 4.2. The equilibrium pH and conductivity of tested electrolytes in this study. P is the mean pore pressure which was kept 2-3 MPa below the confining pressure. T is the temperature during the experiment, which was controlled by the oven. The live electrolyte conductivity was evaluated using an empirical correlation reported by *Börner et al.* (2015).

Ionic strength, M	P, MPa	T, °C	Solution	σ_w, S·m^{-1}	pH values
0.05	0.2	23	Dead	0.550	6.80 ± 0.1
	4.5			0.557	6.75 ± 0.1
	7.5			0.553	6.75 ± 0.1
	10.0			0.555	6.80 ± 0.1
	0.2	40		0.601	6.50 ± 0.1
	4.5			0.601	6.55 ± 0.1
	7.5			0.601	6.50 ± 0.1
	10.0			0.601	6.55 ± 0.1
	4.5		Live	0.505	3.72 ± 0.05
	7.5			0.496	3.43 ± 0.05
	10.0			0.493	3.26 ± 0.05
0.10	0.2	23	Dead	1.015	6.60 ± 0.1
0.20				1.982	6.60 ± 0.1
0.50				4.110	6.70 ± 0.1
1.00				8.090	6.70 ± 0.1

The streaming potential measurements were conducted in a high pressure-high temperature (HPHT) coreflooding apparatus (see **Figure 3.1**). The streaming potential coupling coefficient (C_{SP}) was determined from the ratio between the stabilised voltage, ΔV, and the stabilised pressure difference, ΔP, across the sample following paired-stabilised method (*Vinogradov and Jackson*, 2011). We confirmed that the effect of surface conductivity was negligible in all our experiments and therefore, the zeta potential (ζ) was calculated using the classical Helmholtz-Smoluchowski equation (**Equation 2.24**; *Jouniaux and Pozzi, 1995*), while disregarding the Overbeek's correction for the surface conductivity (Glover, 2015).

The fluid conductivity (σ_w) is the conductivity of the electrolytes (**Table 4.2**). The permittivity (ε) and dynamic viscosity (μ) of dead electrolytes were evaluated using an empirical correlation reported by *Saunders et al.* (2012). The dynamic viscosity of live electrolytes was calculated using the correlation reported by *Islam and Carlson* (2012).

4.3. Results

The zeta potentials measured with dead NaCl solutions of ionic strength between 0.05 M and 1.0 M are shown in **Figure 4.1**. The zeta potential of San Saba remained negative and became larger in magnitude with increasing salinity until 0.2 M, after which it decreased back. This behavior contrasted most of previously published zeta potential data obtained with sandstones containing other than quartz minerals (e.g., Stainton and St. Bees in *Vinogradov et al.,* 2010 and *Jafaar et al.,* 2009; Berea in *Walker and Glover,* 2018). However, a similar anomalous salinity dependence of the zeta potential was observed in Berea sandstones reported by *Li et al.* (2018) thus suggesting that our results were not an experimental artefact.

Li et al. (2018) reported the anomalous behaviour of the zeta potential in Berea sandstone containing kaolinite and feldspars (i.e., albite and microcline), which was attributed to ion exchange resulting in release of Ca^{2+} into the effluent NaCl solution. As similar minerals (kaolinite, albite and microcline) were also present in the San Saba sandstone, we assumed that the same ion exchange releasing multi-valent cations also took place in our experiment. In order to confirm the assumption, the effluent analysis of the experiment had to be conducted. However, due to experimental limitations we could not collect brine samples for detailed chemical analysis, so the mechanism described above remains a hypothesis.

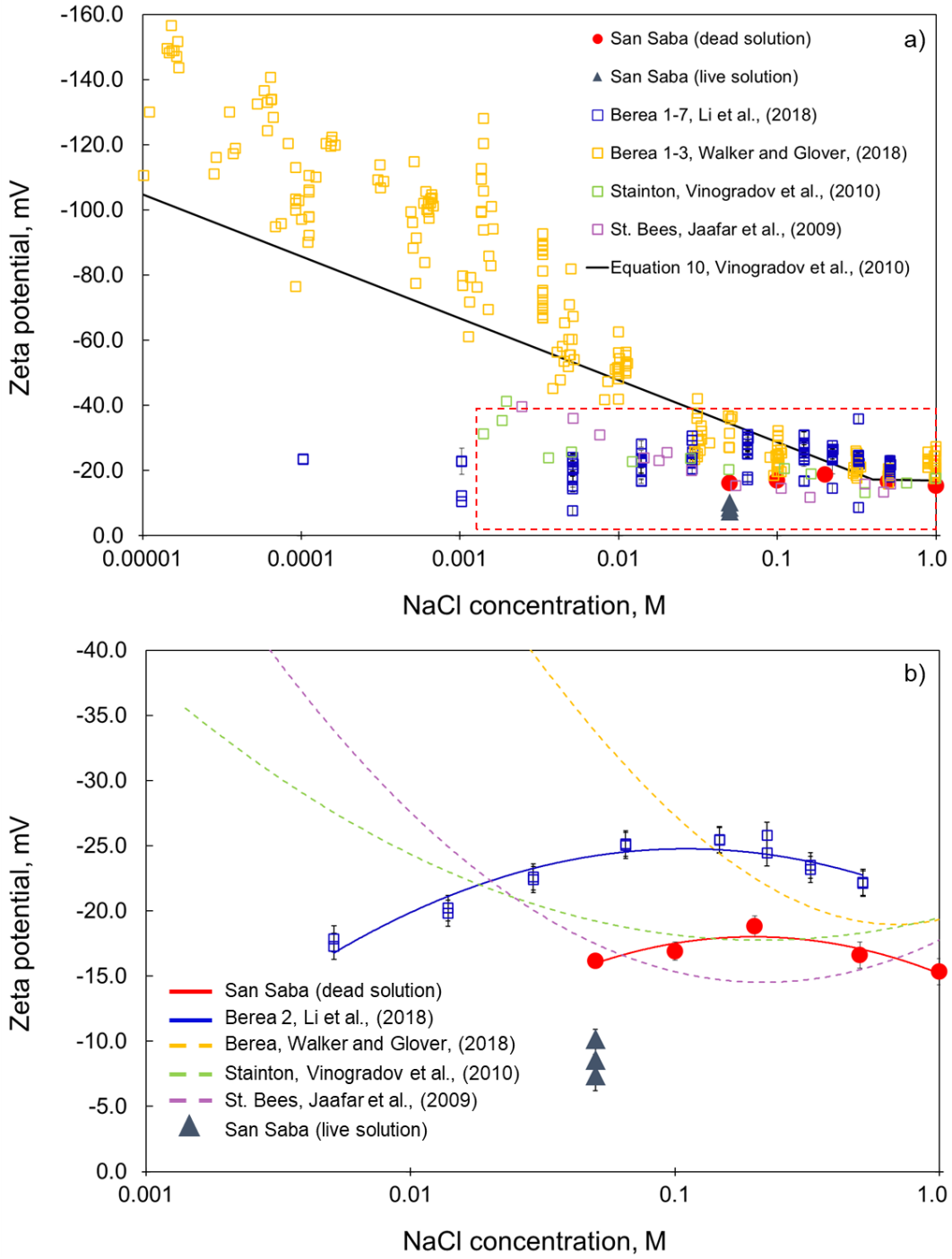

Figure 4.1. (a)The zeta potential of San Saba sandstone (red circles and grey triangle) compared with the published experimental data of clayey sandstones from published. The solid black line in (a) describes the empirical correlation published by Vinogradov et al. (2010). Panel (b) shows the same data as (a) but presents the averaged values of Jaafar et al. (2009), Vinogradov et at. (2010) and Walker and Glover (2018) described by respective trendlines over the salinity range between 0.001 M and 1 M NaCl. The blue trendline corresponds to the experiment with Berea 2 sample from Li et al. (2018), while results for other samples from the study are excluded since their salinity dependence of the zeta potential was qualitatively identical to the blue trendline but offset to larger or smaller in magnitude values. All trendlines in panel (b) are only used to qualitatively describe the salinity dependence of the zeta potential, thus they are based on polynomial regressions drawn through the respective excremental datapoints with $R^2 \geq 0.99$. Error bars of zeta potential represent the experimental uncertainty obtained from the variation in the slope of the linear regression of C_{SP}.

Figure 4.2 reports the measured zeta potentials and pH of dead (a-d) and live (e-f) solutions as a function of pore pressure and temperature. The results presented in **Figures 4.2** and **4.2b** demonstrate that the zeta potentials and pH of dead electrolytes remained independent of the pore pressure, similar to the results on Fontainebleau sample (H22). Note, that all dead electrolyte experiments were conducted in a closed system (*Vinogradov et al.,* 2018), hence preventing contact with air and eliminating the possibility of enhanced dissolution of CO_2. Therefore, zeta potential being independent of pressure our dead electrolytes experiments was attributed to a constant amount of CO_2 dissolved in dead electrolytes, which was also confirmed by the electrolyte pH that remained constant across the tested pore pressures (**Figure 4.2b**).

The temperature dependence of the zeta potential and pH of dead electrolytes is shown in **Figures 4.2c** and **4.2d** and compared with the published results for the clean Fontainebleau sample (H22). The zeta potential of dead electrolytes became smaller in magnitude with increasing temperature reflecting a decrease in pH of the dead solutions with increasing temperature. These observations were qualitatively consistent with previously published data on sandstones at elevated temperature (e.g., *Vinogradov et al.,* 2018; H22). However, a weaker temperature dependence of zeta potential in San Saba was observed in comparison with Fontainebleau as evidenced by the slopes in **Figure 4.2c** (i.e., with the change in the experimental temperature from 23°C to 40°C, an increase of +2.0 mV was observed for the zeta potential in San Saba while a change of +4.3 mV was reported for Fontainebleau). Similarly, a smaller variation of the equilibrium pH of dead electrolytes saturating San Saba was observed with increasing temperature compared with the results reported for Fontainebleau (**Figure 4.2d**).

We finish by reporting the measured zeta potential and pH of live electrolytes in San Saba for three different pore pressure (4.5, 7.5 and 10 MPa) at 40°C with 0.05 M NaCl solutions (**Figures 4.2e** and **4.2f**). The zeta potential of San Saba saturated with live solutions remained negative and became smaller in magnitude with increasing pressure (**Figure 4.2e**). The pH dependence of the zeta potential in San Saba was significantly different form that observed in Fontainebleau sample (H22) as evidenced by a distinct difference in respective slopes of the linear regressions in **Figure 4.2e**. At the same time, the equilibrium pH of live electrolytes saturating San Saba decreased with increasing pressure at the same rate as that of Fontainebleau (**Figure 4.2f**) reflecting an increased amount of dissolved CO_2 that led to increased acidity of the electrolyte (*Adamczyk et al.,* 2009; *Peng et al.,* 2013).

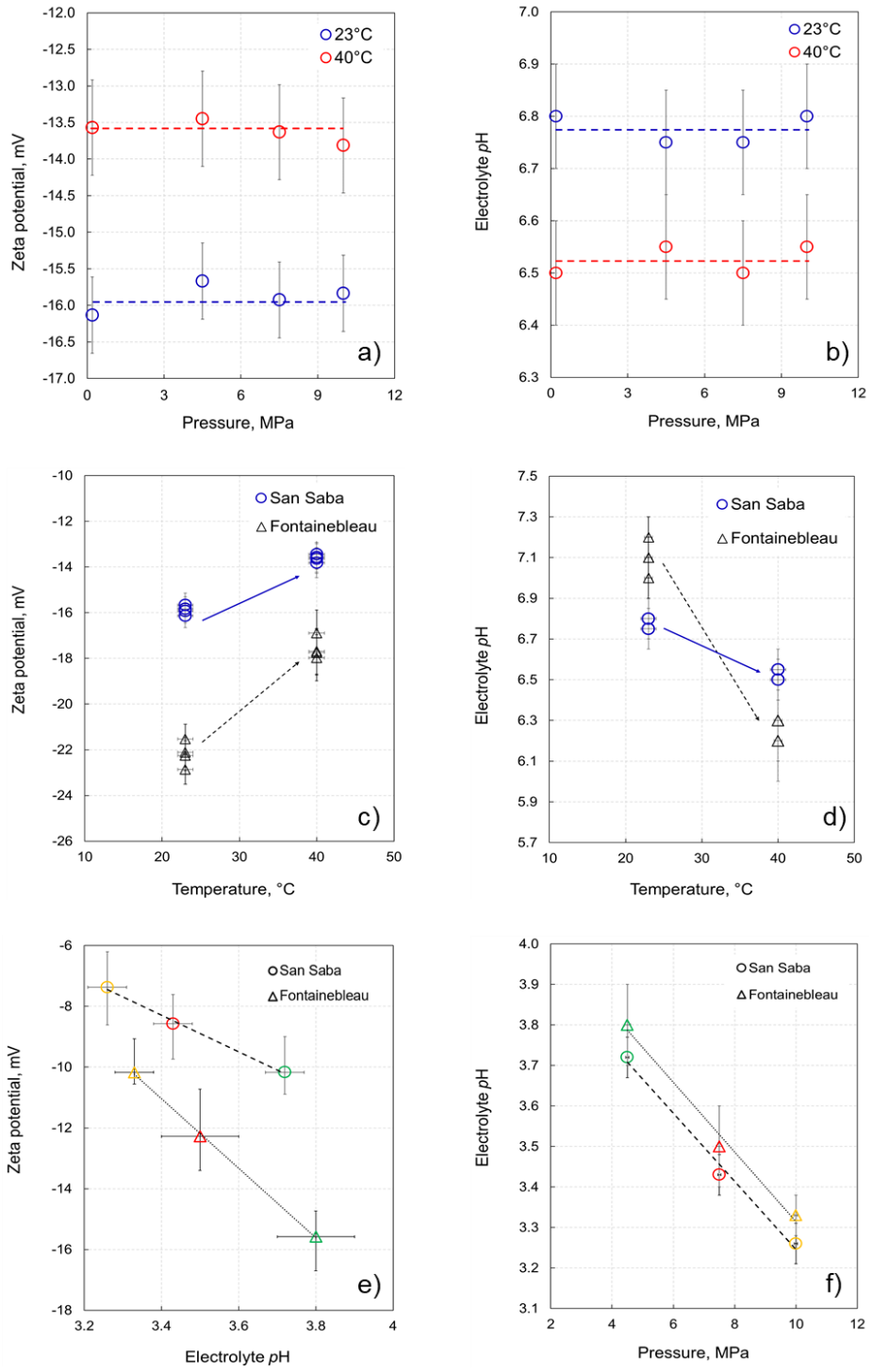

Figure 4.2. Zeta potential (a, c, e) and electrolyte pH (b, d, f) as a function of salinity, temperature and pore pressure. Zeta potentials (a) and pH (b) for the dead solutions were independent of pore pressure since the experiments were conducted in a closed system while the solutions were prepared with atmospheric level of CO_2 corresponding to partial CO_2 pressure of $10^{-3.44}$ atm (Li et al., 2016). Temperature dependence of the zeta potential (c) and pH (d) for dead solutions is compared with previously published data. Live brine zeta potential (e) and pH (f) are compared with previously published data. Green sybos correspond to pore (hence, partial CO_2) pressure of 4.5 MPa, red symbols stand for 7.5 MPa and yellow symbols denote experiments at 10 MPa. The Fontainebleau data presented in these figures were extracted from H22. Error bars of zeta potential represent the experimental uncertainty obtained from the variation in the slope of the linear regression of C_{SP} while error bars of pH represent the variation of pH during the experiment.

4.4. Discussion

A summary plot of the zeta potential as a function of pH for both live and dead NaCl solutions is presented in **Figure 4.3**. The zeta potentials of San Saba were found to be more positive (smaller in magnitude) compared with the values of clean Fontainebleau sandstone for live and dead NaCl electrolytes. We observed a steeper slope of zeta potential versus pH in San Saba (blue dashed line, **Figure 4.3**) compared with Fontainebleau (black dash line, **Figure 4.3**) when the temperature changed from 23°C to 40°C for the dead electrolytes. It is worth mentioning that the dissolved CO_2 remained constant during these dead brine experiments at both temperatures. At the same time, a shallower slope of the zeta potential versus pH was observed in San Saba (purple dash line, **Figure 4.3**) saturated with live NaCl solutions compared with Fontainebleau (green dashed line, **Figure 4.3**) over the range of tested experimental pore pressures between 4.5 MPa and 10.0 MPa. Since the zeta potentials of San Saba and those of clean Fontainebleau samples were obtained under identical conditions of pore pressure, temperature and CO_2 content, we attributed differences in respective zeta potentials to the presence of clay and feldspar minerals in San Saba.

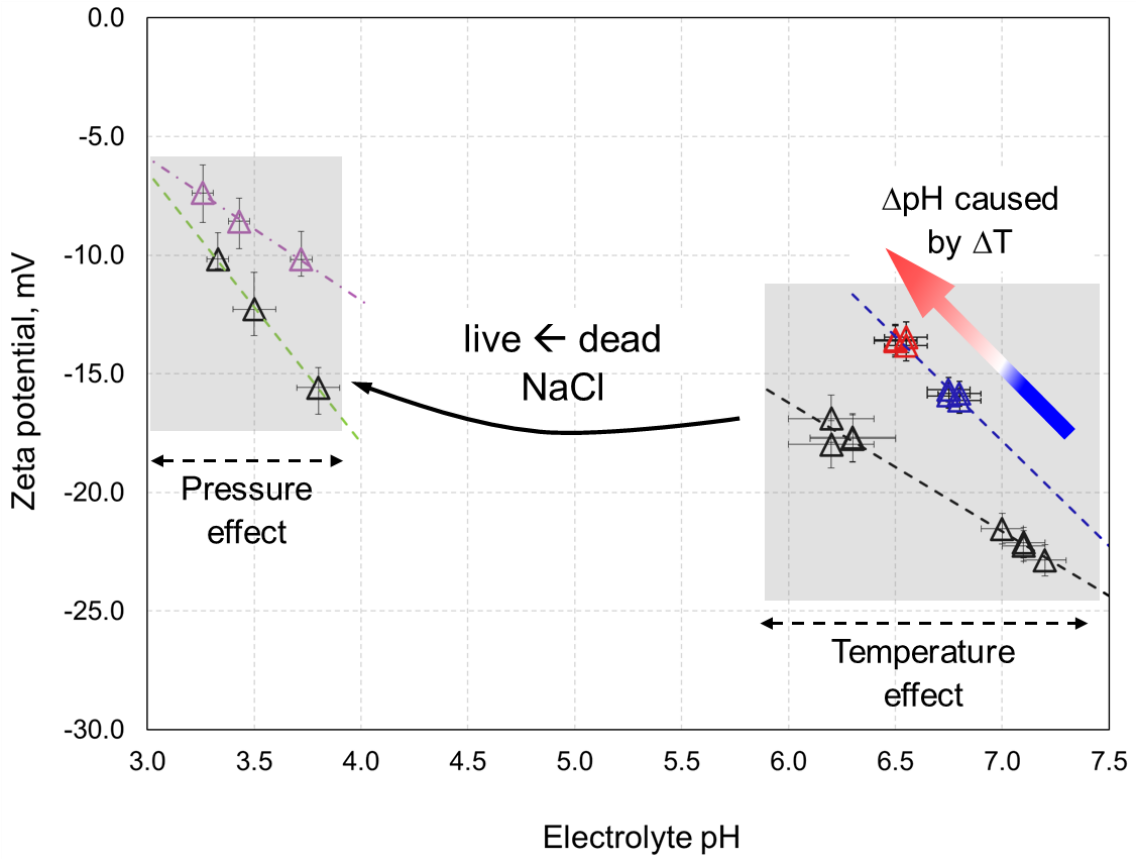

Figure 4.3. Summary of zeta potentials versus pH for dead and live electrolytes. The purple symbols correspond to live electrolytes; the blue and red symbols correspond to dead electrolytes at temperature of 23°C and 40°C, respectively. The previously published data for Fontainebleau sample saturated with dead and live NaCl solutions under the same experimental conditions are denoted by black symbols, and these values were extracted from H22.

A recently published study (*Alarouj et al.,* 2021) suggested that the effective macro-scale zeta potential was an average of the micro-scale zeta potentials from each individual mineral-brine interface. That is, if the mineralogy of the rock sample was dominated by a single mineral such as quartz, then the micro- and macro-scale zeta potentials would be identical. If, on the other hand, various minerals were distributed along the pore walls, as in the case of San Saba sandstone, then the local micro-scale zeta potentials would vary from one mineral to another, and the macro-scale zeta potential will be an average of the micro-scale values depending on the portion of pore walls lined by different minerals.

To evaluate the impact of different minerals on the effective zeta potential of the San Saba sample, additional investigations of the sample were carried out. From X-ray diffraction analysis (XRD), we found the mass fraction of minerals of the bulk sample, in which clays (kaolinite and illite), feldspars (albite and microcline) and quartz were identified as the main components (**Table 4.1**). However, the XRD analysis did not provide the necessary insights on how the identified minerals were distributed in the pore space. To address this question, we also used the scanning electron microscopy (SEM), from which the same minerals were identified as the main constituents of the sample (**Figure 4.4**).

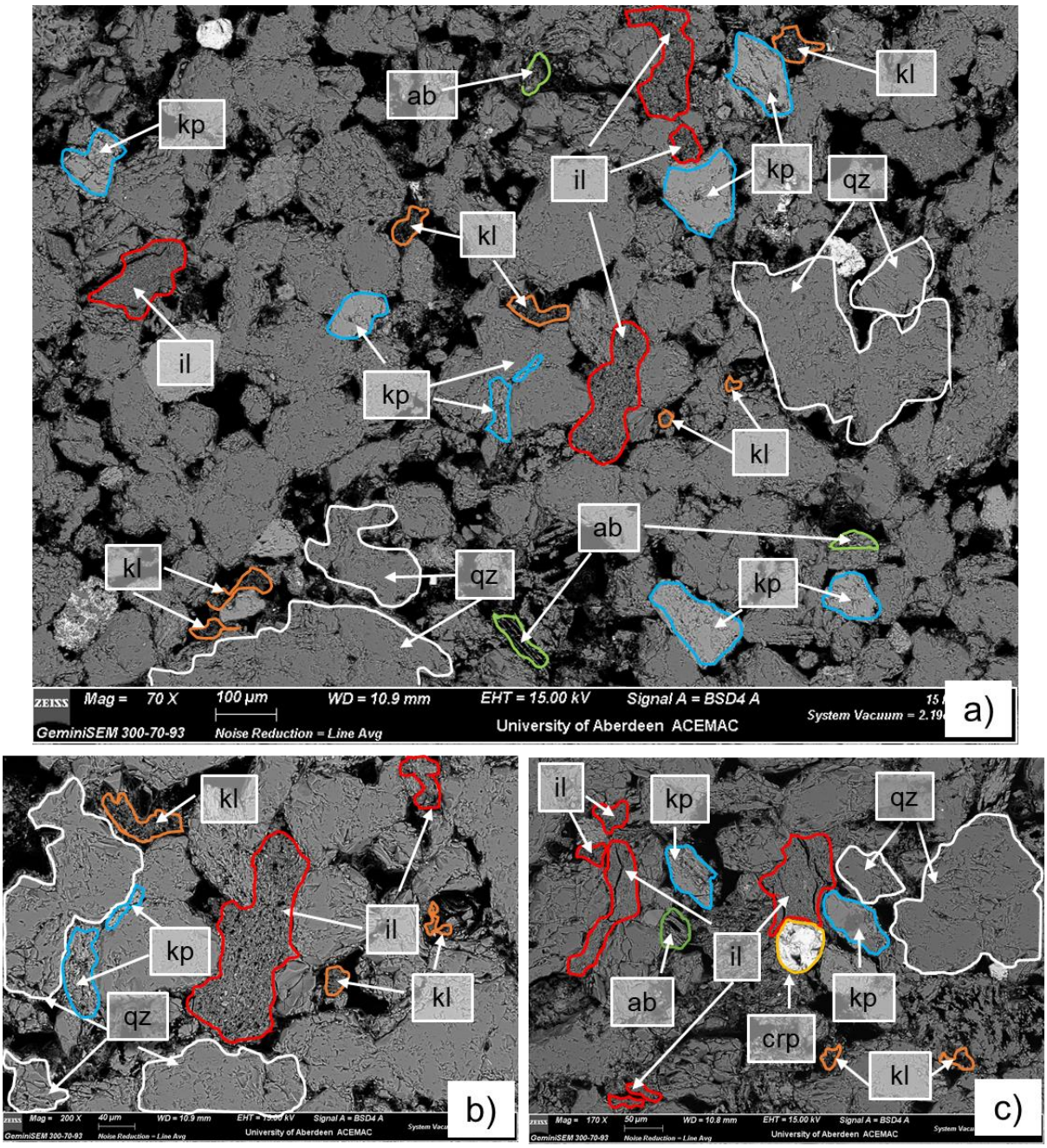

Figure 4.4. Images from SEM analysis of San Saba sandstone, in which the unmarked grey areas correspond to quartz. The abbreviations used in the figure are: qz for quartz, kl for kaolinite, ab for albite, il for illite, kp for K-feldspars (microcline), and crp for chrome spinel. The black color corresponds to pores in the rock sample.

SEM image presented in **Figure 4.4c** also identified a minor inclusion of chrome spinel, which appeared to be an extremely uncommon locality and was only found in a single spot of the thin section. Kaolinite and illite were found to extend towards the middle of large pores (see **Figure 4.4**). Thus, kaolinite and illite were exposed to electrolyte during the streaming potential experiments and were expected to influence both micro- and macro-scale zeta potentials. Similar situation was observed with albite, which was found to extend toward major pores thus interacting with brines during the experiments (**Figures 4.4a** and **4.4c**) Hence, albite was also

expected to contribute to the overall macro-scale zeta potentials. On the other hand, the microcline grains were primarily locked between quartz grains (**Figures 4.4a** and **4.4b**) or had a small area exposed to large pores (**Figure 4.4c**), thus limiting the mineral's interaction with electrolytes during the experiments. Therefore, the contribution of microcline to overall macro-scale zeta potentials was expected to be insignificant despite its relatively significant concentration of c. 2-6%.

To understand the impact of each mineral, we compared the previously reported zeta potentials of the minerals with that of quartz. *Yukselen-Aksoy and Kaya* (2011) reported zeta potentials of kaolinite and quartz for pH range of 3 – 11 in water and found kaolinite zeta potentials to be less negative than quartz. *Hussain et al.* (1996) conducted zeta potential measurements with kaolinite and illite in water for pH range of 2.5 – 11 and found that the magnitude of illite zeta potentials was smaller than that of kaolinite. Furthermore, *Wainipee et al*. (2013) measured zeta potentials of illite and kaolinite with 0.001 M and 0.7 M NaCl and pH range of 1 – 9, and found that the zeta potentials of illite were less negative compared to kaolinite. Therefore, we concluded that the impact of kaolinite and illite on the negative zeta potentials should lead to the following relative magnitudes $|\zeta_{illite}| < |\zeta_{kaolinite}| < |\zeta_{quartz}|$, thus shifting the macro-scale zeta potential of San Saba affected by the clays to more positive values compared with clean Fontainebleau.

A study by *Vidyadhar and Rao* (2007) reported that microcline zeta potential was more negative than quartz in water for pH range of 1.5 – 11. On the other hand, the zeta potential of albite was measured to be less negative than quartz in water for pH range of 1.5 – 11 (*Vidyadhar et al.,* 2002; *Wang et al.,* 2018). *Demir et al.* (2001) investigated the effect of ionic strength of NaCl electrolytes on the zeta potentials of albite and microcline over a wide salinity range (0.0001M – 0.1M NaCl), and found that zeta potential in albite was less negative compared to microcline. Based on these findings, we concluded that the magnitude of the negative zeta potential of albite is the smallest, followed by quartz and microcline ($|\zeta_{albite}| < |\zeta_{quartz}| < |\zeta_{microcline}|$).

Numerous experimental studies investigated dissolution of kaolinite and albite, and the dissolution rates were reported to increase with increasing temperature and decreasing pH (*Carrol and Walther,* 1990; *Harley and Gilkes,* 2000; *Cama et al.,* 2002; *Palandri and Kharaka,* 2004). Thus, we hypothesize that kaolinite, albite and illite dissolved during our experiments releasing multi-valent cations such as Ca^{2+}, Mg^{2+}, Al^{3+} (*Yuan and Pruett*, 1998; *Cama et al.,* 2002; *Li et al.,* 2018), which caused their adsorption and/or exchange at the quartz surface of San Saba making the zeta potential more positive, as was also suggested by previously

published studies of the zeta potential on clayey sandstones (*Li et al.,* 2018; *Alarouj et al.,* 2021).

All in all, based on the bulk composition (**Table 4.1**) and pore-scale distribution of main minerals of San Saba (**Figure 4.4**) we concluded that the main impact on the macro-scale zeta potential came from kaolinite and albite, both of which had higher presence in the bulk (c. 1-3 wt.% and 2-4 wt.%, respectively), and larger available surface area for interactions between ionic species of brines and minerals (i.e., substantial exposure of mineral surfaces to pore fluid in larger pores). Conversely, a smaller amount of illite (c. 1 wt.%) and limited exposure to flowing brines of microcline made their contribution to the macro-scale zeta potential negligible. The experimental results of this study confirmed the hypothesized individual contribution of minerals and demonstrated that both, kaolinite and albite of the San Saba sample made the effective macro-scale zeta potentials in this study more positive in comparison with Fontainebleau data (H22). Moreover, these minerals were more reactive with NaCl solutions thus making the pH dependence of the zeta potential significantly different compared with quartz data across the tested range of pH and temperature (**Figure 4.3**).

4.5. Conclusions

We report for the first time zeta potentials measured on intact clayey San Saba sandstone sample saturated with NaCl solutions of various concentrations and under conditions of temperature, pH, dissolved CO_2 content and pore pressure consistent with CGS. The zeta potential of the San Saba sample was negative for all tested solutions, but when in contact with live electrolytes it decreased with increasing pore pressure due to increased amount of dissolved CO_2 and the corresponding decrease in pH. Conversely, the zeta potential of San Saba and dead electrolytes was found to be independent of the pore pressure condition but decreased with increasing temperatures reflecting respective changes in pH. Furthermore, the zeta potential with both, dead and live solutions was less negative when compared with previous experimental and modelling studies of clean sandstones at similar conditions. An anomalous salinity dependence of the zeta potential was observed with dead NaCl of ionic strength 0.05M – 1.0M, which is uncommon but qualitatively similar to the previously reported data on a different clayey sandstone (*Li et al.,* 2018).

We found that mineralogy of San Saba played a key role in defining the micro- and macro-scale zeta potentials. Specifically, a larger content of kaolinite and albite combined with their substantial presence in large pores made these minerals to chemically interact with flowing brines, which led to a smaller in magnitude macro-scale zeta potential compared with that of pure quartz. Furthermore, increased dissolution rate of kaolinite, illite and albite at elevated temperature and low pH (around 3) resulted in appearance of multi-valent cations in the

electrolyte, which further led to specific adsorption and/or ion exchange at the mineral surface, eventually resulting in smaller in magnitude zeta potentials compared with quartz-NaCl systems. On the other hand, microcline, mostly locked between quartz grains, and small concentration of illite in San Saba did not have noticeable impact on the macro-scale zeta potential. Our results demonstrate that mineralogy of sandstones has a noticeable impact on electrochemical interactions at the mineral-brine interface and must be investigated to predict and explain the salinity, composition, pH and temperature dependence of the effective macro-scale zeta potentials.

Future experimental investigation of zeta potentials is required and planned to study the effect of electrolyte composition, concentration, pore pressure, temperature and CO_2 content in other clayey sandstone samples. In addition, possible impact of surface roughness on the zeta potential under the reservoir condition is an interesting topic to be investigated in future. The results of this study are novel and essential for a broad range of applications including underground gas storage (CO_2/H_2), monitoring of subsurface flows, geothermal sources and hydrocarbon recovery.

Chapter 5 Zeta potential of supercritical CO_2-water-sandstone systems and its impact on wettability and residual trapping of CO_2

5.1. Introduction

To date, there are no available measurements of CO_2-water-rock zeta potential acquired at realistic subsurface conditions and its link to the wettability. Hence, the aim of this chapter is to use the streaming potential method to measure the multi-phase zeta potential when two fluids are present in the pore space. To achieve this aim, the streaming potential experiment was designed to accommodate the supercritical CO_2 as an immiscible phase in the pore space at thermodynamic and chemical equilibrium with rock and CO_2-rich aqueous solutions. The experiments were then conducted over a range of pore pressure, temperature, salt type and constant ionic strength.

5.2. Materials and method

5.2.1. Materials

The same intact Fontainebleau sandstone sample, as the one described in Chapter 3, was used in this study. The petrophysical properties of the rock sample can be found in **Table 3.1** in Chapter 3. To remove any contaminants inside the rock sample, a reported procedure of *AlRoudhan et al.* (2016) to clean the sample prior to conducting the streaming potential experiments is followed.

The experiments were conducted using four different salts solutions (NaCl, $CaCl_2$, $MgCl_2$, and Na_2SO_4) made with reagent-grade salts from Sigma Aldrich, Australia at ionic strength of 0.05M saturated with CO_2 'live water' at the temperature of 40°C and pore pressure of 7.5 MPa. In addition, a single experiment of NaCl live water was commenced at pore pressure of 10 MPa with the same experimental temperature (NaCl-10). A CO_2 cylinder containing pure CO_2 with the mole fraction ≥ 0.99 (supplied by Coregas, Australia) was used to saturate the solution with CO_2 in order to prepare live water experiments.

5.2.2. Multi-phase streaming potential measurements

The streaming potential measurements were conducted at a high pressure-high temperature (HPHT) core flooding cell (see **Figure 3.1**).

To prepare the live water, the reported experimental protocol described in Chapter 3 was followed to make sure a complete equilibrium was established between live water and rock sample before commencing the experiments (see Chapter 3, subsection 3.2.5 for detailed experimental protocol). In summary, to achieve the equilibrium condition, the live water in the

left pump next to core holder (#1L) was flowed through the rock sample (#4) to the receiving pump in the right (#1R) and then back again. This procedure was repeated several times while live water pH and electrical conductivity of the rock sample was regularly measured until stabilised within 2% tolerance. To measure the live water pH, the live water effluent in the receiving pump was pumped back to the injection pump through high-pressure inline pH meter (#13; model number of pH-G-10"-T375-NPT250A-C276, Corr Instruments, LLC, accuracy of 0.01 pH units). For measuring saturated rock conductivity, the internal electrodes (#8) were connected to to a BK Precision 891 LCR meter (0.05% accuracy) and swept over the frequency range of 20 Hz to 300 KHz.

We modified the experimental protocol reported in Chapter 3 to accommodate the multi-phase unsteady state injection of supercritical CO_2 ($scCO_2$) to measure the streaming potential coupling coefficient (C_{SP}) as a function of fluid saturation (S_w, water saturation or S_g, gas saturation). We used a constant injection rate of 1 mL/min during unsteady state drainage and imbibition so that the corresponding capillary number of $Ca = 7.7\times10^{-9} – 2.0\times10^{-8}$ was achieved at the end of drainage (when irreducible water saturation, S_{wirr}, was reached) and $Ca = 2.7\times10^{-7} – 3.0\times10^{-7}$ was achieved at the end of imbibition (when residual gas saturation, S_{gr}, was reached). The capillary number was calculated as $Ca = \frac{v \times \mu}{\sigma}$, where v is Darcy velocity, μ is viscosity; viscosity of supercritical CO_2 at experimental conditions is 2.08×10^{-5} Pa·s at pressure of 7.5 MPa, while 4.78×10^{-5} Pa·s at pressure of 10 MPa (*Heidaryan et al.,* 2011). For live water viscosity (refer to **Appendix A**), it was taken from Chapter 3 using the approach of *Islam and Carlson* (2012). The $scCO_2$-brine interfacial tension (σ) for NaCl, $CaCl_2$, $MgCl_2$ and Na_2SO_4 is 39 $mN\cdot m^{-1}$ while σ =35 $mN\cdot m^{-1}$ for NaCl-10 (*Li et al.,* 2012). Based on the calculated *Ca*, the displacement during drainage and imbibition was a capillary dominated forces.

Prior to conducting the multi-phase experiments, the rock sample was initially characterised by measuring single-phase C_{SP} and zeta potential saturated with live water solutions (S_w = 1), as reported in Chapter 3. Subsequently, the multi-phase coreflooding experiments commenced using the following protocol:

1) The CO_2 cylinder (#10) was connected directly to the left pump (#1L) and pressurised to the target pore pressure that was identical to the single-phase experiment (7.5 MPa or 10.0 MPa). At the same time, the pump on the right (#1R) was set to the same and constant receiving pressure as the left pump to maintain a constant downstream pressure at the outlet of the core holder (#4).

2) The drainage process started by injecting 40 ml (approximately 5 pore volumes, PV) of $scCO_2$ into the rock sample fully saturated with live water (drainage) with a constant injection

rate of 1 ml/min from the left pump (#1L) through the core holder (#4), and then to the right pump (#1R). The core holder (#4) was then closed using inlet and outlet valves from the rest of the setup to keep the core holder pressured. The receiving right pump (#1R) was then depressurised and the volume of live water produced from the rock sample was measured. We assumed that the change in density after reducing the pump's cylinder pressure to 100kPa was less than 1% (*McBride-Wright et al.,* 2015) thus ensuring high accuracy of produced volumes estimates. The above steps were repeated until no more live water was displaced and thus, irreducible water saturation (S_{Wirr}) was reached. The total amount of injected pore volumes required to reach S_{Wirr} was 45 PV. At that stage, the C_{SP} at irreducible water saturation, $C_{SP}(S_{wirr})$, was measured using paired-stabilized (PS) method with the flow rate of 1 mL/min, combined with pressure-ramping (PR) method (*Vinogradov and Jackson,* 2011) with the injection pressure limited to 20 kPa, which corresponded to the injection pressure at the end of drainage. After measurements of $C_{SP}(S_{wirr})$, the core holder (#4) was kept pressured but disconnected from the pumps (#1L and #1R) and left to age with $scCO_2$ for 3 days at 40°C to allow wettability alteration to take place.

Although the mechanism behind the wettability alteration in $scCO_2$-silica-brine systems is still poorly understood, *Herring et al.* (2021) stated that there were two possible reactive transport mechanisms to create a 'patchy' mixed-wet state: i) preferential adhesion of CO_2 to quartz surface and ii) fine migration. As fines are usually formed from detached clay minerals and our tested core sample consisted of pure quartz (>99 wt% quartz), we assumed that the mechanism that took place to alter the wettability was the adhesion of CO_2 onto the rock surface.

The aging time in our experiment was determined empirically to not compromise the stability of the internal electrodes. We observed that, after 6-7 days of aging, the internal electrodes started to deteriorate showing an unstable voltage with very high noise level. Hence, continuing towards the imbibition experiment after this period of aging was impossible and resulted in uninterpretable voltage measurements. Even though the aging time was shortened to 3 days after multiple attempts, we also experimentally confirmed that 3 days of aging allowed for some wettability alteration since the measures zeta potential with a given brine was different between the aged and unaged experiments. By allowing $scCO_2$ to equilibrate with live brine and rock, we hypothesize that 3 days of aging was sufficiently long to allow time for preferential CO_2 adhesion that resulted in wettability alteration.

3) The imbibition process was started by injecting 2.5 PV (c. 20 ml) of the live water into the aged rock sample saturated with immiscible $scCO_2$ and irreducible live water with the same injection rate of 1 ml/min. The core holder was then closed, pH of the live water effluent and

σ_{rw} were measured. The above injection steps were repeated until the volume of produced live water became equal to the volume of injected live water (volume of produced CO_2 was calculated as a difference between the injected and produced volumes), hence the residual gas saturation, S_{gr} ($S_w = 1 - S_{gr}$) was reached. The total pore volume injected to reach S_{gr} was 45 PV. The C_{SP} at residual gas saturation, $C_{SP}(1 - S_{gr})$, was then measured using the PS method with the flow rate of 1 mL/min, combined with the PR method with the injection pressure limited at 20 kPa.

All dead volumes of the experimental setup were accurately measured prior to conducting the multi-phase experiments. Precisely measured volumes of injected and produced fluids combined with the measured dead volumes and sample porosity were used to compute the average water saturation at the end of each injection of CO_2 or live water during drainage or imbibition, respectively.

In Chapter 3, it was experimentally confirmed that surface electrical conductivity of all solutions was negligible at ionic strength of 0.05 M tested in this study (the ratio of brine conductivity to that of the saturated rock sample remained unchanged across tested NaCl concentrations between 0.05 M and 1 M), therefore the water conductivity values reported for single-phase live water experiments were used as the effective water conductivity. Thus, the classical Helmholtz-Smoluchowski (HS) equation could be used to evaluate the multi-phase zeta potential at residual gas saturation (*Hunter,* 1981; *Jouniaux and Pozzi,* 1995):

$$C_{SP} = \frac{\Delta V}{\Delta P} = \frac{\varepsilon \zeta}{\mu \sigma_w} \qquad 5.1$$

where ΔV is the stabilised voltage [V], ΔP is the stabilised pressure [Pa], ε is the water permittivity [F·m^{-1}], μ is the dynamic water viscosity [Pa·s], σ_w is the conductivity of the water [S·m^{-1}]. The stabilised voltage (ΔV) and pressure difference (ΔP) were obtained when S_{gr} was achieved and yielded to $C_{SP}(S_{gr})$. Water permittivity (ε), the dynamic viscosity (μ) and the water conductivity (σ_w) were assumed to be similar to those of the single-phase experiments, and this assumption was confirmed by the same and constant pH of single- and multi-phase experiments. Since these 3 parameters (ε, μ, σ_w) are identical for single- and multi-phase experiments conducted at the same temperature and pore pressure, **Equation 5.2** could be used to evaluate the multi-phase zeta potential at residual gas saturation (ζ_{mp}) from the single-phase zeta potential (ζ_{sp}) and measured C_{SP}:

$$\frac{C_{SP}(S_w = 1 - S_{gr})}{C_{SP}(S_w = 1)} = \frac{\zeta_{mp}}{\zeta_{sp}} \qquad 5.2$$

where $C_{SP}(S_w = 1)$ and ζ_{sp} are the streaming potential coupling coefficient and the zeta potential of single-phase experiments, respectively (see Chapter 3).

5.3. Results and discussion

5.3.1. Streaming potential coupling coefficient measurements at $S_w = S_{wirr}$ and $S_w = 1 - S_{gr}$

Typical results of stabilised voltage and pressure difference from PS experiments, and data from PR experiments for selected experimental conditions are shown in **Figure 5.1**. The noise level of measurements at multi-phase experiments for both S_{wirr} *and* $S_w = 1 - S_{gr}$ conditions (**Figures 5.1a** and **5.1c**) was noticeably higher than in single-phase dead and live water experiments (see **Figures 3.2a** and **3.2c** in Chapter 3). Moreover, we also observed poorer stability of voltage in the multi-phase experiments compared with the single-phase data. Hence, the higher noise level and poorer voltage stability contributed to higher experimental errors of the multi-phase streaming potential coupling coefficient and the interpreted zeta potential (**Figure 5.2**).

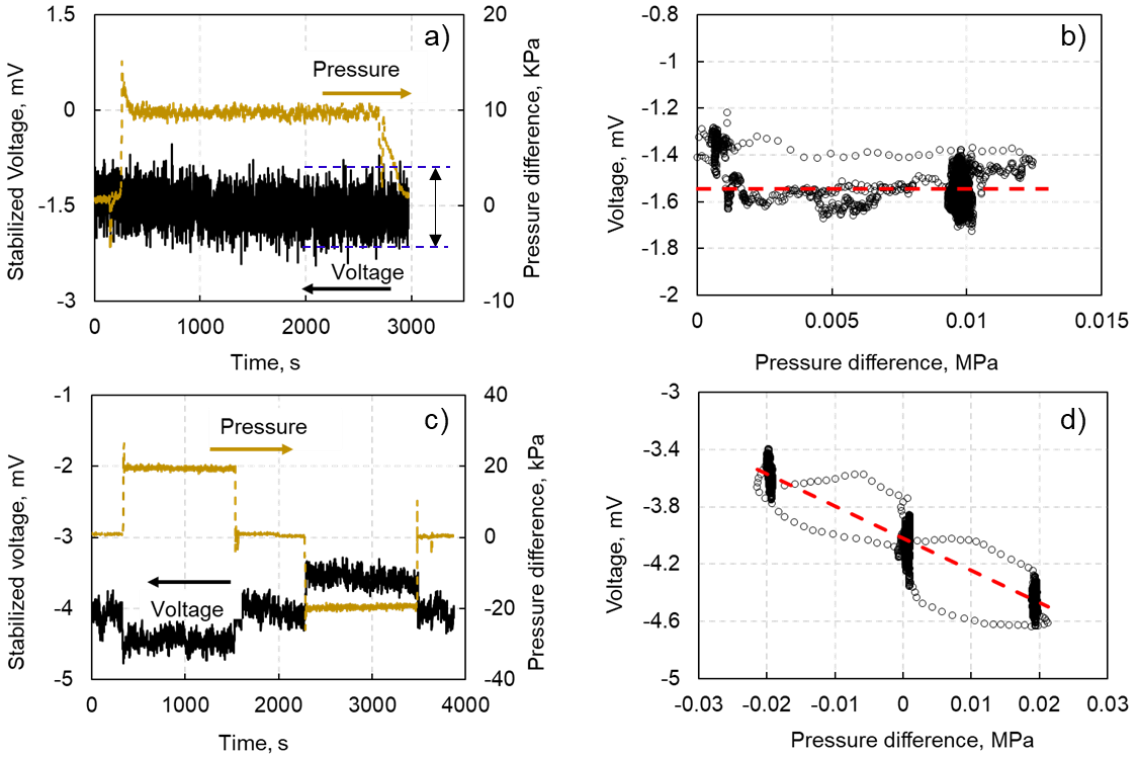

Figure 5.1. a) stabilised voltage and pressure difference of an experiment with $scCO_2$ pumped at 1 mL/min in the presence of live NaCl solution at irreducible saturation (S_{wirr}), pore pressure of 7.5 MPa and temperature of 40°C; b) PR experiment with $scCO_2$ pumped in the presence of live NaCl solution at irreducible saturation (S_{wirr}), pore pressure of 7.5 MPa and temperature of 40°C; c) stabilised voltage and pressure difference of an experiment with live NaCl solution pumped at 1 mL/min in the presence of $scCO_2$ at residual gas saturation ($S_w = 1 - S_{gr}$), pore pressure of 7.5 MPa and temperature of 40°C; d) PR experiment with live NaCl solution pumped at 1 mL/min in the presence of $scCO_2$ at residual gas saturation ($S_w = 1 - S_{gr}$), pore pressure of 7.5 MPa and temperature of 40°C.

The streaming potential coupling coefficient at irreducible water saturation, $C_{SP}(S_{wirr})$, was equal to zero within the experimental uncertainty for all live water experiments (**Figures 5.1a** and **5.1b**), and the result was consistent with the previous studies of *Revil and Cerepi* (2004) and *Vinogradov and Jackson* (2011). In contrast, a non-zero C_{EK} was observed in an experimental study conducted by *Moore et al.* (2004) with liquid CO_2 on Berea rock sample. The observation was later explained by *Vinogradov and Jackson* (2011) and *Vinogradov et al*. (2021) by an unmeasurable amount of connate water mobilised by liquid CO_2, which resulted a non-zero streaming current.

5.3.2. *Multi-phase zeta potential at $S_w = 1 - S_{gr}$ (ζ_{mp})*

The interpreted multi-phase zeta potential (ζ_{mp}) is controlled by individual contribution of the rock-water (ζ_{rw}) and CO_2-water (ζ_{cw}) interfacial zeta potentials (*Jackson et al.,* 2016a; *Collini et al.,* 2020; *Collini and Jackson;* 2022). The measured values of ζ_{mp} were negative for all tested solutions with the largest magnitude observed with $MgCl_2$, and progressively smaller in magnitude with Na_2SO_4, $CaCl_2$, NaCl, and NaCl-10 as shown in **Figure 5.2** and **Table 5.1**. **Figure 5.2** also presents a comparison between the multi-phase and the single-phase zeta potentials for all tested live solutions.

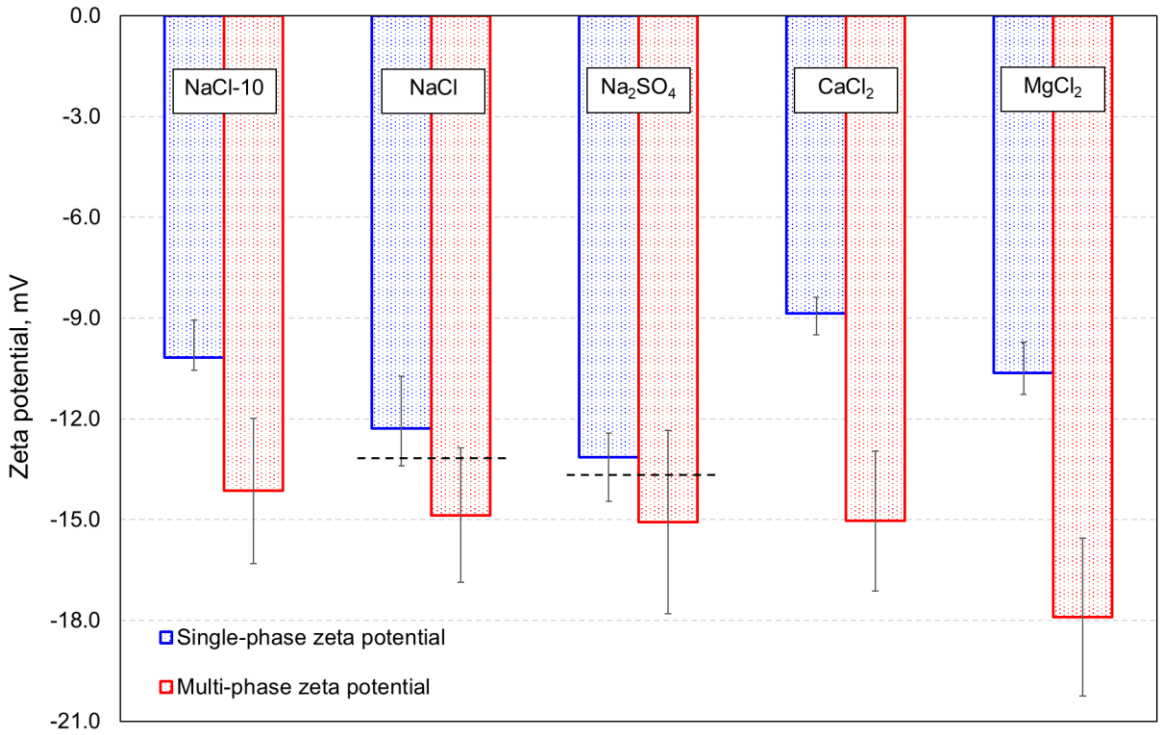

Figure 5.2. Summary of the result of multi-phase (red) zeta potential at residual gas saturation from this study compared with the single-phase (blue) data adapted from Chapter 3. Horizontal dashed line shows both single-phase and multi-phase zeta potential is agreed within experimental uncertainty. Error bars represent the experimental uncertainty of zeta potential obtained from the variation in the slope of the linear regression of C_{SP}.

The ζ_{mp} of NaCl and Na_2SO_4 solutions were found to be identical to the ζ_{sp} values within the experimental uncertainty. On the other hand, the ζ_{mp} of $CaCl_2$, $MgCl_2$ and NaCl-10 were more negative than the ζ_{sp}. The live water pHs in multi-phase experiments were nearly identical to those reported for single-phase (**Table 5.1**) and therefore, there was no change of equilibrium conditions of live water in presence of immiscible $scCO_2$. As the pHs were similar for both experiments, a similar pH dependence of the multi-phase zeta potential compared to single-phase experiment would be expected if the zeta potential was controlled solely by pH (see **Figure 5.3**). However, the multi-phase zeta potentials appeared to behave completely different as function of pH (**Figure 5.3**), therefore, implying that ζ_{mp} were also dependent on the pore space occupancy by $scCO_2$. Thus, we suggest that the micro-scale ζ_{cw} played an essential role in shifting the macro-scale zeta potential to become more negative as a result of wettability alteration that took place in the rock sample during aging.

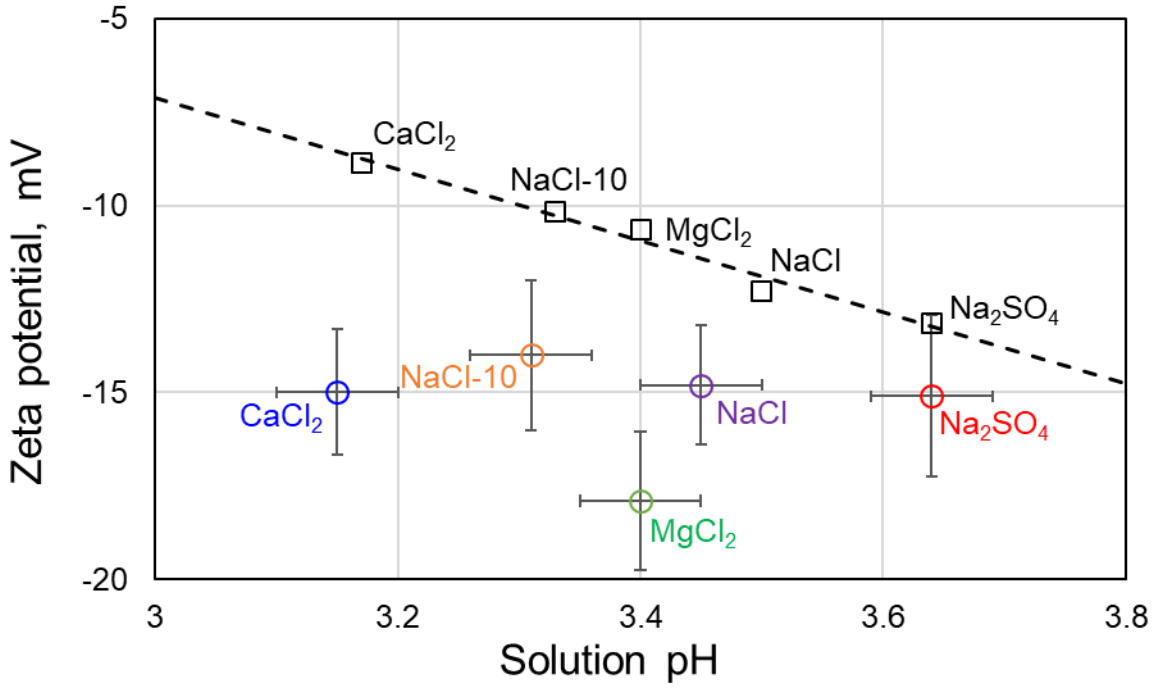

Figure 5.3. Multi- (colored symbols) and single-phase (black symbols) zeta potentials measured for live water-CO_2-sandstone systems. The dashed line represents the proposed pH dependence of single-phase live solution zeta potentials (**Equation 3.5** in Chapter 3). Error bars of zeta potential represent the experimental uncertainty obtained from the variation in the slope of the linear regression of C_{SP} while error bars of pH represent the variation of solution pH during the experiment.

Since the negative ζ_{mp} with NaCl-10, $MgCl_2$ and $CaCl_2$ had larger magnitude than the respective single-phase values (ζ_{sp}), the ζ_{cw} was unambiguously negative and greater in magnitude than ζ_{rw}, and the rock sample became more CO_2-wet. On the other hand, the multi-phase zeta potential with NaCl and Na_2SO_4 implies that either ζ_{cw} was zero or similar in magnitude to the respective single-phase value, or the wettability alteration did not take place.

Furthermore, the results presented in **Figure 5.1** were obtained in coreflooding experiments at $S_w = 1 - S_{gr}$ (i.e., imbibition) conducted at a single flow rate of 1 ml/min. The multi-phase zeta potential interpreted from these experiments, inherently, contained a large uncertainty of c.1.5 mV, which is equivalent to approximately 10% error relative to the reported value. To confirm the change in the zeta potential upon transition from single-phase measurements to the multi-phase ones, we conducted additional PS experiments using at least four different flow rates between 4 ml/min and 12 ml/min with an increment of 2 ml/min (refer to **Appendix C**). Due to technical restrictions of the experimental setup, water saturation could not be measured in these experiments, but was expected to increase compared to the values reported in **Figure 5.4** as a result of the so-called 'high-rate bumps', thus potentially eliminating or reducing the capillary end effects for some solutions (*Almutairi and Le-Hussain,* 2020; *Zivar et al.,* 2021). The results of multi-phase zeta potential from multiple rates were slightly different from single flow rate experiments. However, the main finding that the ζ_{cw} was negative remained unchanged and consistent with the result from single flow rate experiments (refer to **Appendix C**) and hence, increasing our confidence in the results. Moreover, a similar change in ζ_{mp} measured at 1 ml/min relative to the one obtained at high rate also suggests that the capillary end effects were similar for all tested solutions, thus making our interpretation valid.

Table 5.1. Tabulated experimental conditions and results at different water saturation

ID	P, MPa	pH		S_{wirr}	ΔS_w	C_{EK}, mV/MPa		ζ, mV	
		$S_w = 1$	$S_w \neq 1$			$S_w = 1$	$1 - S_{gr}$	$S_w = 1$	$1 - S_{gr}$
NaCl-10	10	3.33	3.31	0.30	0.53	-18.1	-25.1	-10.17	-14.1
Na_2SO_4	7.5	3.64	3.64	0.30	0.51	-24.1	-27.6	-13.15	-15.1
NaCl	7.5	3.50	3.45	0.32	0.43	-19.0	-23.0	-12.28	-14.8
$MgCl_2$	7.5	3.40	3.40	0.30	0.34	-17.8	-30.0	-10.64	-17.9
$CaCl_2$	7.5	3.17	3.15	0.34	0.29	-17.6	-29.9	-8.86	-15.0

ID is the live solution type; P is the pore pressure; S_{wirr} is the irreducible water saturation; ΔS_w is the total change in water saturation during imbibition; S_{gr} is the residual gas (CO_2) saturation. The pH values of $S_w \neq 1$ correspond to all intermediate pH measurement during drainage and imbibition.

5.3.3. Normalised zeta potential, wettability and residual gas (CO_2) saturation

Due to high pressure and elevated temperature conditions of the experiments, it was impossible to directly measure the system's wetting state using conventional methods that rely on spontaneous and forced imbibition cycles (Amott Wettability Index, or USBM). Therefore, to quantify the wetting state and to test the hypothesis that wettability alteration was associated with differences in the multi-phase zeta potentials as a result of presence of different salt species, we investigated the following parameters.

5.3.3.1 Wettability and change in the zeta potential

Jackson et al. (2016a) measured water Amott wettability index (I_w) for their carbonate-water-oil systems and demonstrated that multi-phase zeta potential became progressively more different from the single-phase value as I_w became smaller, reflecting more oil-wet conditions. Consistent with their results, we assumed that the change in the magnitude of the zeta potential in our experiments $\Delta\zeta_{wett}$ (defined as a difference between single-phase ζ_{sp} and multi-phase ζ_{mp}) also increased with a shift of the wetting state towards CO_2-wet. Moreover, *Collini et al.* (2020) reported I_w values of about 0.5, typical for (near) intermediate wettability, for which $\Delta\zeta_{wett}$ was vanishingly small compared with the single-phase ζ_{rw}. This implies, that small values of $|\Delta\zeta_{wett}|$ in our experiments were expected to correspond to either water-wet or intermediate-wet conditions.

On the other hand, small values of $\Delta\zeta_{wett}$ could be comparable with the measurement accuracy, hence suggesting $\Delta\zeta_{wett}$ to be effectively zero within the experimental error. Therefore, to considered $|\Delta\zeta_{wett}|$ in comparison with the experimental uncertainty, and scaled $|\Delta\zeta_{wett}|$ by the reported errors in the respective multi-phase experiments, $\left|\delta\zeta_{1-S_{gr}}\right|$, thus introducing the Reciprocal Scaled zeta potential (ζ_{rs}):

$$\zeta_{rs} = \frac{1}{\left|\frac{\Delta\zeta_{wett}}{\delta\zeta_{mp}}\right|} = \left|\frac{\delta\zeta_{mp}}{\Delta\zeta_{wett}}\right|, \qquad 5.3$$

where $\Delta\zeta_{wett} = \zeta_{1-S_{gr}} - \zeta_{S_w=1}$ is the difference between the multi-phase zeta potential, $\zeta_{mp} \equiv \zeta_{1-S_{gr}}$, and the single-phase zeta potential, $\zeta_{rw} \equiv \zeta_{S_w=1}$, both of which were measured with the same live solution; $\delta\zeta_{mp}$ is the experimental uncertainty in multi-phase zeta potential measurements, $\delta\zeta_{mp} = \frac{(+\delta)+(-\delta)}{2}$ with $+\delta$ and $-\delta$ corresponding to positive and negative experimental errors (see **Appendix A**).

Distinguishing between five different wetting states: strongly water-wet (SWW), weakly water-wet (WWW), intermediate-wet (IW), weakly CO_2-wet (WCW), and strongly CO_2-wet (SCW), this normalisation resulted in the following features of ζ_{rs}:

- $\zeta_{rs} \gg 1$ in SWW systems.
- $\zeta_{rs} \cong 1$ in WWW, IW, WCW systems.
- $\zeta_{rs} \ll 1$ in SCW systems.

To allow a better distinction between WWW, IW and WCW conditions, we employed one additional parameter.

5.3.3.2 Wettability and reciprocal relative permeability gradient

The wetting state is known to affect the shape of the relative permeability curves. Specifically, an increase in NAPF (i.e., CO_2) wetness results in an increase in end-point relative permeability to water (k_{rw}^e at $S_w = 1 - S_{gr}$) and a decrease in residual NAPF saturation (S_{gr}) (e.g., *Owens and Archer,* 1971). Therefore, SWW systems should usually correspond to the lowest k_{rw}^e and highest S_{gr}, while IW, WCW and SCW systems should exhibit high k_{rw}^e and low S_{gr}, although magnitudes of both properties for SCW, WCW and IW systems are similar to one another (e.g., *Heaviside et al.,* 1987). Moreover, a difference in S_{gr} between SWW and SCW cases is typically of order of 0.1 (or 10%), thus potentially making any distinction between the end-point wetting states based on S_{rg} masked by the experimental uncertainty. On the other hand, the difference in k_{rw}^e between SWW and SCW systems is typically of order of 0.4 (*Heaviside et al.,* 1987). Therefore, as a first order approach, the gradient of the relative permeability to water is expected to increase with increasing CO_2 wetness, while the corresponding Reciprocal Relative Permeability Gradient ($RRPG$), defined by **Equation 5.4**, is expected to decrease:

$$RRPG = \frac{1}{\frac{k_{rw}^e}{\left(1 - S_{gr} - S_{wirr}\right)}}, \qquad 5.4$$

It is generally agreed that maximum NAPF recovery (minimum residual NAPF saturation) corresponds to the optimal intermediate-wet state, when there is no specific affinity of the solid phase toward water or NAPF (*Morrow and Heller,* 1985; *Agbalaka et al.,* 2008; *Muggeridge et al.,* 2014; *Guancheng,* 2018). This argument has been proved by several experimental coreflooding results that showed the residual oil saturation after waterflood was maximum at intermediate(mixed)-wet state (*Kennedy et al.,* 1955; *Rathmell et al.,* 1973; *Hendraningrat and Torsæter,* 2015). On the other hand, another study by *Christensen and Tanino* (2017) found that the optimal wettability shifted to more oil-wet for higher oil recovery in an Indiana limestone sample (i.e., the contact angle shifted from 110° - 150°). However, the contact angles were measured separately on the calcite substrate submerged in the oil phase and hence, the in-situ wetting state of the Indiana Limestone during the coreflooding may be different. Therefore, in our case, we agreed with the first argument and expect the lowest residual CO_2 saturation (largest $S_w = 1 - S_{gr}$) to be reached for the optimal intermediate-wet state.

For the five distinct wetting conditions defined above and considering large experimental uncertainty in S_w (c.10% of the reported values), $RRPG$ for each wetting state is expected to follow the trend: $RRPG(SWW) \approx RRPG(WWW) > RRPG(IW) \approx RRPG(WCW) \approx RRPG(SCW)$.

Therefore, the introduced parameter can only be used to distinguish between water-wet and all other wetting states.

5.3.3.3 Wettability indicator

To make a better distinction between different wetting states, we combined $RRPG$ and ζ_{rs} in a single Normalized zeta potential defined as (ζ_n):

$$\zeta_n = \zeta_{rs} \times RRPG, \qquad 5.5$$

The product of ζ_{rs} and $RRPG$, both of which are the smallest for CO_2-wet and largest for water-wet states, allowed us to make a clearer distinction between all wetting conditions as demonstrated in **Figure 5.4**.

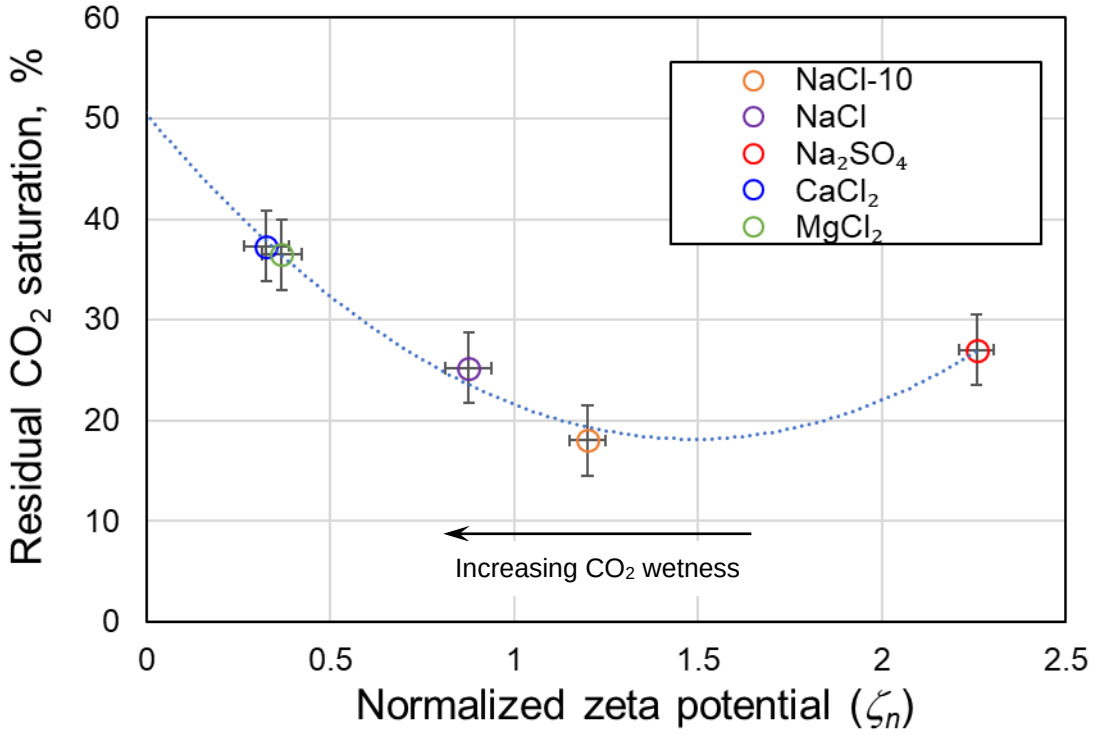

Figure 5.4. Residual CO_2 saturation as a function of the reciprocal normalised zeta potential defined by **Equation 5.5.** The blue dashed line describes the trendline obtained from the data points present in this figure. Error bars represent the experimental uncertainty of zeta potential obtained from the variation in the slope of the linear regression of C_{SP}.

Figure 5.4 demonstrates that the computed ζ_n varied between 0.33 for $CaCl_2$ and 2.26 for Na_2SO_4, while the data points for $CaCl_2$ and $MgCl_2$ were identical with respect to both ζ_n and S_{gr}. Incorporating discussions of previous sections, we concluded:

1. $CaCl_2$ and $MgCl_2$, both corresponded to WCW conditions with the smallest $\zeta_n = 0.33$ and $\zeta_n = 0.37$, respectively. This conclusion is consistent with the smallest $\zeta_{rs} = 0.55$

and $\zeta_{rs} = 0.51$ for $CaCl_2$ and $MgCl_2$, respectively, with both values significantly smaller than unity. The highest S_{gr} for these solutions, although inconsistent with the WCW state, is attributed to capillary end effects, which are expected to be more significant in CO_2-wet systems.

2. Na_2SO_4 corresponded to SWW conditions with the largest $\zeta_n = 2.26$, also confirmed by a significantly larger than unity $\zeta_{rs} = 2.22$.

3. NaCl-10 corresponds to IW resulting in (near) minimum residual CO_2 saturation and consistent with $\zeta_n = 1.19$, placed between small values for CO_2-wet or large values for water-wet conditions, and also confirmed by $\zeta_{rs} = 1.04 \cong 1$.

   NaCl corresponds to WWW conditions with $\zeta_n = 0.88$ of the same order as that for IW state, and also confirmed by higher than minimum S_{gr} and $\zeta_{rs} = 1.27 > 1$, with the latter parameter being smaller than the corresponding value for Na_2SO_4 SWW case.

There are no published experimental data on wettability indices of rocks saturated with brines and supercritical CO_2 (e.g., Amott, USBM method), since such methods are based on spontaneous imbibition tests, which are challenging under CGS conditions of pressure and temperature. Therefore, the results that are presented in **Figure 5.4** can be only qualitatively validated using published contact angle measurements conducted under similar experimental conditions. Firstly, contact angles measured for quartz in contact with live NaCl solution and immiscible supercritical CO_2 indicated that although the system remained water-wet across the range of tested pressures, the contact angles shifted from approximately 50° at 7.5 MPa to approximately 70° at 10 MPa of CO_2 pressure (Figure 7, 350 K dataset in *Iglauer et al.,* 2012). This observation is consistent with our hypothesis of the shift from weakly water-wet state obtained with NaCl at 7.5 MPa to intermediate-wet condition with NaCl at 10 MPa (note, that the contact angle of 70° is close to the value of 80°-100°, typically assigned for intermediate wet rocks), as interpreted from ζ_n and S_{gr} (see **Figure 5.4**).

Furthermore, contact angles of quartz in contact with NaCl, $CaCl_2$ and $MgCl_2$ (*Al-Yaseri et al.,* 2016) were reported to be different for different salts and larger for $CaCl_2$ (c. 43°) and $MgCl_2$ (c. 45°) compared with NaCl (c. 36°). These results are also consistent with our interpretation of the shift towards weakly CO_2-wet conditions with $CaCl_2$ and $MgCl_2$, although all reported by *Al-Yaseri et al.* (2016) contact angles corresponded to water-wet conditions. Due to limited available experimental data, a direct quantitative comparison between our results and contact angles reported in *Al-Yaseri et al.* (2016) was impossible since: 1) the authors reported salt concentration in wt.%, which implied different ionic strengths for NaCl and $CaCl_2$ for the same wt.%; 2) the lowest tested concentration in the paper was 0.5M for NaCl and 0.27M for $CaCl_2$ both of which were significantly higher than tested in this study (ionic strength has strong

impact on the zeta potential, which controls wettability); 3) temperature and pressure conditions in *Al-Yaseri et al.* (2016) were different from those in this study.

Furthermore, the interfacial tension (IFT) of all tested solutions at 7.5 MPa (NaCl, $CaCl_2$, $MgCl_2$, and Na_2SO_4) obtained from literature were found to be constant (≈39 mN·m-1; *Li et al., 2012*) while for NaCl-10 conditions the interfacial tension is ≈35 mN·m-1 (*Li et al.,* 2012). From these IFT values, we argue that the effect of the interfacial tension on the zeta potential and on residual saturation was minimal. Hence, we attribute the measured variation in residual CO_2 saturation observed with different solutions to respective differences in wettability.

To validate the results and hypotheses, future work is planned to expand towards higher salinity, mixed salts, and to accurately assess residual CO_2 saturation using X-ray computer tomography.

5.4. Conclusions

We developed and successfully carried out for the first time measurements of the multi-phase zeta potential in an intact Fontainebleau sandstone sample saturated with live solutions and immiscible $scCO_2$. The results show that:

1. The streaming potential coupling coefficient at the end of drainage was zero, confirming that most of the pore space was occupied by the $scCO_2$, and only immobile live water was at irreducible saturation.

2. The multi-phase zeta potential for all tested solutions at temperature of 40°C and pressures of 7.5 MPa and 10 MPa was negative.

3. The magnitude of zeta potential of the $scCO_2$-water interface (ζ_{cw}) was confirmed to be negative. This result provides an important insight for modelling the disjoining pressure using DLVO theory.

4. Wettability interpreted from the single- and multi-phase zeta potential measurements suggested intermediate-wet conditions were obtained with NaCl-10, strongly water-wet conditions were obtained with Na_2SO_4, weakly water-wet conditions were obtained with NaCl, and weakly CO_2-wet conditions were obtained with $CaCl_2$ and $MgCl_2$. These findings and conclusions are qualitatively consistent with previously published contact angle measurements. Moreover, the interfacial tension of $scCO_2$-water of for all tested solutions remained constant and hence, the effect of interfacial tension on residual CO_2 saturation, wettability and zeta potential was minimal.
5. The introduced normalized zeta potential, which comprises the scaled difference between single- and multi-phase zeta potentials and relative permeability curve gradient, correlates well with residual CO_2 saturation, thus providing a powerful

experimental tool to evaluate residual CO_2 trapping in sandstone reservoirs. Combining two independent properties in ζ_n, each of which implicitly reflects the wetting state, allows to define the wetting state with more confidence using this new parameter as a wettability indicator.

Future experimental work will aim at expanding the parameter space of investigated ionic strength and solution composition. Furthermore, additional data should be acquired for clayey sandstones, as the clay minerals have a significant impact on the zeta potential (*Li et al.,* 2018; *Alaraouj et al.,* 2021). Moreover, X-ray computed tomography should be utilized to accurately assess CO_2 saturation.

Chapter 6 Zeta potential of an intact fractured gneiss sample*

*) *Part of the text in this chapter was prepared for publication and it was accepted during the registration period of my study in Applied Sciences. The final version of the published paper can be seen at* https://doi.org/10.3390/app12010180

6.1. Introduction

Fractured rocks are found in many subsurface geological formations, including hydrocarbon reservoirs (*Berkowitz,* 2002; *Mendez et al.,* 2020), geothermal formations (*Luo et al.,* 2017), CO_2 geological storage sites (*Iding and Ringrose,* 2009; *Ringrose et al.,* 2011; *Le Gallo and De Dios,* 2018) and aquifers (*Abdelaziz and Merkel,* 2012).

Fractures in reservoirs affect subsurface flows and thus, reservoir fluid extraction. At the same time, fractures (either naturally or artificially induced) in CO_2 geological storage formations can lead to potential CO_2 leakage, as they provide an accessible channel for CO_2 to flow. Hence, understanding the subsurface flow in a fractured system is essential to maximise the benefit or minimize the risk in terms of CGS applications.

Furthermore, characterising wettability is important to determine the fluid flow behaviour in subsurface settings. This parameter significantly impacts the efficiency of CGS trapping mechanisms (*Al-Yaseri et al.,* 2016; *Iglauer et al.,* 2015) and hydrocarbon recovery (e.g., *Jackson et al.,* 2016a; *Jackson and Vinogradov,* 2012). However, the wettability characterisation in fractured rocks remains poorly understood.

In order to characterise the wetting state in fractured rocks, the zeta potential can be used. The zeta potential can be measured experimentally in the laboratory using the streaming potential method (SPM). In recent years, the SPM has shown promising results in measuring the zeta potential in an intact rock sample under subsurface pressure and temperature conditions (e.g., *Vinogradov and Jackson,* 2015), and single- and multi-phase flow experiments (e.g., *Jackson et al.,* 2016a). Therefore, we use the SPM to measure zeta potential in fractured rock systems in this study.

It is widely accepted that the polarity and the magnitude of zeta potential depend on rock mineralogy, solution pH, chemical compositions, and temperatures (e.g., *Vinogradov et al.,* 2010; *Jackson and Leinov,* 2012; *Vinogradov et al.,* 2018). Numerous experimental investigations of zeta potential have been conducted on several rock types saturated with water, including sandstone (*Vinogradov et al.,* 2010; *Walker and Glover,* 2018), carbonate (*Jackson et al.,* 2016a; *Al Mahrouqi et al.,* 2017; *Collini et al.,* 2020) and granite (*Tosha et al.,* 2003). In addition, a recent investigation by *Li et al.* (2018) found that the clay minerals in sandstone had a significant impact on the measured zeta potential. However, to date, there are no experimental data on zeta potential in fractured rocks, comprising various minerals.

In order to understand the impact of fracture and a variety of minerals on zeta potential, the study aims to experimentally measure the zeta potential of gneiss samples at confining pressures of 4.0 MPa and 7.0 MPa to represent different fracture apertures. The gneiss sample was selected in this study as a test-rock due to its unique features including essentially zero matrix porosity and permeability (*Liu et al.,* 2016) and presence of important minerals (e.g., quartz, feldspars and micas) all of which are commonly found in the subsurface storage formations. Furthermore, selecting a naturally fractured rock that has non-zero matrix permeability (e.g., fractured carbonate) would make the interpretation of the zeta potential measurements questionable as the electrolyte would flow through both fracture and matrix thus both would contribute to the measured zeta potential averaged over the entire sample. By inducing the flow through a fracture in otherwise impermeable gneiss sample allowed us to isolate and study the effect of fracture aperture on the measured zeta potential and the effect of minerals lining the fracture wall. Therefore, the results of this study are important for wettability characterisation of naturally fractured subsurface settings comprising multiple minerals.

6.2. Materials and methods

An intact cylindrical gneiss sample was used in this study. The rock sample was cored from the Lewisian Gneiss Precambrian Formation in Northwest Scotland, near Clashnessie. Prior to conducting the streaming potential experiments, the unfractured gneiss sample was placed into the coreflooding cell and a flow of NaCl solution through the sample was induced. The inlet pressure was increased to 7 MPa, which corresponded to the maximum experimentally achievable inlet pressure. After reaching the maximum inlet pressure with unfractured sample, no flow through the rock was observed at the outlet, which indicated zero permeability of gneiss matrix within the tested 7 MPa pressure difference, consistent with the results reported by *Liu et al.* (2016).

The investigated gneiss sample was artificially fractured under controlled pressure and along the pre-existing fissures in uniaxial compression apparatus. The fracture was induced horizontally along the flow direction. In order to maintain the cylindrical shape after fracturing, the sample was then wrapped with duct tape. Further, the sample was cleaned using deionized water and methanol following the reported experimental cleaning protocol by *AlRoudhan et al.* (2016). Lastly, the sample was saturated with the aqueous solution of interest inside a vacuum chamber for 24 hours to ensure a fully saturated condition.

In order to understand the effect of a fracture in the rock sample, the experiments were conducted at two different confining pressures, 4.0 MPa and 7.0 MPa. Hence, the fracture

aperture in the rock sample will differ for each condition and result in different permeability. The summary of the Lewisian gneiss properties is presented in **Table 6.1**.

Table 6.1. Summary petrophysical and mineralogy of gneiss sample used in this study

Sample	Lewisian gneiss
Dimensions	Length = 5.40 cm Diameter = 3.80 cm
Liquid Permeability	Confining pressure: 4.0 MPa = 51 ± 1 mD Confining pressure: 7.0 MPa = 43 ± 1 mD
Mineralogy*	35 wt.% quartz 60 wt.% Na-feldspars (plagioclase and albite) 5 wt.% micas (muscovite and biotite)

*) Mineralogy of gneiss sample was obtained from XRD analysis using powdered offcuts. Further, a chip from the sample was polished to produce a thin section, which was analyzed using SEM. These mineral proportions are characteristic of felsic type of Lewisian gneiss, as previously reported by *Weaver and Tarney,* 1981; *MacDonald et al.,* 2017.

The experiments were designed using four different 'dead' solutions of varying ionic strengths and water compositions. These solutions are: 1) the artificial groundwater (AGW) comprising mixed salts, similar to the reported compositions of actual groundwater of the Lewisian Gneiss on the Ilse of Harris (*BGS,* 2001) with the ionic strength of 7.350×10^{-3} M (M=mol/L); 2) The artificial seawater (ASW) consists of the same ionic species as AGW, and the total ionic strength is 0.70 M; 3) low salinity (LS) 7.350×10^{-3} M NaCl solution and 4) high salinity (HS) 0.70 M NaCl solution. During the experiments, the electrical conductivity and solution pH were measured regularly using Jenway 4520 conductivity (Cole-Palmer, 0.5% accuracy) meter and Mettler Toledo FiveGo pH meter (accuracy of 0.01 pH units), respectively. This particular procedure was necessary to ensure the equilibrium conditions in the experiments. The details of ionic composition and equilibrium pH of all tested solutions are presented in **Table 6.2.**

Table 6.2. Chemical composition, equilibrium pH and electrical conductivity of tested solutions.

	AGW*	**LS***	**ASW**	**HS**
$[Na^+]$, M	1.522×10^{-3}	7.350×10^{-3}	0.512	0.700
$[Ca^{2+}]$, M	1.612×10^{-3}	-	0.013	-
$[Mg^{2+}]$, M	0.288×10^{-3}	-	0.042	-
$[Cl^-]$, M	5.072×10^{-3}	7.350×10^{-3}	0.577	0.700
$[SO_4^{2-}]$, M	0.125×10^{-3}	-	0.022	-
pH	6.0 ± 0.1	6.5 ± 0.1	6.2 ± 0.1	6.9 ± 0.1
σ_w, S·m^{-1}	0.069 ± 0.001	0.097 ± 0.001	5.83 ± 0.01	6.13 ± 0.01
Ionic strength, M	7.350×10^{-3}	7.350×10^{-3}	0.700	0.700

*) AGW and LS solutions were prepared from high salinity stock solutions of 0.735 M ionic strength. Hence, errors in molar concentrations of all four tested solutions resulting from inaccuracies in weighing the constituent salts are estimated at ±3% of the reported values.

The streaming potential measurements were conducted in a high pressure-high temperature (HPHT) PEEK coreflooding apparatus located at the University of Aberdeen. We used the paired-stabilized 'PS' method (*Vinogradov and Jackson,* 2011) to obtain stabilised voltage (ΔV) and pressure difference (ΔP) across the rock sample. In 'PS' method, the solution of interest was flowed at a constant rate through the rock sample using a pump until stable pressure and voltage was reached. Further, the flow was terminated, and the flow direction was reversed at the same rate until stable pressure and voltage observed across the rock sample. This step was repeated with at least four different flow rates.

Further, the streaming potential coupling coefficient (C_{SP}) was determined from the slope of a linear regression of stabilised voltage against stabilised pressure where the total current density (j) was zero, and the zeta potential could be interpreted using the Helmholtz-Smoluchowski (HS) equation (e.g., *Jouniaux and Pozzi,* 1995). In this study, we assume negligible contribution of the surface electrical conductivity to the effective electrical conductivity of the aqueous solution occupying a μm-scale fracture (which will be discussed in subsequent sections), and therefore, the classical HS equation is used to evaluate the zeta potential as follows:

$$C_{SP} = \frac{\Delta V}{\Delta P}\Big|_{j=0} = \frac{\varepsilon \zeta}{\mu \sigma_w}, \qquad 6.1$$

where ε is the permittivity of water [F·m^{-1}], ζ is the zeta potential [V], μ is the dynamic viscosity of water [Pa·s], and σ_w is the electrical conductivity of the aqueous solution [S·m^{-1}].

6.3. Results and discussion

6.3.1. Measurements of streaming potential

Here the typical results of the stabilised voltage and pressure difference, and the obtained slope of C_{SP} (**Figure 6.1**) from selected experimental conditions is presented.

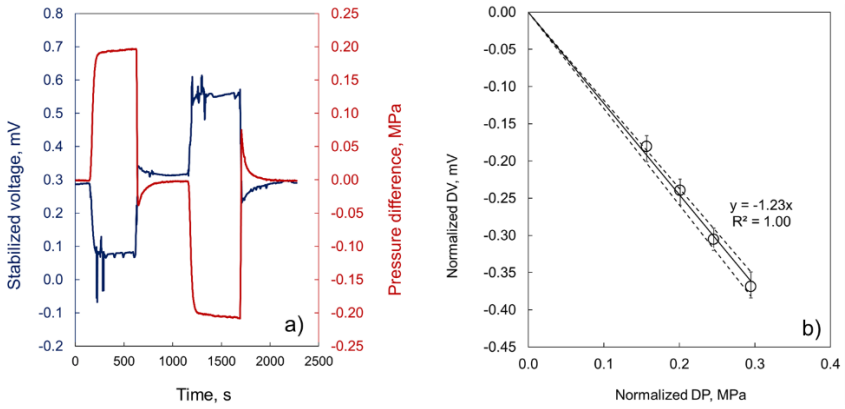

Figure 6.1. Typical results of stabilised voltage and pressure (a) and the obtained streaming potential coupling coefficient (b). (a) 0.7M NaCl solution flowed with a constant rate of 10 ml/min at the confining pressure of 7.0 MPa and (b) C_{SP} for 0.7M NaCl at 7.0 MPa using 4 different flow rates.

6.3.2. Effect of rock type and mineralogy

In order to understand the zeta potential of the gneiss sample, at first, we compare the interpreted zeta potential of gneiss with the published zeta potentials from five different types of rock, including pure sandstone (>99% quartz), clayey sandstone (2-5% clay content), sand packs (>99% quartz), carbonate (>95% calcite) and granite samples saturated with the similar condition of tested ionic strength and composition used in this study (**Figure 6.2**). In addition, we tried to collect the previous data of zeta potential measurements at equilibrium conditions. The individual data points that formed the grey and white shaded areas in **Figure 6.2** are summarized in **Table 6.3**. As far as we know, there is no published data on measured zeta potential at high ionic strength on granite and gneiss rock samples. Hence, the corresponding column in **Table 6.3** is filled with N/A (not available)

Table 6.3. Summary of experimentally measured zeta potential in relevant samples saturated with NaCl and natural solutions.

Sample; mineralogy	**Solution**	**Zeta potential, mV**		**Source**
		LS	**HS**	
Grey shaded area				
Fontainebleau SS; >99 wt.% quartz	NaCl	-52	-20	1, 2
Lochaline SS; >99 wt.% quartz	NaCl	-77	-25	2
Stainton SS; wt.% quartz, 5 wt.% clays and feldspar	NaCl	-26	-16	1
St Bees SS; 90 wt.% quartz, < 5 wt.% clays	NaCl	-31	-16	1, 3
St Bees SS; 90 wt.% quartz, <5 wt.% clays	SW	N/A	-13	1
Doddington SS; 69 wt.% quartz, 5 wt.% clays	NaCl	-22	-10	5
SP; >99 wt.% quartz	TW	-100	N/A	1
SP; >99 wt.% quartz	NaCl	-20	-12	4
Berea SS; 90 wt.% quartz, up to 4 wt.% clays	NaCl	-20	-17	6
Boise SS; 47 wt.% quartz, 26 wt.% plagioclase, 3 wt.% clays	NaCl	-20	-20	2
Inada granite; N/A	KCl	-35	N/A	7
Westerly granite, 38 wt.% plagioclase 29 wt.% quartz	NaCl	-20	N/A	8
Crushed Westerly granite; N/A	KCl/NaCl	-65	N/A	9
Inada granite; N/A	KNO_3	-70	N/A	10
White shaded area				
Ketton LS; 97 wt.% calcite, 3 wt.% dolomite	NaCl	N/A	-6	11
Estaillades LS; 95 wt.% calcite, 4 wt.% dolomite, 1 wt.% anhydrite	NaCl	N/A	-6	11
Portland LS; 96.6 wt.% calcite, 3.4 wt.% quartz	NaCl	N/A	-9	11

Estaillades LS; 95 wt.% calcite, 4 wt.% dolomite, 1 wt.% anhydrite	SW	N/A	-1.25	12
Reservoir BA LS; N/A	ALSW	-4	N/A	13
Reservoir BD LS; N/A	ALSW	-10	N/A	13
Outcrop TE LS; >99 wt.% calcite	Artificial	-15	-2	13
Crushed Iceland spar; 100 wt.% calcite	NaCl	-5[14]	+4[15]	14, 15

LS and HS correspond to low salinity and high salinity data. SS stands for sandstones, SP corresponds to sand packs, LS refers to limestones, SW is natural seawater from southern UK, TW is tap water, and ALSW is artificial low salinity water. The exact ionic strength values in the table vary between 0.001 M and 0.01 M for low salinity and between 0.5 M and 0.75 M for high salinity data. For details, refer to the cited papers. The data sources are: 1 – *Vinogradov et al.,* (2010); 2 – *Walker and Glover,* (2018); 3 – *Jaafar et al.,* (2009); 4 – *Vinogradov et al.,* (2018); 5 – *Vinogradov and Jackson,* (2015); 6 – *Li et al.,* (2018); 7 – *Tosha et al.,* (2003); 8 – *Reppert and Morgan,* (2003); 9 – *Morgan et al.,* (1989); 10 – *Ishido and Mizutani,* (1981); 11 – *Al Mahrouqi et al.,* (2017); 12 – *Jackson et al.,* (2016a); 13 – *Collini et al.,* (2020); 14 – *Heberling et al.,* (2011); 15 – *Heberling et al.,* (2021).

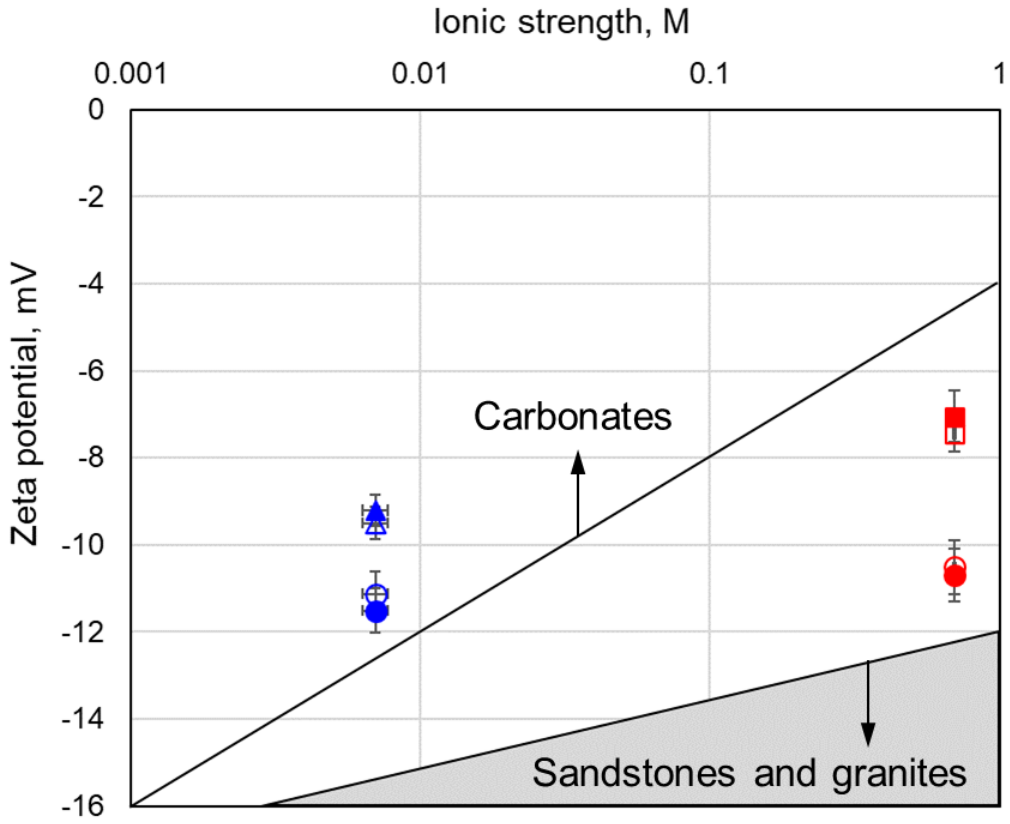

Figure 6.2. Zeta potential of gneiss samples compared with published data on other types of rocks. Circles denote NaCl solutions, triangles correspond to AGW, and squares are ASW. Filled symbols correspond to confining pressure of 7 MPa. Red and blue represent high (0.7M) and low (7.350 × 10-3 M) ionic strength conditions, respectively. Error bars represent the experimental uncertainty obtained from the variation in the slope of the linear regression of C_{SP}.

In **Figure 6.2**, the zeta potentials of gneiss at high ionic strength condition (0.7 M) for all tested solutions were less negative than sand packs, pure sandstones and clayey sandstones, but more negative than carbonates with the similar ionic strength of tested solutions. Moreover, most of the data in **Table 6.3** also indicate a similar trend in the comparison of gneiss zeta

potential with other rock types. Nevertheless, two exceptional cases were found on the zeta potential of gneiss compared with the individual data points of zeta potential in Doddington sandstone (-10 mV) and Portland limestone (-9 mV) saturated with 0.5M NaCl solution. These two rock samples' ionic strength was considerably similar to the zeta potential of ASW in this study. We suggest that a higher clay content in Doddington sandstone and quartz in Portland limestone corresponds to this uncommon behaviour compared to pure silica or calcite rocks. However, their measured zeta potentials were comparable with the result of our interpreted zeta potential of gneiss in ASW and HS NaCl (-7.0 mV to -10.7 mV).

Furthermore, the zeta potentials of gneiss at low ionic strength condition (7.350×10^{-3} M) were less negative compared to both sandstone and carbonate samples (**Figure 6.2**). However, there two exceptions were found on the zeta potential obtained from crushed Iceland spar (-5.0 mV) saturated with 0.01 M NaCl mixed with a small amount of 1.0 mM $CaCl_2$ (*Heberling et al.,* 2011) and BA carbonate core sample (-4.0 mV) obtained from the reservoir with unreported detailed mineralogy saturated with 0.01 M mixed solutions containing divalent ions of Ca^{2+} and Mg^{2+} (*Collini et al.,* 2020). The zeta potential of crushed Iceland spar showed a strong dependency on added $CaCl_2$ (i.e., the range of measured zeta potential is from -3.0 mV with 5 mM $CaCl_2$ to -14 mV with 0.1 mM $CaCl_2$) and unconfirmed equilibrium condition during the experiments. Hence, a direct comparison of our result with crushed Iceland spar seems not applicable. On the contrary, the zeta potential of the BA carbonate core sample was conducted under equilibrium conditions (*Collini et al.,* 2020). However, the 0.01 M mixed solution used in their study (*Collini et al.,* 2020) contained a noticeable amount of Ca^{2+} (1.0 mM) and Mg^{2+} (0.3 mM) with no SO_4^{2-}. As these three ions species are considered as the potential determining ions (i.e., divalent cations shifted zeta potential to become more positive while divalent anions moved the zeta potential to become more negative; PDIs) for carbonates and clays (e.g., *Jackson et al.,* 2016b; *Al Mahrouqi et al.,* 2017), we should expect a more positive measured zeta potential of BA carbonate core sample compared to our zeta potential in gneiss using AGW and LS at similar ionic strength due to the presence of Ca^{2+} and $Mg^{2+}$and the absence of SO_4^{2-}. Further, it is important to note that there were many published experimental data of zeta potentials in carbonates (see Figure 3 in *Jackson et al.,* 2012b), and the range of measured zeta potentials at low ionic strength conditions (≤ 0.01M) was noticeably wide (from -20 mV to +20 mV) for pH value of 7.0. However, as *Al Mahrouqi et al.* (2017) discussed, none of these measurements were conducted at equilibrium conditions. Hence, it prohibited us from comparing our measured zeta potential directly with their results.

In order to understand the impact of gneiss mineralogy on the zeta potential, we collected several studies related to the measurements of the zeta potential in plagioclase (*Nyabeze and McFadzean,* 2016), muscovite (*Nishimura et al.,* 1992), albite (*Jie et al.,* 2014) and biotite

(*Bray et al.,* 2014). However, these studies used an electrophoretic mobility method (EPM) to obtain the zeta potential with unreported equilibrium conditions. Hence, the dissolution of minerals into aqueous solutions, especially when using a single salts solution, is likely to happen, as reported by *Alroudhan et al.* (2016) and *Al Mahrouqi et al.* (2017) for carbonate samples or the one reported by *Reppert and Morgan* (2003) for granite. As a result, a direct comparison between the zeta potentials of these minerals (plagioclase, albite, biotite, and muscovite) and our results is not applicable, except only for qualitative interpretation. In addition, in subsurface conditions, all the minerals are expected to be fully equilibrated with the formation water, thus emphasizing the importance of our laboratory results. The previous studies suggested that zeta potentials on mica and feldspar minerals were negative for the range of 6 – 8 pH values. The smallest magnitude of zeta potential was from plagioclase, followed by albite, biotite and muscovite (i.e., $|\zeta_{plagioclase}| < |\zeta_{albite}| \cong |\zeta_{biotite}| < |\zeta_{muscovite}|$). It was worth mentioning that the values reported for plagioclase ranged between -10 mV and +15 mV, obtained with 10^{-2} M disodium tetraborate solution (*Nyabeze and McFadzean,* 2016).

All in all, the interpreted zeta potential of Lewisian gneiss at low and high ionic strength of single salt and complex solutions were unique. The mineralogy of this rock sample comprises quartz, feldspars and micas, so that the interpreted zeta potential using the streaming potential method is an average of the effective zeta potential from each mineral contribution with water at the interface. Since there are no reported zeta potential measurements of feldspars and micas in contact with various aqueous solutions at equilibrium conditions, we hypothesize that the effective zeta potential on these complex minerals is controlled by multi-valent PDIs, similar to the mechanism of the surface charge development on calcite surface (e.g., *Vinogradov et al.,* 2022b). As a result, the resulting surface charge and the corresponding zeta potential of gneiss consisting of feldspars in our experiments caused the zeta potential to be less negative than in pure quartz systems. Micas in contact with aqueous solutions (*Nishimura et al.,* 1992; *Jie et al.,* 2014) were reported to be more negative than feldspars zeta potential (*Bray et al.,* 2014; *Nyabeze and McFadzean,* 2016). At the same time, the negative zeta potentials measured with micas were smaller in magnitude compared with negative values on silica surface, consistent with a published study of silica and mica minerals in contact with 10^{-3} M KCl solution (*Nishimura, et al.,* 1992). Moreover, previously published studies also reported a shift in the zeta potentials towards more positive values with solutions containing divalent cations relative to NaCl/KCl measurements for all types of minerals, with a more pronounced shift reported with micas (*Adamczyk, et al.,* 2010) and feldspars (compare the results obtained with albite in contact with 10^{-3} M NaCl in Gülgönül, et al., 2012 vs 10^{-3} M $CaCl_2$ in *Demir et al.,* 2003) compared with pure quartz (e.g., *Yukselen-Aksoy and Kaya,* 2011). Hence, the zeta potential in our experiments responded to changes in chemical composition

in a fashion similar to that of calcite/mica/feldspar and became more positive with divalent cations, while the electric charge on the gneiss quartz surface sites was mostly controlled by pH thus remaining insensitive to changes in the electrolyte composition, all of which will be discussed in more detail below. Moreover, the uniqueness of the gneiss zeta potentials was demonstrated by the impact of varying ionic strength, which appeared to be less pronounced than that obtained with either carbonates or pure sandstones (>95 wt.% quartz). Both, the impact of composition and ionic strength on the zeta potential in gneiss samples will be discussed in more detail in the subsequent section.

6.3.3. Effect of ionic strength and complex ions compositions

Figure 6.3 shows the result of zeta potential for four different tested solutions as function of ionic strength compared to carbonate and sandstone samples. The zeta potential of ASW became smaller in magnitude when the ionic strength changed from AGW to ASW (**Figure 6.3a**), consistent with the description of the electrical double layer theory due to collapsing of the double layer with increasing ionic strength (*Hunter,* 1981). On the other hand, the measured zeta potential of LS NaCl was found to be similar to HS NaCl within the experimental uncertainty (see horizontal dashed line in **Figure 6.3b**).

In **Figure 6.3a**, we also observed that the dependency of zeta potential as a function of ionic strength in the gneiss sample was weaker than the general trendline of carbonate (black dashed line) and sandstone (green dashed line) samples saturated with NaCl solutions. However, an anomalous result was reported on zeta potential saturated with NaCl and $CaCl_2$ solutions in several Berea 'clayey' sandstones by *Li et al.* (2018). The zeta potential of Berea sandstones was changed from -18.3 mV at 0.005M NaCl to -21.4 mV at 0.5 M NaCl (see **Figure 6.3**). This result indicates that the effect of increased NaCl ionic strength on zeta potential was less significant and the behaviour of zeta potential at Berea clayey sandstones was the opposite trend of general clean sandstone samples. Further, the zeta potentials of Berea saturated with $CaCl_2$ remained constant (c. -7.0 ± 0.3 mV) with increasing ionic strength solution (0.008 M – 0.8 M). This behaviour was similar to the observed trend of our gneiss result saturated with a single salt NaCl solution (**Figure 6.3b**). Furthermore, the magnitude zeta potential of gneiss sample saturated NaCl solution for both ionic strengths was larger than the tested complex solutions (AGW and ASW). Interestingly, the gneiss zeta potential obtained with ASW (-7.2 ± 0.2 mV) was similar to the zeta potential from Berea sandstone saturated with $CaCl_2$ (-7.0 ± 0.3 mV; *Li et al.,* 2018) and Portland limestone saturated with NaCl (-8.0 ± 0.5 mV; *Al Mahrouqi et al.,* 2017).

Hence, with all these comparisons, we argue that the zeta potentials of the gneiss sample are unique. Our zeta potential results show a different response to increasing ionic strength and

complex water compositions of the tested solution. These results also suggest that the mineralogy of the gneiss sample responds to the presence of divalent ions (Ca^{2+}, Mg^{2+} and SO_4^{2-}). Therefore, in this rock type, the divalent ions of Ca^{2+}, Mg^{2+} and SO_4^{2-} are considered as PDIs similar to carbonates (*Al Mahrouqi et al.,* 2017), feldspars (*Demir et al.,* 2003) and micas (*Adamczyk et al.,* 2010).

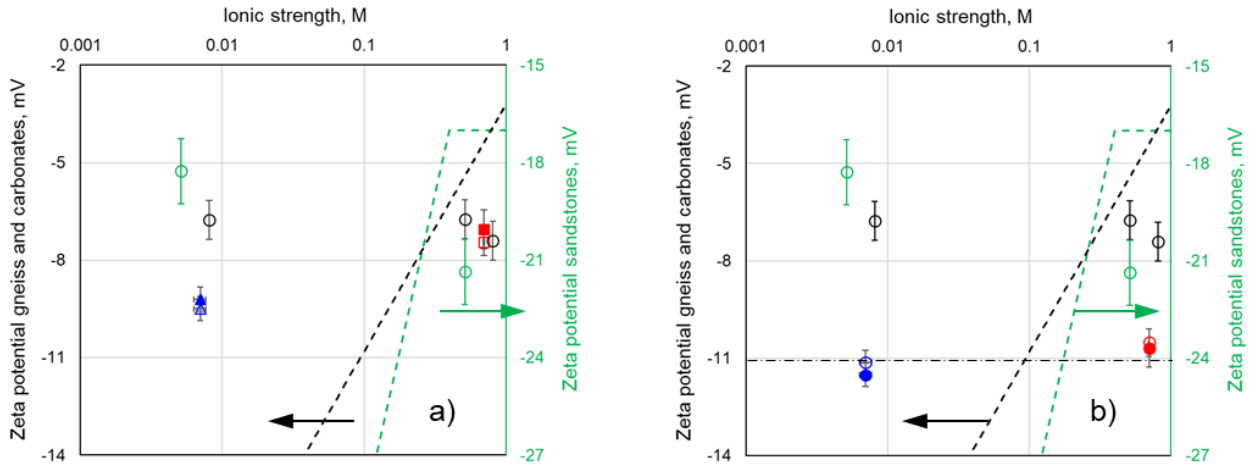

Figure 6.3. Impact of ionic strength on the zeta potential measured on Lewisian gneiss sample saturated with a) AGW and ASW, and b) with NaCl solutions. For comparison, empirical linear regressions for clean sandstones (>95% quartz; *Vinogradov et al.,* 2010) and carbonates saturated with equilibrated NaCl solutions (*Al Mahrouqi et al.,* 2017) are shown in green and black dashed lines, respectively. Filled symbols correspond to the confining pressure of 7 MPa. Green circles represent zeta potentials measured in Berea sandstone saturated with NaCl solutions and averaged over 7 samples (right vertical axis); the black circles correspond to results obtained with Berea sandstones saturated with $CaCl_2$ solutions and averaged over 6 samples (*Li et al.,* 2018). Error bars represent the experimental uncertainty obtained from the variation in the slope of the linear regression of C_{SP}.

6.3.4. Effect of confining pressure

We begin by presenting the zeta potential result for two different confining pressure in the gneiss sample (**Figure 6.4**). The interpreted zeta potentials of the gneiss sample were independent of confining pressures. On the contrary, an increasing confining pressure in the fractured rock sample decreased the apparent permeability from 51 mD at 4 MPa to 43 mD at 7 MPa. This result indicates that the fracture aperture decreases with increasing confining pressure and thus, leads to a potential effect of increasing surface electrical conductivity.

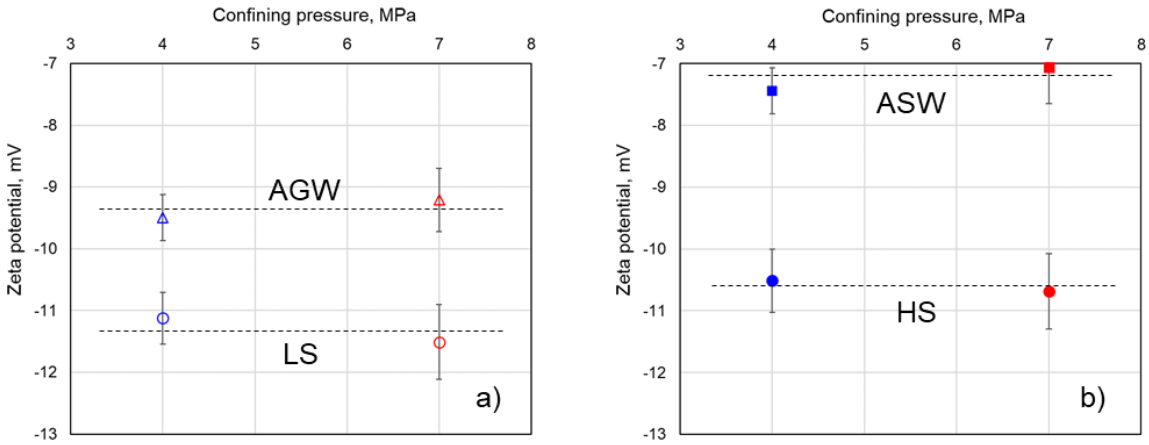

Figure 6.4. Impact of the confining pressure on the zeta potentials measured on Lewisian gneiss sample saturated with aqueous solutions of 0.007 M (a) and 0.7 M (b) ionic strength. Error bars represent the experimental uncertainty obtained from the variation in the slope of the linear regression of C_{SP}.

In order to quantify the effect of the confining pressure on the measured streaming potential, zeta potential and facture aperture, a simple geometry of fractured rock is presented in **Figure 6.5**.

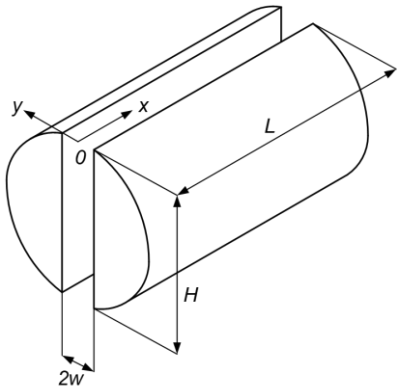

Figure 6.5. The tested fractured rock sample is assumed to have a single fracture of aperture 2w, height H and length L.

As we implemented a PS method during the streaming potential measurements, the condition of one-directional flow with steady state condition was considered. Further, the flow through the facture was consistent with the direction of the rock sample. Hence, for the geometry described in **Figure 6.5** combined with experimental conditions, the Navier Stokes equations are simplified into 1-D flow in the Cartesian coordinate system as follows:

$$\mu \frac{d^2 v_x}{dy^2} = \frac{\Delta P}{L}, \qquad 6.2$$

where $v_x(y)$ is the fluid velocity in *x*-direction inside the fracture. Considering the no-slip boundary conditions at both fracture walls, the fluid velocity profile is given by:

$$V_x = \frac{1}{2\mu}\frac{\Delta P}{L}(y^2 - w^2). \quad 6.3$$

Multiplying **Equation 6.3** by the cross-section area to the flow, $2wH$, and integrating across the fracture aperture (between -*w* and +*w*) yields the well-known cubic law (Neuzil and Tracy, 1981) for the total volumetric flow rate, Q:

$$Q = -\frac{2Hw^3}{3\mu}\frac{\Delta P}{L}. \quad 6.4$$

Now, equating the flow rate given by **Equation 6.4** with that from Darcy's law, $Q = -\frac{2kHw}{\mu}\frac{\Delta P}{L}$, the effective permeability is expressed as:

$$k = \frac{w^2}{3}. \quad 6.5$$

Equation 6.5 is consistent with a recently published study (*Thanh et al.,* 2021) in the limit of a single fracture, and it implies that for a decrease of approximately 16% in sample's permeability (from 51 mD to 43 mD), the corresponding expected decrease in fracture aperture (2*w*) will be around 8% (from 0.782 μm at 4 MPa to 0.718 μm at 7 MPa). Decreasing fracture aperture implies a smaller distance of separation between the fracture walls, and as such higher confining pressure can potentially have an impact on the electrical properties of hydraulically active fractures via increased impact of the surface electrical conductivity and the zeta potential.

To investigate the impact of fracture aperture on the electrokinetic properties of the sample, we consider the streaming current under the steady state experimental conditions and for geometry described in **Figure 6.5**:

$$I_s = 2\int_0^w \Sigma(y)v_x(y)Hdy, \quad 6.6$$

where Σ [C/m^3] is the volumetric charge density. The flow of mobile excess counter-ions that contribute to the streaming current is confined to the diffuse part of the electrical double layer (EDL), which has a thickness of approximately 3 nm for 7.35 × 10^{-3} M and even smaller thickness for higher salinity, so that the thickest expected EDL will still be two orders of magnitude smaller than the estimated fracture aperture. Therefore, we can use this condition

to linearize the flow velocity that contributes to the streaming current in the region adjacent to the fracture walls, where $y \approx w$:

$$QV_x = \frac{1}{2\mu}\frac{\Delta P}{L}(y^2 - w^2) \approx \frac{1}{2\mu}\frac{\Delta P}{L}2w(y - w). \quad 6.7$$

Introducing a new variable $\theta = y - w$, using Poisson equation for the charge density, $\Sigma = -\varepsilon\frac{d^2V}{dy^2}$ (where V is the electric potential and ε is the permittivity of the aqueous solution), substituting **Equation 6.7** into **Equation 6.6**, and integrating by parts yields an expression for the streaming current through the fracture:

$$I_s = -\frac{2wH\varepsilon\zeta}{\mu}\frac{\Delta P}{L}, \quad 6.8$$

where ζ is the zeta potential at $y = \pm w$. We now apply the boundary conditions of zero net current coming in or out of the fracture, and no charge separation along the fracture. In such case, the streaming current must be balanced by the conduction current of equal magnitude and opposite direction. The conduction current is given by Ohm's law:

$$I_c = 2wH\sigma_w\frac{\Delta V}{L} + 2H\sigma_s\frac{\Delta V}{L} = 2wH\frac{\Delta V}{L}\left[\sigma_b + \frac{\sigma_s}{w}\right], \quad 6.9$$

where ΔV is the electric potential difference (voltage) across the fracture, σ_w [S·m^{-1}] is the electrical conductivity of the bulk aqueous solution, and σ_s [S] is the surface electrical conductivity due to the presence of EDL. Using the condition of electro-neutrality, $I_s = -I_c$, the streaming potential coupling coefficient can be expressed:

$$C_{SP} = \frac{\Delta V}{\Delta P} = \frac{\varepsilon\zeta}{\mu\left[\sigma_w + \frac{\sigma_s}{w}\right]}. \quad 6.10$$

Note, that **Equation 6.10** explicitly expresses the effective electrical conductivity of brine with the contribution of the surface conductivity but becomes equal to the classical Helmholtz-Smoluchowski equation (**Equation 6.1**) when the surface conductivity is negligibly small. The zeta potential can now be expressed from the measured streaming potential coupling coefficient as:

$$\zeta = \frac{C_{SP}\mu\left[\sigma_w + \frac{\sigma_s}{w}\right]}{\varepsilon}. \quad 6.11$$

For the two tested ionic strengths of 7.35 × 10^{-3} M and 0.7 M, the permittivity and viscosity of the NaCl solutions can be calculated using the approach described in *Saunders et al.* (2012), while C_{SP} and the electrical conductivity of the solutions were directly measured during the experiments. Rock, fluid and electrokinetic properties for all our NaCl experiments are summarized in **Table 6.4** along with estimates of fracture aperture made using **Equation 6.5**.

Table 6.4. Rock, fluid and electrokinetic properties of NaCl experiments at 7.35 × 10^{-3} M (LS) and 0.7 M (HS) ionic strengths. The confining pressure is denoted by P in the table and k is the measured absolute permeability. The fracture aperture (2w) is interpreted using **Equation 6.5**.

ID	P, MPa	μ, Pa·s	ε, F·m^{-1}	C_{SP}, mV·MPa^{-1}	ζ, mV	k, mD	2w, nm
LS	4	9.33 × 10^{-4}	7.00 × 10^{-10}	-86.4	-11.12	51 ± 1	782
LS	7	9.33 × 10^{-4}	7.00 × 10^{-10}	-89.5	-11.51	43 ± 1	718
HS	4	9.89 × 10^{-4}	6.97 × 10^{-10}	-1.21	-10.52	51 ± 1	782
HS	7	9.89 × 10^{-4}	6.97 × 10^{-10}	-1.23	-10.69	43 ± 1	718

The estimated fracture aperture using the measured permeability of the rock sample is consistent with the values reported for artificially fractured granite sample (*Luo et al.,* 2017). The authors reported the hydraulic aperture of order of 200 μm, which is three orders of magnitude larger than the values estimated for our sample using **Equation 6.5**. However, the values of hydraulic conductivity of 13 cm/s measured by *Luo et al.* (2017), which translates into the permeability of c. 13 × 10^6 mD, is identical to that predicted by **Equation 6.5**, thus validating our approach and estimates.

In order to evaluate the effect of surface electrical conductivity on the interpreted zeta potential, a model published by *Leroy et al.* (2013) in silica-NaCl system was used. Although the model published by *Leroy et al.* (2013) is for silica-NaCl system, to the best of our knowledge, there are no available models for gneiss, or comprising it feldspars and micas. Hence, the only available model that closely replicated our system (note, that gneiss contains 35 wt% of quartz) was the model published by *Leroy et al.* (2013).

The estimated surface conductivity (σ_s) for 7.35 × 10^{-3} M and 0.7M solutions was 3.0 × 10^{-9} S and 4.5 × 10^{-9} S, respectively. Then, the dimensionless Dukhin number (Du) was used to evaluate the surface conductivity for our fracture geometry sample (**Figure 6.5**) and it can be expressed as (*Bocquet and Charlaix*, 2010):

$$Du = \frac{\sigma_s}{w\sigma_w}, \qquad 6.12$$

where w is obtained from the estimated fracture aperture using **Equation 6.5** and σ_w is measured solution conductivity (see **Table 6.2**). The calculated value Du for 7.35 × 10^{-3} M and 0.7M solutions for confining pressure of 4 MPa is 7.9 × 10^{-2} and 1.9 × 10^{-3}, respectively. Further, the calculated result for confining pressure of 7 MPa is 8.6 × 10^{-2} for 7.35 × 10^{-3} M and 2.0 × 10^{-3} for 0.7M. From all the estimated value of Du, where Du << 1.0, explains that the effect of surface conductivity is very small compared to solution conductive and thus, the zeta potential. Therefore, for all tested solutions, the surface conductivity is found to be negligible, and a classical HS equation (**Equation 6.1**) is suitable to interpreted zeta potential from the measured streaming potential coefficient. These results also imply that the estimated fracture aperture of gneiss sample (781 nm for 4.0 MPa and 718 nm for 7.0 MPa) is not small enough to influence the surface electrical conductivity.

6.3.5. Implication for subsurface fractured rock system

In this chapter, the initial analysis of relationship between fracture aperture, zeta potential and overburden pressure are provided.

To evaluate the depths at which surface conductivity of gneiss sample can no longer be neglected, a study by *Luo et al.* (2017) that reported a near-linear correlation between the confining pressure and the hydraulic aperture of artificially fractured granite sample is considered. Thus, using estimates of the surface conductivity value for low salinity solutions (3.0 × 10^{-9} S; see **Table 6.4** for solution conductivity of low salinity), we were able to evaluate the confining pressure and the corresponding depth, at which the surface conductivity becomes significant, satisfying the condition of $Du \approx 0.1$. The aperture that satisfies $Du = 0.1$ was calculated to be 310 nm using **Equation 6.12**, and the corresponding confining pressure was found to be 3.8 MPa, corresponding to a depth of 380 m.

The results from this chapter are useful for characterising the wettability of subsurface geological formations (CGS applications), monitoring subsurface flows (in aquifers, hydrocarbons and geothermal) and assessing hydraulically active fractures (geothermal or aquifers). In addition, this chapter demonstrates that a care should be taken when converting zeta potentials measured in the laboratory on gneiss sample from coupling coefficients that are used in the models.

Since measurements of the zeta potential in fractured rock systems are scarce, this study provides essential novel insights into impact of fracture aperture on the zeta potential, which are essential for interpreting rock wettability or for monitoring flows through fracture networks using self-potential. However, the impact of surface roughness on the zeta potential, especially at fractured rocks remains unclear. Hence, additional experimental investigations are needed to expand the parameters including surface roughness, various confining pressures, different

fractured rock samples (e.g., fractured carbonate), and elevated temperature to see their responses to zeta potential.

6.4. Conclusions

We successfully conducted the measurements of zeta potential in a fractured gneiss sample saturated with NaCl, AGW and ASW for different ionic strength and chemical compositions at confining pressures of 4.0 MPa and 7.0 MPa. The interpreted zeta potential suggests that:

- Zeta potentials of gneiss are unique and dissimilar to sandstones, carbonates, and gneiss individual constitutive minerals i.e., mica and feldspar.
- The negative zeta potential decreases with increasing salinity when the sample is saturated with AGW and ASW, but the rate of the decrease is smaller compared to any other mineral.
- The negative zeta potential is independent of salinity when using NaCl; this feature is similar to what was observed with clayey sandstone (*Li et al.,* 2018), and we hypothesize that this observation is a result of cation exchange in our experiment. However, the zeta potential of gneiss was found to be more positive compared with clayey sandstones saturated with NaCl.
- Significant amount of feldspars and mica present in our gneiss sample were found to be responsible to high sensitivity of the sample to presence of divalent ions (Ca^{2+}, Mg^{2+} and SO_4^{2-}) compared with quartz. Therefore, these ions were identified as PDIs for gneiss making the sample to respond to compositional and concentration variation in a fashion similar to that of carbonate samples.
- The measured C_{SP} of gneiss sample was independent of confining pressure. This result implied that the surface electrical conductivity could be neglected to interpret zeta potential.
- A simple fracture model was developed to estimate the fracture aperture at which surface electrical conductivity could not be negligible. Hence, at such conditions, **Equation 6.11** must be used to evaluate the zeta potential.

The findings from this study have a significant implication of wettability characterisation at subsurface fractured rock system in CGS application (preventing CO_2 leakage), as well as in miscible CO_2-EOR (extracting more oil). For example, the zeta potential obtained from this study can be used for further numerical modelling in DLVO theory to determine the wetting film stability, which is essential parameter for CO_2 trapping mechanism and miscible CO_2-EOR application

Chapter 7 Predictive surface complexation model of the calcite-aqueous solution interface: the impact of high concentration and complex composition of brines*

*) *The text for this chapter was originally prepared for publication and it was accepted during the registration period of my study in Journal of Colloid and Interface Science. The final version of the published paper can be seen at* https://doi.org/10.1016/j.jcis.2021.11.084.

7.1. Introduction

Calcite is a very common mineral on the Earth's surface comprising approximately 4% by weight of Earth's crust. Physico-chemical processes that take place in porous calcite-aqueous solution (water for simplicity) systems are of great importance for a variety of scientific and technological areas. Properties of the calcite mineral surface and the interface between calcite and aqueous solution are important for a broad range of applications including geological storage of nuclear waste and CO_2 (*Harrison and Hester,* 2010), freshwater aquifer management (*Graham et al.,* 2018; *MacAllister et al., 2018*), hydrocarbon production (*Saunders et al.,* 2012), paper production (*Carrasco et al.,* 1998). However, electrochemical properties of the interfaces between calcite and aqueous solutions (specifically, electrical surface charge and zeta potential), especially under conditions relevant to natural subsurface systems (i.e., water chemical composition, temperature, pressure) remain poorly understood because of their microscopic nature, the high reactivity of the calcite mineral, and the lack of relevant measurements and models (*Heberling et al.,* 2014).

The zeta potential is defined as the electrical potential at the shear plane when water flow occurs parallel to the pore surface (*Hunter,* 1981). It is most commonly used to estimate the electrochemical properties of calcite because acid-base potentiometric titration, usually employed to measure the surface charge of minerals, is extremely difficult to carry out for highly reactive calcite (*Eriksson et al.,* 2007). There are many studies that have reported measurement of the zeta potential of various calcite-water systems. However, many reported results are contradictory (see for example Fig. 3 in *Jackson et al.,* 2012b). Most of the experimental studies have reported zeta potential measured with low salinity single-salt solutions (e.g., *Heberling et al.,* 2011; *Li et al.,* 2016), and there is inconsistency in the experimental conditions when some experiments were conducted at equilibrium between the mineral and water while others reported the zeta potential with non-equilibrium solutions (see for example discussion in Section 3 and 4 *Al Mahrouqi et al.,* 2017). The experimental studies have also employed a variety of electrokinetic methods including the electrophoretic mobility (EPM; *Foxall et al.,* 1979) and streaming potential method (SPM; *Thompson and Pownall,* 1989). Each of these experimental techniques suffers from several limitations (*Delgado et al.,* 2007). The EPM applies an electrical field (of magnitude hundred Volts per meter) that

mobilizes charged particles relative to aqueous solution and measuring the resulting mobility. The EPM is conducted on powdered calcite samples suspended in aqueous solution thus potentially exposing fresh mineral surfaces. Moreover, the method is usually limited to solution concentration below 1 M (*Kosmulski and Dahlsten*, 2006). The ratio of the mineral to the solution is also very low (typically few grams per liter) and not representative of real rocks. On the other hand, the SPM applies a pressure difference across the sample and measures a resulting voltage, it can be carried out under equilibrium conditions, on intact rock samples at salinities up to full saturation (e.g., *Cherubini et al.,* 2018, 2019). However, unlike the EPM method, SPM can be time consuming and very challenging for highly reactive minerals such as calcite in highly saline conditions thus limiting its ability to cover a wide range of rock-solution permutations (see for example typical duration of both the equilibration process and individual SPM experiment, as well as the voltage stability issues at high salinity reported in *Alroudhan et al.* (2016). Moreover, the zeta potential values obtained with SPM can be specific to rock type as different carbonate samples may contain different impurities such as anhydrite and dolomite (e.g., *Al Mahrouqi et al.,* 2017).

A model capable of predicting the zeta potential of calcite-water systems at equilibrium as well as non-equilibrium conditions, low to high salinity, and complex solution composition is crucially important. Such model will not only be capable of predicting the zeta potential, but also improve our understanding of the complex electrochemical processes that take place at calcite-water interface. To date, there have been numerous attempts to develop such model with most of published studies using the so-called surface complexation modelling (SCM) approach (e.g., *Heberling et al.,* 2011, 2014; *Li et al.,* 2016). In this method the calcite surface is presented as an ensemble of chemically active surface sites that interact with ions from the adjacent bulk electrolyte. The strength of these interactions is described by the equilibrium constants (similar to chemical reactions), so that the resulting equilibrium concentration of positive and negative surface complexes establishes the net surface charge and the corresponding surface potential (*Davis et al.,* 1978). Depending on the complexity of the aqueous solution, such models can be realized analytically (e.g., *Revill et al.,* 1999) or by using numerical methods already available in software packages such as PHREEQC (e.g., *Parkhurst and Appelo,* 2013).

Studies published to date on SCM have used different approaches to model the zeta potential (**Figure 7.1**): Basic Stern Model (BSM, e.g., *Heberling et al.,* 2011), Triple Layer Model (TLM, e.g., *Wolthers et al.,* 2008), Quad-Layer Model (QLM, e.g., *Alizadeh and Wang,* 2019) and Diffuse Layer Model (DLM, e.g., *Ding and Rahman,* 2018). BSM, TLM and QLM explicitly describe the Stern layer and a layered arrangement of ionic species adsorbed on the mineral surface in the diffuse layer. Both the TLM and QLM distinguish between the Inner Helmholtz

plane (IHP) and the Outer Helmholtz plane (OHP), at which adsorption of de-hydrated and hydrated ions, respectively, takes place (*Wolthers et al.,* 2008). On the other hand, BSM for calcite assumes that adsorption of all ions in compact layer takes place at the OHP (e.g., *Heberling et al.,* 2011, 2014; *Li et al.,* 2016). All three models that explicitly describe the adsorption layers (i.e., BSM, TLM, QLM) also assume that only protonation/deprotonation of hydrated calcite lattice ions take place at the mineral surface. In these models, the surface charge densities are computed at each plane, from which linear, capacitor-like variation of the electric potential between the planes is obtained. Consequently, TLM and QLM simulate separately protonation/deprotonation and salt ion adsorption reactions at three different planes (mineral surface, IHP, OHP), and ascribe two capacitance values to layers confined between the mineral surface and IHP, and between IHP and OHP. In addition, the QLM considers a stagnant diffuse layer, implying that the shear plane is located further away from the OHP. This makes these two models more computationally expensive compared with BSM, which uses only one capacitance and all adsorption reactions are considered to take place at OHP for calcite.

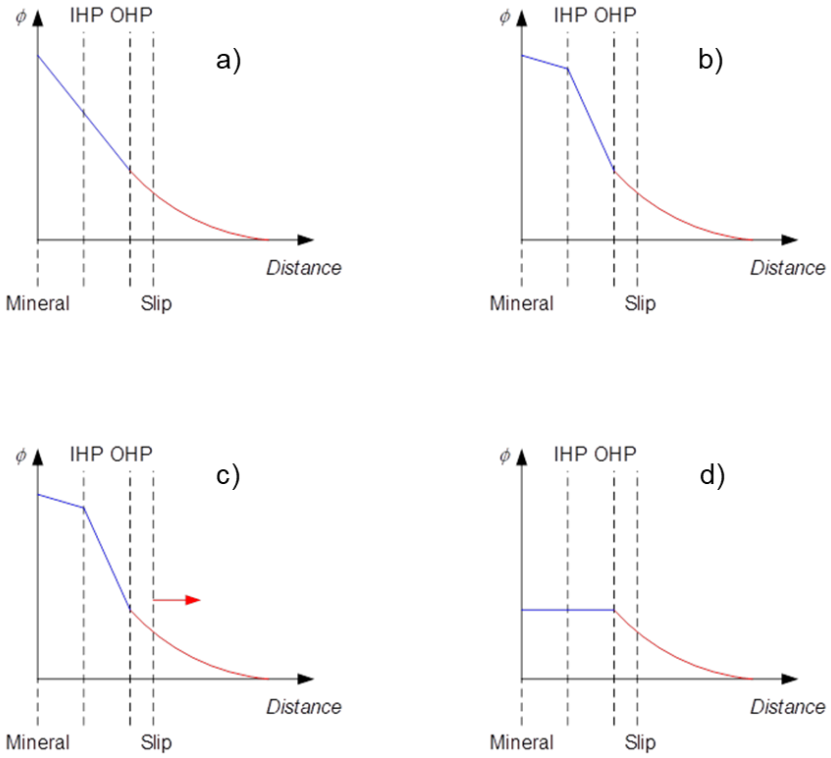

Figure 7.1. Electric potential distribution at the calcite-water interface: a) – BSM (no distinction between IHP and OHP, the slip plane may or may not coincide with OHP); b) – TLM (IHP and OHP are considered separately with different surface complexation reactions taking place at each plane, the slip plane coincides with OHP); c) – QLM (IHP and OHP are considered separately with different surface complexation reactions taking place at each plane, the slip plane does not coincide with OHP and its distance from OHP can be constant or varying with salinity); d) – DLM (IHP and OHP are not considered at all as if there is no separation between the mineral surface and OHP, the slip plane may or may not coincide with mineral/OHP).

On the other hand, DLM assumes that both the protonation/deprotonation and salt ion adsorption reactions take place at the mineral surface thus ignoring the complexity of the Stern layer that comprises the IHP and OHP. Hence, compared to the BSM, TLM, and QLM, the DLM is not sensitive to the capacitance values and is only sensitive to the location of the so-called shear (or slip) plane at which ions can be mobilized by the flow and at which the electric potential is defined as the zeta potential. According to the generally agreed theory of the electrical double layer, concentrations of counter-ions that populate the region beyond the OHP (in the diffuse layer) obey the Boltzmann distribution law where they decrease exponentially towards concentrations of ions in electroneutral bulk electrolyte (outside the diffuse layer). The location of the slip plane is uncertain and is usually used as a fitting parameter to match the model predictions to experimental data (*Heberling et al.,* 2011). The assumed location of the slip plane can also be used in BSM, TLM and QLM as additional fitting parameter, but in contrast with DLM the modelled zeta potential using these models depends on adjustable capacitance values and therefore, the location of the slip plane can be kept constant for matching different experimental datasets. The QLM published by *Alizadeh and Wang* (2019) assumed that the slip plane was dynamic and moved further away from the mineral surface as the ionic strength of the bulk electrolyte decreased. Although the dynamic slip plane model successfully reproduced experimental results, the hypothesis was not clearly justified by the authors or confirmed experimentally.

However, despite the plethora of published SCM studies, all of the simulated results appear to be specific to an experimental dataset. Heberling and co-authors (*Heberling et al.,* 2011, 2014) used fractional charges of individual surface site, the approach that was consistent with that taken by *Wolthers et al.* (2008), who used the Charge Distribution MUltiSite Ion Complexation or CD–MUSIC modeling approach. However, the magnitude of the surface site charges was different. On the other hand, *Van Cappellen et al.* (1993) used integer surface site charges in their BSM. Furthermore, *Heberling et al.* (2011, 2014) used equilibrium constants for adsorption reactions at OHP limited by ion-binding ones that corresponded to pairing of ions in the bulk electrolyte. In contrast, *Pokrovsky and Schott* (2002) estimated their equilibrium constants for adsorption reactions from the correlation between stability of surface sites and stability of the same molecules in the solution. As a result, the equilibrium constants used by *Pokrovsky and Schott* (2002) in their BSM exceeded by several orders of magnitude those used by *Heberling et al.* (2011, 2014) in their BSM. Considering the equilibrium constants of protonation/deprotonation reactions that take place at the mineral surface, a significant variation in their values was also evident across different studies. For instance, *Heberling et al.* (2011) used five-fold larger equilibrium constant for deprotonation of hydrated Ca site compared with their later study (*Heberling et al.,* 2014). At the same time, *Wolthers et*

al. (2008) used twelve orders of magnitude larger equilibrium constant for the same reaction compared with *Heberling et al.* (2011).

Previously published studies that used either BSM or TLM relied on constant Stern layer capacitance, but the reported values used in these studies varied between 0.45 $F \cdot m^{-2}$ (*Heberling et al.,* 2014), 1.24 $F \cdot m^{-2}$ (*Li et al.,* 2016), 17 $F \cdot m^{-2}$ (*Pokrovsky and Schott,* 2002), 52 $F \cdot m^{-2}$ (*Pokrovsky et al.,* 2000) and 100 $F \cdot m^{-2}$ (*Wolthers et al.,* 2008). Therefore, the inconsistency in these values suggests a high degree of freedom and unconstrained variation of simulated zeta potential. Moreover, most of the published SCM simulated the zeta potential of calcite in contact with low salinity (typically less than 0.1 M) single salt solutions (e.g., NaCl) therefore ignoring the effect of divalent ions such as Mg^{2+} and SO_4^{2-} and high ionic strength. Studies that included such reactions reported inconsistent equilibrium constants, with *Heberling et al.,* (2014) predicting adsorption of Ca^{2+} on negative surface sites to be controlled by an equilibrium constant ten orders of magnitude smaller compared with the equilibrium constant calculated from two consecutive reactions described by *Pokrovsky et al.* (2000) and *Pokrovsky and Schott* (2001). All in all, a unique combination of adsorption reactions, their equilibrium constants, capacitance values and charges of the surface sites used in published studies appear to be very specific to the modelled experimental datasets, thus limiting the use of each model for a very narrow range of ionic strength, pH and composition of electrolytes in contact with the calcite mineral.

Therefore, the aim of this study is to develop and validate a new SCM that accurately computes the zeta potential of any calcite-water system as long as the experimental conditions are reproduced in the model. The developed model has proven to be accurate in simulating and predicting zeta potentials at both equilibrium and non-equilibrium conditions, high to low salinity, for any carbonate rock type as long as the dominating mineral is calcite, and for any solution composition as long as the dominating salt is NaCl and concentration of SO_4^{2-} does not exceed that of Ca^{2+} and Mg^{2+}.

7.2. Methodology

To develop a robust predictive model requires detailed description of experimental parameters and conditions. Therefore, we have chosen the data reported by *Al Mahrouqi et al.* (2017) as the most comprehensive experimental work and will briefly describe the experimental conditions and main conclusions.

7.2.1. Description of the experimental data on zeta potential in intact limestone samples

Streaming potential measurements were performed by *Al Mahrouqi et al.* (2017) and *Alroudhan et al.* (2016) on three different carbonate rock samples: Estaillades (*Al Mahrouqi et*

al., 2017), Ketton (*Al Mahrouqi et al.,* 2017) and Portland (*Alroudhan et al.,* 2016). The petrophysical and mineralogical properties of the rock samples are shown in **Table 1**.

Table 7.1. Petrophysical and mineralogical properties of three different carbonate rock samples. Ketton and Estaillades were used in the experiments of by *Al Mahrouqi et al.* (2017), Portland was used by *Alroudhan et al.* (2016).

Property/rock	Ketton	Estaillades	Portland
Porosity (%)	23.0 ± 0.5	28.0 ± 0.5	20.0 ± 0.5
Permeability (Darcy)	1.4 ± 0.4	0.13 ± 0.2	0.005 ± 0.001
Formation factor (F)	13.87 ± 0.5	12.92 ± 0.5	22.04 ± 0.5
Composition (%)	97[a] – calcite	97[a] (95[b]) – calcite	96.6[a] – calcite
	3[a] magnesium	3[a] (4[b]) – magnesium	3.4[a] – quartz
		(1[b]) – anhydrite	

a – mineralogy reported by *Al Mahrouqi et al.,* (2017) using X-ray diffraction (XRD). Magnesium was reported to be likely incorporated into the limestone as dolomite.

b – recent study by *Udoh and Vinogradov*, (2021), identified and confirmed that there was 4% dolomite ($CaMg(CO_3)_2$) and 1% anhydrite ($CaSO_4$) in the Estaillades sample using XRD.

The zeta potential measurements were conducted at room temperature (23^{o}C) with NaCl solutions of varying concentration between 0.05 M (mol/L) and 5.0 M NaCl at equilibrium conditions. Effluent fluid samples were regularly collected for chemical analyses to determine the concentration of Na^+, Ca^{2+}, Mg^{2+}, Cl^-, and SO_4^{2-}. The experimentally confirmed presence of Ca^{2+}, Mg^{2+}, and SO_4^{2-} was explained by partial dissolution of rock samples during the equilibration with NaCl solutions and leaching of these ions.

These studies concluded that the zeta potential of carbonate rock samples was controlled by the concentration of the potential determining ions (PDIs), which were identified to be Ca^{2+}, Mg^{2+}, and SO_4^{2-}.

7.2.2. Calcite surface complexation model development

7.2.2.1 Basic definitions and assumptions

A BSM was used in this study to model the zeta potential of pure calcite in contact with aqueous solutions. The modelling approach was consistent with the most comprehensive and empirically justified model developed by *Heberling et al.* (2011, 2014). Since the content of calcite in all three tested carbonate rock samples (Estaillades, Ketton, Portland) was found to be greater than 95%, it was assumed that calcite was the most dominant mineral in the samples so that only calcite surface sites were considered in the model.

The measured zeta potential with all tested carbonate rocks reflected presence of minerals other than calcite (e.g., dolomite and anhydrite), which led to a non-zero concentration of Mg^{2+} and SO_4^{2-} found in the bulk solution as a result of mineral dissolution during the equilibration process. Therefore, we artificially added the equilibrium concentration of Mg^{2+} and SO_4^{2-} measured in the experiment to our geochemical model of pure calcite. The amount of Ca^{2+} leached into NaCl solutions during the equilibration was either added artificially to the model and equilibration was switched off, or it was not added to the initial solution while the equilibration was activated (see Section 7.2.3 for details).

Consistent with *Heberling et al.* (2011, 2014), calcite (1 0 4) face was assumed to dominate the interface due to its high abundance and the total surface site density of calcium and carbonate surface sites on the calcite (1 0 4) face was set to 4.95 sites per nm^2 for each type of site. However, unlike *Heberling et al.* (2014), this study assumed that the zeta potential could be calculated by considering the shear plane coinciding with the OHP (see **Figure 7.2**), i.e., $\phi_\beta = \phi_d = \zeta$ – the assumption that was also used by *Li et al.* (2016) (no stagnant diffuse layer). *Li et al.,* (2016) considered that the assumption of the presence of a stagnant diffuse layer in *Heberling et al.* (2011) was due to the nature of electrokinetic measurements that were not corrected for surface conductivity effects thus reducing the experimental zeta potentials and then necessitating smaller modelled zeta potentials to be further away from the mineral surface, to match the data.

The 0-plane was defined as the hydrolysis layer located 2.3 Å from the calcite surface defined by the surface of calcium ions, at which only protonation/deprotonation of surface sites took place (*Heberling et al.,* 2014). The surface charge at 0-plane was found to be negative regardless of the concentration and composition of the adjacent solution and pH range of 5-11 tested in our study, similar to the results reported by *Heberling et al.* (2014). On the other hand, the ***β***-plane was set at a distance of 4.6 Å from the surface (*Heberling et al.,* 2014), and we assumed that all the specific adsorption reactions between the surface sites and salt ions from the bulk electrolyte only occurred at the OHP where ions are adsorbed as outer-sphere complexes.

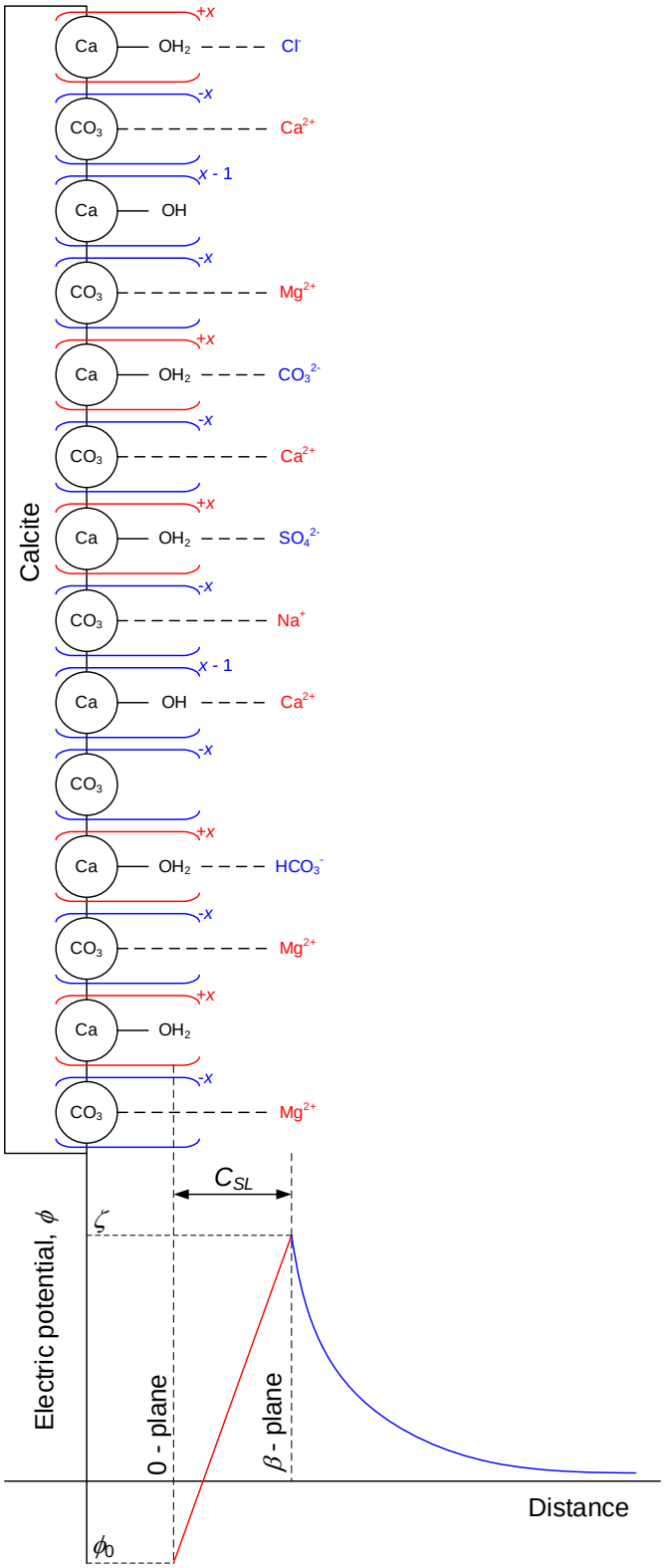

Figure 7.2. Illustration of the Basic Stern Model used in this study. The 0-plane corresponds to the mineral surface where only protonation/deprotonation reactions take place. We used fractional surface charge x = 0.5 for all surface sites. The Stern Layer is confined between the 0-plane and β-plane, with the latter corresponding to the OHP where all adsorption reactions take place and where the zeta potential (ζ) is defined. C_{SL} is the Stern layer capacitance.

7.2.2.2. Adsorption reactions and equilibrium constants

All modelled adsorption reactions between calcite surface sites and ions are listed in **Table 7.2**. The original set of adsorption reactions proposed by *Heberling et al.* (2011, 2014) and *Li et al.,* (2016) was extended to include the reactions between the surface sites and Mg^{2+} and SO_4^{2-} (R9 – R11 in **Table 7.2**). The equilibrium constant of R1 that corresponds to deprotonation of hydrated calcium surface sites was fixed to the value of LogK_1 = -0.5 to yield the relative abundance of positive and negative surface complexes at 0-plane according to *Heberling et al.* (2014).

Among published studies on SCM of calcite, there is no consensus on whether protonation of $> CO_3^{-0.5}$ surface sites on 0-plane should be considered. Some of these studies included the reaction $> CO_3^{-0.5} + H^+ \Leftrightarrow > CO_3H^{+0.5}$ (e.g., *Pokrovsky and Schott,* 2002; *Wolthers et al.,* 2008; *Heberling et al.,* 2011) while other studies (e.g., *Heberling et al.,* 2014; *Li et al.,* 2016) disregarded it. We could not find any published justification for inclusion of $> CO_3^{-0.5}$ protonation based on the experimental data or theoretical analysis. However, there have been several publications in support of excluding the protonation of the $> CO_3^{-0.5}$ surface sites. One theoretical study on hydration of (1 0 4) calcite surface (*Villegas-Jiménez et al.,* 2009) demonstrated that neutral H_2O molecules preferentially 'chemisorbed' into $> Ca^{+0.5}$ to form $> CaOH_2^{+0.5}$ site, and existence of $> CO_3H^{+0.5}$ surface sites was attributed to hydration of carbonate surface groups ($> CO_3OH_2^{-0.5}$) but not direct protonation of the $> CO_3^{-0.5}$ sites. Therefore, in the absence of $> CO_3OH_2^{-0.5}$ there could be no $> CO_3H^{+0.5}$ sites resulting from subsequent dissociation of water molecules $> CO_3OH_2^{-0.5} \Leftrightarrow > CO_3H^{+0.5} + OH^-$. These conclusions were supported by a variety of experimental measurements reported in the paper. Another numerical study (*Kurganskaya and Churakov,* 2018) also predicted low fraction of protonated $> CO_3H^{+0.5}$ sites (<20%) on a variety of calcite mineral geometries for pH between 5 and 11, which is consistent with pH values tested with our model. For pH greater than 7, the fraction of protonated carbonate sites decreased to below 5% according to this study. Moreover, inclusion of the $> CO_3^{-0.5}$ surface site protonation would result in increased pH under simulated equilibrium conditions, thus mismatching the experimentally measured values. Effect of $> CO_3^{-0.5}$ protonation on equilibrium pH will be discussed in more detail in Section 7.3. For these reasons and following *Heberling et al.* (2014) we did not consider hydration of carbonate surface sites in our model.

Table 7.2. Adsorption reactions and their equilibrium constants. Equilibrium constant for R1 was not optimised.

No	Reactions	LogK^{min}	LogK^{max}	LogK^{opt}
	0–plane reactions			
R1	$> \mathrm{CaOH_2^{+0.5}} \Leftrightarrow > \mathrm{CaOH^{-0.5}} + \mathrm{H^+}$	-0.5	-0.5	-0.5
	β–plane reactions			
R2	$> \mathrm{CaOH^{-0.5}} + \mathrm{Na^+} \Leftrightarrow > \mathrm{CaOH^{-0.5}} - \mathrm{Na^+}$	0.09[a]	0.56[b]	0.56
R3	$> \mathrm{CaOH_2^{+0.5}} + \mathrm{Cl^-} \Leftrightarrow > \mathrm{CaOH_2^{+0.5}} - \mathrm{Cl^-}$	-2.10[c]	0.45[d]	-0.64
R4	$> \mathrm{CaOH^{-0.5}} + \mathrm{Ca^{2+}} \Leftrightarrow > \mathrm{CaOH^{-0.5}} - \mathrm{Ca^{2+}}$	1.68[b]	3.40[e]	3.40
R5	$> \mathrm{CaOH_2^{+0.5}} + \mathrm{HCO_3^-} \Leftrightarrow > \mathrm{CaOH_2^{+0.5}} - \mathrm{HCO_3^-}$	0.04[b]	12.50[f]	10.65
R6	$> \mathrm{CaOH_2^{+0.5}} + \mathrm{CO_3^{2-}} \Leftrightarrow > \mathrm{CaOH_2^{+0.5}} - \mathrm{CO_3^{2-}}$	-7.07[b]	6.00[g]	-4.59
R7	$> \mathrm{CO_3^{-0.5}} + \mathrm{Ca^{2+}} \Leftrightarrow > \mathrm{CO_3^{-0.5}} - \mathrm{Ca^{2+}}$	1.68[b]	3.40[h]	3.40
R8	$> \mathrm{CO_3^{-0.5}} + \mathrm{Na^+} \Leftrightarrow > \mathrm{CO_3^{-0.5}} - \mathrm{Na^+}$	0.56[b]	3.40[i]	0.56
R9	$> \mathrm{CaOH^{-0.5}} + \mathrm{Mg^{2+}} \Leftrightarrow > \mathrm{CaOH^{-0.5}} - \mathrm{Mg^{2+}}$	1.66[a]	3.40[j]	2.81
R10	$> \mathrm{CaOH_2^{+0.5}} + \mathrm{SO_4^{2-}} \Leftrightarrow > \mathrm{CaOH_2^{+0.5}} - \mathrm{SO_4^{2-}}$	-2.10[g]	3.30[k]	3.30 → 11.9
R11	$> \mathrm{CO_3^{-0.5}} + \mathrm{Mg^{2+}} \Leftrightarrow > \mathrm{CO_3^{-0.5}} - \mathrm{Mg^{2+}}$	1.68[l]	3.40[l]	2.81

a – *Song et al.,* (2019).
b – *Heberling et al.,* (2014).
c – only one value for the equilibrium constant for R3 was found in the literature (0.45), hence we considered LogK^{min} to be equal to that of R10 due to similarity.
d – *Li et al.,* (2016).
e – only one value for the equilibrium constant for R8 was found in the literature (1.68), hence we considered LogK^{max} to be equal to that of R7 due to similarity.
f – combined from two reactions reported in *Pokrovsky and Schott*, (2001).
g – *Qiao et al.,* (2015a).
h – combined from two reactions reported in *Pokrovsky et al.,* (2000).
i – only one value for the equilibrium constant for R8 was found in the literature (0.56), hence we considered LogK^{max} to be equal to that of R7 due to similarity.
j – only one value for the equilibrium constant for R9 was found in the literature (1.66), hence we considered LogK^{max} to be equal to that of R4 due to similarity.
k – *Qiao et al.,* (2015b).
l – this is a new additional reaction introduced in our model with no values for the equilibrium constant found in the literature, hence we assumed both LogK^{min} and LogK^{max} to be equal to those of R7 due to similarity.

For reactions R2 – R11 we identified ranges of possible variation of equilibrium constants. The ranges were based on previously published values thus defining the minimum and maximum possible equilibrium constant for each reaction, LogK^{min} and LogK^{max}, respectively. Note, that due to lack of published information on some equilibrium constants, their maximum and minimum values were assumed to be similar to those of other adsorption reactions or calculated from published values of consecutive reactions (see caption of **Table 2** for details).

We used the Pitzer theory (pitzer.dat database of PREEQC; *Pitzer,* 1973; *Harvie et al.,* 1984) to calculate the ion activity coefficients for all complexation reactions that take place in the bulk solution at high ionic strength systems (> 0.5 M). For ionic strengths below 0.5 M it was found that there was no noticeable difference in the modelled results obtained using either the Debye-Huckel (phreeqc.dat database of PHREEQC) or Pitzer theory to calculate the ion activity coefficients. Therefore, the Pitzer theory was used throughout the entire range of tested ionic strengths.

7.2.2.3. BSM – capacitance of the Stern layer and electric potential distribution within EDL

The electric potential distribution within the Stern layer, between 0-plane and *β*–plane, is described by a linear variation, similar to the concept of two parallel plates capacitor which it can be expressed as follows:

$$\sigma_0 = C_{SL}\,(\phi_0 - \phi_\beta), \qquad 7.1$$

where σ_0 is the surface charge density at 0-plane (C·m^{-2}), C_{SL} is the specific Stern layer capacitance (or Stern layer capacitance for simplicity) between 0-plane and *β*-plane (F·m^{-2}), ϕ_0 is the electric potential at 0-plane (V) and ϕ_β is the electric potential at *β*-plane (V). The Stern layer capacitance can also be expressed as:

$$C_{SL} = \frac{\varepsilon_o \varepsilon_r}{x}, \qquad 7.2$$

where ε_o is vacuum permittivity (F·m^{-1}), ε_r is relative permittivity of the Stern layer and *x* is the distance between 0-plane and *β*-plane or the thickness of the Stern layer (m). Beyond the *β*-plane, in the diffuse layer, the electric potential distribution is described using the Gouy-Chapman theory based on the Poisson-Boltzmann equation. The electric potential magnitude decreases exponentially with the distance from the mineral surface and ion concentrations follow a Boltzmann distribution.

7.2.2.4. Two-step optimization

Our model was developed through a two-step optimization process applied to experimental zeta potential results obtained with Estaillades and Ketton rock samples saturated with equilibrated NaCl solutions of ionic strengths between 0.05 M and 5 M.

The first-step optimization aimed at determining the equilibrium constants of R2-R11, while the $\log K_{\mathrm{R1}}$ and the Stern layer capacitance (C_{SL}) were kept constant and equal to -0.5 and 1.24 F·m^{-2}, respectively, in accordance with the study of *Li et al.* (2016). The optimization of equilibrium constants of the surface complexation reactions and Stern layer capacitance was a necessary step, as previous studies considered either low salinity (e.g., *Li et al.,* 2016) or moderate salinity solutions (e.g., seawater model by *Song et al.,* 2019) using different sets of the parameters for each ionic strength, thus making their models suitable to very specific experimental conditions. To the best of our knowledge there has been no study that tried SCM for a range of salinities, and especially for ionic strengths above 0.5 M which are typical for many subsurface settings. The first-step optimization was conducted in the following manner:

- Concentration of all ions (Na^+, Ca^{2+}, Mg^{2+}, Cl^- and SO_4^{2-}) and pH reported by *Al Mahrouqi et al.* (2017) were used as input parameters. The concentration of carbon related ions (HCO_3^-, CO_3^{2-}), termed C(4) ions in PHREEQC, was not reported in the corresponding paper, therefore it was calculated from the charge balance equation. It was also assumed that the calculated C(4) concentration could exceed that of Ca^{2+} and C(4) ions that originate from the dissolved atmospheric CO_2 in aqueous solution at equilibrium with air. This assumption is consistent with the experimentally confirmed dissolution of $CaCO_3$ during the equilibration process that resulted in 10^{-3} M of dissolved Ca^{2+}, and hence the same concentration of C(4) (*Alroudhan et al.,* 2016; *Al Mahrouqi et al.,* 2017), which is higher than the equilibrium concentration of 1.5×10^{-5}M of C(4) in solution at equilibrium with air (*Li et al.,* 2016).
- The dissolution and precipitation of calcite was switched off at this optimization step by implementing PREEQC code 'Calcite 0 0' in 'equilibrium_phases' section (*Parkhurst and Appelo,* 2013; *Heberling et al.,* 2014).
- The R2 – R11 equilibrium constants were optimized by minimizing the objective function, *f*, that defines the normalised difference between the observed and the simulated zeta potential and pH:

$$f = \sum\left(\frac{\zeta_{obs}-\zeta_{sim}}{\delta_{\zeta}}\right)^2 + \sum\left(\frac{\mathrm{pH}_{obs}-\mathrm{pH}_{sim}}{\delta_{\mathrm{pH}}}\right)^2, \qquad 7.3$$

where ζ_{obs} is the observed zeta potential (mV), ζ_{sim} is the simulated zeta potential (mV), δ_{ζ} is the experimental uncertainty of the zeta potential (mV), pH_{obs} is the observed pH, pH_{sim} is the simulated pH and δ_{pH} is the experimental uncertainty of pH. Note that pH was included in the objective function since the computed value for a given set of equilibrium constants could be different from the input (experimental) value. Therefore, both directly measured properties (zeta potential and pH) were included in **Equation 7.3**. The optimization was conducted by combining the PHREEQC geochemical code with an optimization software, PEST, in which the Gauss Marquardt Levenberg method was implemented.

- The optimization was repeated three times, with the initial values of all equilibrium constants being either i) the minimum found in literature (LogK^{min}), ii) the maximum reported in the literature (LogK^{max}), or iii) the median within the tested range (see more details in **Table 7.2** caption). This repetitive optimization procedure was required to find the global minimum of f, which corresponded to the best match between the experimentally measured and computed zeta potential and pH, so that the equilibrium constants that corresponded to the smallest f were taken forward.
- The results of the first step optimization procedure are shown in **Table 7.2** (LogK^{opt} column).

It was found that the calculated zeta potentials of Estaillades and Ketton were positive except for Estaillades at ionic strength below 1 M. In contrast, the experimental results showed that the zeta potential of both rock samples remained negative at low ionic strength to become less negative/positive at high ionic strength (**Figure 7.3a**). Moreover, the calculated Ketton zeta potential was more positive compared with that of Estaillades, while the experimental data showed an opposite trend. The more positive zeta potential measured in Estaillades sample could not be explained by different rates of calcite dissolution as the equilibrium Ca^{2+} concentration was found to be higher in Ketton sample (Figure 9a in *Al Mahrouqi et al.,* 2017), which would imply a more positive zeta potential, consistent with our model.

However, a considerably higher concentration of SO_4^{2-} was also reported in experiments with Ketton (Figure 9b in *Al Mahrouqi et al.,* 2017), and more negative zeta potential compared with that of Estaillades sample was attributed to it. The authors demonstrated that the zeta potential was not very sensitive to SO_4^{2-} concentration (Figure 8b in *Al Mahrouqi et al.,* 2017), as long as concentration of all other ions remained unchanged thus implying that high sensitivity to SO_4^{2-} only took place when sulfate content was less or equal to that of the divalent cations. However, the paper did not consider a possibility of Ca^{2+} ions acting as bridges to SO_4^{2-} ions (*Nachbaur et al.,* 1998; *Austad et al.,* 2009; *Elakneswaran et al.,* 2009) thus

enhancing sulfate adsorption when elevated concentration of Ca^{2+} is found in bulk solution. Such bridging ability of Ca^{2+} implies that higher concertation of Ca^{2+} (and/or Mg^{2+}) combined with higher concentration of SO_4^{2-} (as was observed by *Al Mahrouqi et al.,* 2017) should result in overall higher adsorption of sulfate and more negative zeta potential. Keeping in mind that dissolved SO_4^{2-} could only originate from undetected minerals such as anhydrite ($CaSO_4$) or epsomite ($MgSO_4 \cdot 7H_2O$), a higher concentration of sulfate ions would always be accompanied by a higher equilibrium concentration of Ca^{2+} and/or Mg^{2+} as it was indeed reported by *Al Mahrouqi et al.,* (2017). Therefore, we assumed that the reactivity of calcite to SO_4^{2-} was considerably higher for rock samples that leached more sulfate and the constraint on LogK^{max} for R10 was removed, which resulted in a substantially better match to the experimental data (**Figure 7.3b**) and the corresponding value of the optimized equilibrium constant, LogK^{opt}, of 11.9 (Table 2). We expect that including Ca^{2+}–SO_4^{2-} ion bridging in the surface complexation reactions would lower LogK^{opt}. Such inclusion implemented in SCM, would require currently unavailable experimental data to validate the model and therefore, data acquisition and the corresponding SCM adjustments will be conducted in a follow-up study.

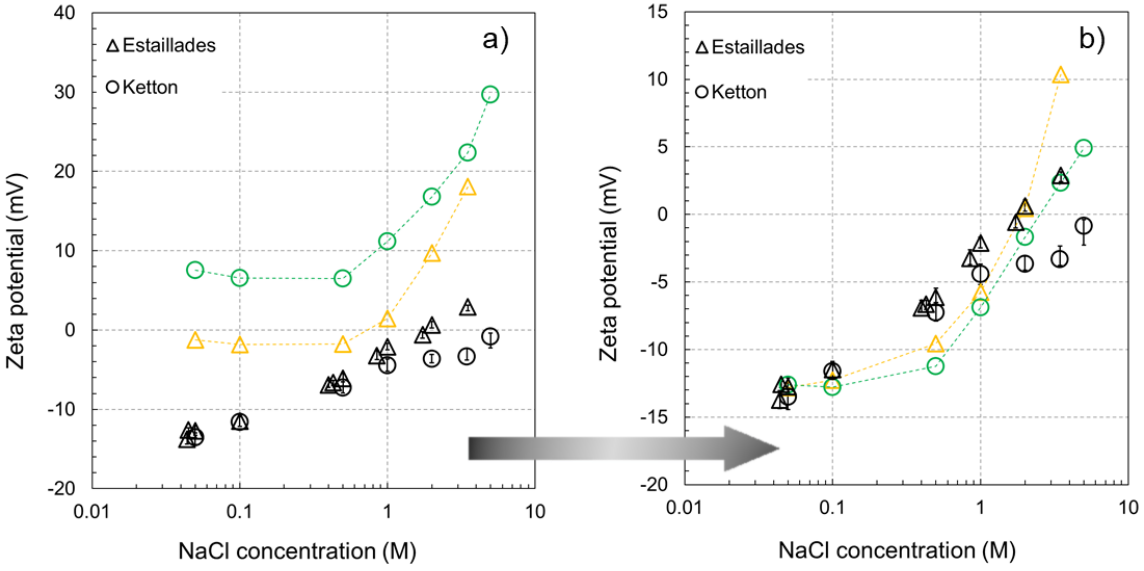

Figure 7.3. Calculated zeta potential after the first step optimization a) with the constraint $-2.10 \leq log\ K_{R10} \leq 3.30$, b) without the constraint $-2.10 \leq log\ K_{R10}$. Black symbols denote the experimental results from *Al Mahrouqi et al.* (2017). Error bars represent the experimental uncertainty, which are referred to the published results of *Al Mahrouqi et al.* (2017).

The calculated concentration of Ca^{2+} and SO_4^{2-} (note, that input pH and concentration of Mg^{2+} were constant at 8.3 and pMg = 4.19, respectively, as reported by *Al Mahrouqi et al.* (2017), pMg = -logC_{Mg} with C denoting the ion concentration in M) for both rock samples is shown in **Figure 7.4**. The computed solution pH and concentration of all other ions (those that are not shown in **Figure 7.4**) remained unchanged and equal to the input values regardless of LogK^{opt} for R10, hence the corresponding plots for these ions are not included in the figure.

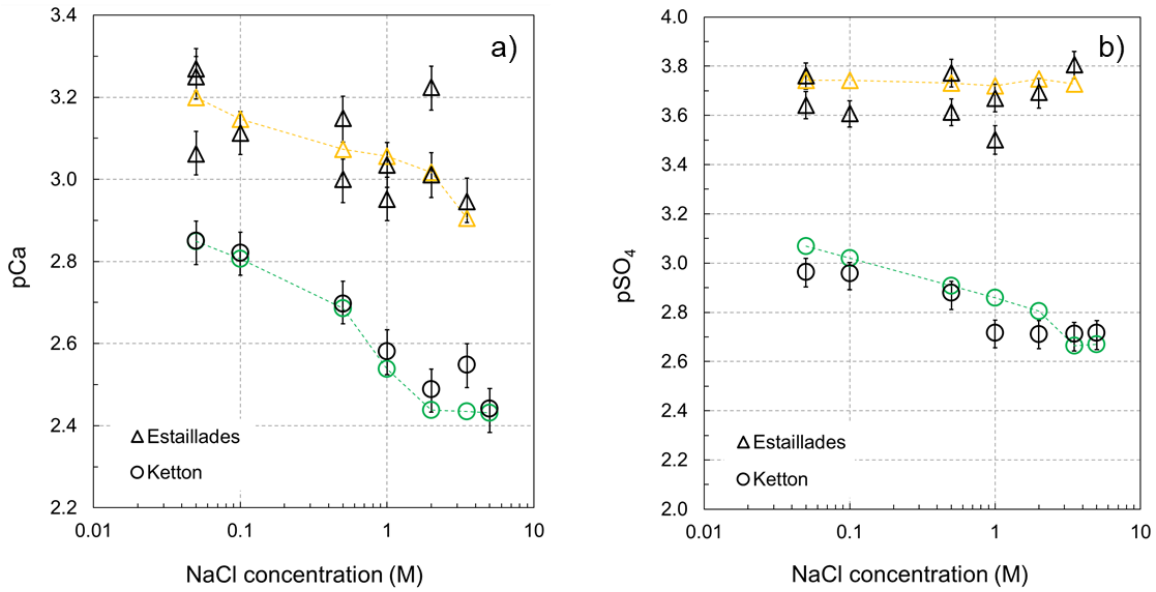

Figure 7.4. Computed pCa (a) and pSO_4 (b) from the first optimization step. Black symbols represent the experimental data (*Al Mahrouqi et al.,* 2017). The results in color correspond to the modelled zeta potential that appears in **Figure 3b**. Error bars represent the experimental uncertainty, which are referred to the published result of *Al Mahrouqi et al.* (2017).

After increasing the $LogK^{opt}$ for R10 to the value of 11.9, the match to the experimental results significantly improved as shown in **Figure 7.3b** for ionic strength ≤ 2 M. However, the simulated zeta potential at ionic strength greater than 2 M remained significantly more positive compared with the observed values, and for the Ketton sample it became positive as opposed to the negative zeta potential obtained from the experiments. Therefore, additional modification to the model was made.

The second step optimization was initiated by fixing the optimal values of all equilibrium constants obtained from the first step optimization. Then, using the same objective function as in the 1st optimization step (**Equation 7.3**), the 2nd step optimization was implemented for each rock sample and each concentration of NaCl solution using the following variables:

- The concentration of Ca^{2+} and SO_4^{2-} was allowed to vary within the reported experimental uncertainty.
- A variable capacitance of the Stern layer was assumed and allowed to vary between 0.2 $F \cdot m^{-2}$ and 1.4 $F \cdot m^{-2}$ (see more detailed discussion in section 7.2.2.5).

The resulting pH and concentration of SO_4^{2-} and Mg^{2+} from the 2nd optimization step remained the same compared with the results of the 1st optimization step. However, to obtain a better match to the experimentally measured zeta potential required a non-monotonic change of the optimized Stern layer capacitance (**Figure 7.5a**) and increased concentration of Ca^{2+} (see the yellow→red shift for Estaillades and green→blue shift for Ketton in **Figure 7.5b**). The computed zeta potential was found to be in a good agreement with the experimental data after

the variable capacitance was implemented (see the yellow→red shift for Estaillades and green→blue shift for Ketton in **Figure 7.6**).

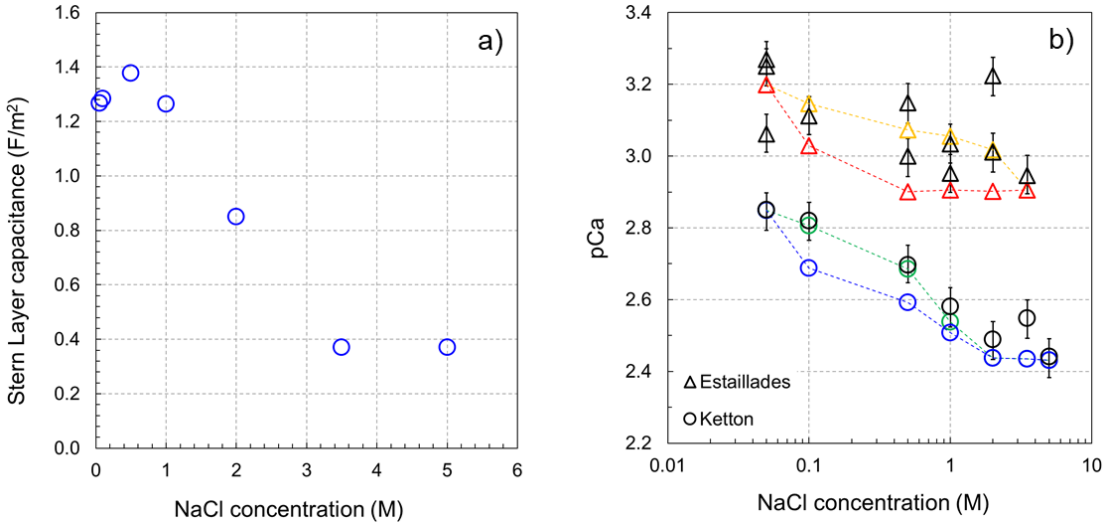

Figure 7.5. Optimized Stern layer capacitance (a) and pCa as a function of NaCl concentration. Black symbols in b) correspond to the experiments of *Al Mahrouqi et al.* (2017). The yellow→red and green→blue shift represent manual adjustment of pCa to obtain a better match to the computed zeta potential in **Figure 7.6**. Error bars in (b) represent the experimental uncertainty, which are referred to the published result of *Al Mahrouqi et al.* (2017).

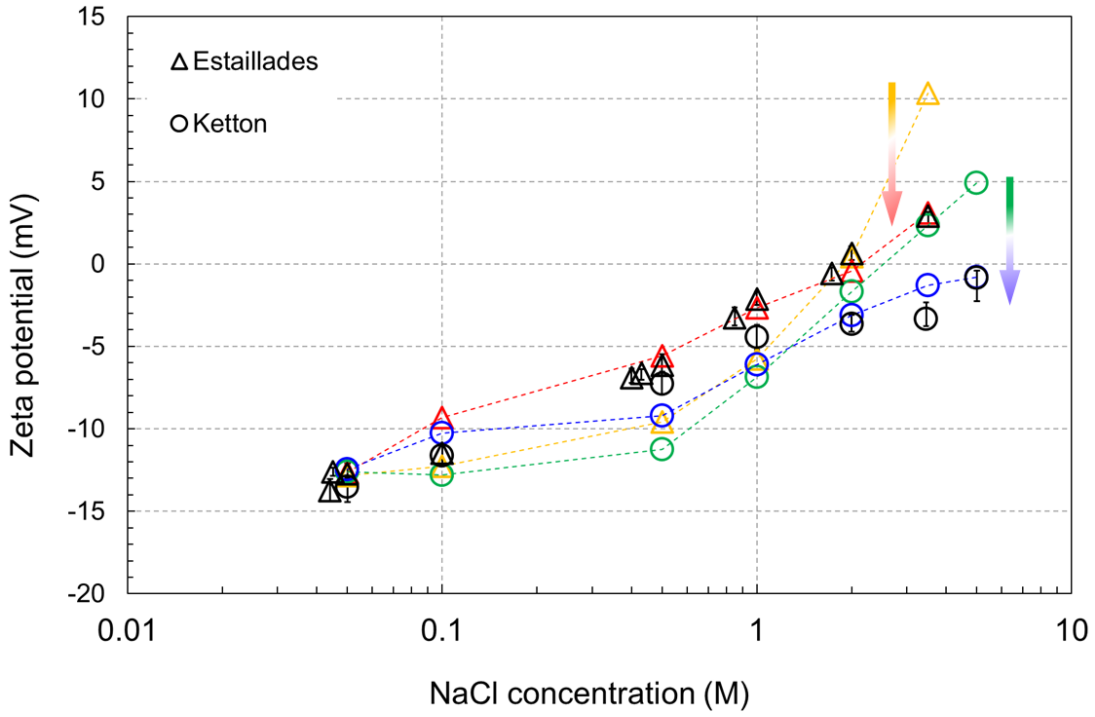

Figure 7.6. Calculated zeta potential after the first and the second step optimization. Black symbols correspond to the experimental data of *Al Mahrouqi et al.* (2017). The yellow→red (Estaillades) and green→blue (Ketton) shifts demonstrate a significant improvement of the match after applying variable Stern layer capacitance. Error bars represent the experimental uncertainty, which are referred to the published result of *Al Mahrouqi et al.* (2017).

7.2.2.5. Variable Stern layer capacitance

As mentioned in the previous section, in order to obtain a good match with the experimentally measured zeta potential it was required to allow the Stern layer capacitance (C_{SL}) to vary and to decrease globally. Following the definition of C_{SL} (**Equation 7.2**), its optimized concentration dependence (**Figure 7.5a**) can be explained by either: i) constant distance between the 0-plane and β-plane, x, and decreasing relative permittivity of the Stern layer, ε_r, with increasing NaCl concentration; ii) constant relative permittivity and increasing with salinity x; iii) increasing with salinity x and decreasing ε_r; or iv) decreasing x and ε_r with increasing salinity so that the rate of decrease of ε_r exceeds that of x. Previously published studies have suggested that hydration diameter of cations decreases considerably with increasing salinity, hence x might become smaller as smaller in diameter ions may have a closer distance of approach to the mineral surface (see for example, results obtained from an analytical model for Mg^{2+} in *Afanas'ev and Ustinov* (2012) and for Na^+ in *Afanasiev et al.* (2009) using the same approach, both verified by various experimental data) thus restricting the possible explanation for the decreasing C_{SL} to option iv). This assumption is also supported by *Brown et al.* (2016) who suggested a substantial compression of the Stern layer with increasing electrolyte salinity, which was interpreted from experimental observations including EPM. In contrast, some molecular dynamics studies (e.g., *Bourg and Sposito,* 2011) suggest that there is no change in x with increasing salt concentration due to the presence of the hydrolysis layer. At the same time, an electric field within the Stern layer that is exerted on polar water molecules results in its polarization and may lead to a substantial decrease in ε_r with increasing salinity (e.g., *Yeh and Berkowitz,* 1999), consistent with options i), iii) and iv). In the light of the above arguments, we assumed option i) in our model, implying constant x and decreasing with salinity ε_r. Note, that we tested hypothesis iv) and found that C_{SL} is significantly less sensitive to the variation of x (even assuming the maximum possible range between fully hydrated Na^+ radius of 4.5 Å and crystallographic Na^+ radius of 0.5 Å at 5 M; *Kielland,* 1973) compared with allowed variation of ε_r (between the value that corresponds to diluted electrolyte, ~80 at a temperature of 20°C and that of structured water in the Stern layer, ~6 (*Heberling et al.,* 2011), but this sensitivity analysis is not presented here.

For simplicity we used a linear regression through optimized values of C_{SL} as shown in **Figure 7.7**:

$$C_{SL} = -0.2232 \times IS + 1.357\ [F \cdot m^{-2}] \qquad 7.4$$

Where IS is the ionic strength of the solution of interest (M). To verify the regression is physically meaningful we assumed a constant distance between 0-plane and β–plane of x =

2.3 Å (*Heberling et al.,* 2014) and used a published equation for the Stern layer relative permittivity (*Conway,* 1981; *Hiemstra and Van Riemsdijk,* 2006):

$$\varepsilon_r = \frac{\varepsilon_z - \varepsilon_s}{1 + b\left(-\frac{d\phi}{x}\right)^2} + \varepsilon_s \qquad 7.5$$

where ε_z is the relative permittivity of the bulk electrolyte (at a given ionic strength and temperature), ε_s is the relative permittivity near the mineral surface (~6; *Hiemstra and Van Riemsdijk,* 2006), $d\phi$ is the electric potential difference (V) between 0-plane with *β*–plane calculated by our model, and $b = 1.2 \times 10^{-17}$ m·V^{-1} is a constant (*Hiemstra and Van Riemsdijk,* 2006). The values of C_{SL} calculated using ε_r computed from Eq. 5, and x = 2.3 Å are plotted in **Figure 7.7** and are in good agreement with the optimized values thus confirming the validity of our approach. Note, that $d\phi$ for **Equation 7.5** were computed by PHREEQC using the linear regression of C_{SL} (blue line in **Figure 7.7**) and provided an excellent match to the zeta potentials, so that non-linear regressions for C_{SL} were not tried as this was not the focus of this study.

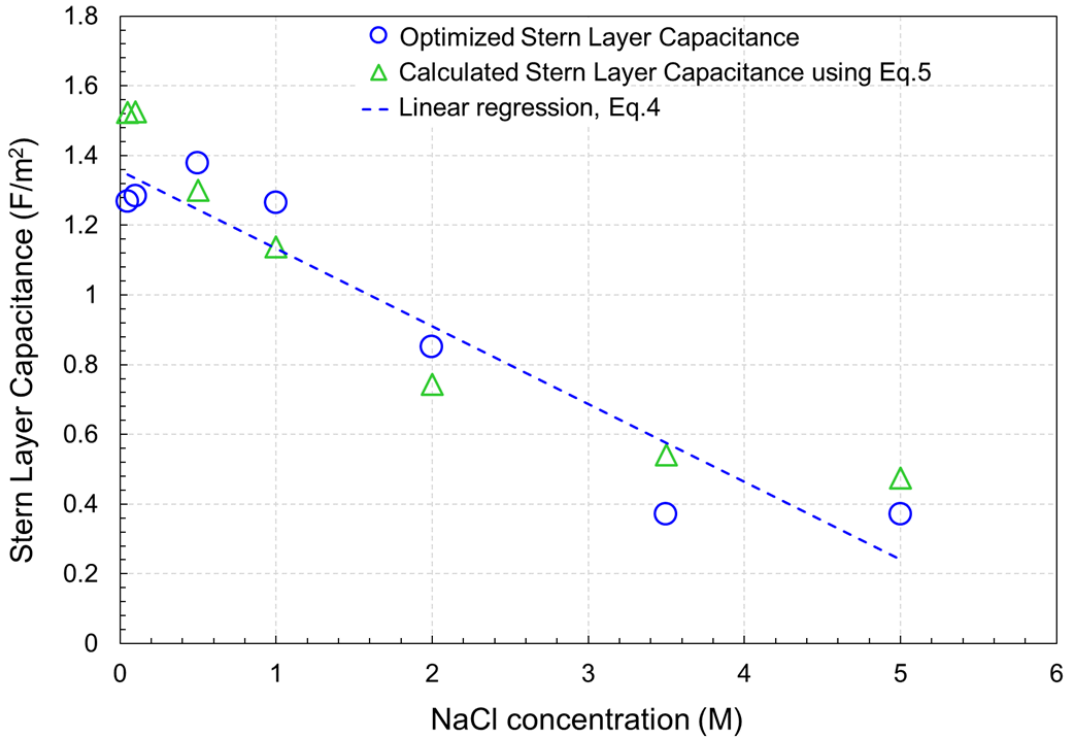

Figure 7.7. Optimized Stern layer capacitance compared with values obtained using **Equation 7.5** and approximated by the linear regression fitted to the optimized values in blue (**Equation 7.4**; quality of match to the optimized values of capacitance in blue is R^2 = 0.91) as a function of ionic strength.

7.2.3. Calcite surface complexation model implementation

To use our model for predicting the zeta potential of calcite in contact with aqueous solutions requires identification of input parameters and model options that accurately replicated the

reported experimental conditions. Therefore, the following steps should be taken to obtain an accurate prediction of the zeta potential:

- Define the *saturation index* and the *amount* (typically, 10 mol to 20 mol to allow sufficient amount of calcite to equilibrate with the solution of interest) in 'EQUILIBRIUM_PHASES' section (see **Appendix B**). A non-zero *amount* should be chosen to replicate chemical equilibration between calcite and water of the experiment of interest, while the *saturation index* should be adjusted so that the computed Ca^{2+} concentration matches the experimental value.
- Define input concentrations of all ions in the modelled solution consistent with the reported values. Note, that the input concentration of Ca^{2+} should be kept at zero and dissolution/precipitation of calcite switched on, when simulating the zeta potential experiments under equilibrium conditions, in which case content of Ca^{2+} in the solution is computed by PHREEQC and cross-compared with the experimental data. Otherwise, the measured concentration of Ca^{2+} should be used while switching off the calcite dissolution option (see examples in the **Appendix B**).
- Use the optimized equilibrium constants for R1-R11 (**Table 7.2**).
- For a given ionic strength, calculate the Stern layer capacitance using the linear regression equation (**Equation 7.4**) and allow PHREEQC to compute the zeta potential. To validate the result cross-compare the simulated pH and concentrations of all ions against the measured values.

7.3. Model validation, results and discussion

Our model described in previous sections was tested against the experimentally measured zeta potential in intact carbonate core samples saturated with aqueous solutions reported by *Al Mahrouqi et al.* (2017), *Jackson et al.* (2016a) and *Li et al.* (2016). The developed model simulated the zeta potential from SPM conducted on three different intact carbonate samples saturated with equilibrated NaCl solutions (*Al Mahrouqi et al.,* 2017), one intact carbonate sample saturated with equilibrated artificial solutions (*Jackson et al.,* 2016a), and crushed Iceland spar sample saturated with unequilibrated NaCl solutions (*Li et al.,* 2016).

7.3.1. Estaillades and Ketton samples saturated with equilibrated NaCl solution

We began modelling the zeta potential with defining the input equilibrium concentration of Na^{+}, Cl^{-}, Mg^{2+}, SO_4^{2-} as reported in the paper. The initial input concentration of Ca^{2+} was set to zero M, partial CO_2 pressure is set to $10^{-3.44}$ atm (consistent with atmospheric CO_2), and dissolution of calcite is switched on (zero default value of the *saturation index* and 20 mol *amount*) to replicate the equilibrium experimental conditions. Applying the specific capacitance values

calculated using **Equation 7.4** for each value of tested ionic strength our model computed the zeta potential and the resulting equilibrium concentration of Ca^{2+}, and the results are shown in **Figures 7.8a** and **7.8b** (note, that simulated pH and concentration of all ions except Ca^{2+} were found to be identical to the experimental values used as input parameters). It can be seen from **Figures 7.8a** and **7.8b** that simulated results for the Ketton sample underestimate the concentration of Ca^{2+} and consequently overestimate the negative zeta potential. To be consistent with the experimental data, the calcite dissolution rate for Ketton was enhanced by setting the *saturation index* to 0.8, so that the modelled equilibrium concentration of Ca^{2+} became comparable with the measured one, which resulted in an excellent correlation between the modelled and measured zeta potential (**Figures 7.8c** and **7.8d**).

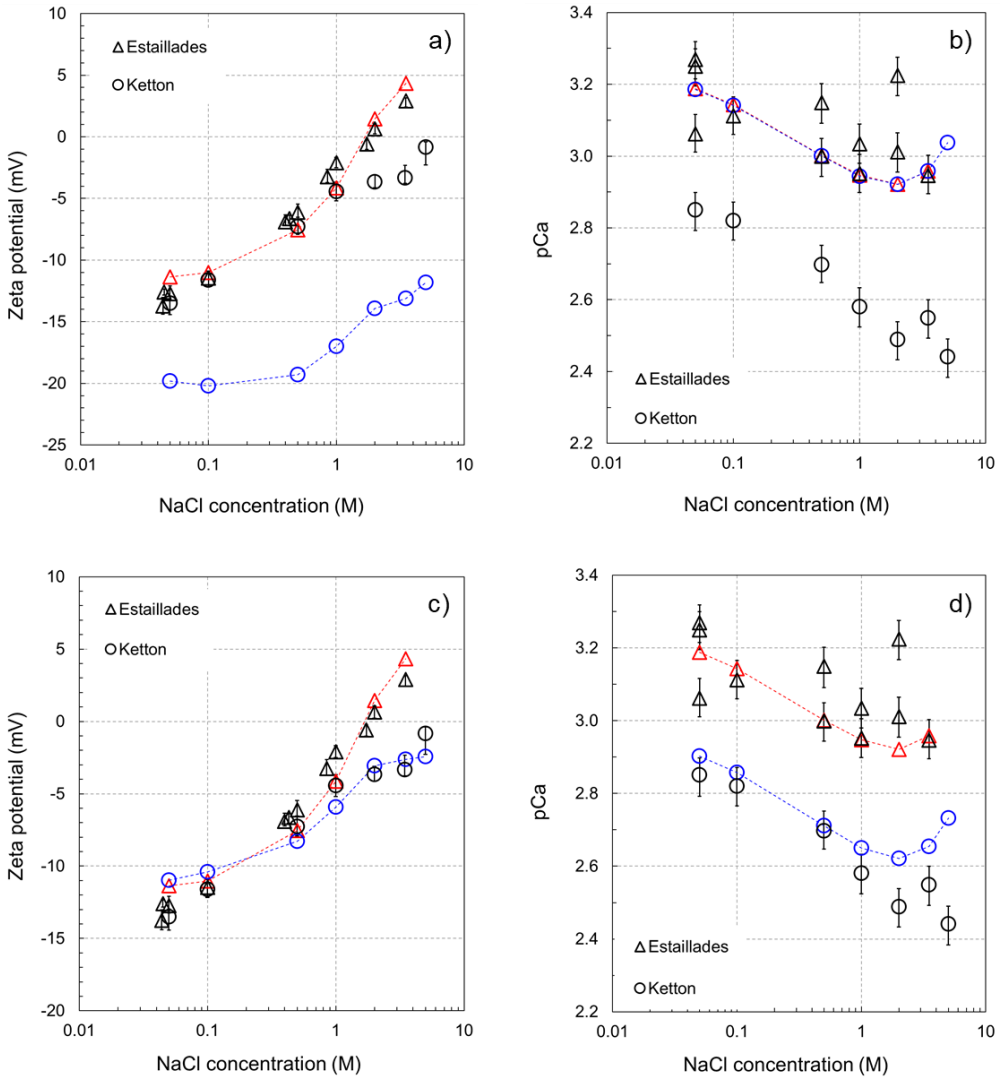

Figure 7.8. Experimentally measured (black symbols) and simulated zeta potential (a, c) and pCa (b, d) at equilibrium conditions for Estaillades and Ketton samples saturated with NaCl solutions. The modelled results were obtained assuming identical saturation index for both rock samples toward NaCl solutions (a, b), and higher saturation index for Ketton (0.80) sample relative to the default value (0) of Estaillades (c, d). Error bars represent the experimental uncertainty, which are referred to the published results of *Al Mahrouqi et al.* (2017).

7.3.2. Portland sample saturated with equilibrated NaCl solution (Al Mahrouqi et al., 2017)

Our model was then applied to simulate the zeta potential obtained from Portland limestone. To evaluate the equilibrium concentration of Ca^{2+} dissolved from the Portland sample we implemented a similar procedure by comparing the computed and measured equilibrium concentration of Ca^{2+}, which was reported to be slightly lower than that for the Ketton sample (compare diamonds and squares in Figure 10a of *Al Mahrouqi et al.,* 2017). A good agreement between the computed and measured Ca^{2+} concentration corresponded to the *saturation index* of 0.6. However, a significantly higher, compared with either Estaillades or Ketton, concentration of SO_4^{2-} was reported for equilibrated solutions in contact with Portland (compare diamonds with squares in Figure 10b of *Al Mahrouqi et al.,* 2017), while the reported concentration of Mg^{2+} in all rock samples was the same (pMg = 4.19). Since SO_4^{2-} in the equilibrated solution could only originate from dissolution of sulfate containing minerals (anhydrite or epsomite), the equilibrium concentration of SO_4^{2-} would not be expected to exceed that of the total concertation of Ca^{2+} and Mg^{2+}, which was not the case reported for Portland sample. We could not explain this discrepancy, and thus assumed that the reported concentration of Ca^{2+} was inaccurate and contained an experimental uncertainty, which resulted in underestimated concentration of the cation. Therefore, we artificially added Ca^{2+} to our simulated aqueous solution, so that the concentration of the added cation was equal to the difference in sulfate concentration across the salinity range: $\Delta[SO_4^{2-}] = [SO_4^{2-}]_{Portland} - [SO_4^{2-}]_{Ketton}$. Note that the difference in sulfate concentration depends on the salinity as shown in **Figure 7.9c**, so that a single value of the *saturation index* could not be used thus justifying our approach of adding Ca^{2+} to the solution artificially. Keeping the *saturation index* equal to 0.6, the total computed concentration of Ca^{2+} increased by the amount equal to $\Delta[SO_4^{2-}]$ (as denoted by the yellow→green shift in **Figure 7.9b**), and we successfully modelled the zeta potential as presented in **Figure 7.9a** (the yellow→green shift in **Figure 7.9a** shows the effect on the computed zeta potential made by adding Ca^{2+} to the solution).

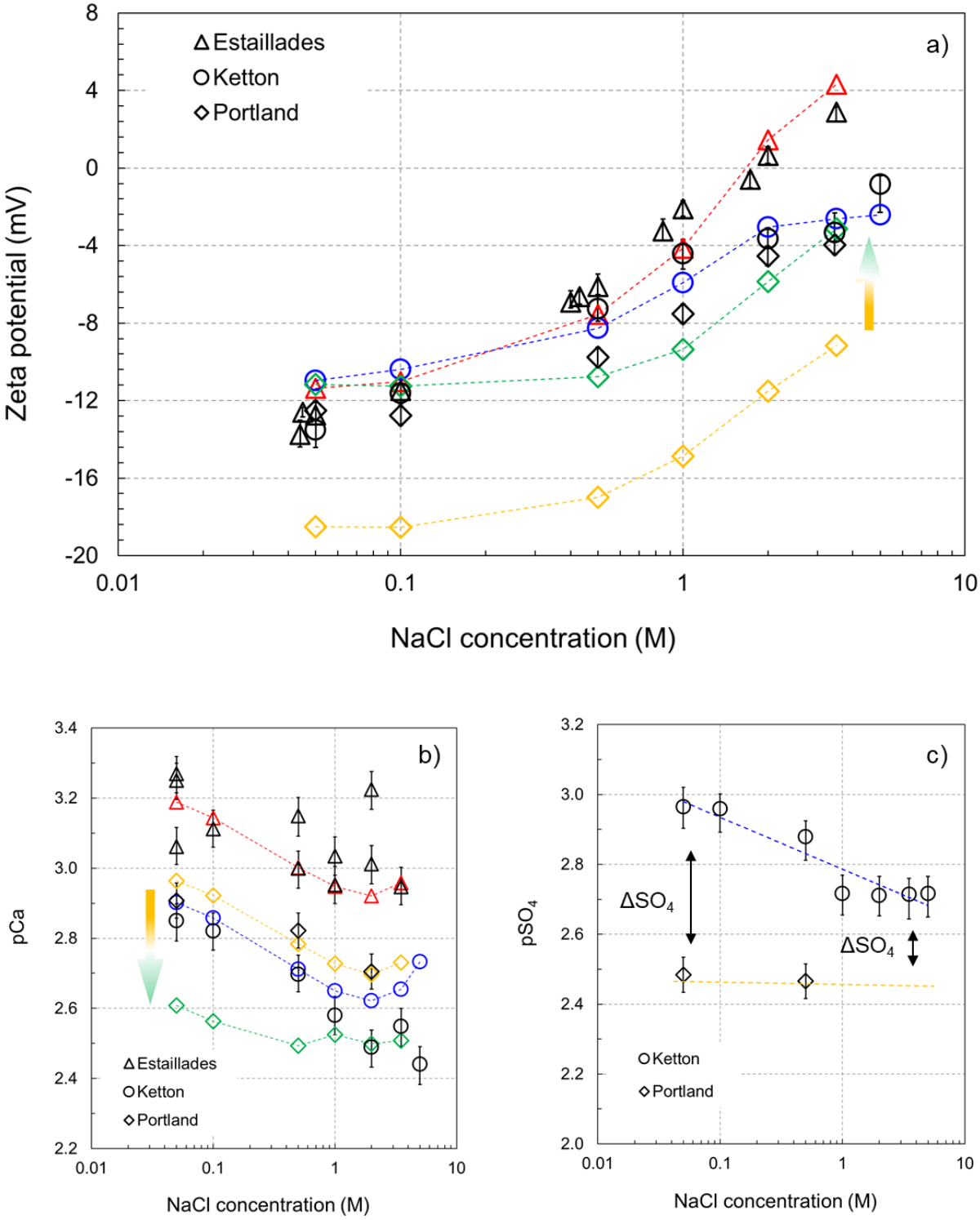

Figure 7.9. Measured and modelled zeta potential (a), pCa (b) and SO_4^{2-} (c) of three natural rock samples. The amount of artificially added Ca^{2+} to the model of Portland equals the reported difference in concentration of SO_4^{2-} as shown in (c) and explained in Section 7.3.2. Yellow diamonds represent the modelled zeta potential (a) and pCa (b) assuming saturation index of 0.6 and zero artificially added Ca^{2+}. The results of the model with artifically added Ca^{2+} are denoted by green diamonds. Error bars represent the experimental uncertainty, which are referred to the published results of *Al Mahrouqi et al.* (2017).

7.3.3. Estaillades sample saturated with artificial natural solutions (Jackson et al., 2016a)

Jackson et al. (2016a) measured zeta potential on Estaillades rock sample saturated with three different equilibrated solutions: low salinity 20dSW (20 times diluted seawater), SW (seawater) representing moderate ionic strength of 0.749 M, and 3.537 M high salinity FMB (formation brine), with detailed composition provided in Table 1 in *Jackson et al.* (2016a). The purpose of these experiments was to simulate the conventional and/or inverted low salinity waterflooding used to maximize oil recovery. To simulate the results, we modelled equilibrium conditions between calcite and the aqueous solutions by using zero initial concentration of Ca^{2+} and the same calcite dissolution rate as in Section 7.3.1. for Estaillades (default zero value of *saturation index*). The results of modelled zeta potential for all three solutions are presented in **Figure 7.10**. Our model could successfully reproduce the measured zeta potential (**Figure 7.10a**). However, the modelled equilibrium pH was significantly higher with 20dSW and significantly lower with FMB experimental data (**Figure 7.10b**) despite the fact that modelled concentrations of all ionic species were found to be identical to the measured ones. We hypothesize that such discrepancy could result from the experimental protocol reported by *Jackson et al.* (2016a) who reported the initial (at time of preparation) pH and ionic concentration of solutions but not the final values established after equilibration with the rock sample.

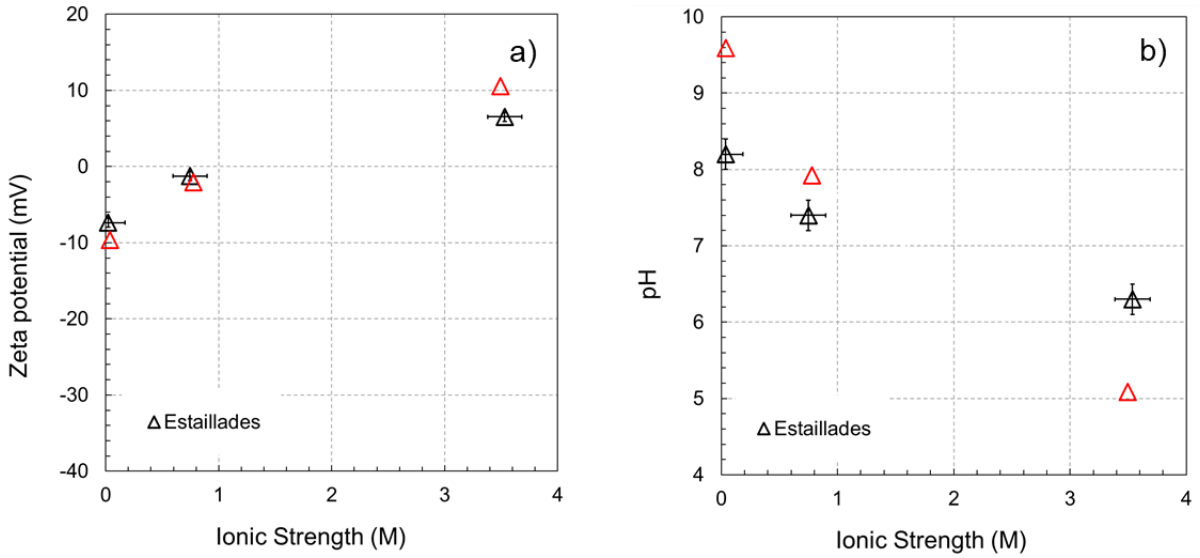

Figure 7.10. Simulated zeta potential (a) and pH (b) of three different brine compositions for Estaillades rock sample plotted as a function of ionic strength. The experimental data denoted by black symbols are extracted from Jackson et al. (2016a). Error bars represent the experimental uncertainty, which are referred to the published results of *Jackson et al.* (2016a).

It is worth mentioning, that equilibrium pH computed by our model in all tested aqueous solutions and rock samples matched the experimentally measured values apart from the results presented in **Figure 7.10**, where the simulaed equiibrium pH was higher than experimental for 20dSW and SW and lower than experimental for FMB. Inclusion of protonation of $> CO_3^{-0.5}$ surface sites without changing the optimized equilibrium constants resulted in increased simulated equilibrium pH compared with the experimental values. Thus, the assumed exclusion of protonation of the $> CO_3^{-0.5}$ surface sites was confirmed for all tested parameters except for FMB, for which such reaction might need to be included, and this will test in a follow-up study.

7.3.4. Iceland spar saturated with NaCl at non-equilibrium conditions (Li et al., 2016)

Finally, our model was tested against the data reported by *Li et al.* (2016) on crushed Iceland spar saturated with 10^{-3} M, 10^{-2} M, and 5×10^{-2} M NaCl not equilibrated with the mineral. Description of the experimental procedure reported by *Li et al.* (2016) did not provide detailed information on the duration of the streaming potential measurements. However, considering the expected high permeability of the crushed samples (comparable to permeability of sandpacks reported by *Vinogradov et al.* (2018) and low salinity solutions used by *Li et al.* (2016), it was assumed that the reported streaming potential measurements on crushed Iceland spar did not last hundreds of hours required for complete equilibration between the mineral and the tested solutions. Therefore, we assumed that only partial equilibration was reached during the experiments and for that reason we modelled the data reported by *Li et al.* (2016) as obtained at non-equilibrium conditions so that any equilibration of calcite was disabled in the model (zero *amount* was set, Section 7.2.3 and **Appendix B**). However, due to partial equilibration expected in the experiments, we artificially added some non-zero initial concentration of Ca^{2+} to the modelled solution. The concentration of dissolved Ca^{2+} in 0.05 M NaCl was adjusted to $10^{-4.2}$ M (expressed as pCa = 4.2 in **Figure 7.11b**) at pH 9, consistent with observations reported by *Alroudhan et al.* (2016). Firstly, we assumed that the amount of dissolved (and therefore artificially added to the model) Ca^{2+} should depend on pH (lower pH would lead to higher concentration of dissolved Ca^{2+}, consistent with higher dissolution rate reported by *Anabaraonye et al.* (2019). Furthermore, the pH dependence of pCa in 0.05 M NaCl experiments was extended throughout the entire range of pH (5-11) using a linear slope of $^{\Delta pCa}/_{\Delta pH} = 0.1$, consistent with calcite dissolution rate reported by *Chou et al.* (1989).

Secondly, we assumed that dissolved Ca^{2+} concentration should also depend on NaCl concentration (higher NaCl concentration would lead to higher concentration of dissolved Ca^{2+} as reported in *Al Mahrouqi et al.,* 2017). Therefore, for NaCl solutions of 10^{-2} M and 10^{-3} M the end-points of pCa were moved up the vertical scale by 0.4 units relative to one another to

reflect on the salinity dependence of calcite dissolution. The value of 0.4 was approximated from the reported calcite dissolution rate as a function of NaCl concentration (*Ruiz-Agudo et al.,* 2009) and assuming duration of the steaming potential measurement experiments conducted by *Li et al.* (2016) to be approximately 10 hours. Ultimately, ascribing the end-point values for Ca^{2+} concentration for each tested NaCl solution on the pH scale (**Figure 7.11b**) and applying linear variation of pCa between these end-points, our model successfully predicted the measured zeta potential (**Figure 7.11a**). Moreover, our model predicts that Ca^{2+} must be added to the modelled solution in order to replicate the experimentally measured zeta potential. Note, that C(4) of the amount equal to the added Ca^{2+} must also be added to the solution in addition to the initial concentration of C(4) that reflects the equilibrium content of dissolved CO_2. Despite the fact that the computed from calcite dissolution or artificially added Ca^{2+} and C(4) to the bulk electrolyte was not reported by *Li et al.* (2016), the adsorption reactions for these ions were included in their SCM. Therefore, we are confident that our approach is consistent with *Li et al.* (2016). Our results also explain how the experimental data from *Li et al.* (2016) was successfully matched by means of non-zero concentration of Ca^{2+} and C(4) in the solution, both of which should increase with decreasing pH. If such pH dependence of Ca^{2+} and C(4) concentration was not applied to the model of *Li et al.* (2016), the simulated zeta potential would become more positive with increasing pH, which is an inverted trend relative to that reported in the paper.

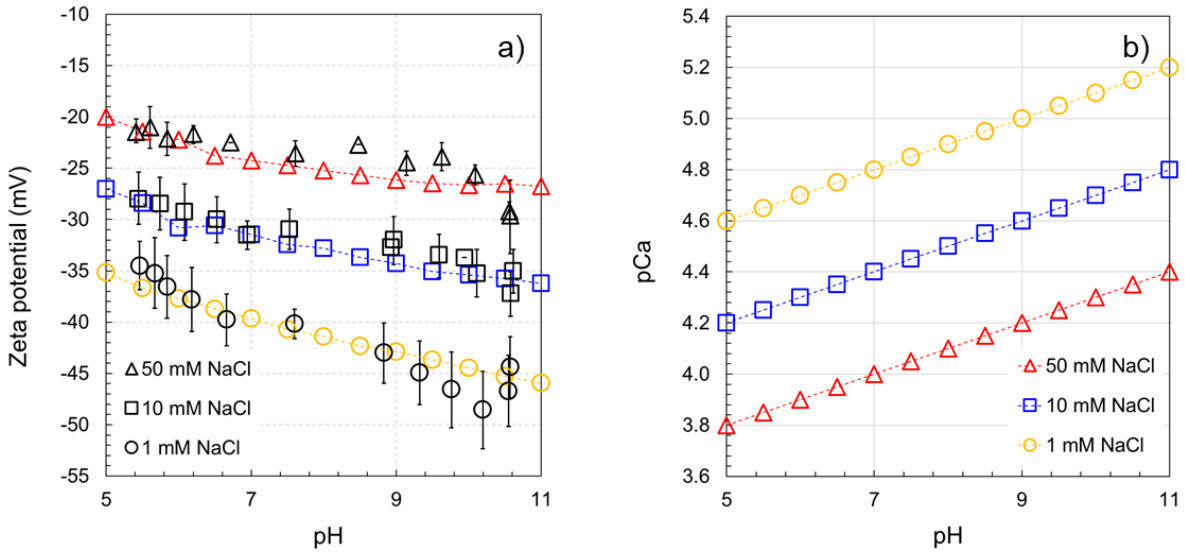

Figure 7.11. Modelled zeta potential (a) and pCa (b) of crushed Iceland spar samples saturated with three different NaCl solutions under non-equilibrium conditions. The modelled zeta potential is plotted in comparison with the experimental data (*Li et al.,* 2016) denoted by black symbols. The slopes and intercepts of the pCa as a function of pH are discussed and defined in Section 7.3.4. Error bars represent the experimental uncertainty, which are referred to the published results of *Li et al.* (2016).

7.3.5. Model capabilities, limitations and implication to carbonate-water subsurface settings

The developed robust SCM uses a set of justified and well-defined calcite surface sites and surface reactions' equilibrium constants combined with physically meaningful salinity dependence of the Stern layer capacitance. The model is capable to accurately predict zeta potential of a variety of carbonate-aqueous solution systems as long as calcite is the dominating mineral comprising natural rocks and the aqueous solution is dominated by NaCl. Moreover, an additional requirement for predictive capability of our model relates to the naturally occurring concentration of SO_4^{2-} in the solution, which has to reflect dissolution of sulfate containing minerals such as anhydrite or epsomite over geological deposition timescale. This requirement implies that the equilibrium concentration of SO_4^{2-} should not exceed the combined concentration of Ca^{2+} and Mg^{2+}.

The set of equilibrium constants proposed in this paper for ambient conditions (25°C and 1 atm) has not been tested to model experimental results obtained with aqueous solutions with artificially added SO_4^{2-} beyond natural occurrence, so that some amendments could be required to model such experiments. Moreover, we have not considered elevated temperature experimental conditions, which would require additional adjustments to the model: i) the equilibrium constants should be adjusted for elevated temperature by using for example the Van't Hoff equation; ii) the relative permittivity of the Stern layer should be recalculated; iii) the distance between the 0-plane and the β-plane should be reduced to account for reduced hydrated diameter of cations at elevated temperature (consistent with *Kuyucak and Chung,* 1994; *Vinogradov et al.,* 2018); iv) the salinity dependence of the Stern layer capacitance should be amended taking into account ii) and iii) so that a new temperature specific regression is used.

Capabilities of our model have a broad range of applications since the approach reported here has demonstrated to provide an accurate prediction of the zeta potential of natural carbonate rock in contact with aqueous solutions, subject to the above conditions. Our model works best for equilibrium experimental conditions as long as concentration of all major ionic species is known. In this sense, our model can significantly improve our understanding of streaming potential measurements and associated flows in shallow aquifers where temperature and pressure are low and therefore, laboratory measurements of pH and concentration of all ions of the solution at aquifer conditions are straight forward. Laboratory experiments should, in this case, assure establishment of full equilibrium between rock and the solution of interest and fluid samples should be analyzed for molar concentration of all ions to be used as input parameters of the model. The modelled zeta potential can then be used to predict flow patterns in critical zones (e.g., *Jougnot et al.,* 2020), permeability heterogeneities (e.g., *Jackson et al.,*

2012a) or even serve as an early warning of saline intrusion (e.g., *Graham et al.,* 2018; *MacAllister et al.,* 2018).

Our model is useful in situations where the exact concentration of all ions is unknown. For example, the model can accurately assess the initial estimate of CO_2 geological storage efficiency. The model would require input from the experimental data, given that laboratory experiments are conducted to establish full chemical equilibrium between carbonate rock and a CO_2-saturated aqueous solution at the target formation conditions of temperature and pressure. Such experiment should report at least one measured concentration (of constituent ions such as Ca^{2+}, Mg^{2+}, SO_4^{2-} or protons, pH) to validate the simulated by our model concentrations (similar to the experiments reported by *Li et al.,* 2018). The modelled zeta potential then can be used to interpret the wetting state using Derjaguin-Landau-Verwey-Overbeek (DLVO) theory (e.g., *Tokunaga,* 2012) and the resulting residual trapping of the gas.

7.4. Conclusions

We report a robust surface complexation model of calcite-water interfaces. The model was developed adopting a two-step optimization, in which the equilibrium constants of surface reactions were initially optimized to match two experimental datasets, while the ionic strength dependence of the Stern layer capacitance was obtained in the second optimization step. The model was applied to successfully predict multiple experimental datasets with an excellent quality of match, and the modelling results demonstrate that:

- The unique set of the optimized equilibrium constants can be used universally to simulate the calcite-water zeta potentials obtained from the streaming potential measurements for all tested systems and conditions.
- The Stern layer capacitance should decrease with increasing salinity to replicate high salinity zeta potentials; the range of varying capacitances was found to be consistent with analytically predicted values (*Hiemstra and Van Riemsdijk,* 2006) and with values used in previously published numerical studies (*Yeh and Berkowitz,* 1999).
- Using experimental composition of investigated solutions as the only input, our model accurately predicts zeta potentials of all tested systems and conditions including natural limestones equilibrated with simple salt and complex solutions of ionic strengths between 0.05 M and 5 M, and crushed calcite not equilibrated with NaCl solutions of ionic strength between 0.001 M and 0.01 M.
- To simulate zeta potentials of natural carbonate-water systems at equilibrium conditions, the developed model requires knowledge of concentration of SO_4^{2-} and Mg^{2+} that leach

from dolomite and anhydrite inclusions, while the equilibrium concentration of Ca^{2+} is produced by the model.

- To simulate zeta potentials of calcite in contact with water under non-equilibrium conditions requires knowledge of either measured in *real-time* Ca^{2+} concentration or duration of the simulated experiment.
- Our model is fully predictive given the required input parameters (e.g., ion concentration) are provided. However, additional surface reactions and/or model adjustments might be required to simulate the zeta potentials for carbonate rock in contact with aqueous solutions in which SO_4^{2-} concentration exceeds that of Ca^{2+} and Mg^{2+} combined, this will be investigated in a follow-up study.

Future work will also aim at acquiring additional experimental data obtained with varying concentration of C(4) and SO_4^{2-} ions under equilibrium conditions to inform the surface complexation model, which will be updated and/or modified to include the hypothesis of ion bridging outside OHP.

Chapter 8 Summary, Conclusions and Future Work

8.1. Summary and conclusions

Understanding the parameters that affect the zeta potential used for characterisation of CGS is essential, as the zeta potential is an important parameter that represent the electrostatic forces to characterises the wettability of geological target formations. Being able to estimate the wettability accurately will give us the advantage of assessing the efficiency of CO_2 trapping during CGS. Recent work by Jackson and co-workers (e.g., *Jackson and Vinogradov,* 2012; *Vinogradov and Jackson,* 2015; *Jackson et al.,* 2016a) proved that the streaming potential method was a promising method to measure the zeta potential in porous saturated rock. Moreover, the method can be used at elevated temperature, high pressure and multi-phase conditions which makes the measured zeta potential representative of the actual conditions of subsurface settings and yet, the zeta potential in such conditions is very limited. This study consists of two main investigations, including the experimental and numerical approach.

This dissertation presents a novel experimental methodology using the streaming potential measurement to accommodate for an injection of CO_2-rich live water at temperatures of 23 °C and 40 °C and at pressures of up to 10.0 MPa. This dissertation reports the first measured zeta potential on a clean sandstone (>99 wt.% quartz) considering two types of solutions (i.e., dead and live solutions) with different types of salts and dissolved CO_2 contents. The zeta potential of the dead solution is independent of the pore pressure, whereas that of the live solution zeta potential increases (becomes smaller in magnitude) with the increase in pore pressure (decrease solution pH). The pore pressure, temperature and salt compositions indirectly affect the pH of the solution, which affects the zeta potential of the dead and live solutions. Therefore, considering a clean sandstone, the zeta potential is controlled by the pH of the solution. In contrast, the zeta potential of clayey sandstone is not entirely dependent on the solution pH. An anomalous behaviour was observed in the zeta potential of the dead solution with the variation in ionic strength (i.e., the zeta potential remained constant with the increase in NaCl concentration). Under the same experimental conditions (pressure and temperature), the live solution zeta potential of clayey sandstone was lower in magnitude than that of clean sandstone. This result can be attributed to the clay and feldspar content in the pore space and their exposure to electrolytes in the larger pores.

This dissertation also reports the novel result of the multi-phase zeta potential of the live solution–scCO_2–rock system and its link to wettability. A wettability indicator was introduced to differentiate between five wetting states, ranging from strongly CO_2-wet to strongly water-wet. The wettability measured from the single- and multi-phase zeta potential measurements

suggests that intermediate-wet conditions were obtained with NaCl-10, strongly water-wet conditions were obtained with Na_2SO_4, weakly water-wet conditions were obtained with NaCl, and weakly CO_2-wet conditions were obtained with $CaCl_2$ and $MgCl_2$.

This dissertation also reports on the impact of fracture apertures with multiple minerals in the rock sample on the zeta potential. The results revealed that the zeta potentials of fractured gneiss are unique compared to sandstones or carbonates owing to their unique mineralogy. The presence of divalent ions (Ca^{2+}, Mg^{2+} and SO_4^{2-}) in the solutions are responsible for changes in the zeta potential and consequently, these ionic species are considered as PDIs for gneiss. Further, the streaming potential coefficients at two different confining pressures (4 MPa and 7 MPa) were similar, suggesting that the surface electrical conductivity is extremely low when a solution flows through the fracture.

Experimentally, obtaining the zeta potential at a high ionic strength and with complex brines poses a significant challenge. Therefore, a model using a surface complexation approach was developed to predict the zeta potential under such conditions, which are typically found in subsurface geological settings. Although our model was developed and validated for carbonates, a key finding suggests that the Stern layer capacitance should decrease with the increase in ionic strength to reproduce the experimental zeta potentials at high ionic strength. This result can be applied to other rock types to simulate the zeta potential using the same approach.

8.2. Future Work

Despite our very encouraging findings, further work is required to address some of the still unknown parameters and confirm our results:

- In chapter 3, the investigation was conducted at constant ionic strength conditions and with single salt solutions. These parameters can be extended to higher ionic strengths (≥ 0.05M) and complex solutions. Moreover, further increasing the temperature (≥ 40°C) and pore pressure (≥ 10 MPa) would affect the amount of dissolved CO_2 and might yield different zeta potential (zero or positive), which still needs to be confirmed. Moreover, in this chapter, we did not cover pH range of 4 – 5.5 in terms of zeta potential measurements. Hence, additional experiments should also address this gap. An impact of surface roughness on the zeta potential should also be investigated in the future.

- In chapter 4, clay and feldspar minerals had a significant impact on dead and live water zeta potential. In order to gain a better understanding of zeta potential when water is in contact with these minerals, additional experiments are needed for sandstone

samples containing different amounts of different minerals. Moreover, our NaCl live water was limited to 0.05M ionic strength, so additional experiments with higher ionic strength are desirable and should be combined with different temperatures and pore pressures to investigate the impact of these parameters on zeta potentials of clayey sandstone. In addition, the effect of surface roughness on the zeta potential at clayey sandstone should be planned for future work.

- In chapter 5, we found that the multi-phase zeta potential was sensitive to salt type of aqueous solutions and pore pressures. However, our experiments were also limited to constant ionic strength and a single value of elevated temperature. Thus, further investigation using various ionic strengths, mixed salt solutions, different temperatures and pore pressures are necessary to address this issue. Further, the X-ray micro-computed tomography is recommended for future experiments to enable accurate quantification of the residual CO_2 saturation. Different rock samples such as carbonate and clayey sandstone should also be tested to obtain the relationship between the multi-phase zeta potential and wettability.

- Chapter 6 provides new insights into effects of fracture aperture on the zeta potential. However, our results are limited to two different confining pressures and ambient temperature. As the fracture aperture depends on confining pressure (directly related to reservoir depth) and temperature, extending experimental parameter space to include elevated temperature, higher pore pressure, complex brine composition and high ionic strength should be considered in future work. Moreover, acquiring new data on other fractured rock samples (e.g., fractured carbonate) is also beneficial.

- As presented in chapter 7, the surface complexation mode was validated for brines with low concentration of C(4) and SO_4^{2-} ions. At the same time, at the moment there are very limited (or non-existent) experimental data on the zeta potential with higher content of C(4) and SO_4^{2-}. To address this knowledge gap, experimental work to investigate the isolated effect of C(4) and SO_4^{2-} ions on the zeta potential of calcite is underway, but the outcome of this study will have to be used to improve the current model in future. Furthermore, the concept of decreasing capacitance with increasing salinity should be probed for other rock types (e.g., sandstone).

- In this dissertation, a wide range of single- and multi-phase zeta potentials at various conditions (pressures, temperatures and dissolved CO_2) in intact several rock samples (clean sandstone, clays sandstone and fractured gneiss) saturated with dead and live water were measured experimentally. Moreover, a reliable predictive surface complexation model for carbonates was also developed. These results can be utilised

for further modelling studies using DLVO theory to investigate the total disjoining pressure and thus, the wettability of the potential subsurface reservoir for the application of CO_2 geo-sequestration. Furthermore, a pore-scale modelling approach should also be considered for future work to improve the understanding of the changes in the zeta potential of water-CO_2-rock system and its link to the wettability alteration in porous media.

References

Abdelaziz, R. and Merkel, B.J., 2012. Analytical and numerical modeling of flow in a fractured gneiss aquifer. *Journal of Water Resource and Protection*, *4*(08), pp.657.

Adair, J.H., Suvaci, E., Sindel, J., 2001. Surface and Colloid Chemistry. In Buschow, K.H.J, Chan, R.W., Flemings, M.C., Ilschner, B., Kramer, E.J., Mahajan, S., and Veyssiere, P. (eds). *Encyclopedia of Materials: Science and Technology*. Elsevier, pp.1–10.

Adamczyk, K., Prémont-Schwarz, M., Pines, D., Pines, E. and Nibbering, E.T., 2009. Real-time observation of carbonic acid formation in aqueous solution. *Science*, *326*(5960), pp.1690-1694.

Adamczyk, Z., Zaucha, M. and Zembala, M., 2010. Zeta potential of mica covered by colloid particles: a streaming potential study. *Langmuir*, *26*(12), pp.9368-9377.

Afanas'ev, V.N. and Ustinov, A.N., 2012. Hydration numbers and the state of water in hydration spheres of magnesium chloride and magnesium sulfate solutions. *Russian Journal of Inorganic Chemistry*, *57*(8), pp.1107-1122.

Afanasiev, V.N., Ustinov, A.N. and Vashurina, I.Y., 2009. State of hydration shells of sodium chloride in aqueous solutions in a wide concentration range at 273.15− 373.15 K. *The Journal of Physical Chemistry B*, *113*(1), pp.212-223.

Agartan, E., Trevisan, L., Cihan, A., Birkholzer, J., Zhou, Q., Illangasekare, T.H., 2015. Experimental study on effects of geologic heterogeneity in enhancing dissolution trapping of supercritical CO_2. *Water Resources Research, 51*, pp.1635–1648.

Agbalaka, C., Dandekar, A.Y., Patil, S.L., Khataniar, S. and Hemsath, J.R., 2008, October. The effect of wettability on oil recovery: A review. In *SPE Asia Pacific Oil and Gas Conference and Exhibition*. Society of Petroleum Engineers.

Ahmed, T., 2010. Fundamentals of Rock Properties. In *Reservoir engineering handbook*. Gulf professional publishing, pp. 189-287.

Al Mahrouqi, D., Vinogradov, J. and Jackson, M.D., 2016. Temperature dependence of the zeta potential in intact natural carbonates. *Geophysical Research Letters*, *43*(22), pp.11-578.

Al Mahrouqi, D., Vinogradov, J. and Jackson, M.D., 2017. Zeta potential of artificial and natural calcite in aqueous solution. *Advances in Colloid and Interface Science*, *240*, pp.60-76.

Al Saadi, F., Wolf, K. and Kruijsdijk, C.V., 2017. Characterization of Fontainebleau sandstone: quartz overgrowth and its impact on pore-throat framework. *Journal of Petroleum & Environmental Biotechnology*, *7*(328), pp.1-12.

Alarouj, M., Collini, H. and Jackson, M.D., 2021. Positive zeta potential in sandstones saturated with natural saline brine. *Geophysical Research Letters*, *48*(20), pp.e2021GL094306.

Ali, M., Jha, N.K., Pal, N., Keshavarz, A., Hoteit, H. and Sarmadivaleh, M., 2021. Recent advances in carbon dioxide geological storage, experimental procedures, influencing parameters, and future outlook. *Earth-Science Reviews*, pp.103895.

Alizadeh, A. and Wang, M., 2019. Flexibility of inactive electrokinetic layer at charged solid-liquid interface in response to bulk ion concentration. *Journal of Colloid and Interface Science*, *534*, pp.195-204.

Al-Khdheeawi, E.A., Vialle, S., Barifcani, A., Sarmadivaleh, M. and Iglauer, S., 2018. Effect of wettability heterogeneity and reservoir temperature on CO_2 storage efficiency in deep saline aquifers. *International Journal of Greenhouse Gas Control*, *68*, pp.216-229.

Al-Khdheeawi, E.A., Vialle, S., Barifcani, A., Sarmadivaleh, M. and Iglauer, S., 2017. Influence of CO_2-wettability on CO_2 migration and trapping capacity in deep saline aquifers. *Greenhouse Gases: Science and Technology*, *7*(2), pp.328-338.

Almutairi, A. and Le-Hussain, F., 2020. Effect of injection rate on oil water relative permeability accounting for capillary pressure and outlet end effects. In *International Petroleum Technology Conference*. Society of Petroleum Engineers.

AlRatrout, A., Raeini, A.Q., Bijeljic, B. and Blunt, M.J., 2017. Automatic measurement of contact angle in pore-space images. *Advances in Water Resources*, *109*, pp.158-169.

Alroudhan, A., Vinogradov, J. and Jackson, M.D., 2016. Zeta potential of intact natural limestone: Impact of potential-determining ions Ca, Mg and SO_4. *Colloids and Surfaces A: Physicochemical and Engineering Aspects*, *493*, pp.83-98.

Al-Shajalee, F., Arif, M., Sari, A., Wood, C., Al-Bayati, D., Xie, Q. and Saeedi, A., 2020. Low-salinity-assisted cationic polyacrylamide water shutoff in low-permeability sandstone gas reservoirs. *Energy & Fuels*, *34*(5), pp.5524-5536.

Al-Yaseri, A., Ali, M., Ali, M., Taheri, R. and Wolff-Boenisch, D., 2021. Western Australia basalt-CO_2-brine wettability at geo-storage conditions. *Journal of Colloid and Interface Science*, *603*, pp.165-171.

Al-Yaseri, A.Z., Lebedev, M., Barifcani, A. and Iglauer, S., 2016. Receding and advancing (CO_2+brine+quartz) contact angles as a function of pressure, temperature, surface roughness, salt type and salinity. *The Journal of Chemical Thermodynamics*, *93*, pp.416-423.

Amott, E., 1959. Observations relating to the wettability of porous rock. *Transactions of the AIME*, *216*(1), pp.156-162.

Anabaraonye, B.U., Crawshaw, J.P. and Trusler, J.M., 2019. Brine chemistry effects in calcite dissolution kinetics at reservoir conditions. *Chemical Geology*, *509*, pp.92-102.

Anderson, W, 1986a. Wettability literature survey-part 1: rock/oil/brine interactions and the effects of core handling on wettability. *Journal of petroleum technology*, *38*(10), pp.1125-1144.

Anderson, W., 1986b. Wettability literature survey-part 2: Wettability measurement. *Journal of Petroleum Technology*, *38*(11), pp.1246-1262.

André, L., Audigane, P., Azaroual, M. and Menjoz, A., 2007. Numerical modeling of fluid–rock chemical interactions at the supercritical CO_2–liquid interface during CO_2 injection into a carbonate reservoir, the Dogger aquifer (Paris Basin, France). *Energy Conversion and Management*, *48*(6), pp.1782-1797.

Andrew, M., Bijeljic, B. and Blunt, M.J., 2014. Pore-scale contact angle measurements at reservoir conditions using X-ray microtomography. *Advances in Water resources*, *68*, pp.24-31.

Aquilina, L., Pauwels, H., Genter, A. and Fouillac, C., 1997. Water-rock interaction processes in the Triassic sandstone and the granitic basement of the Rhine Graben: Geochemical investigation of a geothermal reservoir. *Geochimica et Cosmochimica Acta*, *61*(20), pp.4281-4295.

Arif, M., Lebedev, M., Barifcani, A. and Iglauer, S., 2017. CO_2 storage in carbonates: Wettability of calcite. *International Journal of Greenhouse Gas Control*, *62*, pp.113-121.

Austad, T., Strand, S. and Puntervold, T., 2009. Is wettability alteration of carbonates by seawater caused by rock dissolution? In: SCA *International Symposium of the Society of Core Analysts, September 2009, Noordwijk, Netherlands,* Society of Core Analysts.

Baklid, A., Korbol, R. and Owren, G., 1996. Sleipner Vest CO_2 disposal, CO_2 injection into a shallow underground aquifer. In *SPE Annual Technical Conference and Exhibition*. Society of Petroleum Engineers.

Benson, S.M. and Cole, D.R., 2008. CO_2 sequestration in deep sedimentary formations. *Elements*, *4*(5), pp.325-331.

Berkowitz, B., 2002. Characterizing flow and transport in fractured geological media: A review. *Advances in Water Resources*, *25*(8-12), pp.861-884.

BGS (2001). Final report on groundwater investigations on Harris, British Geological Survey Commissioned Report CR/01/69.

Bocquet, L. and Charlaix, E., 2010. Nanofluidics, from bulk to interfaces. *Chemical Society Reviews*, *39*(3), pp.1073-1095.

Börner, J.H., Herdegen, V., Repke, J.U. and Spitzer, K., 2015. The electrical conductivity of CO_2-bearing pore waters at elevated pressure and temperature: a laboratory study and its implications in CO_2 storage monitoring and leakage detection. *Geophysical Journal International*, *203*(2), pp.1072-1084.

Bourg, I.C. and Sposito, G., (2011). Molecular dynamics simulations of the electrical double layer on smectite surfaces contacting concentrated mixed electrolyte ($NaCl–CaCl_2$) solutions. *Journal of Colloid and Interface Science*, *360*(2), pp.701-715.

BP., 2021. Statistical Review of World Energy. *BP (British Petroleum company)*. Available at www.bp.com

Bray, A.W., Benning, L.G., Bonneville, S. and Oelkers, E.H., 2014. Biotite surface chemistry as a function of aqueous fluid composition. *Geochimica et Cosmochimica Acta*, *128*, pp.58-70.

Brown, M.A., Goel, A. and Abbas, Z., 2016. Effect of electrolyte concentration on the stern layer thickness at a charged interface. *Angewandte Chemie*, *128*(11), pp.3854-3858.

Bruant, R.G., Jr., Jr., Celia, M.A., Guswa, A.J., Peters, C.A., 2002. Peer reviewed: Safe storage of co_2 in deep saline aquifiers. *Environmental Science & Technology, 36*, pp. 240A-245A.

Bueno, V., Bosi, A., Tosco, T. and Ghoshal, S., 2022. Mobility of solid and porous hollow SiO_2 nanoparticles in saturated porous media: Impacts of surface and particle structure. *Journal of Colloid and Interface Science*, *606*, pp.480-490.

Busireddy, C. and Rao, D.N., 2004. Application of DLVO theory to characterize spreading in crude oil-brine-rock systems. In *SPE/DOE Symposium on Improved Oil Recovery*. Society of Petroleum Engineers.

Butler, C., 2020. Carbon Capture and Storage Is About Reputation, Not Economics. *Institute for Energy Economics and Financial Analysis (IEEFA)*. Available at *www.ieefa.org*.

Butt, H.J., Liu, J., Koynov, K., Straub, B., Hinduja, C., Roismann, I., Berger, R., Li, X., Vollmer, D., Steffen, W. and Kappl, M., 2022. Contact angle hysteresis. *Current Opinion in Colloid & Interface Science*, pp.101574.

Cabahug, M.R.S. and Angcoy Jr, E.C., 2013. Modeling the reservoir fluids of acidic geothermal wells in Mahanagdong, Leyte, Philippines. *Procedia Earth and Planetary Science*, *7*, pp.105-108.

Calabrese, C., McBride-Wright, M., Maitland, G.C. and Trusler, J.M., 2019. Extension of vibrating-wire viscometry to electrically conducting fluids and measurements of viscosity and

density of brines with dissolved CO_2 at reservoir conditions. *Journal of Chemical & Engineering Data*, *64*(9), pp.3831-3847.

Cama, J., Metz, V. and Ganor, J., 2002. The effect of pH and temperature on kaolinite dissolution rate under acidic conditions. *Geochimica et Cosmochimica Acta*, *66*(22), pp.3913-3926.

Carrasco, F., Mutjé, P. and Pelach, M.A., 1998. Control of retention in paper-making by colloid titration and zeta potential techniques. *Wood Science and Technology*, *32*(2), pp.145-155.

Carroll, S.A. and Walther, J.V., 1990. Kaolinite dissolution at 25 degrees, 60 degrees, and 80 degrees C. *American Journal of Science*, *290*(7), pp.797-810.

Cerepi, A., Loisy, C., Toullec, R., Burlot, R., Galaup, S. and Schmutz, M., 2006. Electrical behaviour of saturated and unsaturated geological carbonate porous systems. *Studies in Surface Science and Catalysis*, pp.713-719.

Chau, T.T., Bruckard, W.J., Koh, P.T.L. and Nguyen, A.V., 2009. A review of factors that affect contact angle and implications for flotation practice. *Advances in colloid and interface science*, *150*(2), pp.106-115.

Chen, L., Wang, M., Kang, Q., Tao, W., 2018. Pore scale study of multiphase multicomponent reactive transport during CO_2 dissolution trapping. *Advances in Water Resources, 116*, pp.208–218.

Cherubini, A., Garcia, B., Cerepi, A. and Revil, A., 2018. Streaming potential coupling coefficient and transport properties of unsaturated carbonate rocks. *Vadose Zone Journal*, *17*(1), pp.1-12.

Cherubini, A., Garcia, B., Cerepi, A. and Revil, A., 2019. Influence of CO_2 on the electrical conductivity and streaming potential of carbonate rocks. *Journal of Geophysical Research: Solid Earth*, *124*(10), pp.10056-10073.

Chiaramonte, L., Zoback, M.D., Friedmann, J. and Stamp, V., 2008. Seal integrity and feasibility of CO_2 sequestration in the Teapot Dome EOR pilot: geomechanical site characterization. *Environmental Geology*, *54*(8), pp.1667-1675.

Chou, L.E.I., Garrels, R.M. and Wollast, R., 1989. Comparative study of the kinetics and mechanisms of dissolution of carbonate minerals. *Chemical geology*, *78*(3-4), pp.269-282.

Christensen, M. and Tanino, Y., 2017. Waterflood oil recovery from mixed-wet limestone: dependence upon the contact angle. *Energy & Fuels*, *31*(2), pp.1529-1535.

Clark, D.E., Oelkers, E.H., Gunnarsson, I., Sigfússon, B., Snæbjörnsdóttir, S., Aradóttir, E.S., Gíslason, S.R., 2020. CarbFix2: CO_2 and H_2S mineralization during 3.5 years of continuous injection into basaltic rocks at more than 250°C. *Geochimica et Cosmochimica Acta, 279*, pp.45–66.

Collini, H. and Jackson, M.D., 2022. Relationship between zeta potential and wettability in porous media: insights from a simple bundle of capillary tubes model. *Journal of Colloid and Interface Science*, *608*, pp.605-621.

Collini, H., Jackson, M., 2021. Zeta potential of the crude oil-brine interface and implications for controlled salinity waterflooding. In: *IOR 2021, April 2021*. European Association of Geoscientists & Engineers, pp. 1–12.

Collini, H., Li, S., Jackson, M.D., Agenet, N., Rashid, B. and Couves, J., 2020. Zeta potential in intact carbonates at reservoir conditions and its impact on oil recovery during controlled salinity waterflooding. *Fuel*, *266*, p.116927.

Connolly, P.R., Yan, W., Zhang, D., Mahmoud, M., Verrall, M., Lebedev, M., Iglauer, S., Metaxas, P.J., May, E.F. and Johns, M.L., 2019. Simulation and experimental measurements of internal magnetic field gradients and NMR transverse relaxation times (T2) in sandstone rocks. *Journal of Petroleum Science and Engineering*, *175*, pp.985-997.

Conway, B.E., 1981. Ionic hydration in chemistry and biophysics. Elsevier Scientific Publishing Company, Amsterdam, Netherlands.

Coop, M.R. and Willson, S.M., 2003. Behavior of hydrocarbon reservoir sands and sandstones. *Journal of Geotechnical and Geoenvironmental Engineering*, 129(11), pp.1010-1019.

Crundwell, F.K., 2017. On the mechanism of the dissolution of quartz and silica in aqueous solutions. *ACS omega*, *2*(3), pp.1116-1127.

Daily, W., Ramirez, A., LaBrecque, D. and Nitao, J., 1992. Electrical resistivity tomography of vadose water movement. *Water Resources Research*, *28*(5), pp.1429-144.

Dake, L.P., 1983. *Fundamentals of reservoir engineering*. Elsevier.

Datta, S., Conlisk, A.T., Li, H.F. and Yoda, M., 2009. Effect of divalent ions on electroosmotic flow in microchannels. *Mechanics Research Communications*, 36(1), pp.65-74.

Davis, J.A., James, R.O. and Leckie, J.O., 1978. Surface ionization and complexation at the oxide/water interface: I. Computation of electrical double layer properties in simple electrolytes. *Journal of Colloid and Interface Science*, *63*(3), pp.480-499.

Davis, S.J., Caldeira, K. and Matthews, H.D., 2010. Future CO_2 emissions and climate change from existing energy infrastructure. *Science*, *329*(5997), pp.1330-1333.

de Coninck, H. and Benson, S.M., 2014. Carbon dioxide capture and storage: issues and prospects. *Annual Review of Environment and Resources*, *39*, pp.243-270.

Delgado, Á.V., González-Caballero, F., Hunter, R.J., Koopal, L.K. and Lyklema, J., 2007. Measurement and interpretation of electrokinetic phenomena. *Journal of Colloid and Interface Science*, *309*(2), pp.194-224.

Demir, C., Abramov, A.A. and Çelik, M.S., 2001. Flotation separation of Na-feldspar from K-feldspar by monovalent salts. *Minerals Engineering*, *14*(7), pp.733-740.

Demir, C., Bentli, I., Gülgönül, I. and Çelik, M.S., 2003. Effects of bivalent salts on the flotation separation of Na-feldspar from K-feldspar. *Minerals Engineering*, 16(6), pp.551-554.

Ding, H. and Rahman, S.R., 2018. Investigation of the impact of potential determining ions from surface complexation modeling. *Energy & Fuels*, *32*(9), pp.9314-9321.

Ding, S., Xi, Y., Jiang, H. and Liu, G., 2018. CO_2 storage capacity estimation in oil reservoirs by solubility and mineral trapping. *Applied Geochemistry*, *89*, pp.121-128.

Donaldson, C., and Alam, W. 2008. *Wettability*. Gulf Publishing Company

Donaldson, E.C., Thomas, R.D. and Lorenz, P.B., 1969. Wettability determination and its effect on recovery efficiency. *Society of Petroleum Engineers Journal*, *9*(1), pp.13-20.

Druckenmiller, M.L. and Maroto-Valer, M.M., 2005. Carbon sequestration using brine of adjusted pH to form mineral carbonates. *Fuel Processing Technology*, 86(14-15), pp.1599-1614.

Edmunds, W.M. and Smedley, P.L., 2000. Residence time indicators in groundwater: the East Midlands Triassic sandstone aquifer. *Applied Geochemistry*, *15*(6), pp.737-752.

Edmunds, W.M., Bath, A.H. and Miles, D.L., 1982. Hydrochemical evolution of the East Midlands Triassic sandstone aquifer, England. *Geochimica et Cosmochimica Acta*, *46*(11), pp.2069-2081.

Elakneswaran, Y., Nawa, T. and Kurumisawa, K., 2009. Electrokinetic potential of hydrated cement in relation to adsorption of chlorides. *Cement and Concrete Research*, *39*(4), pp.340-344.

El-Maghraby, R.M., Pentland, C.H., Iglauer, S. and Blunt, M.J., 2012. A fast method to equilibrate carbon dioxide with brine at high pressure and elevated temperature including solubility measurements. *The Journal of Supercritical Fluids*, *62*, pp.55-59.

Eriksson, R., Merta, J. and Rosenholm, J.B., 2007. The calcite/water interface: I. Surface charge in indifferent electrolyte media and the influence of low-molecular-weight polyelectrolyte. *Journal of colloid and interface science*, *313*(1), pp.184-193.

Flude, S. and Alcade, J., 2020. Carbon capture and storage has stalled needlessly – three reasons why fears of CO_2 leakage are overblown. *The Conversation,* March 2020. Available at: *https://theconversation.com/carbon-capture-and-storage-has-stalled-needlessly-three-reasons-why-fears-of-co-leakage-are-overblown-130747*.

Foxall, T., Peterson, G.C., Rendall, H.M. and Smith, A.L., 1979. Charge determination at calcium salt/aqueous solution interface. *Journal of the Chemical Society, Faraday Transactions 1: Physical Chemistry in Condensed Phases*, *75*, pp.1034-1039.

Fujii, T., Sato, Y., Lin, H., Inomata, H. and Hashida, T., 2009. Evaluation of CO_2 sorption capacity of rocks using a gravimetric method for CO_2 geological sequestration. *Energy Procedia*, *1*(1), pp.3723-3730.

Garcia, J.E., 2001. *Density of aqueous solutions of CO_2* (No. LBNL-49023). Lawrence Berkeley National Lab. (LBNL), Berkeley, CA, United States.

Gilmore, K.A., Neufeld, J.A. and Bickle, M.J., 2020. CO_2 dissolution trapping rates in heterogeneous porous media. *Geophysical Research Letters*, *47*(12), pp.e2020GL087001.

Gislason, S.R., Wolff-Boenisch, D., Stefansson, A., Oelkers, E.H., Gunnlaugsson, E., Sigurdardottir, H., Sigfusson, B., Broecker, W.S., Matter, J.M., Stute, M. and Axelsson, G., 2010. Mineral sequestration of carbon dioxide in basalt: A pre-injection overview of the CarbFix project. *International Journal of Greenhouse Gas Control*, *4*(3), pp.537-545.

Global CCS Institute, 2021. Global Status of CCS 2021 – CCS Accelerating to Net Zero. *Global CCS Institute*.

Glover, P.W. and Jackson, M.D., 2010. Borehole electrokinetics. *The Leading Edge*, *29*(6), pp.724-728.

Glover, P.W.J., 2015. 11.04 Geophysical properties of the near surface earth: electrical properties. *Treatise on geophysics*, *11*, pp.89-137.

Glover, P.W.J., 2018. Modelling pH-dependent and microstructure-dependent streaming potential coefficient and zeta potential of porous sandstones. *Transport in Porous Media*, *124*(1), pp.31-56.

Gozalpour, F., Ren, S.R. and Tohidi, B., 2005. CO_2 EOR and storage in oil reservoir. *Oil & Gas Science and Technology*, *60*(3), pp.537-546.

Graham, M.T., MacAllister, D.J., Vinogradov, J., Jackson, M.D. and Butler, A.P., 2018. Self-potential as a predictor of seawater intrusion in coastal groundwater boreholes. *Water Resources Research*, *54*(9), pp.6055-6071.

Green, D.W. and Willhite, G.P., 1998. *Enhanced oil recovery*, Henry L. Doherty Memorial Fund of AIME, Society of Petroleum Engineers, Richardson, Texas.

Gregory, J., 1975. Interaction of unequal double layers at constant charge. *Journal of Colloid and Interface Science*, *51*(1), pp.44-51.

Guancheng, J., 2018. Evaluation Methods and Influencing Factors of Gas Wettability. In *Gas wettability of reservoir rock surfaces with porous media*. Gulf Professional Publishing, pp. 29-84.

Guancheng, J., 2018. *Gas wettability of reservoir rock surfaces with porous media*. Gulf Professional Publishing.

Gulamali, M.Y., Leinov, E. and Jackson, M.D., 2011. Self-potential anomalies induced by water injection into hydrocarbon reservoirs. *Geophysics*, *76*(4), pp.F283-F292.

Gülgönül, İ., Karagüzel, C., Çınar, M. and Çelik, M.S., 2012. Interaction of sodium ions with feldspar surfaces and its effect on the selective separation of Na-and K-feldspars. *Mineral Processing and Extractive Metallurgy Review*, *33*(4), pp.233-245.

Haartsen, M.W. and Pride, S.R., 1997. Electroseismic waves from point sources in layered media. *Journal of Geophysical Research: Solid Earth*, *102*(B11), pp.24745-24769.

Harley, A.D. and Gilkes, R.J., 2000. Factors influencing the release of plant nutrient elements from silicate rock powders: a geochemical overview. *Nutrient Cycling in Agroecosystems*, *56*(1), pp.11-36.

Harvie, C.E., Møller, N. and Weare, J.H., 1984. The prediction of mineral solubilities in natural waters: The Na-K-Mg-Ca-H-Cl-SO_4-OH-HCO_3-CO_3-CO_2-H_2O system to high ionic strengths at 25°C. *Geochimica et Cosmochimica Acta*, *48*(4), pp.723-751.

Heaviside, J., Brown, C.E. and Gamble, I.J.A., (1987), September. Relative permeability for intermediate wettability reservoirs. *In SPE Annual Technical Conference and Exhibition*. Society of Petroleum Engineers.

Heberling, F., Bosbach, D., Eckhardt, J.D., Fischer, U., Glowacky, J., Haist, M., Kramar, U., Loos, S., Müller, H.S., Neumann, T. and Pust, C., 2014. Reactivity of the calcite–water-interface, from molecular scale processes to geochemical engineering. *Applied Geochemistry*, *45*, pp.158-190.

Heberling, F., Klačić, T., Raiteri, P., Gale, J.D., Eng, P.J., Stubbs, J.E., Gil-Díaz, T., Begović, T. and Lützenkirchen, J. 2021. Structure and surface complexation at the calcite (104)–water interface. *Environmental Science & Technology*, *55*(18), pp.12403-12413.

Heberling, F., Trainor, T.P., Lützenkirchen, J., Eng, P., Denecke, M.A. and Bosbach, D., 2011. Structure and reactivity of the calcite–water interface. *Journal of Colloid and Interface Science*, *354*(2), pp.843-857.

Heidaryan, E., Hatami, T., Rahimi, M. and Moghadasi, J., 2011. Viscosity of pure carbon dioxide at supercritical region: Measurement and correlation approach. *The Journal of Supercritical Fluids*, *56*(2), pp.144-151.

Hendraningrat, L. and Torsæter, O., 2015. Metal oxide-based nanoparticles: revealing their potential to enhance oil recovery in different wettability systems. *Applied Nanoscience*, *5*, pp.181-199.

Herring, A.L., Sun, C., Armstrong, R.T., Li, Z., McClure, J.E. and Saadatfar, M., 2021. Evolution of Bentheimer Sandstone Wettability During Cyclic scCO_2-Brine Injections. *Water Resources Research*, *57*(11), pp.e2021WR030891.

Hesse, M.A., Orr, F.M., Tchelepi, H.A., 2008. Gravity currents with residual trapping. *Journal of Fluid Mechanics, 611,* pp.35–60.

Hester, R.E. and Harrison, R.M. (eds), 2010. *Carbon capture: sequestration and storage*. Royal Society of Chemistry.

Hidayat, M., Sarmadivaleh, M., Derksen, J., Vega-Maza, D., Iglauer, S. and Vinogradov, J., 2022. Zeta potential of CO_2-rich aqueous solutions in contact with intact sandstone sample at temperatures of 23°C and 40°C and pressures up to 10.0 MPa. *Journal of Colloid and Interface Science*, *607*, pp.1226-1238.

Hiemstra, T. and Van Riemsdijk, W.H., 2006. On the relationship between charge distribution, surface hydration, and the structure of the interface of metal hydroxides. *Journal of Colloid and Interface Science*, *301*(1), pp.1-18.

Hiemstra, T., Van Riemsdijk, W.H. and Bolt, G.H., 1989. Multisite proton adsorption modeling at the solid/solution interface of (hydr) oxides: A new approach: I. Model description and evaluation of intrinsic reaction constants. *Journal of Colloid and Interface Science*, *133*(1), pp.91-104.

Higgs, S., Da Wang, Y., Sun, C., Ennis-King, J., Jackson, S.J., Armstrong, R.T. and Mostaghimi, P., 2022. In-situ hydrogen wettability characterisation for Underground Hydrogen Storage. *International Journal of Hydrogen Energy*, *47*(26), pp.13062-13075.

Hirasaki, G.J., (1991). Wettability: fundamentals and surface forces. *SPE Formation Evaluation*, *6*(02), pp.217-226.

Hubbe, M.A., 2001. Paper, wetting and penetration of liquids into. In *Encyclopedia of Materials: Science and Technology*, Pergamon, pp.6735-6739.

Hunter, R.J., 1981. *Zeta potential in colloid science: principles and applications*. Academic press.

Hussain, S.A., Demirci, Ş. and Özbayoğlu, G., 1996. Zeta potential measurements on three clays from Turkey and effects of clays on coal flotation. *Journal of Colloid and Interface Science*, *184*(2), pp.535-541.

Ibekwe, A., Pokrajac, D. and Tanino, Y., 2020. Automated extraction of in situ contact angles from micro-computed tomography images of porous media. *Computers & Geosciences*, *137*, pp.104425.

Iding, M. and Ringrose, P., 2009. Evaluating the impact of fractures on the long-term performance of the In Salah CO_2 storage site. *Energy Procedia*, *1*(1), pp.2021-2028.

IEA, 2022. Global Energy Review: CO_2 Emissions in 2021. *International Energy Agency (IEA)*. Available at: https://www.iea.org/reports/global-energy-review-co2-emissions-in-2021-2

Iglauer, S., 2017. CO_2-water-rock wettability: Variability, influencing factors, and implications for CO_2 geostorage. *Accounts of Chemical Research, 50*, pp.1134–1142.

Iglauer, S., 2018. Optimum storage depths for structural CO_2 trapping. *International Journal of Greenhouse Gas Control*, *77*, pp.82-87.

Iglauer, S., Ali, M. and Keshavarz, A., 2021. Hydrogen Wettability of Sandstone Reservoirs: Implications for Hydrogen Geo-Storage. *Geophysical Research Letters*, *48*(3), pp.e2020GL090814.

Iglauer, S., Al-Yaseri, A.Z., Rezaee, R. and Lebedev, M., 2015a. CO_2 wettability of caprocks: Implications for structural storage capacity and containment security. *Geophysical Research Letters*, *42*(21), pp.9279-9284.

Iglauer, S., Mathew, M.S. and Bresme, F., 2012. Molecular dynamics computations of brine–CO_2 interfacial tensions and brine–CO_2–quartz contact angles and their effects on structural

and residual trapping mechanisms in carbon geo-sequestration. *Journal of Colloid and Interface Science*, *386*(1), pp.405-414.

Iglauer, S., Pentland, C.H. and Busch, A., 2015b. CO_2 wettability of seal and reservoir rocks and the implications for carbon geo-sequestration. *Water Resources Research*, *51*(1), pp.729-774.

Iglauer, S., Salamah, A., Sarmadivaleh, M., Liu, K. and Phan, C., 2014. Contamination of silica surfaces: Impact on water– CO_2–quartz and glass contact angle measurements. *International Journal of Greenhouse Gas Control*, *22*, pp.325-328.

IPCC, 2005. IPCC Special Report on carbon dioxide capture and storage. Prepared by Working Group III of the Intergovernmental Panel on Climate Change, Metz, B., Davidson, O., de Coninck, H., Loos, M., and Meyer, L. (eds). Cambridge University Press, Cambridge, United Kingdom.

IPCC, 2018. Global Warming of 1.5°C. An IPCC Special Report on the impacts of global warming of 1.5°C above pre-industrial levels and related global greenhouse gas emission pathways, in the context of strengthening the global response to the threat of climate change, sustainable development, and efforts to eradicate poverty. Prepared by Masson-Delmotte, V., P. Zhai, H.-O. Pörtner, D. Roberts, J. Skea, P.R. Shukla, A. Pirani, W. Moufouma-Okia, C. Péan, R. Pidcock, S. Connors, J.B.R. Matthews, Y. Chen, X. Zhou, M.I. Gomis, E. Lonnoy, T. Maycock, M. Tignor, and T. Waterfield (eds.). In Press.

Ishido, T. and Mizutani, H., 1981. Experimental and theoretical basis of electrokinetic phenomena in rock-water systems and its applications to geophysics. *Journal of Geophysical Research: Solid Earth*, *86*(B3), pp.1763-1775.

Islam, A.W. and Carlson, E.S., 2012. Viscosity models and effects of dissolved CO_2. *Energy & Fuels*, 26(8), pp.5330-5336.

Israelachvili, J.N., 1974. The nature of van der Waals forces. *Contemporary Physics*, 15(2), pp.159-178.

Jaafar, M.Z., Vinogradov, J. and Jackson, M.D., 2009. Measurement of streaming potential coupling coefficient in sandstones saturated with high salinity NaCl brine. *Geophysical Research Letters*, *36*(21).

Jackson, M. D., and Leinov, E. 2012. On the validity of the “thin” and “thick” double-layer assumptions when calculating streaming currents in porous media. *International Journal of Geophysics*, pp.897807.

Jackson, M.D. and Vinogradov, J., 2012. Impact of wettability on laboratory measurements of streaming potential in carbonates. *Colloids and Surfaces A: Physicochemical and Engineering Aspects*, *393*, pp.86-95.

Jackson, M.D., Al-Mahrouqi, D. and Vinogradov, J., 2016a. Zeta potential in oil-water-carbonate systems and its impact on oil recovery during controlled salinity water-flooding. *Scientific Reports*, *6*, pp.1-13.

Jackson, M.D., Butler, A.P. and Vinogradov, J., 2012b. Measurements of spontaneous potential in chalk with application to aquifer characterization in the southern UK. *Quarterly Journal of Engineering Geology and Hydrogeology*, *45*(4), pp.457-471.

Jackson, M.D., Gulamali, M.Y., Leinov, E., Saunders, J.H. and Vinogradov, J., 2012a. Spontaneous potentials in hydrocarbon reservoirs during waterflooding: Application to water-front monitoring. *SPE Journal*, *17*(1), pp.53-69.

Jackson, M.D., Vinogradov, J., Hamon, G. and Chamerois, M., 2016b. Evidence, mechanisms and improved understanding of controlled salinity waterflooding part 1: Sandstones. *Fuel*, *185*, pp.772-793.

Jardani, A., Revil, A., Bolève, A. and Dupont, J.P., 2008. Three-dimensional inversion of self-potential data used to constrain the pattern of groundwater flow in geothermal fields. *Journal of Geophysical Research: Solid Earth*, *113*(B9).

Jie, Z., Weiqing, W., Jing, L., Yang, H., Qiming, F. and Hong, Z., 2014. Fe (III) as an activator for the flotation of spodumene, albite, and quartz minerals. *Minerals Engineering*, *61*, pp.16-22.

Jougnot, D., Roubinet, D., Guarracino, L. and Maineult, A., 2020. Modeling streaming potential in porous and fractured media, description and benefits of the effective excess charge density approach. In Biswas, A. and Sharma, S.P. (eds). *Advances in Modeling and Interpretation in Near Surface Geophysics*. Springer, Cham, pp. 61-96.

Jouniaux, L. and Pozzi, J.P., 1995. Streaming potential and permeability of saturated sandstones under triaxial stress: Consequences for electrotelluric anomalies prior to earthquakes. *Journal of Geophysical Research: Solid Earth*, *100*(B6), pp.10197-10209.

Jouniaux, L. and Zyserman, F., 2016. A review on electrokinetically induced seismo-electrics, electro-seismics, and seismo-magnetics for Earth sciences. *Solid Earth*, *7*(1), pp.249-284.

Jouniaux, L., Maineult, A., Naudet, V., Pessel, M. and Sailhac, P., 2009. Review of self-potential methods in hydrogeophysics. *Comptes Rendus Geoscience, 341*(10-11), pp.928-936.

Juanes, R., Spiteri, E.J., Orr Jr, F.M. and Blunt, M.J., 2006. Impact of relative permeability hysteresis on geological CO_2 storage. *Water Resources Research*, *42*(12).

Kaszuba, J.P., Janecky, D.R. and Snow, M.G., 2003. Carbon dioxide reaction processes in a model brine aquifer at 200°C and 200 bars: implications for geologic sequestration of carbon. *Applied Geochemistry*, *18*(7), pp.1065-1080.

Kelemen, P., Benson, S.M., Pilorgé, H., Psarras, P. and Wilcox, J., 2019. An overview of the status and challenges of CO_2 storage in minerals and geological formations. *Frontiers in Climate*. Available at *https://www.frontiersin.org/articles/10.3389/fclim.2019.00009/full*.

Kennedy, H.T., Burja, E.O. and Boykin, R.S., 1955. An investigation of the effects of wettability on oil recovery by water flooding. *The Journal of Physical Chemistry*, *59*(9), pp.867-869.

Kielland, J., (1937). Individual activity coefficients of ions in aqueous solutions. *Journal of the American Chemical Society*, *59*(9), pp.1675-1678.

Kim, M.S. and Kwak, D.H., 2017. Effect of zeta potential on collision-attachment coefficient and removal efficiency for dissolved carbon dioxide flotation. *Environmental engineering science*, *34*(4), pp.272-280.

Kim, T.W., Tokunaga, T.K., Shuman, D.B., Sutton, S.R., Newville, M. and Lanzirotti, A., 2012. Thickness measurements of nanoscale brine films on silica surfaces under geologic CO_2 sequestration conditions using synchrotron X-ray fluorescence. *Water Resources Research*, 48(9).

Kosmulski, M. and Dahlsten, P., 2006. High ionic strength electrokinetics of clay minerals. *Colloids and Surfaces A: Physicochemical and Engineering Aspects*, *291*(1-3), pp.212-218.

Kosmulski, M., Mączka, E., Janusz, W. and Rosenholm, J.B., 2002. Multiinstrument study of the electrophoretic mobility of quartz. *Journal of Colloid and Interface Science, 250*(1), pp.99-103.

Kou, Z., Wang, T., Chen, Z. and Jiang, J., 2021. A fast and reliable methodology to evaluate maximum CO_2 storage capacity of depleted coal seams: A case study. *Energy*, *231*, p.120992.

Koukouzas, N., Kypritidou, Z., Purser, G., Rochelle, C.A., Vasilatos, C. and Tsoukalas, N., 2018. Assessment of the impact of CO_2 storage in sandstone formations by experimental studies and geochemical modeling: The case of the Mesohellenic Trough, NW Greece. *International Journal of Greenhouse Gas Control*, *71*, pp.116-132.

Krevor, S.C., Pini, R., Zuo, L. and Benson, S.M., 2012. Relative permeability and trapping of CO_2 and water in sandstone rocks at reservoir conditions. *Water Resources Research*, *48*(2).

Kulkarni, V.S. and Shaw, C., 2015. *Essential chemistry for formulators of semisolid and liquid dosages*. Academic Press.

Kung, C.H., Sow, P.K., Zahiri, B. and Mérida, W., 2019. Assessment and interpretation of surface wettability based on sessile droplet contact angle measurement: challenges and opportunities. *Advanced Materials Interfaces*, *6*(18), p.1900839.

Kurganskaya, I. and Churakov, S.V., 2018. Carbonate dissolution mechanisms in the presence of electrolytes revealed by grand canonical and kinetic Monte Carlo Modeling. *The Journal of Physical Chemistry C*, *122*(51), pp.29285-29297.

Kuyucak, S. and Chung, S.H., 1994. Temperature dependence of conductivity in electrolyte solutions and ionic channels of biological membranes. *Biophysical Chemistry*, *52*(1), pp.15-24.

Kwok, D.Y. and Neumann, A.W., 1999. Contact angle measurement and contact angle interpretation. *Advances in colloid and interface science*, *81*(3), pp.167-249.

Le Gallo, Y. and De Dios, J.C., 2018. Geological model of a storage complex for a CO_2 storage operation in a naturally-fractured carbonate formation. *Geosciences*, *8*(9), p.354.

Leduc, M., Matthews, H.D. and de Elía, R., 2016. Regional estimates of the transient climate response to cumulative CO_2 emissions. *Nature Climate Change*, *6*(5), pp.474-478.

Leetaru, H.E., Frailey, S., Morse, D., Finley, R.J., Rupp, J.A., Drahozval, J.A. and McBride, J.H., 2009. Carbon sequestration in the Mt. Simon Sandstone saline reservoir. In *Carbon Dioxide Sequestration in Geological Media—State of the Science*. American Association of Petroleum Geologists.

Leroy, P., Devau, N., Revil, A. and Bizi, M., 2013. Influence of surface conductivity on the apparent zeta potential of amorphous silica nanoparticles. *Journal of Colloid and Interface Science*, *410*, pp.81-93.

Li, S., Collini, H. and Jackson, M.D., 2018. Anomalous zeta potential trends in natural sandstones. *Geophysical Research Letters*, *45*(20), pp.11-068.

Li, S., Leroy, P., Heberling, F., Devau, N., Jougnot, D. and Chiaberge, C., 2016. Influence of surface conductivity on the apparent zeta potential of calcite. *Journal of Colloid and Interface Science, 468*, pp.262-275.

Li, X. and Fang, Z.M., 2014. Current status and technical challenges of CO_2 storage in coal seams and enhanced coalbed methane recovery: an overview. *International Journal of Coal Science & Technology*, *1*(1), pp.93-102.

Li, X., Boek, E.S., Maitland, G.C. and Trusler, J.M., 2012. Interfacial Tension of (Brines+ CO_2): $CaCl_2$ (aq), $MgCl_2$ (aq), and Na_2SO_4 (aq) at Temperatures between (343 and 423) K, Pressures between (2 and 50) MPa, and Molalities of (0.5 to 5) mol· kg^{-1}. *Journal of Chemical & Engineering Data*, *57*(5), pp.1369-1375.

Li, X., Peng, C., Crawshaw, J.P., Maitland, G.C. and Trusler, J.M., 2018. The pH of CO_2-saturated aqueous NaCl and $NaHCO_3$ solutions at temperatures between 308 K and 373 K at pressures up to 15 MPa. *Fluid Phase Equilibria*, *458*, pp.253-263.

Liebscher, A., Martens, S., Moller, F. and Kuhn, M., 2013. On-shore CO_2 storage at the Ketzin pilot site in Germany. In Gluyas J., and Mathias S. (eds). *Geological Storage of Carbon Dioxide (CO_2)*. Woodhead Publishing, pp. 287-300.

Liu, L., Suto, Y., Bignall, G., Yamasaki, N. and Hashida, T., 2003. CO_2 injection to granite and sandstone in experimental rock/hot water systems. *Energy Conversion and Management*, *44*(9), pp.1399-1410.

Liu, L., Xu, W.Y., Wang, H.L., Wang, W. and Wang, R.B., 2016. Permeability evolution of granite gneiss during triaxial creep tests. *Rock Mechanics and Rock Engineering*, *49*(9), pp.3455-3462.

Liu, Y., Hou, M., Yang, G. and Han, B., 2011. Solubility of CO_2 in aqueous solutions of NaCl, KCl, $CaCl_2$ and their mixed salts at different temperatures and pressures. *The Journal of Supercritical Fluids*, *56*(2), pp.125-129.

Lorne, B., Perrier, F. and Avouac, J.P., 1999. Streaming potential measurements: 1. Properties of the electrical double layer from crushed rock samples. *Journal of Geophysical Research: Solid Earth*, *104*(B8), pp.17857-17877.

Lu, T., Gilfedder, B.S., Peng, H., Niu, G. and Frei, S., 2021. Effects of clay minerals on the transport of nanoplastics through water-saturated porous media. *Science of the Total Environment*, *796*, p.148982.

Luo, J., Zhu, Y., Guo, Q., Tan, L., Zhuang, Y., Liu, M., Zhang, C., Xiang, W. and Rohn, J., 2017. Experimental investigation of the hydraulic and heat-transfer properties of artificially fractured granite. *Scientific reports*, *7*(1), pp.1-10.

Lv, P., Liu, Y., Wang, Z., Liu, S., Jiang, L., Chen, J. and Song, Y., 2017. In situ local contact angle measurement in a CO_2–brine–sand system using microfocused X-ray CT. *Langmuir*, *33*(14), pp.3358-3366.

MacAllister, D.J., Jackson, M.D., Butler, A.P. and Vinogradov, J., 2018. Remote detection of saline intrusion in a coastal aquifer using borehole measurements of self-potential. *Water Resources Research*, *54*(3), pp.1669-1687.

MacAllister, D.J., Jackson, M.D., Butler, A.P. and Vinogradov, J., 2016. Tidal influence on self-potential measurements. *Journal of Geophysical Research: Solid Earth*, 121(12), pp.8432-8452.

MacDonald, J. M., Magee, C. and Goodenough, K. M. 2017. Dykes as physical buffers to metamorphic overprinting: an example from the Archaean–Palaeoproterozoic Lewisian Gneiss Complex of NW Scotland. *Scottish Journal of Geology*, *53*, pp.41-52.

Matter, J.M., Stute, M., Snæbjörnsdottir, S.Ó., Oelkers, E.H., Gislason, S.R., Aradottir, E.S., Sigfusson, B., Gunnarsson, I., Sigurdardottir, H., Gunnlaugsson, E. and Axelsson, G., 2016. Rapid carbon mineralization for permanent disposal of anthropogenic carbon dioxide emissions. *Science*, *352*(6291), pp.1312-1314.

McBride-Wright, M., Maitland, G.C. and Trusler, J.M., 2015. Viscosity and density of aqueous solutions of carbon dioxide at temperatures from (274 to 449) K and at pressures up to 100 MPa. *Journal of Chemical & Engineering Data*, *60*(1), pp.171-180.

Mendez, J.N., Jin, Q., González, M., Zhang, X., Lobo, C., Boateng, C.D. and Zambrano, M., 2020. Fracture characterization and modeling of karsted carbonate reservoirs: a case study in Tahe oilfield, Tarim Basin (western China). *Marine and Petroleum Geology*, *112*, p.104104.

Millero, F.J., 2007. The marine inorganic carbon cycle. *Chemical reviews*, *107*(2), pp.308-341.

Millero, F.J., DiTrolio, B., Suarez, A.F. and Lando, G., 2009. Spectroscopic measurements of the pH in NaCl brines. *Geochimica et Cosmochimica Acta*, *73*(11), pp.3109-3114.

Mirzaei-Paiaman, A., 2022. Analysis of the bounded and unbounded forms of USBM wettability index. *Energy Geoscience*, *3*(1), pp.94-102.

Misra, R.P., de Souza, J.P., Blankschtein, D. and Bazant, M.Z., 2019. Theory of surface forces in multivalent electrolytes. *Langmuir*, *35*(35), pp.11550-11565.

Molari, M., Guilini, K., Lott, C., Weber, M., de Beer, D., Meyer, S., Ramette, A., Wegener, G., Wenzhöfer, F., Martin, D. and Cibic, T., 2018. CO_2 leakage alters biogeochemical and ecological functions of submarine sands. *Science Advances*, *4*(2), pp.eaao2040.

Moore, J.R., Glaser, S.D., Morrison, H.F. and Hoversten, G.M., 2004. The streaming potential of liquid carbon dioxide in Berea sandstone. *Geophysical research letters*, 31(17).

Morgan, F. D., E. R. Williams, and T. R. Madden., 1989. Streaming potential properties of Westerley granite and applications, *Journal of Geophysical Research: Solid Earth*, *94*(B9), pp.12,449– 12,461.

Morra, M., Cassinelli, C., Torre, E. and Iviglia, G., 2018. Permanent wettability of a novel, nanoengineered, clinically available, hyaluronan-coated dental implant. *Clinical and Experimental Dental Research*, *4*(5), pp.196-205.

Morrow, N.R. and Heller, J.P., 1985. Fundamentals of enhanced recovery. In Donaldson, E., Chilingarian, G., and Yen, T (eds) in *Enhanced Oil Recovery, I, Fundamentals and Analyses.* Elsevier, pp. 47-44.

Morrow, N.R., 1975. The effects of surface roughness on contact: angle with special reference to petroleum recovery. *Journal of Canadian Petroleum Technology*, *14*(4).

Morse, J.W. and Arvidson, R.S., 2002. The dissolution kinetics of major sedimentary carbonate minerals. *Earth-Science Reviews*, *58*(1-2), pp.51-84.

Muggeridge, A., Cockin, A., Webb, K., Frampton, H., Collins, I., Moulds, T. and Salino, P., 2014. Recovery rates, enhanced oil recovery and technological limits. *Philosophical Transactions of the Royal Society A*, *372* (2006), pp.20120320.

Nabi, A., Sun, R., Ansari, U., Kou, G., Lv, D., Cao, G. and Aixian, H., 2019. Comparative Analysis on the Minimum Miscible Pressure Regulation and Control Between Oil and CO_2. In *International Field Exploration and Development Conference,* Springer, pp. 3566-3579.

Nachbaur, L., Nkinamubanzi, P.C., Nonat, A. and Mutin, J.C., 1998. Electrokinetic properties which control the coagulation of silicate cement suspensions during early age hydration. *Journal of Colloid and Interface Science*, *202*(2), pp.261-268.

Navarro, J., Raghuraman, B., Bryant, I.D. and Supp, M., 2006. Streaming potential applications in oil fields. In *SPE Annual Technical Conference and Exhibition*. Society of Petroleum Engineers

Neuzil, C.E. and Tracy, J.V., 1981. Flow through fractures. *Water Resources Research*, *17*(1), pp.191-199.

Nishimura, S., Tateyama, H., Tsunematsu, K. and Jinnai, K., 1992. Zeta potential measurement of muscovite mica basal plane-aqueous solution interface by means of plane interface technique. *Journal of Colloid and Interface Science*, 152(2), pp.359-367.

NOAA, 2020. Global Monitoring Laboratory. *National Oceanic and Atmospheric Administration*. Available at *https://gml.noaa.gov/*.

Nyabeze, W. and McFadzean, B., 2016. Adsorption of copper sulphate on PGM-bearing ores and its influence on froth stability and flotation kinetics. *Minerals Engineering*, *92*, pp.28-36.

Ogilvy, R.D., Meldrum, P.I., Kuras, O., Wilkinson, P.B., Chambers, J.E., Sen, M., Pulido-Bosch, A., Gisbert, J., Jorreto, S., Frances, I. and Tsourlos, P., 2009. Automated monitoring of coastal aquifers with electrical resistivity tomography. *Near Surface Geophysics*, *7*(5-6), pp.367-376.

Owens, W.W. and Archer, D., (1971). The effect of rock wettability on oil-water relative permeability relationships. *Journal of Petroleum Technology*, 23(07), pp.873-878.

Palandri, J.L. and Kharaka, Y.K., 2004. *A compilation of rate parameters of water-mineral interaction kinetics for application to geochemical modeling*. U.S Geological Survey.

Parkhurst, D.L. and Appelo, C.A.J., 2013. *Description of input and examples for PHREEQC version 3: a computer program for speciation, batch-reaction, one-dimensional transport, and inverse geochemical calculations*. U.S. Geological Survey.

Patil, R.H., Colls, J.J. and Steven, M.D., 2010. Effects of CO_2 gas as leaks from geological storage sites on agro-ecosystems. *Energy*, *35*(12), pp.4587-4591.

Peng, C., Crawshaw, J.P., Maitland, G.C., Trusler, J.M. and Vega-Maza, D., 2013. The pH of CO_2-saturated water at temperatures between 308 K and 423 K at pressures up to 15 MPa. *The Journal of Supercritical Fluids*, *82*, pp.129-137.

Peng, R., Di, B., Glover, P.W., Wei, J., Lorinczi, P., Liu, Z. and Li, H., 2020. Seismo-electric conversion in shale: experiment and analytical modelling. *Geophysical Journal International*, *223*(2), pp.725-745.

Peng, R., Di, B., Glover, P.W., Wei1, J., Lorinczi, P., Ding, P., Liu, Z., Zhang, Y. and Wu, M., 2019. The effect of rock permeability and porosity on seismoelectric conversion: experiment and analytical modelling. *Geophysical Journal International*, *219*(1), pp.328-345.

Pentland, C.H., El-Maghraby, R., Iglauer, S. and Blunt, M.J., 2011. Measurements of the capillary trapping of super-critical carbon dioxide in Berea sandstone. *Geophysical Research Letters*, 38(6).

Phan, K.K.T., Truong, T., Wang, Y. and Bhandari, B., 2021. Formation and stability of carbon dioxide nanobubbles for potential applications in food processing. *Food Engineering Reviews*, *13*(1), pp.3-14.

Pires, J.C.M., Martins, F.G., Alvim-Ferraz, M.C.M. and Simões, M., 2011. Recent developments on carbon capture and storage: an overview. *Chemical Engineering Research and Design*, *89*(9), pp.1446-1460.

Pitzer, K.S., 1973. Thermodynamics of electrolytes. I. Theoretical basis and general equations. *The Journal of Physical Chemistry*, *77*(2), pp.268-277.

Pogge von Strandmann, P.A.E., Burton, K.W., Snæbjörnsdóttir, S.O., Sigfússon, B., Aradóttir, E.S., Gunnarsson, I., Alfredsson, H.A., Mesfin, K.G., Oelkers, E.H., Gislason, S.R., 2019. Rapid CO_2 mineralisation into calcite at the CarbFix storage site quantified using calcium isotopes. *Nature Communication*s,*10*, pp.1–7.

Pokrovsky, O.S. and Schott, J., 2001. Kinetics and mechanism of dolomite dissolution in neutral to alkaline solutions revisited. *American Journal of Science*, *301*(7), pp.597-626.

Pokrovsky, O.S. and Schott, J., 2002. Surface chemistry and dissolution kinetics of divalent metal carbonates. *Environmental Science & Technology*, *36*(3), pp.426-432.

Pokrovsky, O.S., Mielczarski, J.A., Barres, O. and Schott, J., 2000. Surface speciation models of calcite and dolomite/aqueous solution interfaces and their spectroscopic evaluation. *Langmuir*, *16*(6), pp.2677-2688.

Qi, R., LaForce, T.C., Blunt, M.J., 2009. Design of carbon dioxide storage in aquifers. *International Journal of Greenhouse Gas Control, 3*, pp.195–205.

Qiao, C., Johns, R., Li, L. and Xu, J., 2015a. Modeling low salinity waterflooding in mineralogically different carbonates. In: SPE *Annual Technical Conference and Exhibition, September 2015, Texas, USA*. Society of Petroleum Engineers.

Qiao, C., Li, L., Johns, R.T. and Xu, J., 2015b. A mechanistic model for wettability alteration by chemically tuned waterflooding in carbonate reservoirs. *SPE Journal*, *20*(4), pp.767-783.

Rahman, T., Lebedev, M., Barifcani, A. and Iglauer, S., 2016. Residual trapping of supercritical CO_2 in oil-wet sandstone. *Journal of Colloid and Interface Science*, *469*, pp.63-68.

Rathmell, J.J., Braun, P.H. and Perkins, T.K., 1973. Reservoir waterflood residual oil saturation from laboratory tests. *Journal of Petroleum Technology*, *25*(2), pp.175-185.

Raza, A., Gholami, R., Rezaee, R., Rasouli, V. and Rabiei, M., 2019. Significant aspects of carbon capture and storage–A review. *Petroleum*, *5*(4), pp.335-340.

Ré, C.L., Kaszuba, J.P., Moore, J.N. and McPherson, B.J., 2014. Fluid–rock interactions in CO_2-saturated, granite-hosted geothermal systems: Implications for natural and engineered systems from geochemical experiments and models. *Geochimica et Cosmochimica Acta*, *141*, pp.160-178.

Reppert, P. M., and F. D. Morgan., 2003. Temperature-dependent streaming potentials: 2. Laboratory, *Journal of Geophysical Research: Solid Earth, 108*(B11), pp.2547.

Revil, A. and Cerepi, A., 2004. Streaming potentials in two-phase flow conditions. *Geophysical Research Letters*, *31*(11).

Revil, A. and Jardani, A. 2013. *The Self-Potential Method: Theory and Applications in Environmental Geosciences*. Cambridge: Cambridge University Press.

Revil, A. and Pezard, P.A., 1998. Streaming electrical potential anomaly along faults in geothermal areas. *Geophysical Research Letters*, *25*(16), pp.3197-3200.

Revil, A., Pezard, P.A., Glover, P.W.J., 1999. Streaming potential in porous media: 1. Theory of the zeta potential. *Journal of Geophysical Research: Solid Earth*, *104*(B9), pp.20021–2003.

Ringrose, P.S., Roberts, D.M., Gibson-Poole, C.M., Bond, C., Wightman, R., Taylor, M., Raikes, S., Iding, M. and Østmo, S., 2011. Characterisation of the krechba CO_2 storage site: critical elements controlling injection performance. *Energy Procedia*, *4*, pp.4672-4679.

Ronov, A.B. and Yaroshevsky, A.A., 1969. Chemical Composition of the Earth's Crust. In Hart, P. (ed). *The Earth's Crust and Upper Mantle*, 13, pp.37-57.

Roubinet, D.; Linde, N.; Jougnot, D.; Irving, J. 2016. Streaming potential modeling in fractured rock: Insights into the identification of hydraulically active fractures. *Geophysical Research Letters*, *43*, pp.4937–4944.

Ruan, S., Chen, S., Zhu, X., Zeng, Q., Liu, Y., Lai, J. and Yan, D., 2021. Matrix wettability and mechanical properties of geopolymer cement-polydimethylsiloxane (PDMS) hybrids. *Cement and Concrete Composites*, *124*, p.104268.

Rudawska, A., 2019. Surface treatment in bonding technology. Academic Press.

Ruiz-Agudo, E., Putnis, C.V., Jiménez-López, C. and Rodriguez-Navarro, C., 2009. An atomic force microscopy study of calcite dissolution in saline solutions: The role of magnesium ions. *Geochimica et Cosmochimica Acta*, *73*(11), pp.3201-3217.

Rupp, F., Liang, L., Geis-Gerstorfer, J., Scheideler, L. and Hüttig, F., 2018. Surface characteristics of dental implants: A review. *Dental Materials*, *34*(1), pp.40-57.

Saunders, J.H., Jackson, M.D., Gulamali, M.Y., Vinogradov, J. and Pain, C.C., 2012. Streaming potentials at hydrocarbon reservoir conditions. *Geophysics*, *77*(1), pp.E77-E90.

Schmidt, R.B., Bucher, K., Drüppel, K. and Stober, I., 2017. Experimental interaction of hydrothermal Na-Cl solution with fracture surfaces of geothermal reservoir sandstone of the Upper Rhine Graben. *Applied Geochemistry*, *81*, pp.36-52.

Shehata, A.M. and Nasr-El-Din, H.A., 2015. Zeta potential measurements: Impact of salinity on sandstone minerals. In: SPE *International Symposium on Oilfield Chemistry, April 2015, Texas, USA.* Society of Petroleum Engineers.

Shi, J.Q., Imrie, C., Sinayuc, C., Durucan, S., Korre, A. and Eiken, O., 2013. Snøhvit CO_2 storage project: Assessment of CO_2 injection performance through history matching of the injection well pressure over a 32-months period. *Energy Procedia*, *37*, pp.3267-3274.

Sill, W., 1983. Self-potential modeling from primary flows, *Geophysics, 48* (1), pp.76-86.

Snæbjörnsdóttir, S.Ó., Gislason, S.R., Galeczka, I.M. and Oelkers, E.H., 2018. Reaction path modelling of in-situ mineralisation of CO_2 at the CarbFix site at Hellisheidi, SW-Iceland. *Geochimica et Cosmochimica Acta*, *220*, pp.348-366.

Snæbjörnsdóttir, S.Ó., Sigfússon, B., Marieni, C., Goldberg, D., Gislason, S.R., Oelkers, E.H., 2020. Carbon dioxide storage through mineral carbonation. *Nature Reviews Earth & Environment, 1*, pp.90–102.

Soltanian, M.R., Amooie, M.A., Gershenzon, N., Dai, Z., Ritzi, R., Xiong, F., Cole, D. and Moortgat, J., 2017. Dissolution trapping of carbon dioxide in heterogeneous aquifers. *Environmental Science & Technology*, *51*(13), pp.7732-7741.

Song, J., Rezaee, S., Zhang, L., Zhang, Z., Puerto, M., Wani, O.B., Vargas, F., Alhassan, S., Biswal, S.L. and Hirasaki, G.J., 2019. Characterizing the influence of organic carboxylic acids and inorganic silica impurities on the surface charge of natural carbonates using an extended surface complexation model. *Energy & Fuels*, *33*(2), pp.957-967.

Soroush, M., Wessel-Berg, D. and Kleppe, J., 2013, April. Effects of wetting behaviour on residual trapping in CO_2-brine systems. In *SPE Western Regional & AAPG Pacific Section Meeting 2013 Joint Technical Conference*.

Sprunt, E.S., Mercer, T.B. and Djabbarah, N.F., 1994. Streaming potential from multiphase flow. *Geophysics*, *59*(5), pp.707-711.

Thanh, L.D. and Sprik, R., 2016. Zeta potential in porous rocks in contact with monovalent and divalent electrolyte aqueous solutions. *Geophysics*, *81*(4), pp.D303-D314.

Thanh, L.D., Jougnot, D., Do, P.V., Hue, D.T.M., Thuy, T.T.C. and Tuyen, V.P., 2021. Predicting electrokinetic coupling and electrical conductivity in fractured media using a fractal distribution of tortuous capillary fractures. *Applied Sciences*, *11*(11), p.5121.

Thompson, D.W. and Pownall, P.G., 1989. Surface electrical properties of calcite. *Journal of Colloid and Interface Science*, *131*(1), pp.74-82.

Tokunaga, T.K., 2012. DLVO-based estimates of adsorbed water film thicknesses in geologic CO_2 reservoirs. *Langmuir*, *28*(21), pp.8001-8009.

Tong, D., Trusler, J.M. and Vega-Maza, D., 2013. Solubility of CO_2 in aqueous solutions of $CaCl_2$ or $MgCl_2$ and in a synthetic formation brine at temperatures up to 423 K and pressures up to 40 MPa. *Journal of Chemical & Engineering Data*, *58*(7), pp.2116-2124.

Tosha, T.; Matsushima, N.; Ishido, T. 2003. Zeta potential measured for an intact granite sample at temperatures to 200°C. *Geophysical Research Letters, 30*, pp.1295.

Treiber, L.E. and Owens, W.W., 1972. A laboratory evaluation of the wettability of fifty oil-producing reservoirs. *Society of petroleum engineers journal*, *12*(06), pp.531-540.

Tudek, J., Crandall, D., Fuchs, S., Werth, C.J., Valocchi, A.J., Chen, Y. and Goodman, A., 2017. In situ contact angle measurements of liquid CO2, brine, and Mount Simon sandstone core using micro X-ray CT imaging, sessile drop, and Lattice Boltzmann modeling. *Journal of Petroleum Science and Engineering*, *155*, pp.3-10.

Udoh, T. and Vinogradov, J., 2021. Controlled salinity-biosurfactant enhanced oil recovery at ambient and reservoir temperatures—an experimental study. *Energies*, *14*(4), p.1077.

Ushikubo, F.Y., Enari, M., Furukawa, T., Nakagawa, R., Makino, Y., Kawagoe, Y. and Oshita, S., 2010. Zeta-potential of micro-and/or nano-bubbles in water produced by some kinds of gases. *IFAC Proceedings Volumes*, *43*(26), pp.283-288.

Valle, L.M., Rodríguez, R., Grima, C. and Martínez, C., 2018. Effects of supercritical CO_2 injection on sandstone wettability and capillary trapping. *International Journal of Greenhouse Gas Control*, *78*, pp.341-348.

Van Cappellen, P., Charlet, L., Stumm, W. and Wersin, P., 1993. A surface complexation model of the carbonate mineral-aqueous solution interface. *Geochimica et Cosmochimica Acta*, *57*(15), pp.3505-3518.

Vidyadhar, A. and Rao, K.H., 2007. Adsorption mechanism of mixed cationic/anionic collectors in feldspar-quartz flotation system. *Journal of Colloid and Interface Science*, *306*(2), pp.195-204.

Vidyadhar, A., Rao, K.H. and Forssberg, K.S.E., 2002. Adsorption of n-tallow 1, 3-propanediamine–dioleate collector on albite and quartz minerals, and selective flotation of albite from greek stefania feldspar ore. *Journal of Colloid and Interface Science*, *248*(1), pp.19-29.

Villegas-Jiménez, A., Mucci, A. and Whitehead, M.A., 2009. Theoretical insights into the hydrated (10.4) calcite surface: Structure, energetics, and bonding relationships. *Langmuir*, *25*(12), pp.6813-6824.

Vinogradov, J. and Jackson, M.D., 2011. Multiphase streaming potential in sandstones saturated with gas/brine and oil/brine during drainage and imbibition. *Geophysical Research Letters*, 38(1).

Vinogradov, J. and Jackson, M.D., 2015. Zeta potential in intact natural sandstones at elevated temperatures. *Geophysical Research Letters*, *42*(15), pp.6287-6294.

Vinogradov, J., Hidayat, M., Kumar, Y., Healy, D. and Comte, J.C., 2022a. Laboratory measurements of zeta potential in fractured Lewisian gneiss: implications for the characterization of flow in fractured crystalline bedrock. *Applied Sciences*, *12*(1), p.180.

Vinogradov, J., Hidayat, M., Sarmadivaleh, M., Derksen, J., Vega-Maza, D., Iglauer, S., Jougnot, D., Azaroual, M. and Leroy, P., 2022b. Predictive surface complexation model of the calcite-aqueous solution interface: The impact of high concentration and complex composition of brines. *Journal of Colloid and Interface Science*, *609*, pp.852-867.

Vinogradov, J., Hill, R. and Jougnot, D., 2021. Influence of pore size distribution on the electrokinetic coupling coefficient in two-phase flow conditions. *Water*, *13*(17), p.2316.

Vinogradov, J., Jaafar, M.Z. and Jackson, M.D., 2010. Measurement of streaming potential coupling coefficient in sandstones saturated with natural and artificial brines at high salinity. *Journal of Geophysical Research: Solid Earth*, *115*(B12).

Vinogradov, J., Jackson, M.D. and Chamerois, M., 2018. Zeta potential in sandpacks: Effect of temperature, electrolyte pH, ionic strength and divalent cations. *Colloids and Surfaces A: Physicochemical and Engineering Aspects*, *553*, pp.259-271.

Vogt, C., Klitzsch, N. and Rath, V., 2014. On self-potential data for estimating permeability in enhanced geothermal systems. *Geothermics*, *51*, pp.201-213.

von Strandmann, P.A.P., Burton, K.W., Snæbjörnsdóttir, S.O., Sigfússon, B., Aradóttir, E.S., Gunnarsson, I., Alfredsson, H.A., Mesfin, K.G., Oelkers, E.H. and Gislason, S.R., 2019. Rapid CO_2 mineralisation into calcite at the CarbFix storage site quantified using calcium isotopes. *Nature Communications*, *10*(1), pp.1-7.

Wainipee, W., Cuadros, J., Sephton, M.A., Unsworth, C., Gill, M.G., Strekopytov, S. and Weiss, D.J., 2013. The effects of oil on As (V) adsorption on illite, kaolinite, montmorillonite and chlorite. *Geochimica et Cosmochimica Acta*, *121*, pp.487-502.

Walker, E. and Glover, P.W.J., 2018. Measurements of the relationship between microstructure, pH, and the streaming and zeta potentials of sandstones. *Transport in porous media*, *121*, pp.183-206.

Walker, E., Glover, P.W.J. and Ruel, J., 2014. A transient method for measuring the DC streaming potential coefficient of porous and fractured rocks. *Journal of Geophysical Research: Solid Earth*, *119*(2), pp.957-970.

Wang, W., Cong, J., Deng, J., Weng, X., Lin, Y., Huang, Y. and Peng, T., 2018. Developing effective separation of feldspar and quartz while recycling tailwater by HF pretreatment. *Minerals*, *8*(4), pp.149.

Weaver, B. L., and Tarney, J., 1981. Lewisian Gneiss geochemistry and Archaean crustal development models, *Earth and Planetary Science Letters, 55,* pp.171– 180.

Whittaker, S.G. and Rostron, B., 2003. Geologic storage of CO_2 in a carbonate reservoir within the Williston Basin, Canada: an update. In *Greenhouse Gas Control Technologies-6th International Conference*, pp. 385-390.

Wolthers, M., Charlet, L. and Van Cappellen, P., 2008. The surface chemistry of divalent metal carbonate minerals; a critical assessment of surface charge and potential data using the charge distribution multi-site ion complexation model. *American Journal of science*, *308*(8), pp.905-941.

Xie, Q., Saeedi, A., Pooryousefy, E. and Liu, Y., 2016. Extended DLVO-based estimates of surface force in low salinity water flooding. *Journal of Molecular Liquids*, *221*, pp.658-665.

Xie, Y., Xiang, H., Shi, P., Guo, J. and Wang, H., 2017. Enhanced separator wettability by LiTFSI and its application for lithium metal batteries. *Journal of Membrane Science*, *524*, pp.315-320.

Yang, J. and Zhou, Y., 2020. An automatic in situ contact angle determination based on level set method. *Water Resources Research*, *56*(7), pp.e2020WR027107.

Yeh, I.C. and Berkowitz, M.L., 1999. Dielectric constant of water at high electric fields: Molecular dynamics study. *The Journal of Chemical Physics*, *110*(16), pp.7935-7942.

Yuan, J. and Pruett, R.J., 1998. Zeta potential and related properties of kaolin clays from Georgia. *Mining, Metallurgy & Exploration*, *15*(1), pp.50-52.

Yukselen-Aksoy, Y. and Kaya, A., 2011. A study of factors affecting on the zeta potential of kaolinite and quartz powder. *Environmental Earth Sciences*, *62*(4), pp.697-705.

Zanganeh, P., Goharrizi, A.S., Ayatollahi, S., Feilizadeh, M. and Dashti, H., 2020. Efficiency improvement of solar stills through wettability alteration of the condensation surface: An experimental study. *Applied Energy*, *268*, pp.114923.

Zeebe, R.E. and Wolf-Gladrow, D., 2001. *CO_2 in seawater: equilibrium, kinetics, isotopes*. Elsevier.

Zhao, H., Dilmore, R., Allen, D.E., Hedges, S.W., Soong, Y. and Lvov, S.N., 2015a. Measurement and modeling of CO_2 solubility in natural and synthetic formation brines for CO_2 sequestration. *Environmental science & technology*, *49*(3), pp.1972-1980.

Zhao, H., Dilmore, R.M. and Lvov, S.N., 2015b. Experimental studies and modeling of CO_2 solubility in high temperature aqueous $CaCl_2$, $MgCl_2$, Na_2SO_4, and KCl solutions. *AIChE Journal*, *61*(7), pp.2286-2297.

Zhao, H., Fedkin, M.V., Dilmore, R.M. and Lvov, S.N., 2015c. Carbon dioxide solubility in aqueous solutions of sodium chloride at geological conditions: Experimental results at 323.15, 373.15, and 423.15 K and 150 bar and modeling up to 573.15 K and 2000 bar. *Geochimica et Cosmochimica Acta*, *149*, pp.165-189.

Zivar, D., Pourafshary, P. and Moradpour, N., 2021. Capillary desaturation curve: does low salinity surfactant flooding significantly reduce the residual oil saturation? *Journal of Petroleum Exploration and Production*, *11*, pp.783-794.

Appendix A Compilation of experimental data

Table A.1. Summary of experimental data zeta potential in single-phase Fontainebleau sample

Solution	Pore P, MPa	CO_2 content	Confining P, MPa	T, °C	σ_w, S/m	σ_{rw}, S/m	pH	δ(pH)	μ, Pa-s	μ, Pa-s	μ, err	xCO2	ε_r	C_{EK}, mV/MPa	ζ, mV	+δ(ζ), mV	-δ(ζ), mV
NaCl	0.2	Dead	4 - 3.5	23	0.55	0.0093	7.10	0.10	9.373E-04	9.349E-04	0.26%	-	6.997E-10	-29.9	-22.111	0.65	0.65
	4.5		6.5 -7	23	0.55	0.0092	7.00	0.10	9.373E-04	9.335E-04	0.41%	-	6.997E-10	-29.9	-21.529	0.65	0.65
	7.5		10.5 - 11	23	0.56	0.0090	7.10	0.10	9.373E-04	-	-	-	6.997E-10	-29.9	-22.252	0.65	0.65
	10		12 - 12.5	23	0.55	0.0098	7.20	0.10	9.373E-04	9.321E-04	0.55%	-	6.997E-10	-30.7	-22.859	0.65	0.65
	0.2		3 - 3.5	40	0.61	0.0108	6.30	0.20	6.573E-04	6.528E-04	0.68%	-	6.491E-10	-28.8	-17.734	1.00	1.00
	4.5		6.5 -7	40	0.60	0.0105	6.30	0.20	6.572E-04	6.534E-04	0.58%	-	6.491E-10	-28.3	-17.686	1.00	1.00
	7.5		10.5 - 11	40	0.61	0.0101	6.20	0.20	6.573E-04	-	-	-	6.491E-10	-28.5	-17.974	1.00	1.00
	10		12 - 12.5	40	0.60	0.0099	6.20	0.20	6.572E-04	6.539E-04	0.51%	-	6.491E-10	-28.3	-16.890	1.00	1.00
	4.5	Live	6.5 -7	40	0.65	0.0112	3.80	0.10	6.997E-04	-	-	1.47E-02	6.491E-10	-23.6	-15.580	0.84	1.12
	7.5		10.5 - 11	40	0.64	0.0110	3.50	0.10	7.153E-04	-	-	2.00E-02	6.491E-10	-19.0	-12.280	1.55	1.12
	10		12 - 12.5	40	0.55	0.0095	3.33	0.05	7.194E-04	-	-	2.14E-02	6.491E-10	-18.1	-10.169	1.10	0.39
Na_2SO_4	0.2	Dead	3 - 3.5	23	0.34	0.0057	7.80	0.10	9.362E-04	9.229E-04	1.43%	-	6.998E-10	-56.4	-25.046	0.65	0.65
	7.5		10.5 - 11	23	0.34	0.0058	7.70	0.10	9.362E-04	-		-	6.998E-10	-55.6	-24.370	0.65	0.65
	0.2		3 - 3.5	40	0.46	0.00773	6.70	0.20	6.566E-04	6.658E-04	1.40%	-	6.491E-10	-43.1	-19.596	1.00	1.00
	7.5		10.5 - 11	40	0.46	0.0078	6.70	0.20	6.566E-04	-	-	-	6.491E-10	-44.8	-20.715	1.00	1.00
	7.5	Live	10.5 - 11	40	0.54	0.0093	3.60	0.10	7.142E-04	-	-	1.99E-02	6.491E-10	-24.1	-13.147	0.72	1.32
$CaCl_2$	0.2	Dead	3 - 3.5	23	0.37	0.0063	6.20	0.10	9.364E-04	9.179E-04	1.97%	-	6.998E-10	-26.5	-13.202	0.65	0.65
	7.5		10.5 - 11	23	0.37	0.0063	6.20	0.10	9.364E-04	9.185E-04	1.91%	-	6.998E-10	-26.9	-13.433	0.65	0.65
	0.2		3 - 3.5	40	0.51	0.0084	5.60	0.20	6.568E-04	-	-	-	6.491E-10	-25.3	-12.557	1.00	1.00
	7.5		10.5 - 11	40	0.51	0.0084	5.50	0.20	6.568E-04	-	-	-	6.491E-10	-25.4	-12.555	1.00	1.00
	7.5	Live	10.5 - 11	40	0.50	0.0085	3.17	0.05	7.157E-04	-	-	2.03E-02	6.491E-10	-17.6	-8.856	0.48	0.65
$MgCl_2$	0.2	Dead	3 - 3.5	23	0.36	0.0066	6.90	0.10	9.363E-04	-	-	-	6.998E-10	-28.0	-14.460	0.65	0.65
	7.5		10.5 - 11	23	0.36	0.0064	6.80	0.10	9.363E-04	-	-	-	6.998E-10	-28.4	-14.138	0.65	0.65
	0.2		3 - 3.5	40	0.48	0.0081	6.05	0.20	6.567E-04	-	-	-	6.491E-10	-27.4	-13.047	1.00	1.00
	7.5		10.5 - 11	40	0.48	0.0082	6.10	0.20	6.567E-04	-	-	-	6.491E-10	-27.3	-13.196	1.00	1.00
	7.5	Live	10.5 - 11	40	0.59	0.0101	3.40	0.05	7.149E-04	-	-	2.009E-02	6.491E-10	-17.8	-10.638	0.92	0.62

Directly measured
Calculated using Sanders et al., [2012]
Calculated using Islam and Carlson [2012]
Calculated using σ_{rw} and F

From Kestin et al., [1981]
From Abdulgatov and Azizov, [2006]
From Korosi and Fabuss, [1968]
xCO2 calculated from Zhao et al., [2015b, 2015c]

Table A.2. Summary of experimental data zeta potential in single-phase San Saba sample

IS,M	Pore P, MPa	CO_2 content	Confining P, MPa	T, ^oC	σ_w, S/m	pH	δ(pH)	μ, Pa-s	ε_r	C_{EK}, mV/MPa	ζ, mV	+δ(ζ), mV	-δ(ζ), mV
0.5	0.2	Dead	3.5 - 4	23	0.550	6.8	0.10	9.37E-04	7.00E-10	-21.9	-16.13	0.52	0.52
	4.5		6.5 -7	23	0.557	6.75	0.10	9.37E-04	7.00E-10	-21.0	-15.67	0.52	0.52
	7.5		10.5 - 11	23	0.553	6.75	0.10	9.37E-04	7.00E-10	-21.5	-15.93	0.52	0.52
	10		12 - 12.5	23	0.555	6.8	0.10	9.37E-04	7.00E-10	-21.3	-15.84	0.52	0.52
	0.2		3 - 3.5	40	0.601	6.5	0.10	6.57E-04	6.49E-10	-22.3	-13.57	0.65	0.65
	4.5		6.5 -7	40	0.601	6.55	0.10	6.57E-04	6.49E-10	-22.1	-13.45	0.65	0.65
	7.5		10.5 - 11	40	0.601	6.5	0.10	6.57E-04	6.49E-10	-22.4	-13.63	0.65	0.65
	10		12 - 12.5	40	0.601	6.55	0.10	6.57E-04	6.49E-10	-22.7	-13.81	0.65	0.65
	4.5	Live	6.5 -7	40	0.505	3.72	0.05	6.99E-04	6.49E-10	-18.7	-10.17	1.18	0.72
	7.5		10.5 - 11	40	0.496	3.43	0.05	7.15E-04	6.49E-10	-15.7	-8.57	0.96	1.16
	10		12 - 12.5	40	0.493	3.26	0.05	7.19E-04	6.49E-10	-13.5	-7.37	1.17	1.24
0.1	0.2	Dead	3.2	23	1.015	6.6	0.1	9.40E-04	7.00E-10	-12.4	-16.91	0.70	0.70
0.2	0.2		3.2	23	1.982	6.6	0.1	9.48E-04	6.99E-10	-7.0	-18.80	0.80	0.80
0.5	0.2		3.2	23	4.110	6.7	0.1	9.72E-04	6.98E-10	-2.9	-16.59	1.00	1.00
1	0.2		3.2	23	8.090	6.7	0.1	1.02E-03	6.97E-10	-1.3	-15.35	1.00	1.00

Table A.3. Summary of experimental data zeta potential in multi-phase Fontainebleau sample

Solution	Pore P, MPa	Confining P, MPa	σ_w, S/m	pH	δ(pH)	μ, Pa-s	ε_r	Displacement	S_w	S_{gr}	k_{rw}^e	C_{EK}, mV/MPa	ζ, mV	+δ(ζ), mV	-δ(ζ), mV
NaCl	7.5	10.5 - 11	0.637	3.50	0.10	7.153E-04	6.4908E-10	Drainage (S_{wirr})	0.32	0.68		0.0	0.0	0.0	0.0
		10.5 - 11	0.637	3.40	0.10	7.153E-04	6.4908E-10	Imbibition (1-S_{gr})	0.75	0.25	0.615292	-23.0	-14.86	2.00	2.00
		10.5 - 12	0.637	3.40	0.10	7.153E-04	6.4908E-10	Multirates				-16.1	-10.39	1.69	2.69
	10	12 - 12.5	0.554	3.33	0.05	7.194E-04	6.4910E-10	Drainage (S_{wirr})	0.30	0.70		0.0	0.0	0.0	0.0
		12 - 12.5	0.554	3.31	0.05	7.194E-04	6.4910E-10	Imbibition (1-S_{gr})	0.83	0.17	0.4548096	-25.2	-14.14	2.15	2.15
		13 - 12.5	0.554	3.31	0.05	7.194E-04	6.4910E-10	Multirates				-16.5	-9.26	2.15	1.57
Na_2SO_4	7.5	10.5 - 11	0.540	3.60	0.10	7.142E-04	6.4910E-10	Drainage (S_{wirr})	0.22	0.78		0.0	0.0	0.0	0.0
		10.5 - 11	0.540	3.64	0.10	7.142E-04	6.4910E-10	Imbibition (1-S_{gr})	0.73	0.27	0.4178677	-27.6	-15.07	2.73	2.73
		10.5 - 12	0.540	3.64	0.10	7.142E-04	6.4910E-10	Multirates				-26.2	-14.29	1.30	2.00
$CaCl_2$	7.5	10.5 - 11	0.496	3.17	0.05	7.157E-04	6.4911E-10	Drainage (S_{wirr})	0.34	0.66		0.0	0.0	0.0	0.0
		10.5 - 11	0.496	3.15	0.05	7.157E-04	6.4911E-10	Imbibition (1-S_{gr})	0.63	0.37	0.4894544	-29.9	-15.04	2.08	2.08
		10.5 - 12	0.496	3.15	0.05	7.157E-04	6.4911E-10	Multirates				-22.6	-11.37	0.94	1.01
$MgCl_2$	7.5	10.5 - 11	0.589	3.40	0.05	7.149E-04	6.4909E-10	Drainage (S_{wirr})	0.30	0.70		0.0	0.0	0.0	0.0
		10.5 - 11	0.589	3.40	0.05	7.149E-04	6.4909E-10	Imbibition (1-S_{gr})	0.64	0.36	0.4637232	-30.0	-17.90	2.34	2.34
		10.5 - 12	0.589	3.40	0.05	7.149E-04	6.4909E-10	Multirates				-23.3	-13.95	0.59	1.86

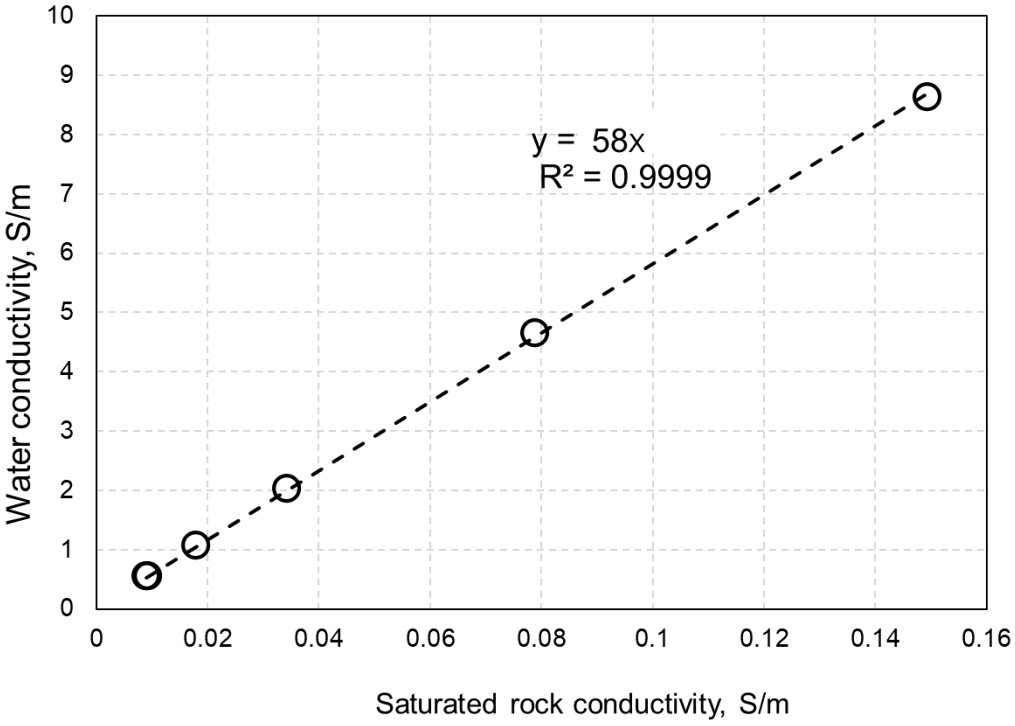

Figure A.1. Intrinsic formation factor of Fontainebleau sandstone sample

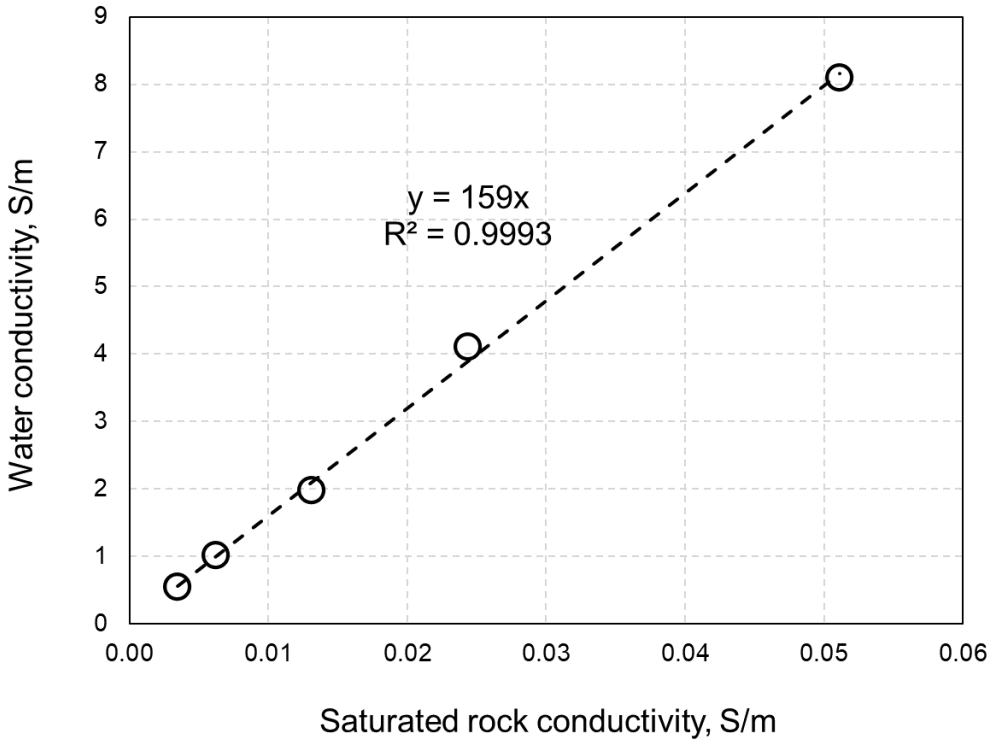

Figure A.2. Intrinsic formation factor of San Saba sandstone sample

Appendix B PHREEQC code examples

In examples below, text that follows the # symbol is not part of the code, but comments aimed at clarifying the meaning of program keywords and values

EQUILIBRIUM_PHASES #basic description
Calcite 0 20
0 is the default *saturation index*; 20 is the available *amount* of calcite in mol. The *saturation index* can be either negative or positive to hinder or enhance calcite dissolution, respectively. To prevent any dissolution or precipitation of calcite during the equilibration, the *amount* should be set to zero.

CO2(g) -3.44# defines partial CO_2 pressure at equilibrium with atmospheric air equal to $10^{-3.44}$ atm

----

EQUILIBRIUM_PHASES #example 1 – simulation of established equilibrium between calcite and water, *default* saturation index (Estaillades). The computed equilibrium concentration of Ca^{2+} dissolved in 0.05 M NaCl is pCa=3.18
Calcite 0 20
CO2(g) -3.44

SOLUTION 1
temp 25
units mol/L
Na 0.05
Cl 0.05 charge #the **charge** keyword forces charge balance of the solution by adjusting concentration of Cl
Mg 0.0000645 #experimental
S(6) 1.800E-4 #experimental
SAVE SOLUTION 1

EQUILIBRIUM_PHASES #example 2 – simulation of established equilibrium between calcite and water, *adjusted* saturation index (Ketton). The computed equilibrium concentration of Ca^{2+} dissolved in 0.05 M NaCl is pCa=2.90
Calcite 0.80 20
CO2(g) -3.44

SOLUTION 2
temp 25

units mol/L
Na 0.05
Cl 0.05 charge
Mg 0.0000645 #experimental
S(6) 0.011 #experimental
SAVE SOLUTION 2

EQUILIBRIUM_PHASES #example 3 – simulation of no established equilibrium between calcite and water (Iceland Spar), default saturation index non-zero input concentration of Ca^{2+}.
Calcite 0 0
CO2(g) -3.44

SOLUTION 3
temp 25
units mol/L
Na 0.05
Cl 0.05 charge
Ca 0.0000631 #equivalent to pCa=4.2 interpreted from Figure 2a (Alroudhan, et al., 2016) assuming 10 hours of partial equilibration during the experiment, which results in pH=9.
SAVE SOLUTION 3

Appendix C Multi-rate streaming potential experiments at $S_w = 1 - S_{gr}$

The results of all multi-rate PS experiments at $S_w = 1 - S_{gr}$, along with the summary of all multi-phase zeta potentials interpreted from the multi-rate tests and compared with the respective single-phase values are presented in the figure below.

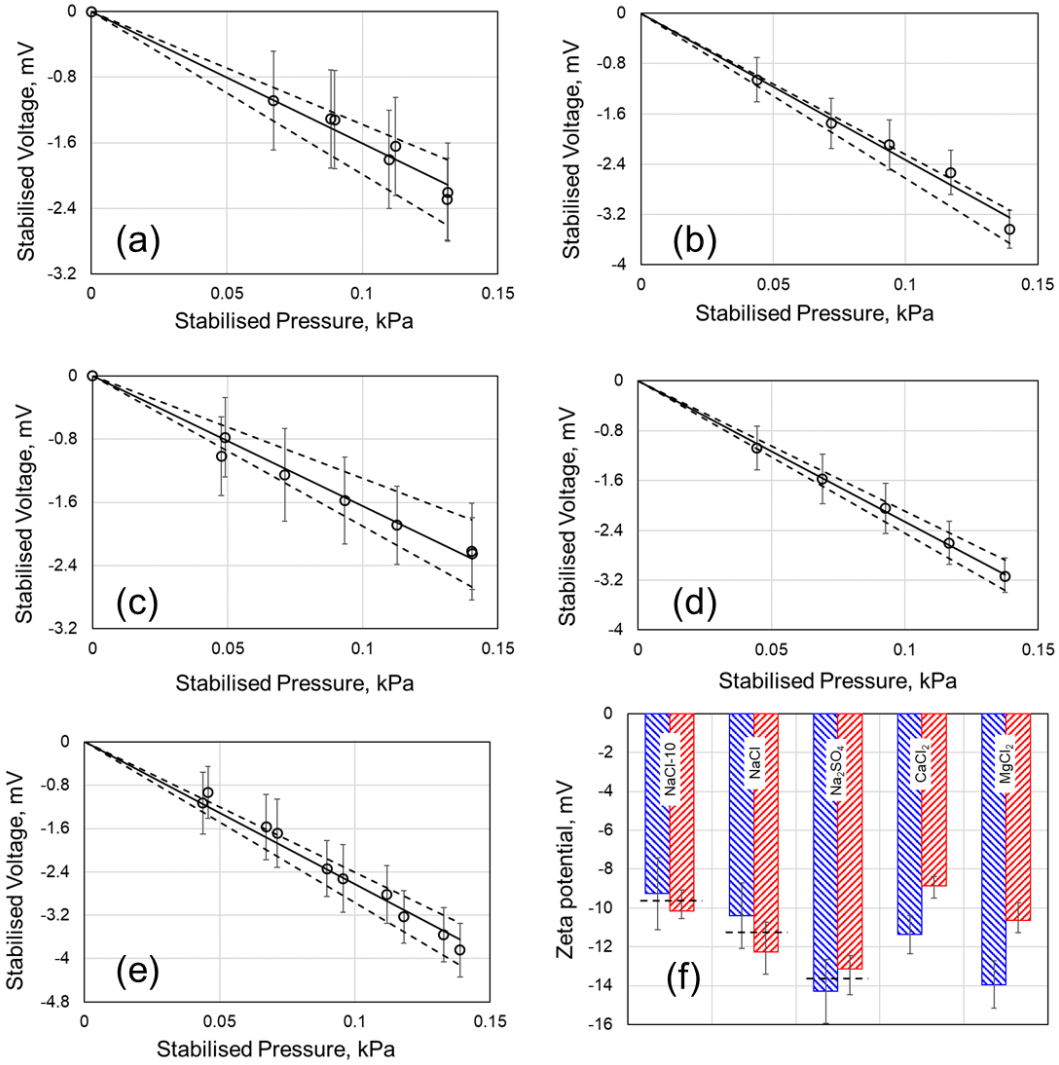

Figure C.1. The slope on the stabilised pressure difference vs stabilised voltage (solid line) corresponds to the streaming potential coupling coefficient for (a) NaCl, (b) $MgCl_2$, (c) NaCl-10, (d) $CaCl_2$ and (e) Na_2SO_4 solutions. The dashed lines represent the upper and lower limits of the coupling coefficient within the experimental errors; the variation of the slope within the limits of the dashed lines corresponds to the uncertainty of the coupling coefficient and the multi-phase zeta potential. (f) Shows the multi-phase zeta potentials in comparison with the single-phase data. As a result of invoking multiple flow rates, the error in the multi-phase zeta potential decreased thus increasing our confidence in the results of (f).

The results for $CaCl_2$ and $MgCl_2$ shown in **Figure 5.C1f** demonstrate that ζ_{cw} is unambiguously negative, consistent with our conclusion based on single-rate experiments. Moreover, as expected, a higher flow rate resulted in reduction of S_w at the end of the imbibition experiment, hence producing additional (unknown) amount of CO_2 and reducing the impact of C_water-CO_2 interfacial zeta potential on the multi-phase value thus bringing ζ_{sp} and ζ_{mp} closer to each other, and in the case of NaCl-10 eliminating the difference completely.

Appendix D Permission

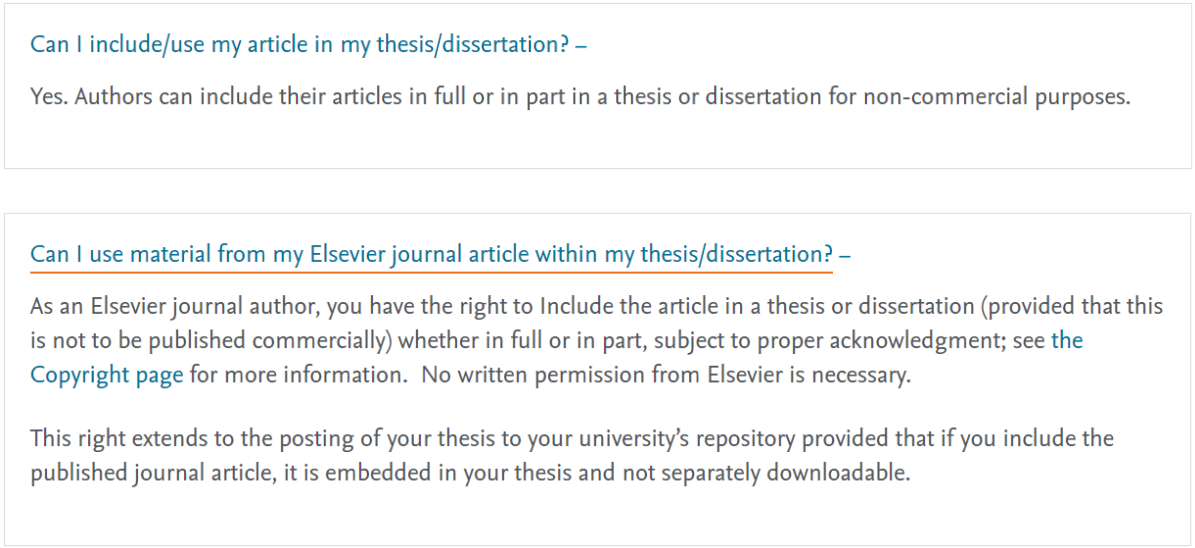

Can I include/use my article in my thesis/dissertation? –

Yes. Authors can include their articles in full or in part in a thesis or dissertation for non-commercial purposes.

Can I use material from my Elsevier journal article within my thesis/dissertation? –

As an Elsevier journal author, you have the right to Include the article in a thesis or dissertation (provided that this is not to be published commercially) whether in full or in part, subject to proper acknowledgment; see the Copyright page for more information. No written permission from Elsevier is necessary.

This right extends to the posting of your thesis to your university's repository provided that if you include the published journal article, it is embedded in your thesis and not separately downloadable.

Figure D.1. Screenshot from Elsevier permission guidelines